A STUDY OF BOND BETWEEN FIBRE REINFORCED POLYMER AND CONCRETE UNDER QUASI-STATIC AND IMPACT LOADING

by

Yashar Khalighi

B.Sc., Sharif University of Technology, 2000
M.Sc., Sharif University of Technology, 2001

A THESIS SUBMITTED IN PARTIAL FULFILLMENT OF
THE REQUIREMENTS FOR THE DEGREE OF

DOCTOR OF PHILOSOPHY

in

The Faculty of Graduate Studies

(Civil Engineering)

THE UNIVERSITY OF BRITISH COLUMBIA

(Vancouver)

August 2009

ABSTRACT

This thesis examines the typical behavior of the interface bond between a selection of FRP treatments and various types of surface preparation on reinforced concrete beams under loading. It also describes an innovative specimen that enables examination of bond properties using a notched beam under a four-point bending test. The thesis also studies the bond between FRP and concrete under impact loading and discusses the strain rate sensitivity of the FRP–concrete bond.

Three surface treatment methods (water jetting, sandblasting, and jackhammering), two bonding agents (aromatic isocyanate (ATPRIME®) and vinyl ester), and three FRP systems (sprayed glass fiber reinforced polymer, sprayed carbon fiber reinforced polymer, and glass fiber reinforced polymer wrap) were investigated. The influences of FRP bond length, specimen notch depth, and a wide range of loading rates (creep, quasi-static loading, and impact loading) on bond behavior were also investigated. The notched beam specimen was also used to understand the debonding mechanism under impact loading. An impact setup was successfully developed to measure the bond stress and fracture energy of the FRP–concrete bond.

Bond strength values and toughness values were calculated for different surface treatments, FRP application methods, and bonding agents used. The FRP–concrete bond strength was found to be a strain rate sensitive parameter that increases as the strain rate increases. A dynamic improvement factor (DIF) was defined to characterise the influence of different material and strain rate parameters on bond strength. A correlation was found to relate dynamic improvement factor to strain rate for different surface preparation types.

An attempt was made to calibrate the energy and traction parameters of the cohesive element in ABAQUS to reproduce the same load displacement behavior as observed in the test from a modeled beam. Using different ABAQUS cohesive zone parameters, the load displacement behavior of the beam was modeled. Even though the

load displacement did not completely match the tests, similar magnitudes of displacement and stress were achieved and the debonding mechanism was similar to the reality.

TABLE OF CONTENTS

LIST OF TABLES

LIST OF FIGURES

ACKNOWLEDGEMENTS

This work was carried out in the materials laboratory of the Department of Civil Engineering, University of British Columbia.

I would express my deepest gratitude to my supervisor; Dr. Nemy Banthia, for the trust, support, encouragement, and freedom that I was given throughout my doctoral program. His optimism, enthusiastic attitude toward research and everyday life accompanied me throughout the entire research program and will accompany me throughout my future career.

I would like to also thank Dr. Sydney Mindess for supporting me in my research. I learned a lot from him and Dr. Pat McGrath for his support and review of my thesis. His intelligence and sense of research amazed me. The Killam Foundation, Michael Smith Foundation, and ISIS Canada (Intelligent Sensing for Innovative Structures) are also thanked for supporting me during my doctoral program.

As experimental work formed a significant part of this research, I am deeply indebted to the technicians of the Civil Engineering Workshop for their valuable services in helping me in my experiments. In particular, my thanks go to Scott Jackson and Doug Smith, who set-up the instrumentation systems and impact machine. I would like to also thank my colleagues, Sayed M. Soleimani, Rishi Gupta, Aidin Zadeh, John Zhang and Alden Kung for their valuable help during my research.

To my family:

Thank you for your support, patience and love.

CHAPTER 1
INTRODUCTION

1.1 Introduction

As concrete ages it frequently sustains tension cracking, which has led to the desire for a system capable of strengthening and repairing old and damaged concrete. Fibre reinforced polymer (FRP) is on the leading edge of such repair systems. FRP is a fibre and resin matrix composite that is applied to concrete to boost its capacity. FRP can be applied as a wrap or as a spray; this report focuses on the spray variety of FRP.

Because demolishing and rebuilding damaged structures is expensive, a method of repairing such structures is often desired. FRP is an excellent material for this purpose because of its high tensile strength, high strength to weight ratio, and its corrosion and impact resistance. FRP is also an excellent candidate because of its ease of application. FRP can be sprayed on to the tension side of a concrete member of a structure in situ, making field application easy and efficient.

The strength added to the concrete by the FRP is dependent primarily on the strength of the surface bond between concrete and FRP. The strength of this bond can be improved with various surface preparation techniques and curing conditions.

Our understanding of the bond between FRP and concrete is very limited. Many researchers have tried to evaluate the bond using different setups. However, owing to the

major differences between the specimen and test setups, the results are not comparable. Because FRP systems are used extensively for seismic retrofits and to strengthen structures to withstand potential explosions or terrorist attacks, understanding the response of FRP under impact loading is important. No data on the impact response of the FRP–concrete bond was found in the literature. In this research, a novel specimen was developed and used under an impact setup (also developed at the University of British Columbia (UBC)) to investigate the bond under dynamic loading.

1.2 History/Background

Since the early 1900s, concrete has become the most widely used structural material for large buildings and structures in North America. However, many of these buildings and structures are approaching the end of their design life, and their concrete members are showing signs of deterioration, such as cracking and rebar corrosion. Today, in Canada and the United States, that number could easily be over 100,000. In a report published by the American Society of Civil Engineers in New Jersey, 36% of the state's bridges were found structurally deficient or functionally obsolete. The 2006 nationwide average for bridges either deficient or obsolete in the United States were approximately 25% [1.1].

The magnitude of this problem has led to the development of various repair techniques. One technique includes filling a crack with epoxy through pressure injection. Another involves bonding steel plates with adhesive to the concrete surface across the crack. However, these techniques are very expensive or have limited applications (e.g., steel plates are heavy and corrode with time), creating the need for more versatile and cost-effective solutions.

One of the most recently developed techniques involves the use of FRP jackets or sheets that are bonded to the concrete surface using epoxy resins. FRP has high tensile and bending strengths, often 10 times greater than that of steel, thus increasing the tensile strength of the concrete around the stress-concentrated area of a crack.

However, what sets FRP apart is that it is light, easy to install, has non-corrosive properties, and is aesthetically pleasing.

In the early 2000s, Professor Banthia of UBC created a spray-on FRP, which has many improved properties over those of standard FRP jackets, leading to its increasingly widespread use. The spray-on FRP has short, randomly distributed fibres, in contrast to the FRP jackets, which have continuous, unidirectional fibres. This gives the spray-on FRP better multi-purpose properties. However, the main advantage of the spray-on FRP is its simple and fast installation, which involves simply spraying the FRP on the concrete surface and then compacting it pneumatically. The FRP then bonds to the concrete surface as it hardens. The mode of installation of the spray-on FRP also allows the installer to customize the fibre content as well as the dimensions of the FRP repair, based on the specific application.

As the FRP has extremely high tensile strength, it is very unlikely that the FRP itself would ever break. The only question surrounding the effectiveness of this technique is the strength of the bond between the FRP and the concrete surface, as this is the component most likely to fail. Premature interfacial debonding research has now become the main focus of research efforts to improve the FRP–concrete system. Specifically, the research to alleviate premature debonding is focused on surface preparation of the concrete by methods such as sandblasting, treatment with a water jet, and jackhammering. As well, development of different resin types is being investigated. If advancements can be made in these areas, then FRP may be the material of choice for all structural retrofitting worldwide.

1.3 Research significance

Even though many researchers have tested the bond between FRP and concrete, their use of different test specimens with complicated geometries and setups means that their test results cannot be compared. In this research a novel specimen is developed to

evaluate the bond. This notched beam specimen can be produced in any concrete laboratory and tested under the usual four-point testing machine.

One advantage of the four-point bending test developed here is that in this test the repair material is loaded indirectly under shear, which is a far better simulation of the real-life loading scenario (for example, in a repaired girder of a bridge) than direct tensile tests and/or pull-out/push-out testing.

Another focus of this research is the study of the novel spray-on FRP system and its comparison to traditional wrapped systems.

The final phase of this Ph.D. research is dedicated to study of the behavior of a bond under impact loading. The importance of understanding this issue is clear when one considers the volume of FRP use in seismic retrofitting and strengthening against explosive loads. There is no data found in the literature on the impact response of the FRP–concrete bond.

1.4 Thesis organization

Existing test methods are reviewed and discussed in Chapter 2. In Chapter 3 are descriptions of the properties of the materials used and the way the sprayed and wrapped FRPs are applied. As well, the strain gauge application method is discussed. Chapter 4 is a step-by-step description of how and why the author has developed the novel notched beam specimen to evaluate the bond. Chapter 5 outlines development of the test specimens. In Chapter 6 the quasi-static tests are discussed and the effects of loading rate, surface preparation, and material type are studied. Chapter 7 summarizes the development of impact setup and quasi-static system, and in Chapter 8 the impact behavior of the bond is studied using the novel specimen developed and different surface preparations. Also, the performances of different methods of application (sprayed vs. wrapped) are discussed. In Chapter 9, the strain-rate sensitivity of the bond is discussed using the bond strength and ductility values (defined as the area under the load

displacement curve in this thesis) calculated in Chapter 8 for various drop heights (strain rates) and surface preparations. The debonding of the FRP–concrete interface is modeled using the program ABAQUS in Chapter 10. Chapter 11 gives conclusions and suggestions for areas for future research.

CHAPTER 2
LITERATURE REVIEW

2.1 Introduction

In this chapter, the current standard tests for bond are compared, and the limitation and disadvantages of each test method are discussed. Also, different non-experimental methods for understanding bonds are suggested, including microscopic and numerical investigations. The literature on the behavior of concrete under impact loading is also reviewed.

2.2 Existing bond tests

2.2.1 Slant shear test

In the first tests developed, the bond ultimate stress limit under combined shear and compressive load was measured. The first test of this nature was the Arizona slant shear test [2.2]. In this test the strength of 6 × 12 cylindrical repaired concrete samples are compared with control specimens. Figure 2.1 shows a diagram of this test. Repair is performed on concrete half-cylinders to give a bond plane of 30°, and the surfaces are prepared such that they represent on-site conditions. One of the major problems in that test was the difficulty in casting specimens. The test was developed and simplified the test, using rectangular test specimens instead of cylindrical ones [2.3]. The Arizona slant shear test can also be used for testing crack repair materials and repair mortars. As

reported by Meier [2.2], this method has been recommended in British Standard: BS 6319: Methods for testing concrete repair materials.

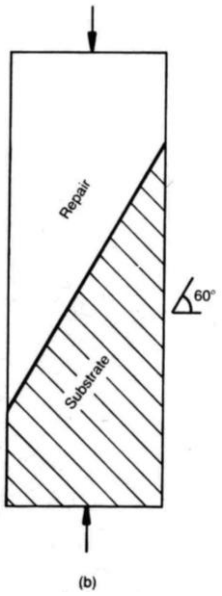

Figure 2.1. *Slant shear test.*

Another type of test that has also been developed to measure the bond properties is the pull-off test. In this test, bond strength is measured directly by applying a direct tensile load to a core of repair/substrate that is separated from the main body. Other attempts have been made to apply shear forces directly to a repair bond using torque instead of tension. The major advantage of these tension and torque pull-off tests is the capability of using them in situ in order to measure bond properties in real conditions [2.2].

A number of other tests are mentioned in a RILEM technical report; these include direct tensile tests, double shear tests, bending tests, and peel tests [2.2].

2.2.2 Core pull-off test (applicable to cementitious and FRP patches)

The pull-off test method is a tensile test method. Unlike the other tests that are used for laboratory testing purposes, this test can be used in the field in order to measure real bond properties and evaluate real conditions.

In this test a "partial core" is separated by drilling through the repair and substrate, and a metal dolly, glued to the end of the core, is used to apply tension load (Figure 2.2). Details and technique are reported in a recent CIRIA report [2.3]. It has been shown that the core pull-off test is a good method to minimize the effects of flaws, stress concentration, and mismatch properties. The technique is sensitive to eccentricity of loading, coring depth, and dolly stiffness. A well-designed experiment can remove, or at least minimize, the effects of eccentricity and dolly stiffness [2.3].

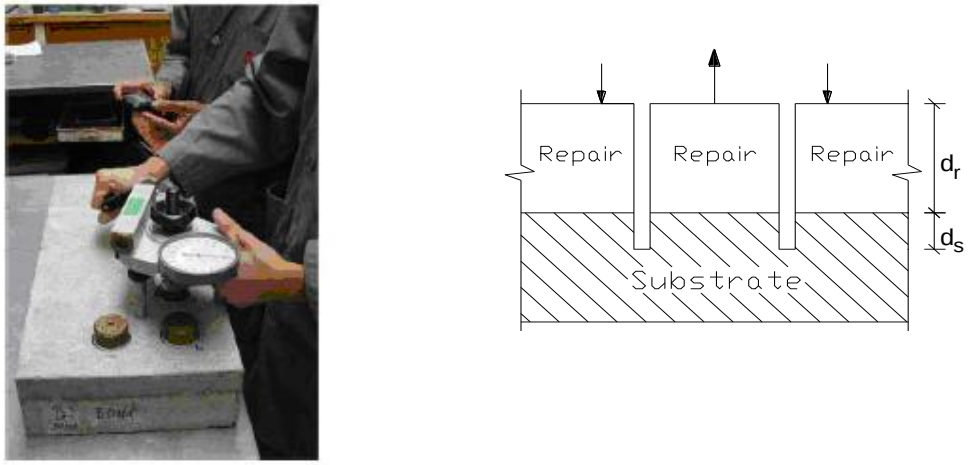

Figure 2.2. *Core pull-off test.*

2.2.3 Pull-apart shear tests

In these tests, a direct shear force is exerted on externally bonded FRP by pushing or pulling the two bond surfaces apart (Figure 2.3). There are many different setups (loading apparatus) used by different researchers. A setup used by Xiao et al. [2.19] is shown in Figure 2.4. Stress distribution in a simple shear bond test used by Woods [2.20] is shown in Figure 2.5. Using such a setup, fracture toughness can be evaluated both at the initiation of cracking and during the propagation phase. Both single-lap and double-lap specimens have been used; they each have their advantages and disadvantages.

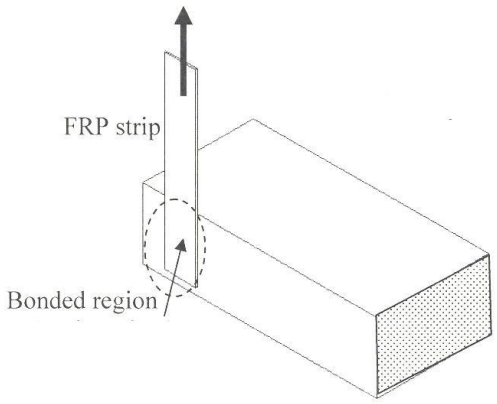

***Figure 2.3**. A simple shear pull-apart test*.

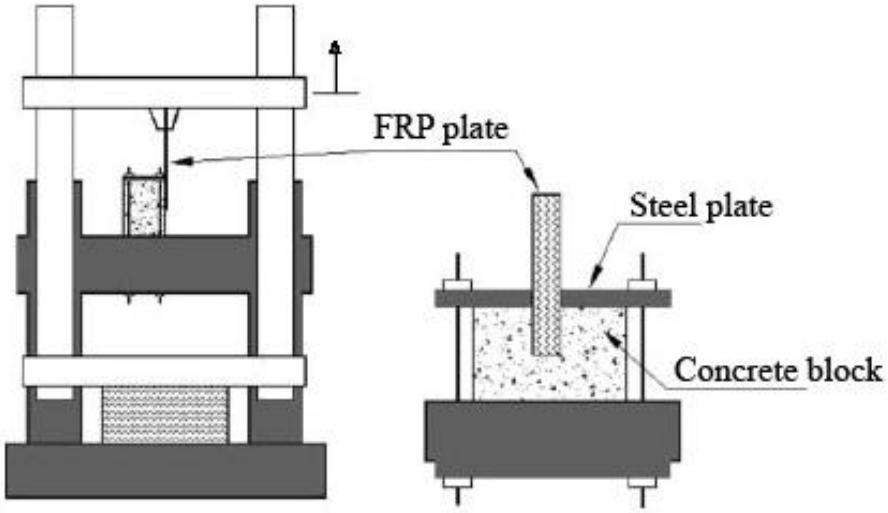

***Figure 2.4**. A shear bond test [2.18]*.

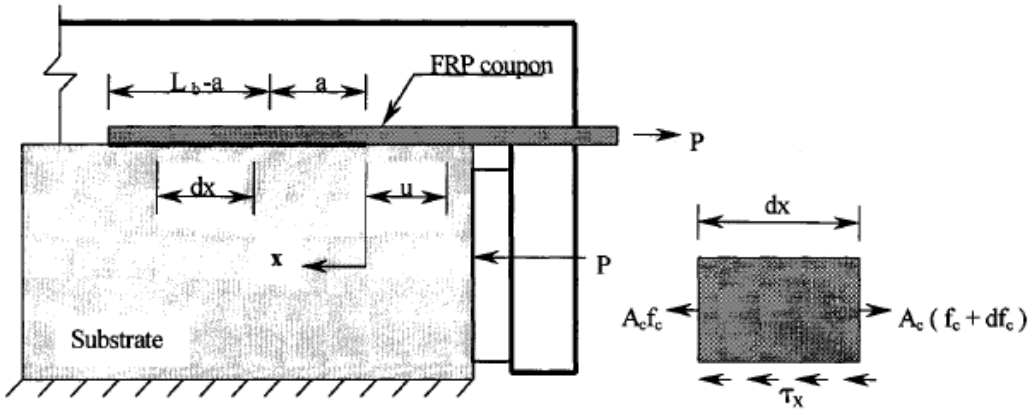

***Figure 2.5.** Free body diagram o an FRP element in a shear bond test [2.18]*.

2.2.4. Peel test

A typical peel test is shown in Figure 2.6. This test has been used by Karbhari et al. [2.21] and by Au and Büyüköztürk [2.22]. Often central to the use of such a test procedure is to attempt to quantify interface fracture toughness and understand the influence of various parameters on interfacial failure and crack growth resistance.

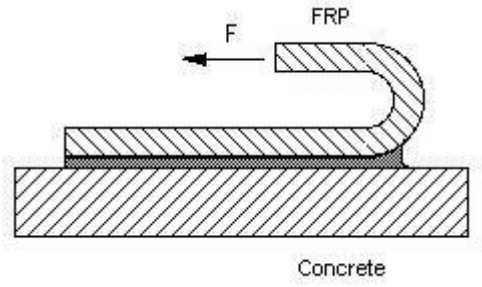

Figure 2.6. *A peel test [2.18].*

2.2.5. Modified three-point test

In a study entitled "Influence of aggregate structure on mode-III interfacial fracture between concrete and CFRP" by Weimer and Haupert [2.4], a three-point bending test was modified to investigate the interface between a composite and a concrete component. A schematic view of their test instrument is shown in Figure 2.7. The objective of their test was to investigate the interfacial shear strength between a composite and a concrete component. The results can be representative of the properties of repair systems used for shear strengthening.

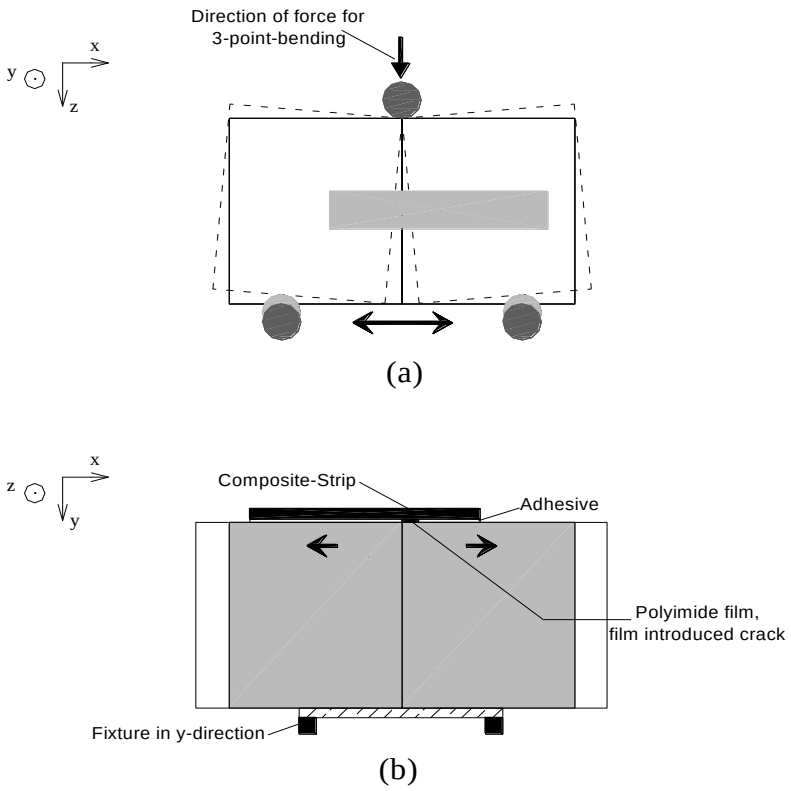

Figure 2.7. *Schematic view of flexural testing.*

2.2.6. Torque test (for in situ shear test)

Ali et al. [2.9], in their study of shear properties of FRP–concrete bond in the field, have modified the core test to enable shear test in situ. The main instrument is a set consisting of a torque wrench, a frame to give a smooth rotation, and a data recorder (Figure 2. 8). Specimens are formed by drilling into concrete until a core with a depth just beneath the bond face is obtained. Then a circular steel disc is glued to the surface of the core and a torsional force is applied until failure of the partial core occurs [2.9]. A limitation of this test is that it reports only a peak value and no fracture energy properties of bond can be evaluated.

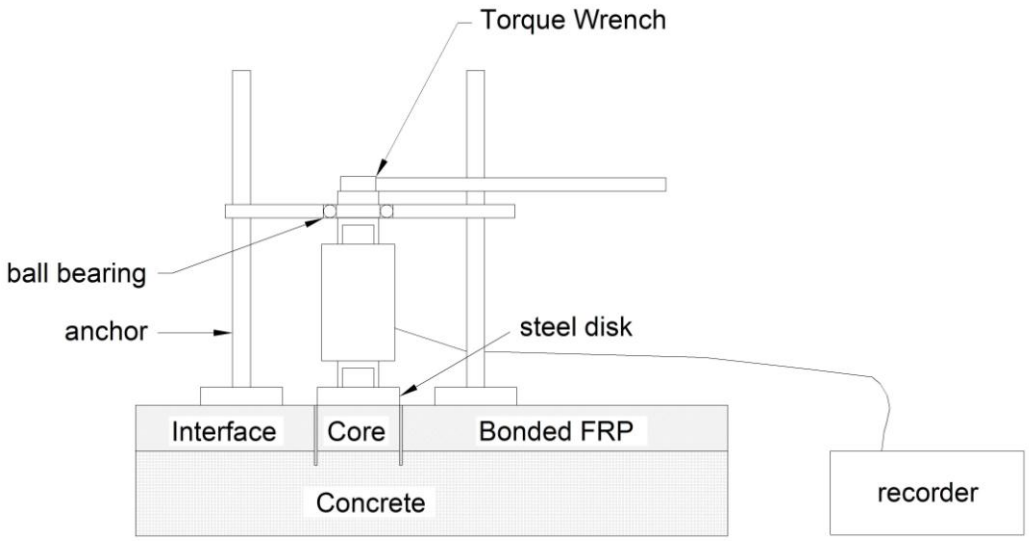

Figure 2.8. *Torque test instrument.*

2.3. Evaluation of standard test methods

Table 2.1 compares the limitations and advantages of the existing standard test methods.

Table 2.1. *Summary of existing tests' advantages and limitations*

Bond test	Failure mode	Advantages	Limitations
Core pull-off	Tension	Can be performed in situ	Returns only a peak value
		Easy to apply	
Shear pull-apart	Shear		Sensitive to the apparatus
Peel	Mixed tension and shear	Can quantify the interfacial fracture energy	
Slant shear	Shear		Specific geometry for specimen needed
			Not sensitive to surface preparation
Three point	Shear	Can quantify the interfacial fracture energy	
Toque	Shear	Can be performed in situ	Returns only a peak value

Reviewing the current test methods, one could learn the following:

1. Repair technology does not as yet incorporate a complete understanding of bonding properties.
2. The tests in which the load is directly applied to the bonded components are not representative of the repair conditions in real-world projects. In the real-life situation, usually the stress is transferred to the repair material indirectly from the repaired structure.
3. Our understanding of bond in most of these tests is based primarily on peak values. However, better indices, such as fracture energy, are more suitable measures of interface properties.
4. More in situ and non-destructive tests should be developed in order to evaluate the conditions of repairs performed and also to monitor the projects through their lifetimes.

Some ideas can be obtained from recent test methods developed in composite materials, the aerospace industry, dentistry, etc. While these methods may be too expensive to be applied for construction purposes, they are still worth investigation.

2.4. Non-destructive tests

2.4.1 Impact-echo test

The impact-echo method is a non-destructive testing technique that is used for detecting flaws in many types of concrete structure. In this test, transient stress waves are introduced into the structure by an impact source at a point on the surface. The waves propagate and are reflected by flaws, interfaces, and external boundaries.

A displacement transducer is also used for monitoring responses that are caused by reflected waves. These waves reflect other times, and so a resonance is produced by numbers of reflections. Depending on the depth of the specimen, a peak in the amplitude–frequency curve is observed, and therefore the depth of any other interface or discontinuity can be determined by amplitude–frequency curves resulting from impact-

echo tests [2.10] (Figure 2.9). $f = CP/2T$; therefore $T = CP/2f$ where T is depth, CP is P-wave speed, and f is frequency.

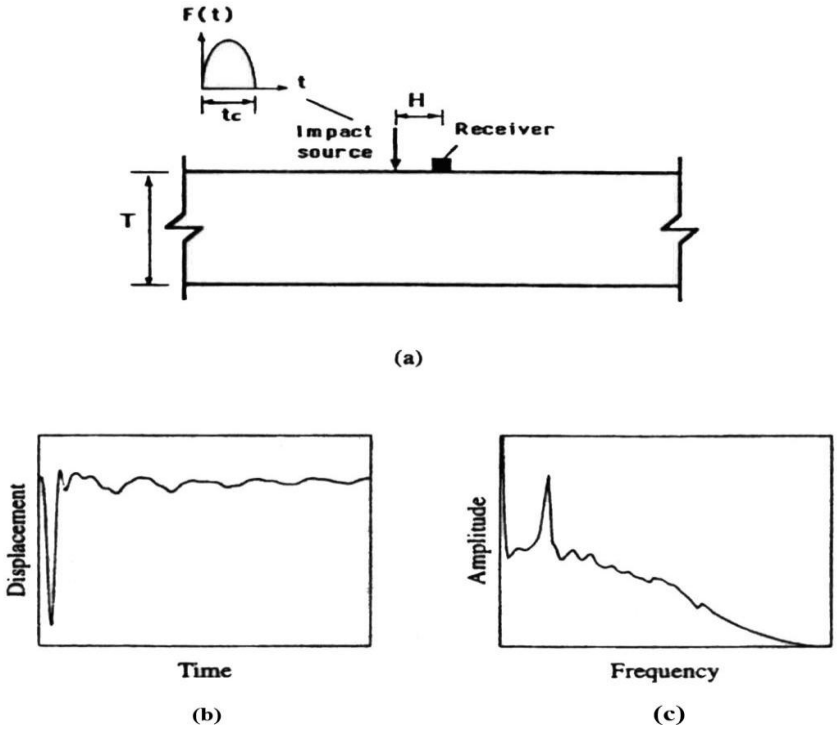

Figure 2.9. *Impact-echo test: (a) test configuration, (b) displacement waveform, (c) amplitude spectrum [2.10].*

Ming and co-workers [2.10, 2.11] have used this method to study interfacial bond quality of FRP to concrete and have investigated the effect of the unbonded fraction of area and the bond tensile strength on impact-echo amplitude spectra. Their results show that the depth of interface with zero unbonded area cannot be determined by this method and also that a very small unbonded fraction of area does not have a significant effect on spectra. However, as the unbonded fraction of area increases to about 20%, P-wave reflections from the unbonded fraction produce a noticeable peak at the frequency corresponding to the depth of interface. This is especially effective for unbonded fractions between 20% and 50%. After increasing from 50% the peak frequency decreases, and when this amount is greater than 80% the spectra are similar to the responses from cracked specimens [2.10].

2.4.2 MEMS adhesive bond degradation sensor

Wilson et al. [2.12] have used a new technique to non-destructively monitor corrosion damage in airframes. The adhesive bond degradation (ADB) microelectro-mechanical systems (MEMS) smart sensor can be permanently installed during the repair and can contain bond degradation sensors to monitoring damage throughout life. These sensors measure the conductivity between the sensor and opposing metal. Some of the sensors are in contact with metal plates that are called physical sensors. The loss of continuity from a sensor indicates the loss of bonding at that point. Some sensing elements are not initially connected to plates and act as chemical ion detectors, detecting bond degradation prior to complete loss of bonding. This ion buildup is a result of chemical activity due to penetration of water and degradation of the metal/epoxy interface (Figure 2.10) [2.12]. The limitations of this test include high cost and inability to report strength values.

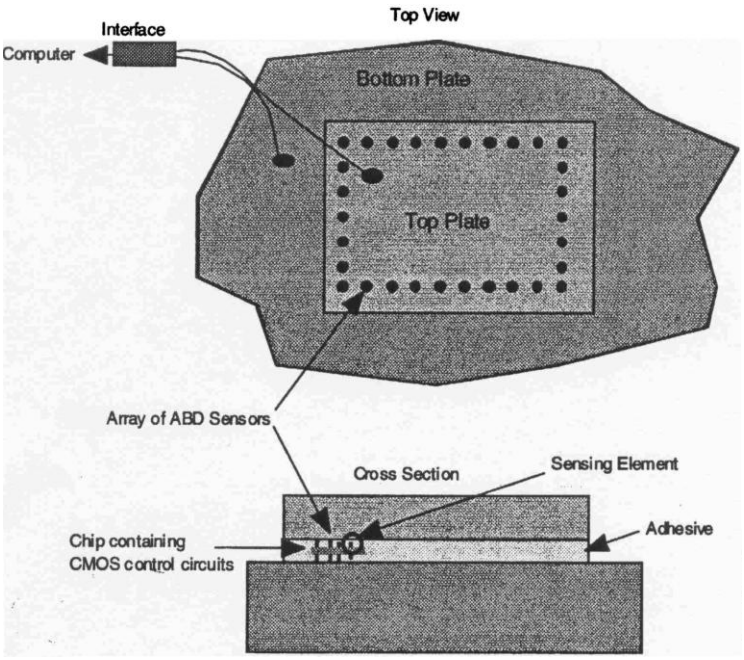

Figure 2.10. *Example of monitoring a bonded repair with an upper metal plate over a lower metal plate [2.18].*

2.5 Numerical modeling

As it is not feasible to test every strengthening technique in real-world situations to determinate the amount of additional capacity due to strengthening, reliable analytical methods are required to numerically simulate the influence of these overlays [2.13]. In a study by Saiidi et al. [2.13] reinforced concrete beams strengthened by concrete overlays are modeled using a shear spring element at the bond line with zero thickness idealized by a bilinear softening relationship. The shear spring element is an element for which the displacement is related to the traction by numbers of stiffness parameters. A microcomputer program called URCCO written in FORTRAN 77 was developed for this work, and a reasonably close agreement between the calculated and measured moments was noted [2.13]. As shown in Figure 2.11, tensile stresses are of a larger magnitude than shear stresses.

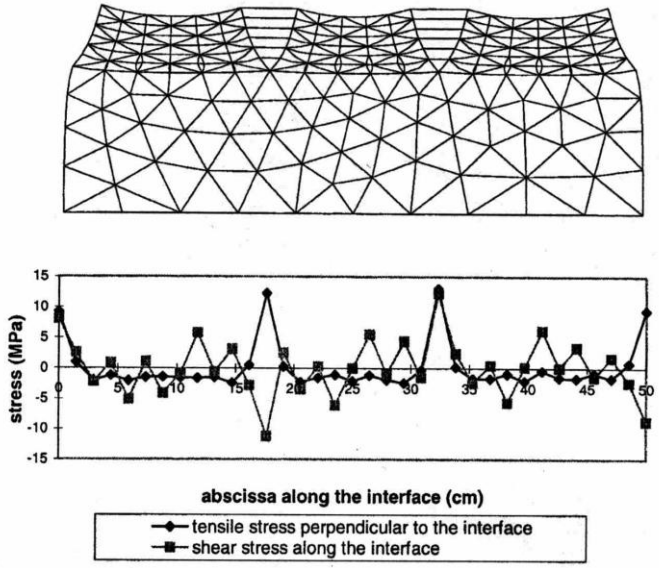

Figure 2.11. *Finite element modeling for obtaining stresses along and perpendicular to the interface [2.14].*

In another paper by Granju [2.14] to investigate debonding of thin cement-based overlays, a finite element modeling is used because of the lack of an appropriate test to accurately characterize the mechanical behavior of the interface. The numerical analysis was performed by CESAR code, and the tensile stress perpendicular to the base overlay interface was confirmed as the designing parameter.

2.6 Microscopic investigations

Sometimes, microscopic examinations are beneficial to explain reasons for events and investigate the nature of problems. Two case studies are given here as examples of microscopic investigations.

Warner et al. [2.16], in research on surface preparation for concrete overlays, used microscopic examination of core specimens from projects where failure has occurred in the substrate and observed a network of very fine micro-cracks or horizontal micro-cracking in the substrate, just below the interface (Figure 2.12).

Another example of microscopic examination is Kasselouri et al.'s [2.17] study of a novel repair material of silica fume and calcium hydroxide. The formation of concrete components is investigated in this research: "As it concerns the interface between the damage mortar and the repair material, sufficient formation of C-S-H can be observed. (Figure 2.13(a) and (b)). The form of the crystals is more similar to that of the hydrated cement mortar. After 18 months of hydration the structure of the SF-Ca(OH)2 mixture (Figure 2.13(b) upper left part) is very condensed and well adhered on the mortar mass (Figure 2.13(b) lower right area)." [2.17].

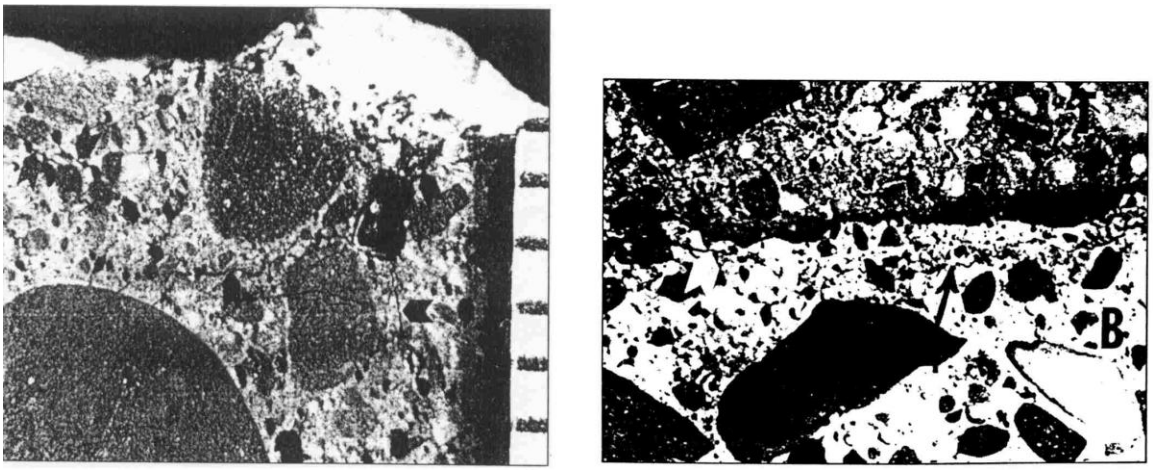

Figure 2.12. *Warner et al.'s [2.16] microscopic investigations on repairs: left, network of very fine micro-cracks immediately below the bond line; right, horizontal micro-crack in parent concrete immediately below the bond.*

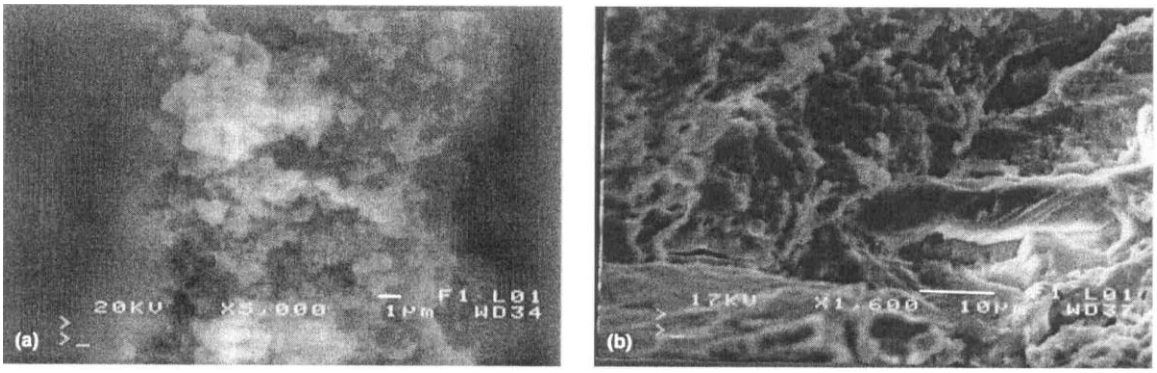

Figure 2.13. *Kasselouri et al.'s [2.17] study on performance of silica fume hydroxide mixture as a repair material: (a) SEM of a 2 month hydrated cement mortar (M × 10,000), (b) SEM of an 18 month hydrated cement mortar (M – 5000).*

2.7. Behavior of concrete beams under impact loading

Impact and impulsive loadings can be important for some structures. Examples of these loadings include vehicle, aircraft or ship accident; falling and swinging objects; flying objects generated by explosion; extreme water-wave action; internal or external gaseous explosion; extreme wind loading; and detonation of highly explosive materials.

The earliest dynamic tests on concrete in compression date back to 1917 [2.24]. After many years of inactivity, more dynamic tests on concrete have been carried out in the past 50 years. Many researchers such as Atchley and Furr [2.25], Scott et al. [2.26], Dilger et al. [2.27], Malkar et al. [2.28], and Soroushian et al. [2.29] found an increase of about 25% in both stress and strain at failure by increasing the rate of loading, while other researchers such as Watstein [2.30] and Malvar and Ross [2.31] reported 85% and sometimes more than 100% increase in compressive strength of concrete under dynamic loads. Concrete static compressive strength [2.35], aggregate type [2.32], and concrete condition (i.e., wet versus dry) [2.33] also affect the strain-rate sensitivity of concrete compressive strength. In general, the lower the static concrete strength, the higher the strength gain due to strain rate. Also, the higher the strain rate is, the higher dynamic improvement factor (dynamic strength divided by quasi-static strength) expected. For

the dynamic strength of the concrete, $f_{cd}^{'}$, US Department of the Army Technical Manual [2.34] suggests a 25% increase over the static concrete strength, $f_{c}^{'}$.

The tensile strength of concrete, as reported by Malvar and Ross [2.31], is more sensitive to strain rates compare to its compressive strength. They reported a 600% increase in concrete tensile strength when the strain rate was increased from 10^{-6} to 200 s^{-1}. They proposed the following equations for the effect of high strain rates on tensile strength of concrete:

$$DIF = \frac{f_{td}}{f_{ts}} = \left(\frac{\dot{\varepsilon}}{\dot{\varepsilon}_s} \right)^{\delta} \qquad if \ \ \dot{\varepsilon} \le 1 s^{-1} \tag{2.1}$$

$$DIF = \frac{f_{td}}{f_{ts}} = \beta \left(\frac{\dot{\varepsilon}}{\dot{\varepsilon}_s} \right)^{1/3} \qquad if \ \ \dot{\varepsilon} > 1 s^{-1} \tag{2.2}$$

where

$\log \beta = (6\delta) - 2$

$\delta = \frac{1}{1 + 8(f_{c}^{'} / f_{co}^{'})}$

DIF = $\frac{f_{td}}{f_{ts}}$ = Dynamic Increase Factor

f_{td} = dynamic tensile strength of concrete, MPa

f_{ts} = static tensile strength of concrete, MPa

$\dot{\varepsilon}$ = high strain rate up to 10^{4} s^{-1}

$\dot{\varepsilon}_s$ = static strain rate between 10^{-6} to 10^{-5} s^{-1}

$f_{c}^{'}$ = compressive strength of concrete, MPa

$f_{co}^{'}$ = fraction of the compressive strength of concrete, can be assumed 10 MPa

Wakabayashi et al. [2.36] performed dynamic tests on reinforced concrete beams under a high strain rate of 0.01 s^{-1}. They found that load carrying capacity of reinforced concrete beams increased by about 30% when a high strain-rate loading was applied. They also found that the compressive strength of concrete and the tensile strength of steel increased linearly with the logarithm of strain rate.

Banthia [2.41] used a drop weight impact machine to carry out impact tests on reinforced concrete beams. He found that the peak bending loads obtained under impact loading were higher than those obtained under static loading. He pointed out that after a certain hammer drop height, increase in the peak bending loads was not significant. He also concluded that shear reinforcement enhanced the impact resistance of reinforced concrete beams by confining the concrete and increasing the beam's ductility. For reinforced concrete beams made of high-strength concrete, he found that an increase in the stress rate decreased their rigidity and hence, their ductility, and contrary to the behavior of normal strength reinforced concrete beams, an increase in the drop hammer height actually reduced the fracture energy.

Bentur et al. [2.42] rightly mentioned that the inertial loading (i.e., the load required to accelerate the specimen) effect must be separated from the total load measured by the instrumented tup (striking top weight). They concluded that in many instances only a small portion of the total load was involved in beam bending itself.

Kishi et al. [2.43] studied the ultimate strength of flexural-failure-type reinforced concrete beams under impact loading. They tested eight simply supported reinforced concrete beams with a clear-span of 2 m. Impact tests were performed using a free-falling 200 kg steel weight dropped onto the mid-span. They recorded impact force experienced by the falling steel weight, reaction forces at the supports, and the mid-span deflection, while impact velocity (1 to 6 m/s), rebar ratio (0.42% to 2.98%) and cross-sectional area of the beams (160 mm × 240 mm, 200 mm × 220 mm, and 160 mm × 160 mm) were taken as variables. The V_{usc} / P_{usc} was in the range of 1.90 to 6.04, where V_{usc} is static shear capacity (kN) and P_{usc} is the static bending capacity (kN). They

assumed that when the cumulative residual displacement of reinforced concrete beam approached 2% of its clear span, the ultimate failure occurred. They also noticed that the impact force increased very rapidly up to a maximum value at the very beginning of the test and decreased to almost zero, irrespective of the beam type. In contrast, they observed that the reaction force (evaluated as summing the values recorded by the supports) increased linearly to a maximum value, stayed at almost the same value until the displacement reached its maximum value, and then decreased to zero. They assumed a parallelogram for the reaction–displacement relationship. From these observations they concluded that the maximum reaction force, instead of the maximum impact force, should be used to estimate the reinforced concrete beam flexural strength under impact loading. They found that the maximum reaction force for all reinforced concrete beams exceeded two times their static bending capacity. They also calculated that the input kinetic energy to reinforced concrete beams was 1.1 to 2.0 times higher than the absorbed energy by beams during the failure (area under the reaction force vs. mid-span displacement).

In another study Kishi et al. [2.45] tested 19 simply supported reinforced concrete beams all with dimensions 200 mm × 400 mm × 2400 mm. An impact load was applied at mid-span by dropping a 400 kg steel weight. They also used instrumented supports to record reaction forces of the reinforced concrete beams during the impact loading. Tensile reinforcing bar ratio for all beams was 0.027 but different shear reinforcing bar ratios were used (i.e., 0.0, 0.002, and 0.004). For all beams, the static bending capacity was higher than static shear capacity, meaning that they should fail in shear. They observed that the reaction force, irrespective of beam type, increased almost linearly to an absolute maximum value with an increment of the impact velocity. After this point, the reaction force did not increase by increasing the impact velocity. Contradictory to Ando et al. [2.44], they found that the ratio of R_{ud} / P_{us} (ultimate dynamic capacity to ultimate static capacity) for all reinforced concrete beams was in the range of 2.7 to 3.1 (this ratio was reported in the range of 1.0 to 1.5 by Ando et al. [2.44]).They concluded that when static bending capacity was higher than static shear

capacity, the impact-resistant design for shear-failure-type reinforced concrete beams could be performed by using the static shear capacity.

In a study by Kishi et al. [2.43] load cells were used at the supports and at the impact point (steel weight) and the following was observed:

1. There was a high-frequency component in the impact force at the very beginning of the impact force.
2. When impact force reached its maximum value, no deflection was yet recorded at the mid-span.
3. Primary stiffness estimated using the reaction force was similar to that of static loading.
4. The reaction force wave behaved similarly to the displacement wave.

From these observations, they suggested that the impact-resistant capacity may be more rationally estimated by the maximum reaction force rather than using the maximum impact force.

Abbas et al. [2.47] proposed a three-dimensional nonlinear finite element analysis of reinforced concrete targets under impact loading. They showed that their model was capable of carrying out impact analysis and predicting cracking.

CHAPTER 3
MATERIALS

3.1 Concrete

3.1.1 Mix design

Two different mix designs were used for the batching of the test samples. These are shown in Table 3.1. The first mix design was changed due to excessive water to cement ratio and high steel fibre content. The high water content resulted in some segregation and the high fibre content made the concrete too difficult to handle.

Table 3.1. *Concrete mix design*

		Concrete constituents (kg/m^3)				
Mix #	**Samples**	**Cement**	**Aggregate (SSD)**		**Water**	**Steel fibres**
			Coarse	**Fine**		
1	Batch 1	292	896	887	184	74
2	All other	301	923	913	165	55

3.1.2 Cement

The cement used in all of the mix designs was a normal CSA Type 10 Portland cement (Type I ASTM).

3.1.3 Aggregate

Best practice for Portland cement concretes is to use a continuous (dense) aggregate gradation [3.1]. This reduces the amount of void space between the aggregates within the concrete. The mix design employed might be more accurately described as a gap graded distribution, because there seems to be a small fraction of particles missing between the coarse and fine aggregate mix. This gap graded mix is common in North America because of reported easier workability.

The aggregate included in the concrete mix design consisted of coarse and fine materials. The coarse aggregate used can be defined as crushed gravel comprised of individual particles 7–15 mm in diameter. The fine aggregate selected for the mix design is a medium-coarse sand mixture with grain sizes typically between 1 and 5 mm in diameter. Figures 3.1 and 3.2 show the material used for the mix design with a comparative scale.

Figure 3.1. *Coarse gravel aggregate size.*

Figure 3.2. *Medium-coarse sand particle size.*

Table 3.2 shows that both mix designs incorporated individual coarse and fine aggregate weight fractions of just less than 40%. This means both mix designs had a total percentage aggregate by weight of between 76% and 78%.

Table 3.2. *Aggregate percentage*

Batch #	Number of samples	Aggregate				Total % aggregate
		Coarse (g)	% Coarse	Fine (g)	% Fine	
1	12	35.50	38.4%	35.14	38.0%	76.4%
2	24	45.88	39.1%	45.41	38.7%	77.9%
3	12	45.88	39.1%	45.41	38.7%	77.9%

3.1.4 Water

The water added to all of the mix designs was potable water from the building supply

3.1.5 Steel fibres

The steel fibres added to the mix design were 30 mm long with an approximate rectangular cross section of 1 mm by 0.5 mm. The ends of the fibres had been pinched, causing the material to expand outward, which anchors the fibres in the concrete. This

helps to prevent the steel fibres from pulling out, giving the concrete increased tensile strength. Figure 3.3 shows a single steel fibre with a comparative scale.

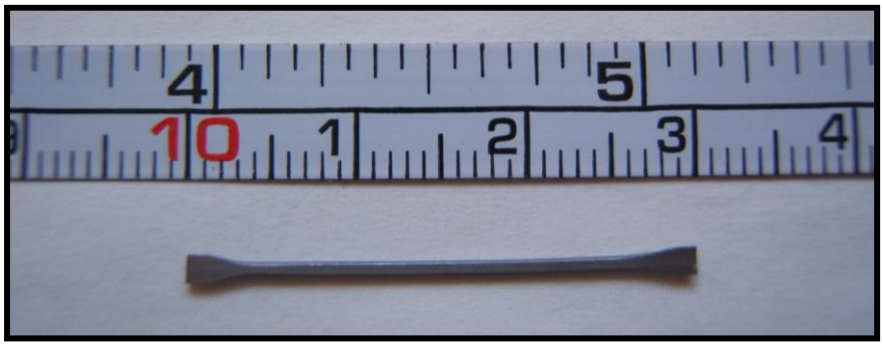

Figure 3.3. *Steel fibre in concrete.*

3.1.6 Curing

The specimens were water cured in the curing tank for 7 days and then were kept in the curing room for 21 days. Specimens were taken out of curing room and left in the laboratory area for an extra week so that the surface of the concrete could be dried before the specimens were moved to the FRP factory.

3.1.7 Compressive strength

The average compressive strength was tested to be 28.1 MPa for batch 1 (mix design 1) and 33.1 MPa for the rest of the specimens (mix design 2).

3.2 GFRP spray system

The glass fibre reinforced polymer (GFRP) spray system is made up of resin, catalyst, coupling agent, and glass fibre. In this section, the property of each component is discussed first. Then the physical properties of the GFRP are described, and at the end, the mechanical properties of the sprayed GFRP as tested are reported.

3.2.1 GFRP spray components

3.2.1.1 Resin

AROPOL 7241T-15 polyester resin manufactured by Ashland Specialty Chemicals was used by the GFRP company that was used to spray the specimens. Physical and mechanical properties of this resin are listed in Table 3.3.

Table 3.3. *Physical and mechanical properties of polyester resin [3.2]*

Property	Value	Unit
Density of liquid	1.07	g/cm^3
Density of solid	1.17	g/cm^3
Tensile strength	62	MPa
Tensile elastic modulus	3.65	GPa
Elongation at break	2.5	%
Flexural strength	105	MPa
Flexural modulus	40.7	GPa

3.2.1.2 Catalyst

The catalyst is used to initiate curing of the resin. The catalyst used by the FRP factory was methyl ethyl ketone peroxide (MEKP) manufactured by Ashland Specialty Chemicals. On average, MEKP was added as 3% by volume of polyester resin.

3.2.1.3 Bonding agent

The bonding agent is used to improve the GFRP to concrete bond. Two types of bonding agents are used in this research: aromatic isocyanate, commercially known as ATPRIME® (referred to as Resin 1), and vinyl ester (referred to as Resin 2).

ATPRIME® 2, manufactured by Reichhold Company, which was used as the coupling agent, is a two-component urethane-based primer system that can be applied with a brush or roller to prepared surfaces to form chemical bonding. These two components are mixed before using in the ratio of one part from component A with two parts from component B. The mixture can be used after 30 min. Blended ATPRIME® 2 has a pot life of 12 h at 27ºC.

3.2.1.4 Glass fibre

Advantex® 360RR chopper roving manufactured by Owens Corning was used by the FRP factory. Physical and mechanical properties of this glass fibre roving are listed in Table 3.4. The chopping and application process will be described in Chapter 4.

Table 3.4. *Physical and mechanical properties of Advantex® glass fibre [3.2]*

Property	Value	Unit
Density	2624	kg/m^3
Diameter	9–30	μm
Tensile strength	3200–3750	MPa
Elastic modulus	80	GPa
Elongation at break	4.5	%

3.2.2 Physical properties of the sprayed GFRP

Previous research by Boyd [3.3] at the University of British Columbia, who studied the properties of sprayed GFRP containing different fibre lengths, indicated that a fibre length of 32 mm was optimum for this study. This gave a higher strain at rupture compared with other fibre lengths.

3.2.2.1 Fibre volume fraction

The fibre volume fraction for final cured sprayed GFRP composite was found to be 24.7% using the method described in ASTM D2584 [3.4]

3.2.2.2 Tensile properties

Sprayed FRP coupons were made with similar thickness (4 mm) and application direction and process to test the tensile properties of FRP. These coupons were cut from a laminate plate, which was made by spraying a flat sheet of GFRP onto a pane of glass. Two notches were also made at the middle of the specimens to dictate the failure location.

Sprayed GFRP coupons were tested using a Baldwin 400 kip Universal Testing Machine. A gauge length of 50 mm at the middle of the specimen was used. The displacement was measured using an LVDT-based extensometer attached to the specimen (LVDT, linear variable differential transformer). Test setup is shown in Figure 3.4. Applied load and displacement were recorded constantly with a data acquisition system. Stress–strain data were calculated using the average cross-sectional area measured by a caliper. The stress–strain curve is shown in Figure 3.5, showing a modulus of elasticity of 14 GPa and tensile strength of 70 MPa.

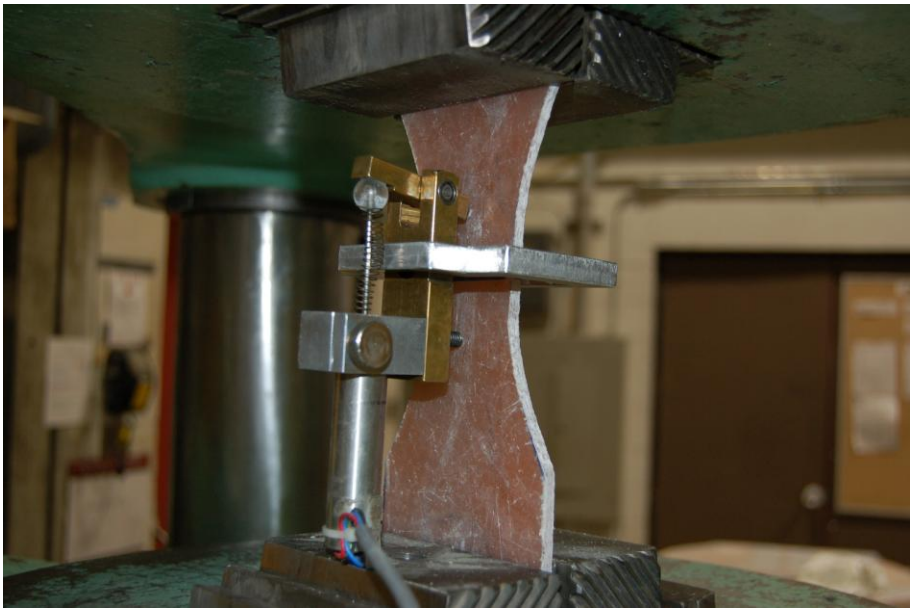

Figure 3.4. *Tensile testing of sprayed GFRP.*

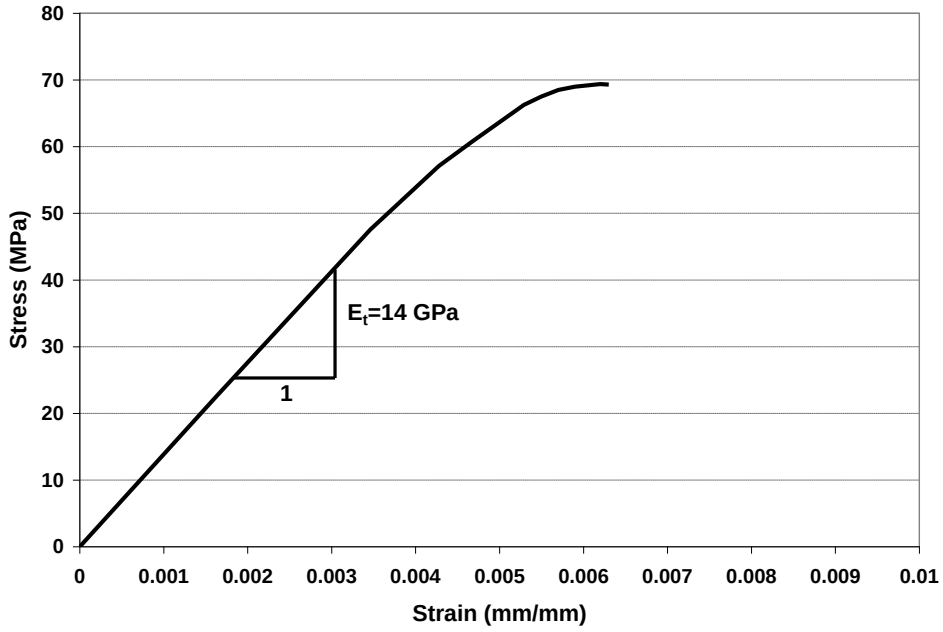

*Figure **3.5.** Stress–strain behavior of sprayed GFRP coupon under tensile stress.*

3.3 GFRP fabric (Wabo®MBrace) system

The GFRP Wabo®MBrace system was used in this research. The components are primer, putty, saturant, and glass fibre, which are manufactured by Degussa Construction Chemicals [3.5].

3.3.1 Primer

Wabo®MBrace primer is the first material that is applied to the substrate. It is a low viscosity, 100% solids, polyamine cured epoxy. Once applied, the primer penetrates the pore structure of cementitious substrate and provides a high bond base coat for the Wabo®MBrace system. The primer consists of two components, Part A and Part B, which are mixed by the weight ratio of 100 to 30 (Part A to Part B). Wabo®MBrace primer can be applied at temperatures of 10ºC and 50ºC. Physical and mechanical properties of Wabo®MBrace primer are listed in Table 3.5.

Table 3.5. *Physical and mechanical properties of Wabo®MBrace primer [3.5]*

Property	Value	Unit
Density	1102	kg/m^3
Installed thickness (approx)	0.075	mm
Tensile yield strength	14.5	MPa
Tensile strain at yield	2.0	%
Tensile elastic modulus	717	MPa
Tensile ultimate strength	17.2	MPa
Tensile rupture strain	40	%
Poisson's ratio	0.48	
Compressive yield strength	26.2	MPa
Compressive strain at yield	4.0	%
Compressive elastic modulus	670	MPa
Compressive ultimate strength	28.3	MPa
Compressive rupture strain	10	%
Flexural yield strength	24.1	MPa
Flexural strain at yield	4.0	%
Flexural elastic modulus	595	MPa
Flexural ultimate strength	24.1	MPa

3.3.2 Putty

Wabo®MBrace putty is a two part epoxy and is the second component that is applied. It levels the surface and provides a smooth surface to which the Wabo®MBrace saturant will be applied. It also consists of two parts A and B that are mixed by weight ratio of 100 to 30 (Part A to Part B). Wabo®MBrace putty can be applied before or after the primer coat has achieved full cure, but should be applied within 48 h of applying the Wabo®MBrace primer to the substrate to ensure proper adhesion. Parts A and B must be mechanically premixed separately for 3 min. After premixing, Parts A and B should be blended using a mechanical mixer for about 3 min, until a homogeneous mixture is achieved. Wabo®MBrace putty can be applied at temperatures of 10ºC to 50ºC. Physical and mechanical properties of Wabo®MBrace putty are listed in Table 3.6 [3.5].

Table 3.6. *Physical and mechanical properties of Wabo®MBrace putty [3.5]*

Property	Value	Unit
Density	1258	kg/m^3
Tensile yield strength	12	MPa
Tensile strain at yield	1.5	%
Tensile elastic modulus	1800	MPa
Tensile ultimate strength	15.2	MPa
Tensile rupture strain	7	%
Poisson's ratio	0.48	
Compressive yield strength	22.8	MPa
Compressive strain at yield	4	%
Compressive elastic modulus	1076	MPa
Compressive ultimate strength	22.8	MPa
Compressive rupture strain	10	%
Flexural yield strength	26.2	MPa
Flexural strain at yield	4	%
Flexural elastic modulus	895	MPa
Flexural ultimate strength	27.6	MPa
Flexural rupture strain	7	%

3.3.3 Saturant

Wabo®MBrace saturant encapsulates carbon, glass, or aramid fibre fabrics. It is also a two part epoxy. Wabo®MBrace saturant provides a high-performance FRP laminate when reinforced with the fibres. It consists of two components, Part A and Part B, that are mixed by a weight ratio of 100 to 34 (Part A to Part B). Wabo®MBrace saturant can be applied before or after the primer and putty coats have achieved full cure but should be applied within 48 h of applying the Wabo®MBrace putty to the substrate to ensure proper adhesion. Parts A and B must be mechanically premixed separately for 3 min. After premixing, Parts A and B should be blended using a mechanical mixer until a homogeneous mixture is achieved, which requires approximately 3 min additional mixing time. The saturant can be applied at temperatures of 10ºC to 50ºC. Physical and mechanical properties of Wabo®MBrace saturant are listed in Table 3.7.

Table 3.7. *Physical and mechanical properties of Wabo®MBrace saturant [3.5]*

Property	Value	Unit
Density	983	kg/m^3
Tensile yield strength	54	MPa
Tensile strain at yield	2.5	%
Tensile elastic modulus	3034	MPa
Tensile ultimate strength	55.2	MPa
Tensile rupture strain	3.5	%
Poisson's ratio	0.40	
Compressive yield strength	86.2	MPa
Compressive strain at yield	5	%
Compressive elastic modulus	2620	MPa
Compressive ultimate strength	86.2	MPa
Compressive rupture strain	5	%
Flexural yield strength	138	MPa
Flexural strain at yield	3.8	%
Flexural elastic modulus	3724	MPa
Flexural ultimate strength	138	MPa
Flexural rupture strain	5	%

3.3.4 Glass fibre fabrics

Wabo®MBrace E-glass fibre fabrics are dry fabrics constructed of high quality E-glass fibres. Physical and mechanical properties of Wabo®MBrace E-glass fibre fabric are listed in Table 3.8 [3.5].

Table 3.8. *Physical and mechanical properties of Wabo®MBrace E-glass fibre fabric (EG 900) [3.5]*

Property	Value
Density	2600 kg/m^3
Nominal thickness	0.353 mm/ply
Ultimate tensile strength	3600 MPa
Tensile elastic modulus	80 GPa
Ultimate rupture strain	4.5%

3.3.5 Fabric GFRP mechanical properties

The properties of Wabo®MBrace EG 900, which is a glass fibre reinforced polymer as per the manufacturer's report, are shown in Table 3.9. The stress–strain relationship for this product is reported in Figure 3.6 [3.5].

Table 3.9. *Wabo®MBrace EG 900 properties*

Tensile properties	Value	Unit
Ultimate tensile strength	1517	MPa
Tensile elastic modulus	72.4	GPa
Ultimate tensile strength per unit width	0.536	kN/mm/ply
Tensile modulus per unit width	25.6	kN/mm/ply
Ultimate rupture strain	2.1	%

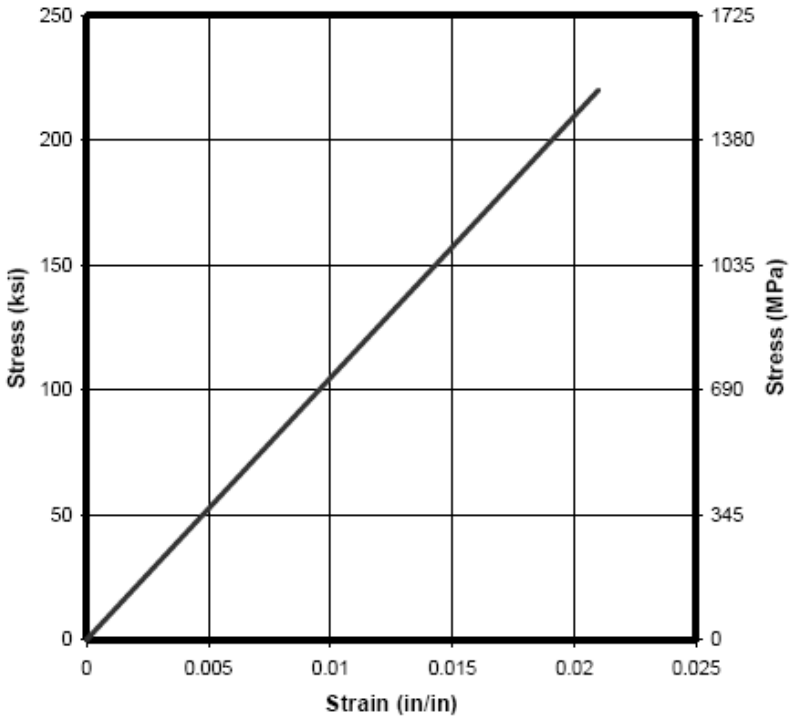

Figure 3.6. *Stress–strain curve for Wabo®MBrace E-glass fibre fabric (EG 900) [3.5].*

CHAPTER 4
SPECIMEN PREPARATION STEPS

4.1 Concrete sample preparation

Concrete beam specimens of various sizes (see Chapters 5, 6, and 7) were cast using the mix proportions given in Chapter 3 for the evaluation of bond properties in the quasi-static, impact, and dynamic tests. Samples were cast in the laboratory mixer, moist cured for 28 days, and allowed to dry in the laboratory air until further preparation (see below). Once the hydration process had given the samples sufficient strength, they were notched and divided into specific treatment categories. The samples in each group subsequently received the required surface treatment and fibre reinforced polymer (FRP) coating. A detailed account of the process is outlined below.

4.1.1 Notching

The idea of notching the concrete came from the desire to simulate failure of the concrete at a known point and test the bonding strength of the FRP over the notch. Forty-five samples (all but three) required notching, and this was done using a water cooled, diamond tipped, concrete saw. A 3 mm wide slit in the concrete was created, as shown in Figure 4.1. The slit was created in the side adjacent to the top surface.

Figure 4.1. *Notched specimen.*

4.2 Surface preparation

At this point a permanent marker was used to label each sample, describing the appropriate surface treatment and sample number. This categorized the samples into 13 groups of different surface preparations, resin types, and FRP applications.

The surface preparations applied to the samples were chosen for their likelihood of being used in the industry should an FRP process be applied on an existing concrete structure as a mitigative measure. The surface preparations used were sandblasting, forced water jet, jackhammering, and no surface preparation.

4.2.1 Sandblasting

During sandblasting, care was taken to ensure that all of the sandblasted samples received similar surface treatments. For the specimens, the sandblasting was performed at the maximum pressure of 3000 psi. Achieving consistency among samples was difficult, as the pressure and volume of sand fluctuated greatly as the sandblaster operated. In spite of this, the surface preparations were fairly uniform across all of the samples treated. For the initial specimens, after the samples had been sandblasted, they were washed off using a pressure washer to

ensure loose particles were removed. This however, resulted in a wet surface that had to be dried again for 1 week. The researcher decided to eliminate these specimens and use pressured air to clean the specimens after sandblasting. This would ensure that the moisture does not affect the final bond strength of the FRP and is more practical in the field. The final result of the sandblasting on the surface of the concrete is a uniform rough and abrasive plane. Figure 4.2 shows the sandblasting equipment used for the surface preparation.

\\

Figure 4.2. *Sandblaster.*

4.2.2 Jackhammering

The second surface treatment was applied by abrading the surface of samples using an air-powered hammer. Applying this treatment was more difficult than sandblasting, since hammering too close to the notch could result in the loss of substantial material along the notch. One sample, shown in Figure 4.3, had to be discarded because the hammering resulted in a large chunk of concrete being removed around the notch. A flaw this large would have affected the structural integrity of the beam and the bond, possibly leading to inaccurate results. Thus, these samples were discarded. Similar to the sandblasted samples, all hammered samples were cleaned off using pressured air. The final result of the

jackhammering on the surface of the concrete is a rough, non-uniform, pitted surface with gouges of various depths averaging about 2 mm, as shown in Figure 4.3.

Figure 4.3. *Jackhammered sample showing damaging effect of surface preparation.*

4.2.3 Water jet

The final surface treatment to be applied was water blasting the sample with a high force water jet at 1750 psi. The final result of the water jet on the surface of the concrete was minimal and perhaps ineffective, as there were no visual or physical signs of surface abrasion. The surface looked identical to the non-washed side, so the researcher believes the main role of the pressure wash is to remove loose particles from the surface of concrete.

4.3 Spray FRP application

The spray FRP is a process of spraying a resin/catalyst and glass fibre mixture on to the concrete using a spray gun with a mounted chopper unit. The FRP is then rolled and allowed to cure, resulting in a high strength product. The details are outlined below.

4.3.1 Preparation

Before the FRP was applied, the application surface of each sample was treated with acetone to dry any water from the sample and remove impurities

from the concrete face that would have an adverse effect on the bonding between the FRP and the concrete. Impurities could include any greases, oils, fingerprints, and other impurities that could prevent an optimal bond. After cleaning, the samples were coated with one of two bonding agents as described in Section 4.5.3. This is a bi-functional binder, which must bind to the concrete on one side and to the FRP on the other. The samples are then left to dry to ensure no moisture was present on the application face; this would also increase the possibility of a poor bond. With the samples cleaned, dried, and ready to be sprayed one last step involved taping of the face of each individual sample to ensure the spray was applied (for the majority of the samples) to only the desired area. These processes and all of the spraying occurred at John's Custom Fiberglass Ltd, Surrey, BC.

4.3.2 Spray gun

The sprayed FRP was applied to the samples just as the name implies, by spraying it on. This was done using a spray gun, shown in Figure 4.4. One nozzle sprays the resin/catalyst mixture and a mounted hub discharges the chopped fibres. These two streams are aligned such that they combine mid-spray and continue to the concrete sample together as one mixture.

Figure 4.4. *FRP spray gun.*

4.3.3 Glass fibres

The glass fibres are made up of bundles of extremely fine fibres of glass; these bundles resemble twine. The spooled glass fibre is fed to the spray gun in a roving format (Figure 4.5), which feeds two separate lines simultaneously to the chopper unit of the spray gun (see Figure 4.4). This unit is mounted on the spray gun. It cuts (chops) the glass fibres into their desired lengths by passing the fibres between two rotating wheels inside the hub, one of which is equipped with a number of blades fixed around its circumference. As the rollers rotate, the fibres being drawn in are cut into individual lengths and ejected from the hub with the help of a pressurized air supply.

The fibre length is changed by using a roller with a different number of blades. The optimal fibre length decided upon and used for the project was 31.75 mm (1.25 in.).

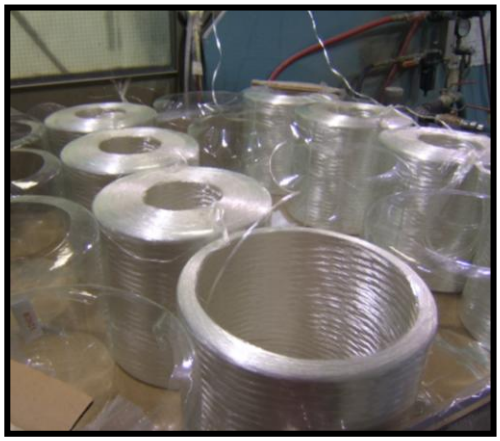

Figure 4.5. *Spooled glass fibres.*

4.3.4 Carbon fibres

Carbon fibres were also used instead of glass in a set of small specimens to investigate the influence of fibre type. The carbon fibre used was also spooled, and so the application process was the same as that for the glass. Minor

inconveniences occurred because the carbon fibre did not cut with as high efficiency.

4.3.5 Resin/bonding agent combinations

A test was performed that compared different bonding agents (namely Resin 1 and Resin 2). Technically, there is no difference between the resins, and the nomenclature used refers to the use of a different bonding agent for each type. The majority of the samples received Resin 1, which used a bonding agent called "ATPRIME®" (aromatic isocyanate). Resin 2, used for three comparative samples, used a bonding agent called "vinyl ester". Both bonding agents are brush-on products, but the ATPRIME® is an epoxy-type product that involves combining two components to achieve the desired properties. A major difference, however, is the time it takes for each to set before the FRP spray can be applied. The ATPRIME® requires 12 h, whereas the vinyl ester only needs approximately 1.5 h.

4.3.6 Application process

The resin/catalyst and glass fibre mixture is the fibre reinforced polymer denoted as the FRP. This was sprayed on to the samples using the spray gun in a back-and-forth motion, passing over the samples repeatedly to ensure an even distribution. What had been applied to the concrete face at this point was a somewhat three-dimensional matrix layer of loose FRP. This was then manually rolled using a small ribbed roller to expel as much air as possible from between the fibres and in essence to reduce the thickness of the sprayed layer, creating a two-dimensional matrix. The rollers were applied using several passes and in different directions to make sure as much air as possible was forced out. The amount of FRP spray applied to the face to begin with was sufficient to ensure that once the rolling had been done the FRP thickness was 2 mm. Figure 4.6 shows the spray and roll FRP application.

Figure 4.6 *Spray and roll FRP application.*

4.3.7 Curing

The samples must then be left to cure. The rate of setting is dependent upon the level of catalyst in the resin mixture and can range between 20 min and 2 h. As the resin hardens this produces durable FRP with a high strength capacity. After the FRP hardened, a rotary cutting tool was used to remove the excess FRP around the edges of the marks drawn earlier.

4.4 Wrap FRP (Wabo®MBrace) system

The wrap FRP in the Wabo®MBrace system was a process of applying a woven fibreglass sheet to the sample as opposed to spraying individual fibreglass strands in a random orientation. The process took 3 days, since three layers were applied and each required 24 h to set before the next could be done. The details are outlined below.

4.4.1 Preparation

Disregarding the surface preparation and FRP type, it was desired that all the concrete samples be identical. Any material that filled the base of the notch and hardened would effectively change the strength characteristics of the concrete. To prevent the added solvents from filling the notch, each sample had

folded paper towel inserted into the notch to bridge the gap. The paper towel remained in the slot for the duration of the tests.

4.4.2 Woven glass fibre quilt

Instead of randomly oriented sprayed fibres, the FRP wrap consisted of laying down a woven quilt of glass fibres. To get the appropriate size, the wrap is simply cut from a large roll of the material using basic stationary scissors. Figure 4.7 shows the glass fibre quilt used.

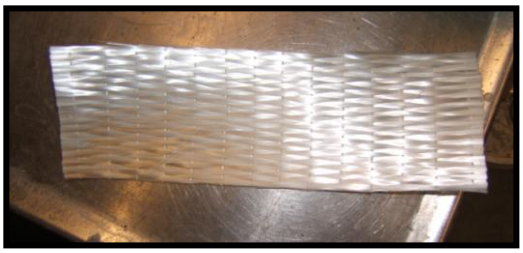

Figure 4.7. *FRP quilt.*

4.4.3 Application process and setting

With the notch filled, the epoxy primer (see Section 3.3.1) was the first layer to coat the concrete face. It was applied to the whole face of the concrete, not just inside the marked outline for the FRP wrap textile. This needed to stand for 24 h before the epoxy layer (see Section 3.3.2), was rolled on. The putty gave the block face a glossy grey colour, and again the sample needed to cure for 24 h. The final application rolled on was the blue epoxy saturant (see Section 3.3.3), which again coated the entire concrete face. Once this was evenly applied, the woven glass fibre textile (see Section 3.3.4), which had been cut to the shape of the traced stencil (which consequently had been covered by the putty layer and needed to be redrawn) was laid down and pressed into the wet saturant. Once the glass fibre sheet was in place, a second layer of saturant was rolled on, sealing the fibre pad between the saturant layers. The final stage is demonstrated in

Figure 4.8. Each surface agent consisted of two components mixed together to get the desired product.

Figure 4.8. *Applying the saturant.*

CHAPTER 5
DEVELOPMENT OF TEST SPECIMENS

5.1 Test series I: 350 mm × 100 mm × 100 mm specimens

The first set of specimens was chosen to be 350 mm × 100 mm × 100 mm. Easier handling and lower cost of the test were the main reasons for this choice.

To better understand the bonding between FRP and concrete, various combinations of surface preparation of the concrete and two different resin types were used. Table 5.1 outlines the concrete specimen distribution, including their various preparation differences, totaling 36 samples. The samples tested were all of common size, 35 cm in length with a 10 cm by 10 cm cross-sectional area.

All of the concrete used was mixed containing steel fibre reinforcement to promote the failure of the specimen at the interface between the concrete and the FRP and not internally in the concrete sample itself. In addition to the FRP samples, three control sample types were used to compare un-reinforced concrete with no surface damage to a notched sample representing a crack.

Table 5.1. *Sample notation for the various treatments*

Comparison variable	Surface preparation	FRP type	FRP length (mm)	# of specimens
Control samples	—	—	—	3
	—	—	—	3
Surface preparation	None	Sprayed GFRP – Resin 1	130/100	3
	Water jet	Sprayed GFRP – Resin 1	130/100	3
	Sandblast	Sprayed GFRP – Resin 1	130/100	3
	Jackhammer	Sprayed GFRP – Resin 1	130/100	3
Resin type/ FRP type	Sandblast	Spray GFRP – Resin 2	130/100	3
	Sandblast	CFRP	130/100	3
	Sandblast	Wrap (Wabo Mbrace)	130/100	3
	Jackhammer	Wrap (Wabo Mbrace)	130/100	3
Bond length	Sandblast	Sprayed GFRP – Resin 1	130/70	3
	Sandblast	Sprayed GFRP – Resin 1	130/120	3
Loading rate	Water jet	Sprayed GFRP – Resin 1	130/100	12
	Total number of specimens			48

5.1.1 Testing processes

The testing process was the same for every sample regardless of its FRP type or treatment. Except as noted otherwise, the following process was used for all samples discussed in Chapters 5 and 6. Each sample was fitted with an aluminum vise and placed, simply supported, in the Instron loading frame. The sample was fitted with two electronic displacement prongs that relayed information to the computer console. Once these prongs were set up (back side zeroed at 2.7 mm and front side zeroed at 2.0 mm) the machine was then able to follow the displacement of the sample due to the loading. A controller keypad was used to raise the sample until the middle of the sample was loaded in four-point bending to 0.2 kN. At this point the sample was fully prepared for testing, and the last instructions were given through the machine's computerized interface.

The simple schematic in Figure 5.1 shows the four-point bending under which each sample was load tested and the failure mode of the spray-on FRP. The failure

representation of the concrete has been greatly exaggerated to show the mechanics of the debonding. The sample is placed on two fixed bottom supports while loaded by two arms from above. As shown, the load points above the sample are each 50 mm from the notch centre. The bottom supports are 100 mm from the loads and thus 150 mm from the notch centre. Similar to Figure 5.1, Figure 5.2 shows the four-point bending of an actual sample with arrows representing the location of the imposed forces. The displacements are measured by linear variable differential transformers (LVDTs) connected to the yoke. The yoke enables us to exclude support deformation. Therefore, the displacement measured is the mid-span centerline deflection.

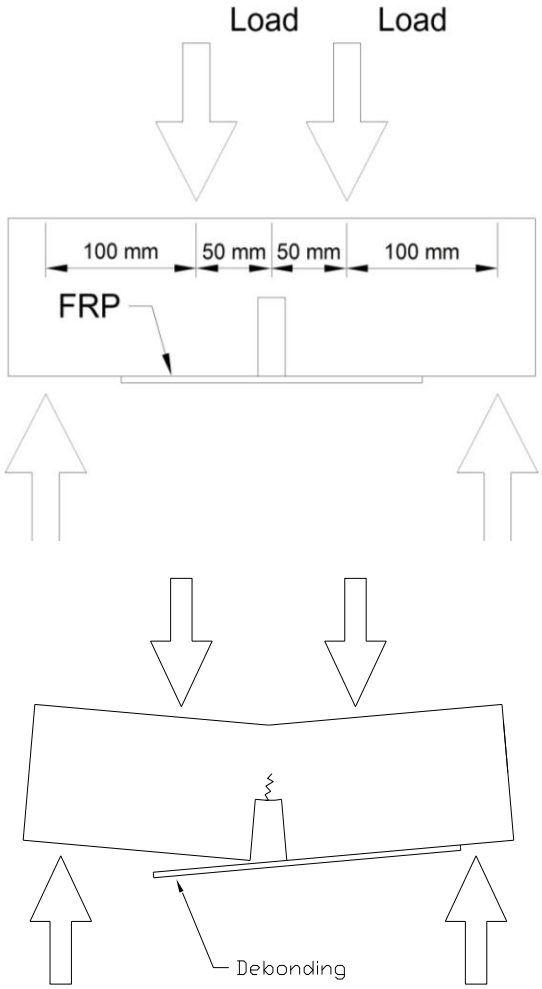

Figure 5.1. *Schematic of the test.*

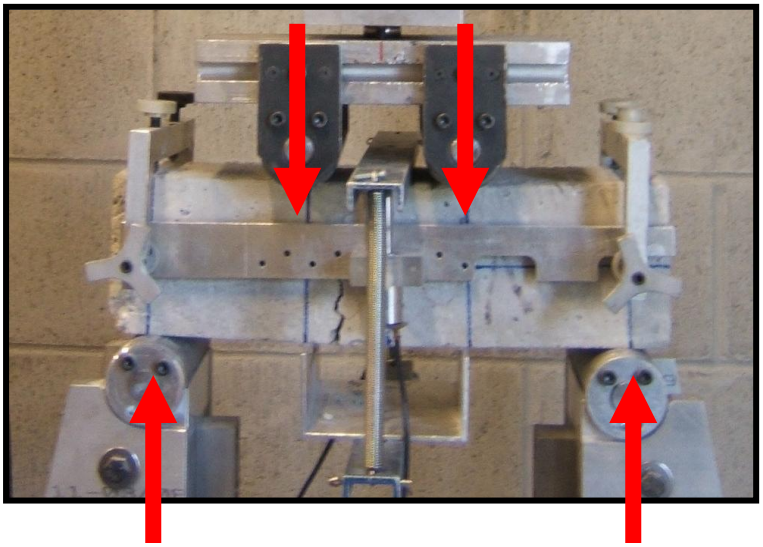

Figure 5.2. *Sample loaded under four-point bending.*

The samples were tested in terms of constant applied displacement, which means the machine applied the exact forces required to produce the imputed displacement. If the actual rate of displacement slowed to below the desired rate, the machine increased the loading stress, and it similarly reduced the load if the sample experienced a deflection rate in excess of the imputed value. A displacement rate of 0.05 mm/min was used. The data collected from this interface was transferred to a computer that plotted the load as a function of displacement. Plots developed showed areas of partial failure (cracking), elastic deformation, and ultimate failure where the concrete could no longer provide resistance. Figure 5.3 shows the Instron 8802 series machine used for all specimens tested, with a sample assembled.

Figure 5.3. *Sample loaded on the Instron testing machine.*

Different types of failure were witnessed and are discussed in the following sections of this chapter. Also, the load displacement graphs of each sample are correlated in groups and compared with one another. To measure the vertical deformation of the beam, two LVDTs were used, one on either side of the sample. To allow for maximum displacement during loading he LVDTs were set up so that they were barely touching the surface. Tests were done using a yoke setup that averages displacement over the two halves of the sample.

5.1.2 Testing results

The results of the testing were largely as expected, with two exceptions. Attempts were made to represent the data in the form of the actual bond shear strength, but because of the insufficient bonded length, only ultimate bending loads, P_{ult}, of the specimens are compared.

The average ultimate load and failure mechanism for all of the sample types are given in the following subsections.

5.1.2.1 Un-notched – no FRP

Three un-notched samples with no FRP were tested in the laboratory for baseline comparisons. All three samples failed in the same manner, with a vertical crack progressing upward from the bottom of the sample through to the top. An example of an un-notched sample is shown in Figure 5.4. As shown in Figure 5.5, they also had similar load vs. displacement curves.

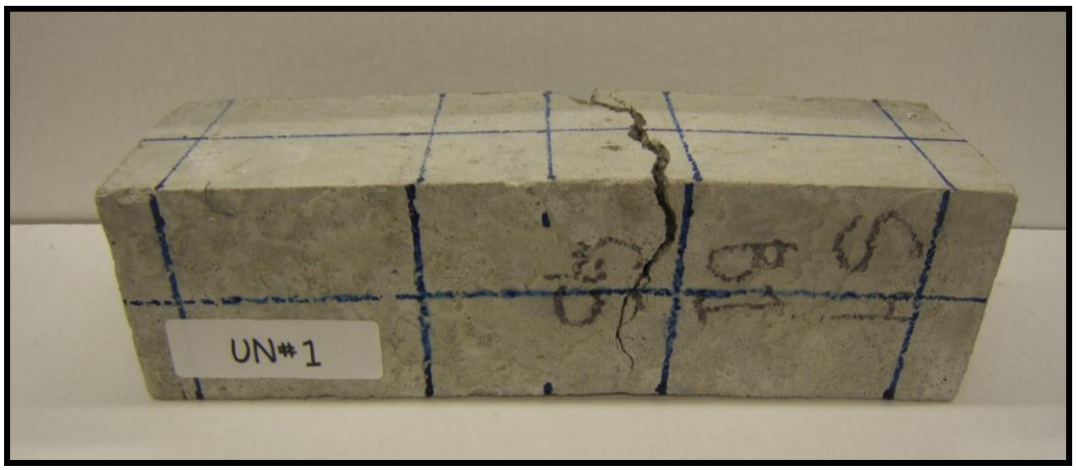

Figure 5.4. *Sample UN-1 after failure.*

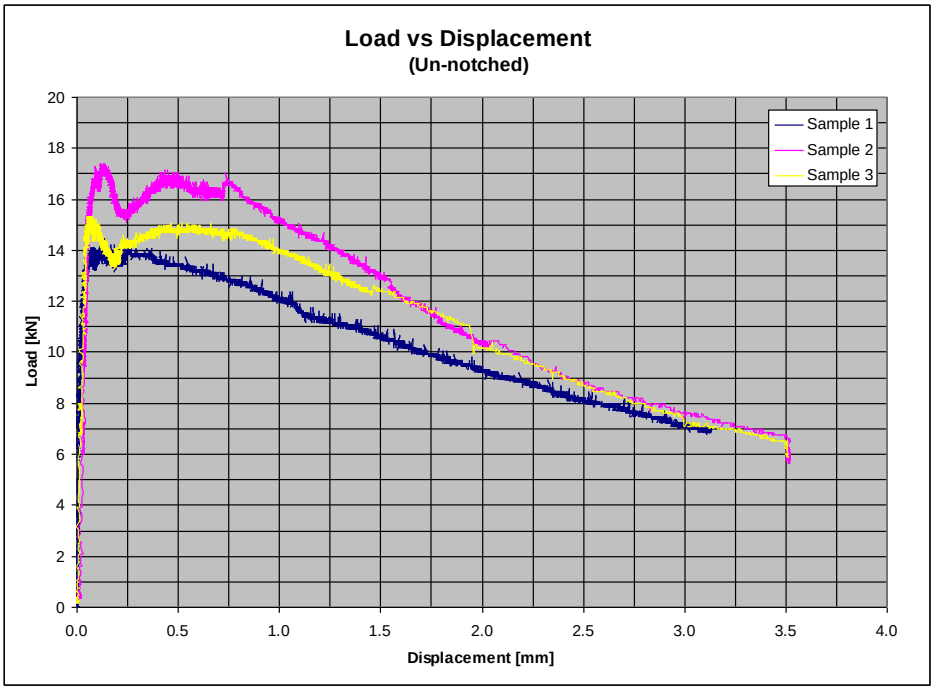

Figure 5.5. *Un-notched – no FRP: load vs. displacement.*

All three samples were also similar in terms of the ultimate load that the beams withstood. The standard deviation is relatively small compared with the average load of 15.7 kN, assuring that the data is reliable. The ultimate load for each sample can be found in Table 5.2.

Table 5.2. *Ultimate load values (un-notched – no FRP)*

	P_{ult} [kN]]
Sample 1	14.48
Sample 2	17.42
Sample 3	15.34
Average	15.74
Std. Dev.	1.51

5.1.2.2 Notched – no FRP

Three notched samples without FRP were made and tested to create a baseline for comparison. All three samples failed in a similar manner, in which the crack began at the notch and propagated upwards to the point of load application. Figure 5.6 shows a notched control sample. The blue markings were used to position the load supports and

the aluminum vice that held the displacement prongs. Figure 5.7 shows that the load vs. displacements curves for each sample are quite similar, differing only in the length of the plastic region. This discrepancy may be due to inconsistent steel fibre concentrations.

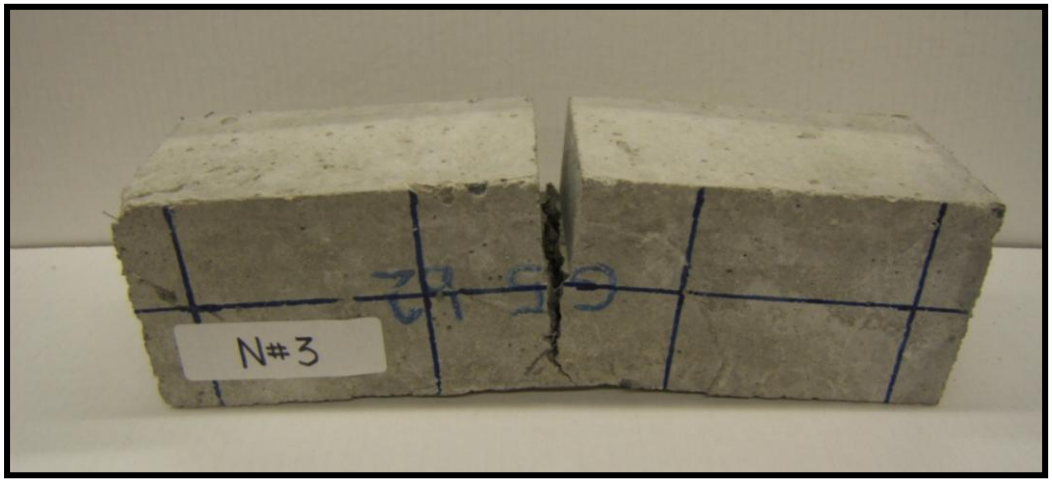

Figure 5.6. *Sample N-3 after failure.*

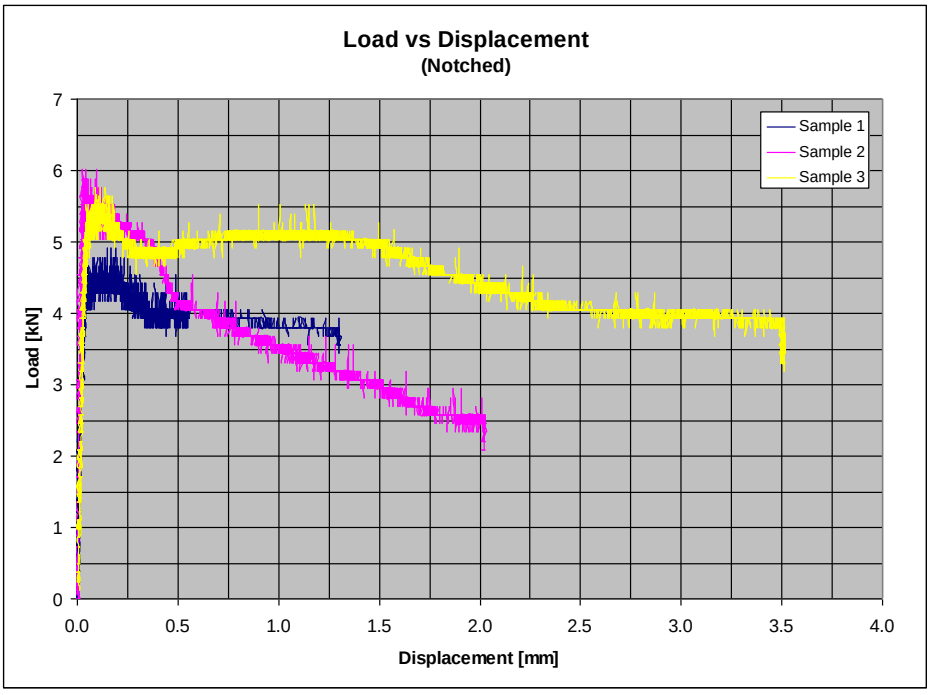

Figure 5.7. *Notched – no FRP: load vs. displacement.*

All three samples tested were also consistent in their values of P_{ult}, failing at an average load of 5.56 kN. The small standard deviation relative to ultimate load further ensures the accuracy of our results. The ultimate load for each sample can be found in Table 5.3.

Table 5.3. *Ultimate load values (notched – no FRP)*

	P_{ult} [kN]
Sample 1	4.91
Sample 2	6.01
Sample 3	5.77
Average	**5.56**
Std. Dev.	0.58

5.1.2.3 No surface preparation – Resin 1 (ATPRIME®)

Three samples were then created using no surface preparation and ATPRIME® bonding agent. All three samples failed via the debonding of the short, 10 cm, FRP side. Figure 5.8 shows a sample after failure.

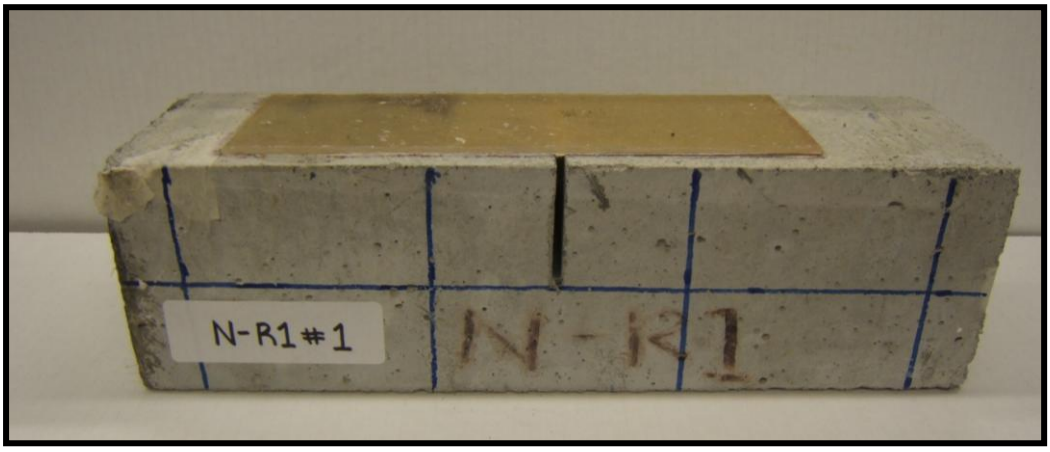

Figure 5.8. *Sample N-R1-1 after failure.*

As is evident in Figure 5.9 and Table 5.4, the third sample tested exhibited an unusually large P_{ult}. Figure 5.10 shows a sample with the FRP removed and the steel fibres visible beneath. The protrusion of steel fibres, which then become embedded in the FRP application, can increase the bond strength.

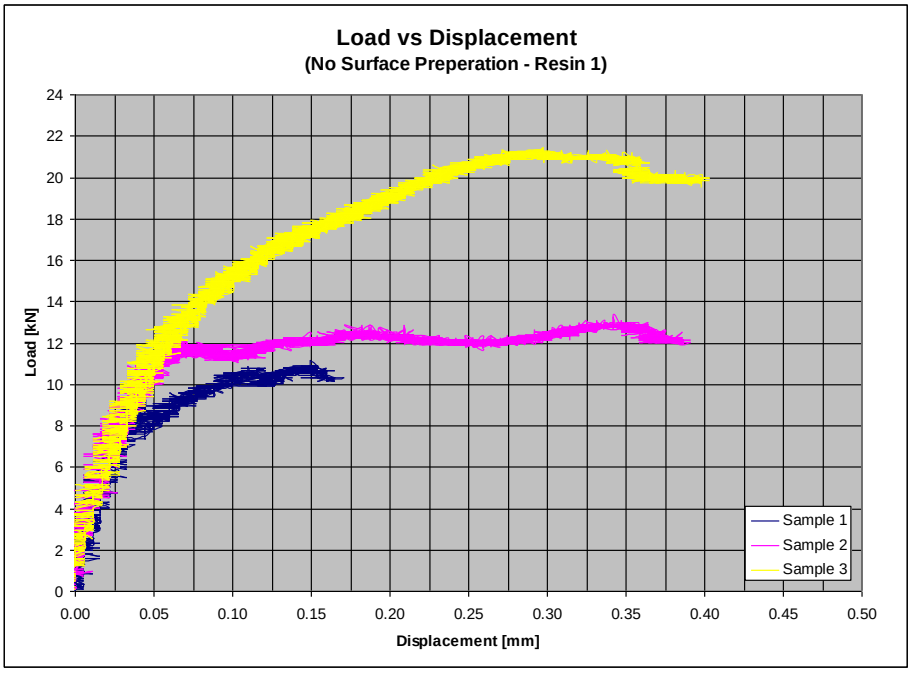

Figure 5.9. *No surface preparation – Resin 1: load vs. displacement.*

Table 5.4. *Ultimate load values (no surface preparation – Resin 1)*

	P_{ult} [kN]
Sample 1	11.16
Sample 2	13.37
~~Sample 3~~	~~21.47~~
Average	**12.27**
Std. Dev.	1.56

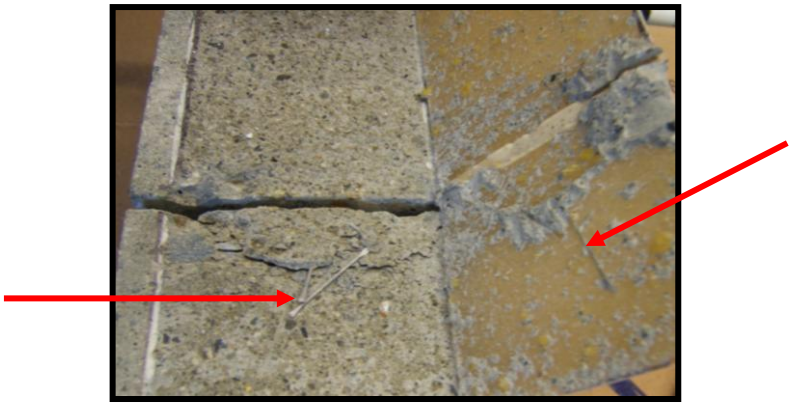

Figure 5.10.*. Protruding steel fibres.*

5.1.2.4 Water jet – Resin 1

Three samples prepared with water jet surface treatment and Resin 1 were tested to compare with the effectiveness of samples using different surface preparations. Two of the samples reached debonding failure on the longer, 13 cm side of the FRP application, whereas one failed on the shorter, 10 cm side. Figure 5.11 shows a sample after failure. As shown in Figure 5.12, all three samples exhibited similar displacements for the given loading rates at testing.

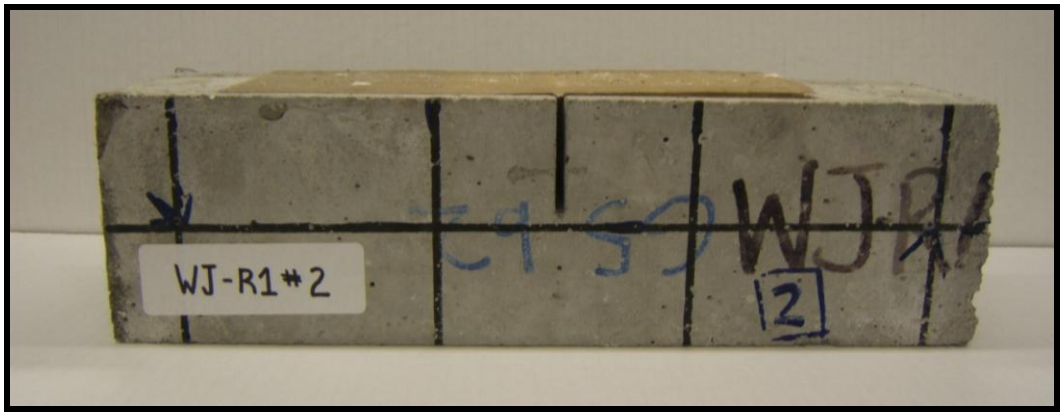

Figure 5.11. *Sample WJ-R1-2 after failure.*

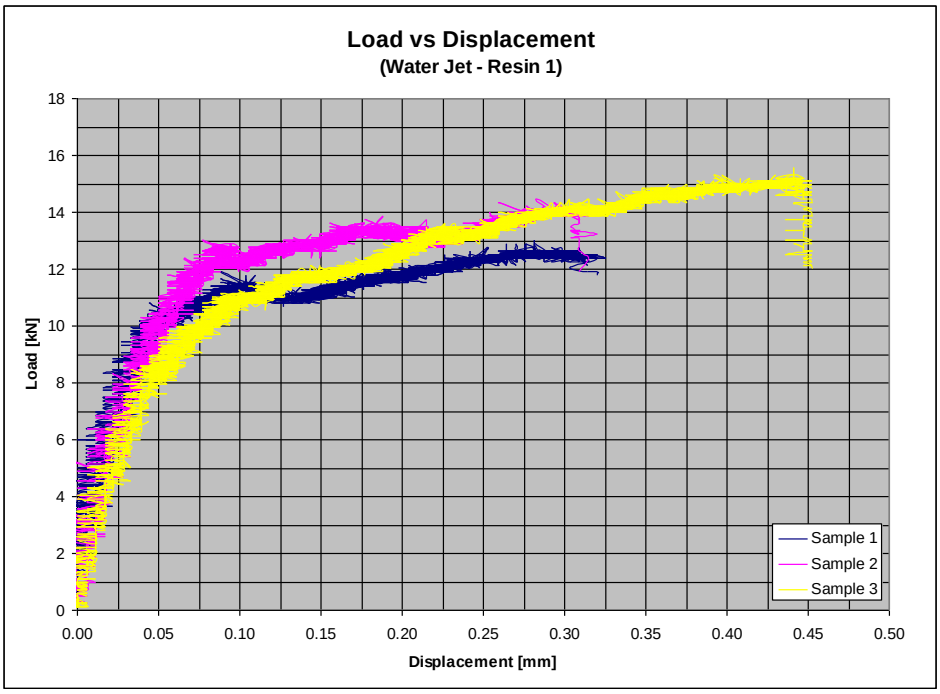

Figure 5.12. *Water jet – Resin 1: load vs. displacement.*

As seen in Table 5.5, the distribution of the data is consistent for the three samples, showing a P_{ult} of 14.35 kN and a standard deviation of 1.29 kN. These values suggest that the results are reliable because of the small variation in the ultimate load. The average ultimate load for samples with water jet – Resin 1 is slightly larger than that of samples discussed in Section 5.1.2.3 with no surface preparation, which have an average ultimate load of 12.27 kN.

Table 5.5. *Ultimate load values (water jet – Resin 1)*

	P_{ult} [kN]
Sample 1	13.00
Sample 2	14.48
Sample 3	15.58
Average	**14.35**
Std. Dev.	1.29

5.1.2.5 Sandblast – Resin 1

Two samples with sandblast surface treatment were tested to observe the behavior of this treatment juxtaposed with other surface preparations. One of the samples had a noticeably uneven loading surface prior to testing, which may have resulted in imbalanced debonding along the FRP and concrete interface. This sample had debonding failure occur on the longer, 13 cm side of the FRP application. The other sample in this set failed on the shorter, 10 cm side and displayed cracking in the concrete around the notch. Figure 5.13 shows a sample after failure. The load versus displacement curve for these samples has a consistent distribution and is shown in Figure 5.14.

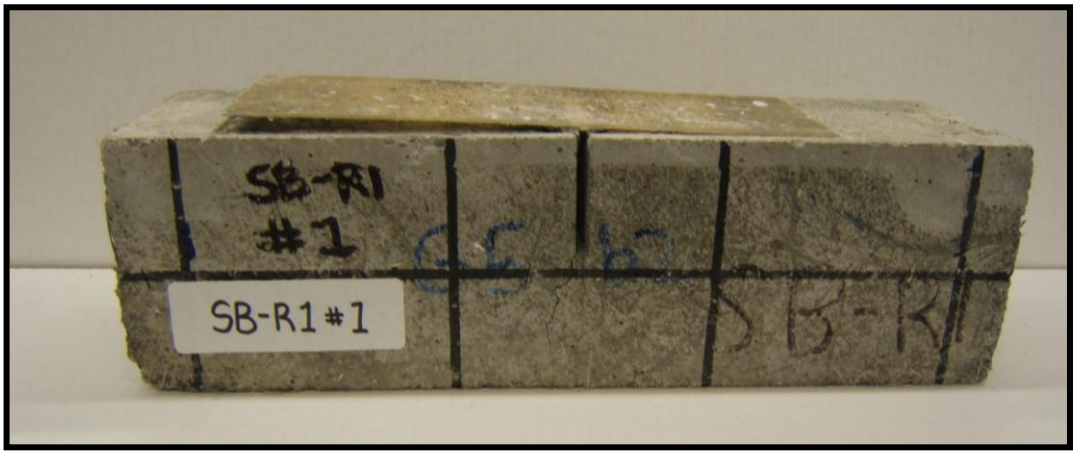

Figure 5.13. *Sample SB-R1-1 after failure.*

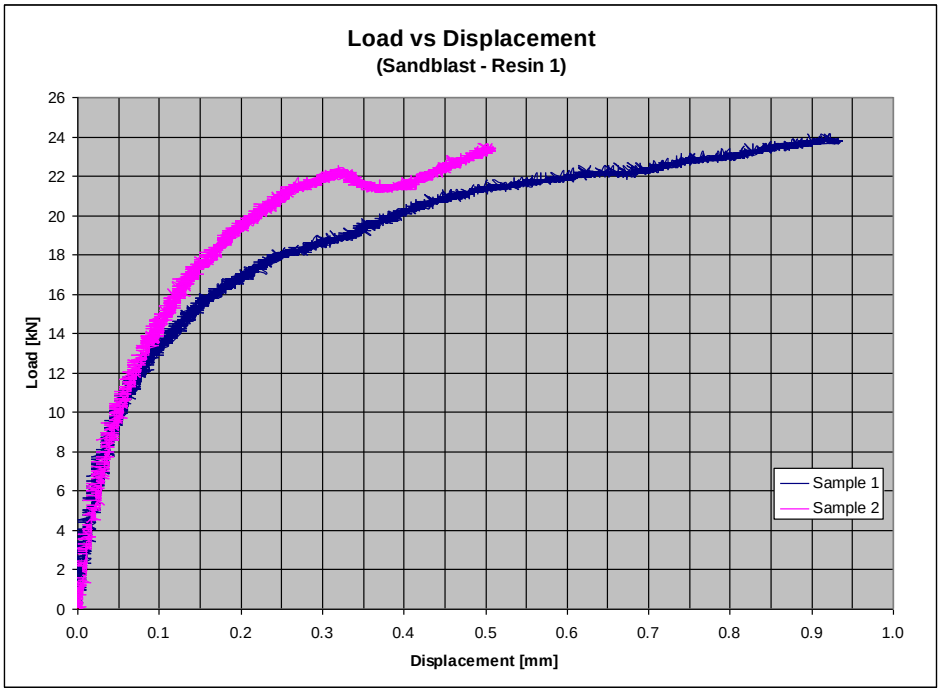

Figure 5.14. *Sandblasted – Resin 1: load vs. displacement.*

The ultimate load values shown in Table 5.6 reveal significantly larger results compared with the no surface preparation and water jet samples using the same resin type. The average P_{ult} of 23.92 kN with the standard deviation of 0.35 kN support consistent results. However, it should be noted that only two samples were tested in this set.

Table 5.6. *Ultimate load values (sandblast – Resin 1)*

	P_{ult} [kN]
Sample 1	24.17
Sample 2	23.68
Average	**23.92**
Std. Dev.	0.35

5.1.2.6 Jackhammer – Resin 1

Three samples were treated with a jackhammer surface preparation to show the effect of increased surface roughness and effective bond length compared with the previous surface preparations of water jet and sandblasting. Figure 5.15 shows surface abrasion from the jackhammer treatment. Two of the samples in this set debonded on the longer, 13 cm side of the applied FRP, and one debonded on the shorter, 10 cm side. One of the samples that failed on the longer applied FRP side (Figure 5.16) exhibited small deformities as a result of an inconsistency in its preparation. However, this did not affect the results of the testing. As seen in Figure 5.17, all three samples displayed similar loading behavior.

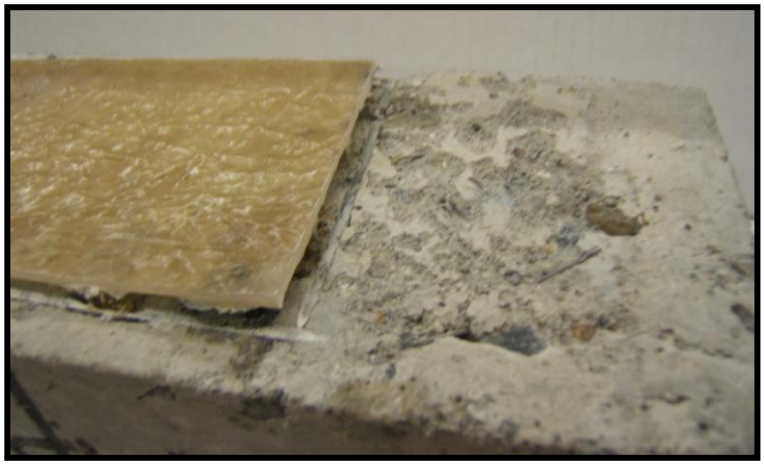

Figure 5.15. *Surface abrasion from jackhammer (JH-R1-2).*

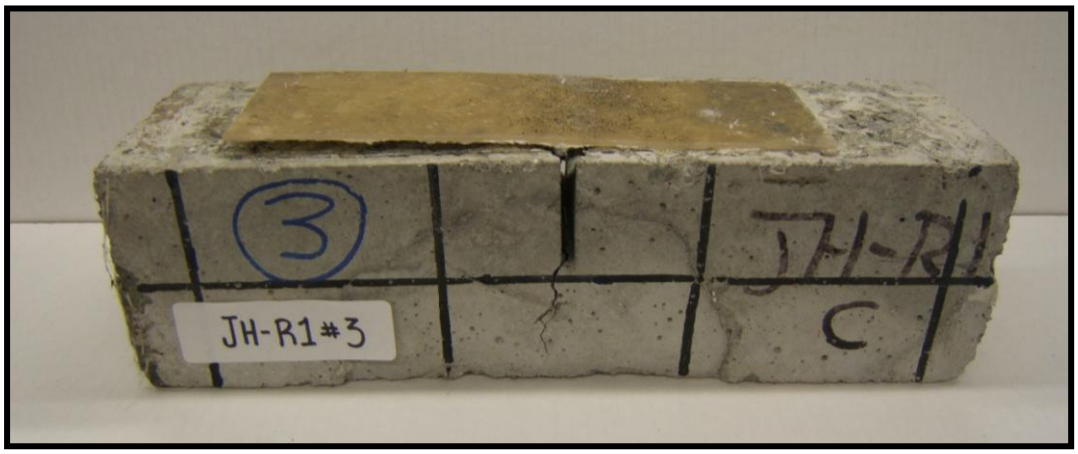

Figure 5.16. *Sample JH-R1-3 after failure.*

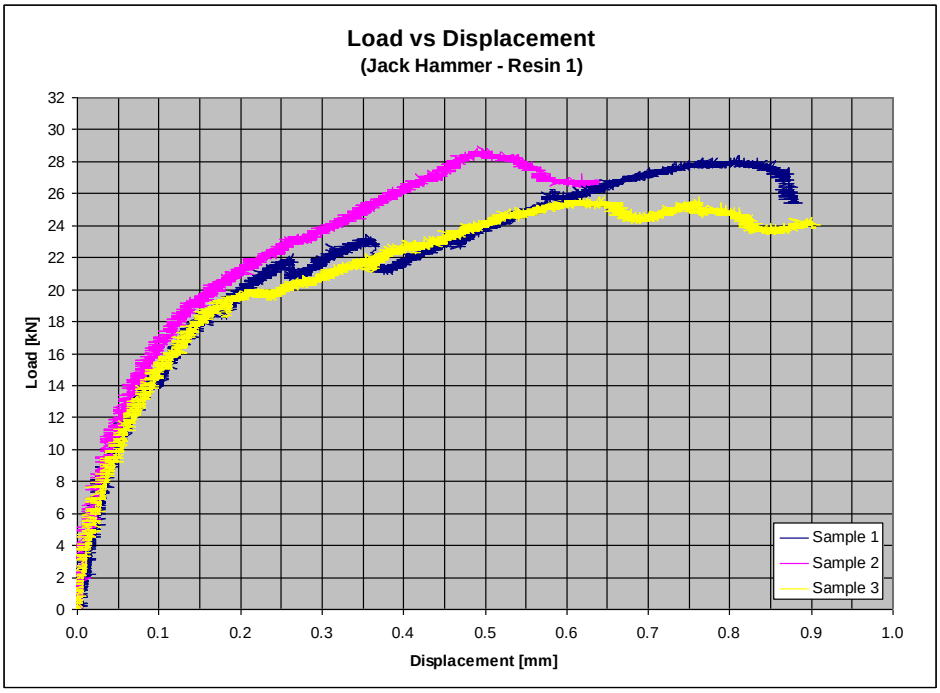

Figure 5.17. *Notched – no FRP: load vs. displacement.*

The results of testing this set of samples show an increase in the ultimate load when in contrast with the other types of surface preparation, signifying that increased roughness and effective bond length produce higher ultimate loads in the bond between

FRP and concrete. As shown in Table 5.7, the P_{ult} for this set is 27.73 kN with a standard deviation of 1.62, which can be considered reliable.

Table 5.7. *Ultimate load values (jackhammer – Resin 1)*

	P_{ult} [kN]
Sample 1	28.34
Sample 2	28.95
Sample 3	25.89
Average	**27.73**
Std. Dev.	1.62

5.1.2.7 Sandblast – Resin 2

Three samples were made using a different bonding agent (denoted here as Resin 2). The purpose was to assess the effectiveness of the commonly used bonding agent 1. The sample tested did, however, fail via the debonding of the short side (Figure 5.18). The shape of the load versus displacement curve shown in Figure 5.19 is as would be expected.

Figure 5.18. *Sample SB-R2-1 after failure.*

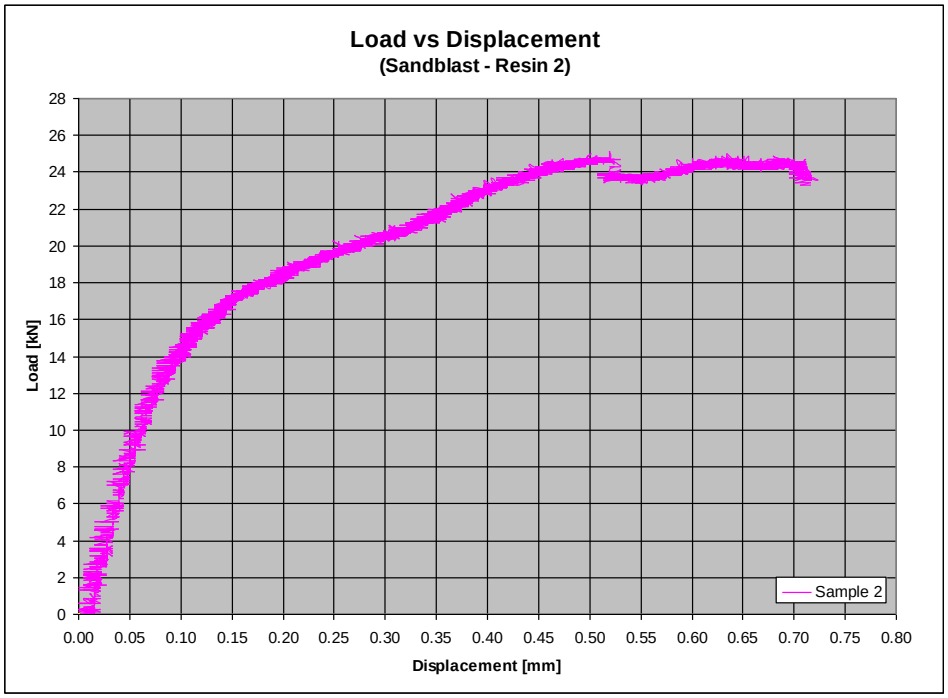

Figure 5.19. *Sandblasted – Resin 2: load vs. displacement.*

The FRP on two of the three specimens were debonded before testing. The load at failure for the one sample tested was 25.15 kN Further testing must be completed to make any justifiable conclusions on the effectiveness of Resin 2.

5.1.2.8 Sandblast – carbon fibre reinforced polymer

Three samples were sprayed with a carbon fibre reinforced polymer (CFRP). It was expected the high strength of the carbon fibre would cause the FRP to be much stronger than the bond. This, however, was not the case. The first two samples failed through a crack in the FRP with the majority of the bond remaining intact (see Figures 5.20 and 5.21). As the crack progressed through the FRP the strength dropped suddenly and then slowly picked up again. This behavior can be seen in the load vs. displacement plot in Figure 5.22. The final sample, unlike the first two, failed at the CFRP–concrete bond with one side of the FRP completely de-bonding.

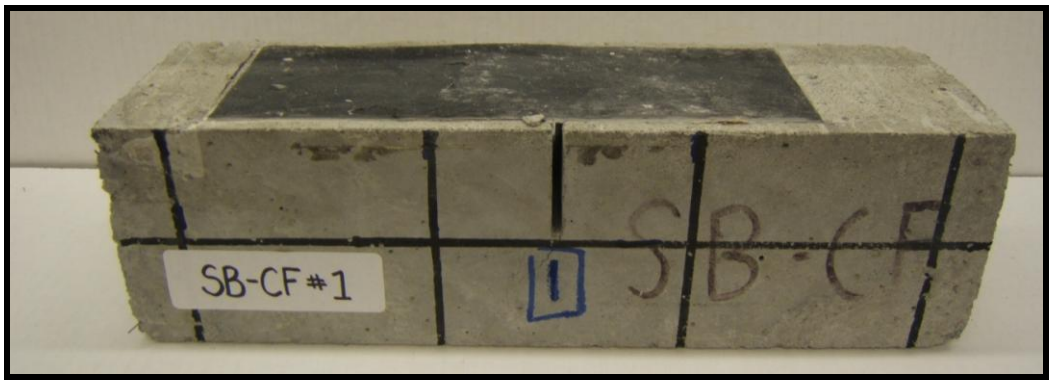

Figure 5.20. *Sample SB-CF-1 after failure.*

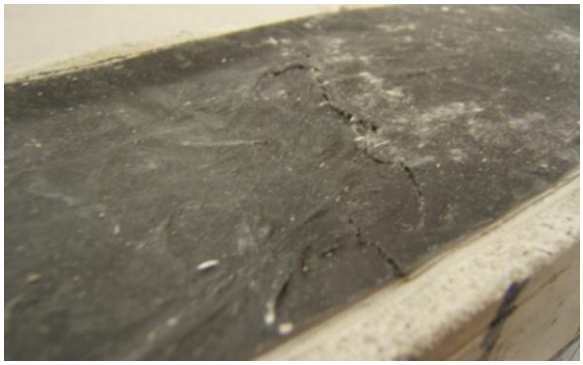

Figure 5.21. *Failure of CFRP.*

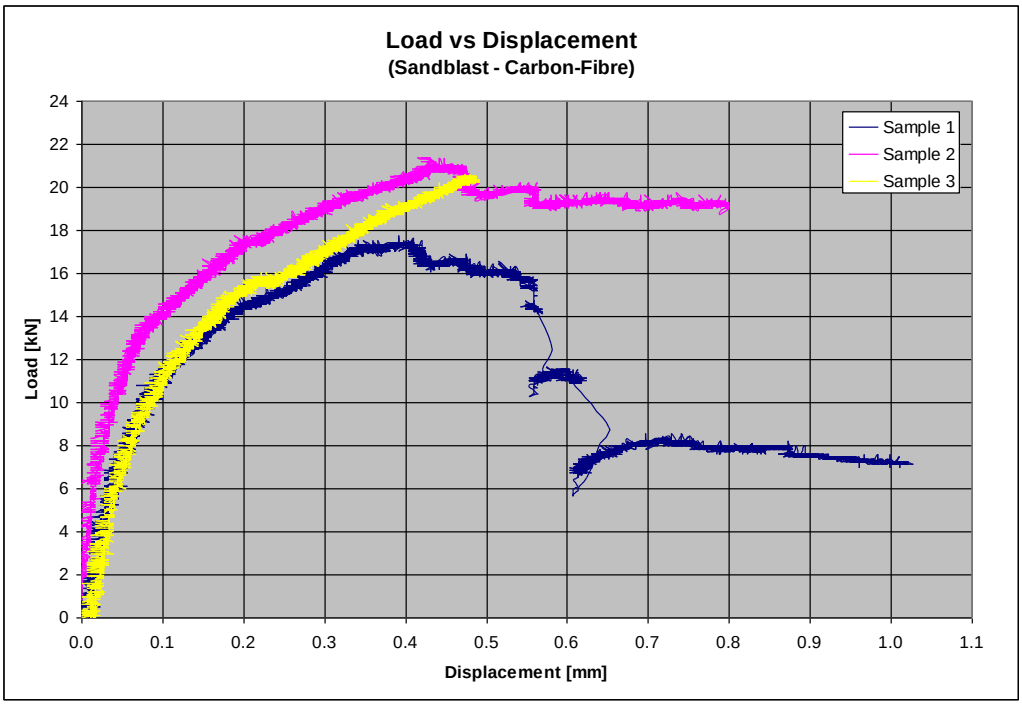

Figure 5.22. *Sandblasted – carbon fibre: load vs. displacement.*

Despite the different failure methods all the samples had relatively similar ultimate loads (Table 5.8). The similar values suggest that the bond and tensile strengths are very similar for the sample specifications. Any comparisons made with these values should note that they do not accurately represent the bond strength.

Table 5.8. *Ultimate load values (sandblast – carbon fibre)*

	P_{ult} [kN]
Sample 1	17.79
Sample 2	21.35
Sample 3	20.61
Average	**19.91**
Std. Dev.	1.88

5.1.2.9 Sandblast – wrap

Three samples were sandblasted and then strengthened with a wrap FRP rather than the spray application used in the majority of our samples. Unfortunately, ideal test results were not obtained with these three samples, as there was not a premature debonding failure between the FRP and the concrete, but rather a shear failure in the concrete itself (Figures 5.23 and 5.24).

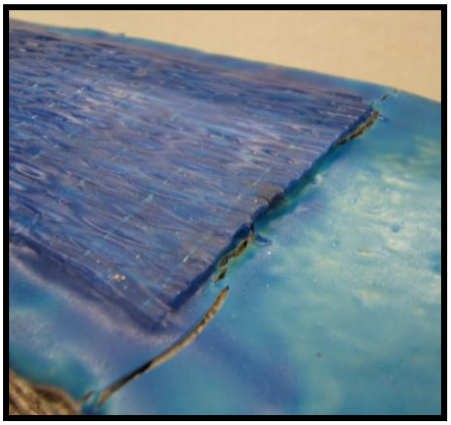

Figure 5.23. *Sample SB-W-2 after failure.*

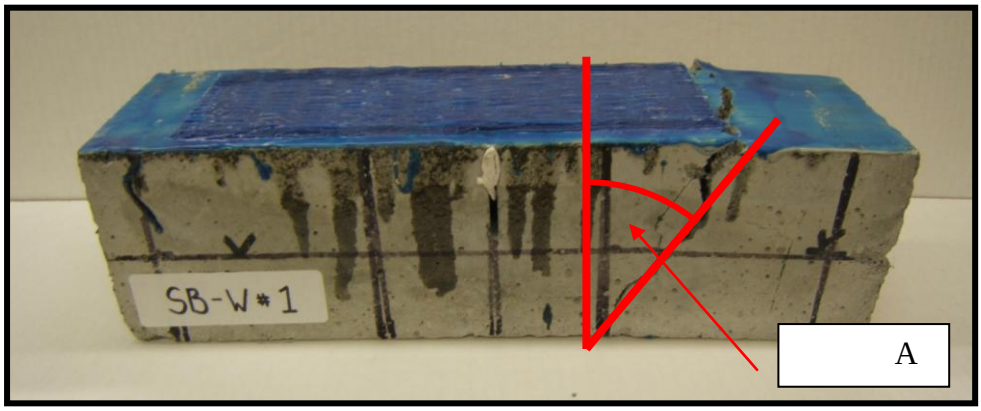

Figure 5.24. *Sample SB-W-1 after failure.*

The three samples had varying ultimate loads ranging from 28.71 to 35.70 kN, with an average ultimate strength of 32.22 kN and a standard deviation of 3.50 kN (Table 5.9). The samples did not fail as a result of debonding. For these specimens, the debonding failure load is higher than shear failure ultimate load. This shear failure is illustrated in Figure 5.24; the cracking occurred at approximately 45° to the direction of loading. It should be noted that all samples failed along relatively the same angle, beginning on the bottom edge where the wrap was applied, precisely at the end of the wrap cloth. Another confirmation of the failure mode being in the concrete itself is illustrated in Figure 5.25, showing a near linear load path up to the failure point. This type of behavior is typical for failure of pure fibre reinforced concrete. While all samples failed in the same manner, with comparable load versus displacement curves and ultimate strength values, the data obtained from these tests did not provide a useful comparison to the sandblasted – sprayed FRP samples. The only possible conclusion that can be drawn from these samples is that the ultimate load required to cause bond failure is higher than the ultimate load required to cause shear failure of concrete.

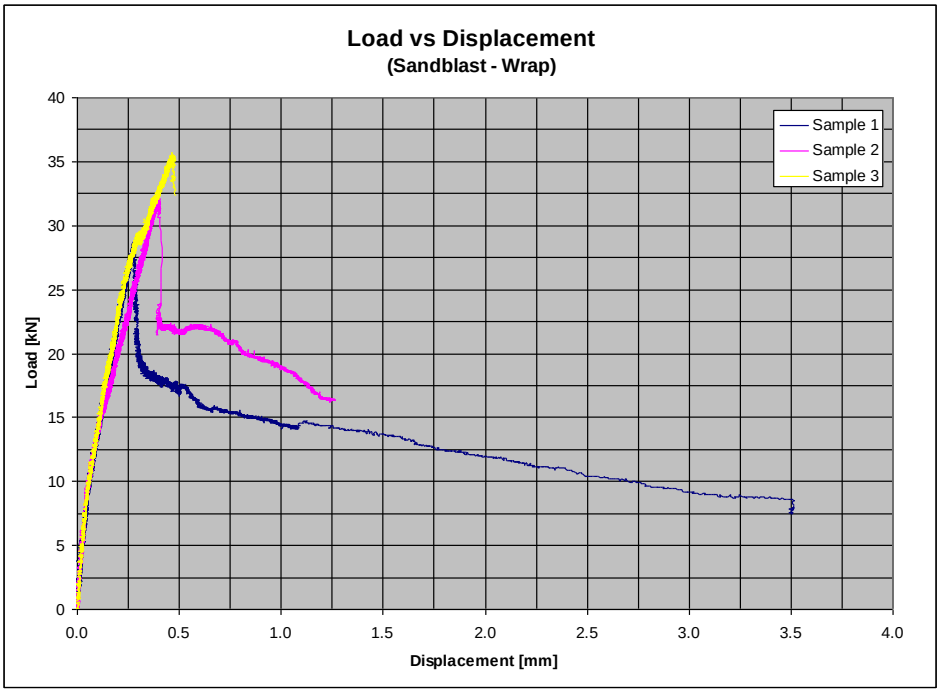

Figure 5.25. *Sandblasted – wrap: load vs. displacement.*

Table 5.9. *Ultimate load values (sandblast – wrap)*

	P_{ult} [kN]
Sample 1	28.71
Sample 2	32.26
Sample 3	35.70
Average	**32.22**
Std. Dev.	3.50

5.1.2.10 Jackhammer – wrap

The surfaces of three samples were jackhammered, resulting in a more abrasive surface and more surface area for the bond of the FRP to the concrete. The wrap FRP was then applied to these samples as it had been to the three sandblasted samples. As with the sandblasted – wrap FRP samples, the jackhammered samples saw failures not in the bond between the concrete and the FRP, but instead in the concrete itself (Figure 5.26).

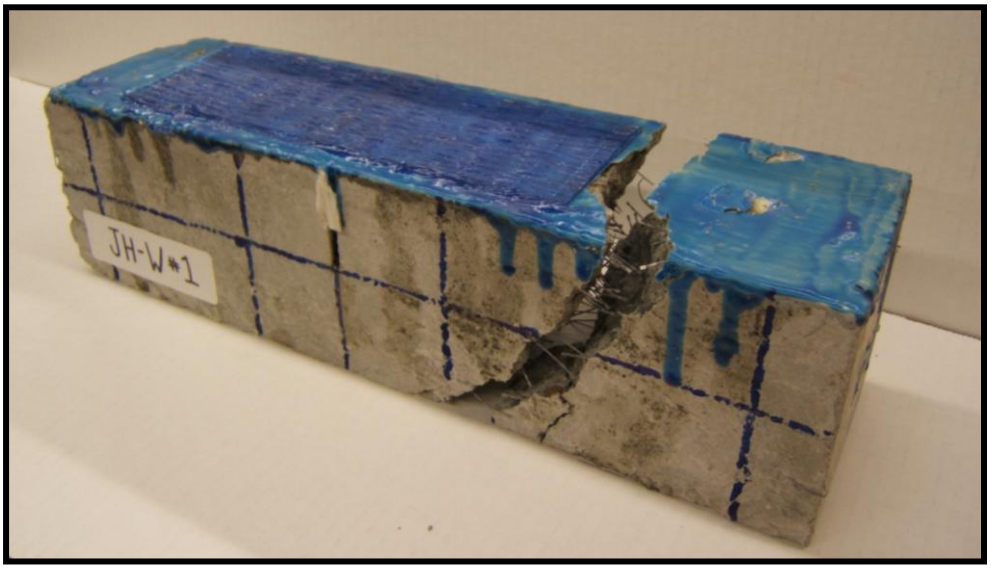

Figure 5.26. *Sample JH-W-1 after failure.*

The three jackhammered samples failed under a slightly higher ultimate load with an average of 36.68 kN and a standard deviation of 1.59 kN (Table 5.10). These samples failed with a cracking angle close to 45° to the angle of loading, and the bottom crack was initiated at the edge of the FRP wrap. These three samples all exhibited near linear behavior prior to failure, as illustrated in Figure 5.27, indicative of steel fibre reinforced concrete. Again, it is hard to draw comparisons between these samples and the sprayed FRP samples, as a bond failure was not initiated. The only conclusion that can be drawn here is that the strength of the bond is greater than that of the shear strength of the concrete. (Note that the sample shown in Figure 5.26 was allowed to continue loading once the concrete had realistically failed in an attempt to fully break the concrete in two.)

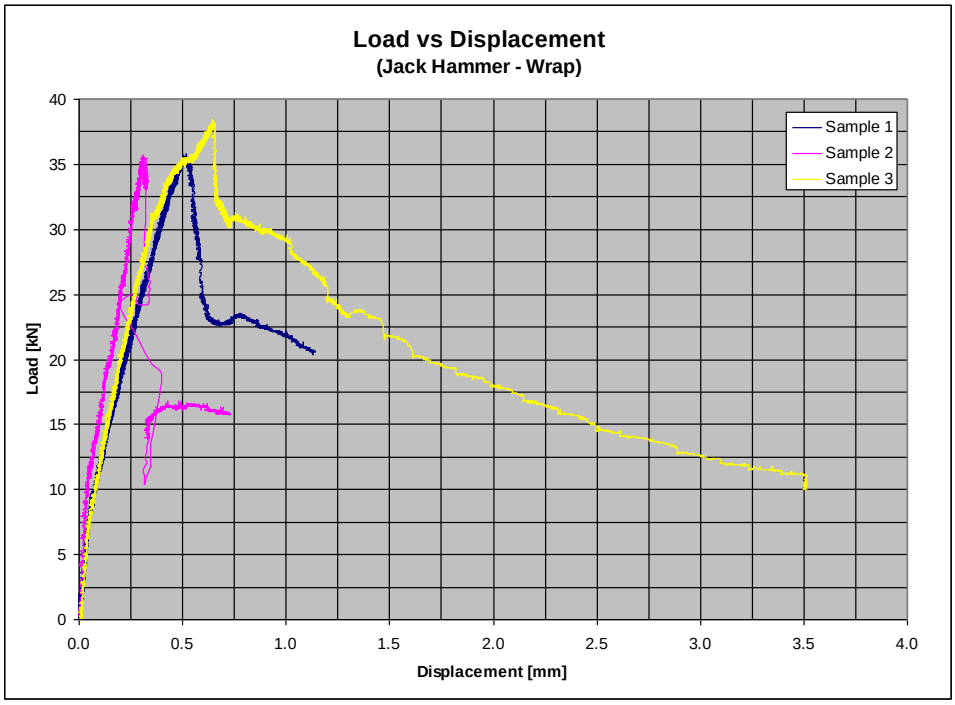

Figure 5.27. *Jackhammer – wrap: load vs. displacement.*

Table 5.10. *Ultimate load values (jackhammer – wrap)*

	P_{ult} [kN]
Sample 1	35.82
Sample 2	35.70
Sample 3	38.52
Average	**36.68**
Std. Dev.	1.59

5.1.2.11 Sandblast – 7 cm length

Three samples were made in which the varying bond length was set at 7 cm. As would be expected, all three samples failed via the debonding of the 7 cm side (see Figures 5.28 and 5.29). As illustrated in Figure 5.30, all three samples exhibited a similar load versus displacement curve, again differing only in the length of the plastic region.

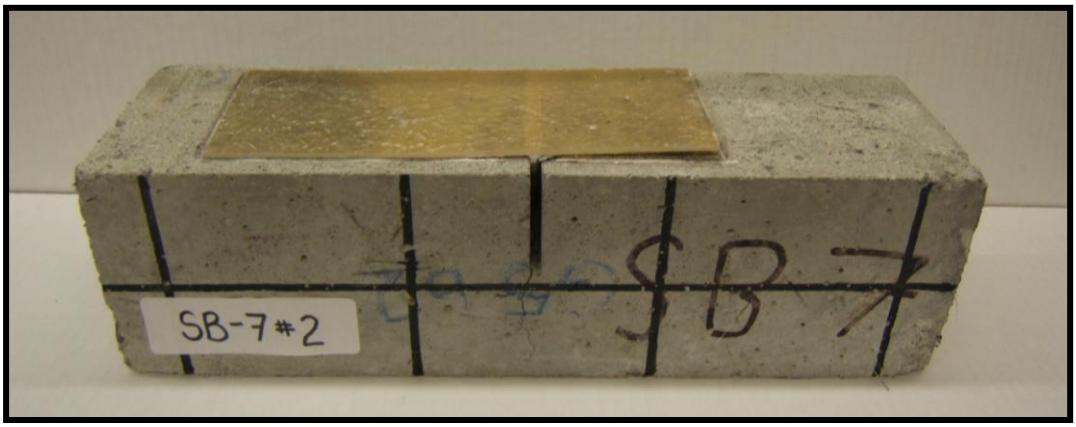

Figure 5.28. *Sample SB-7-2 after failure.*

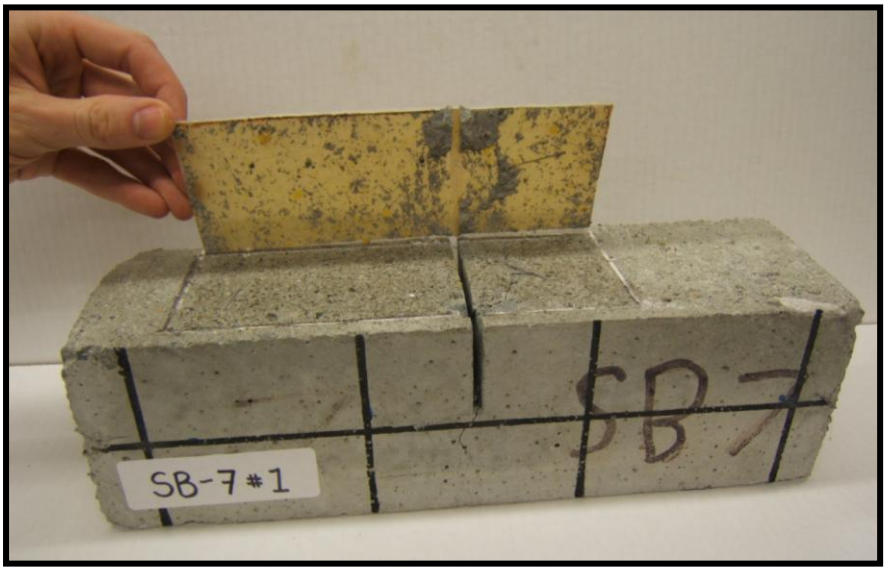

Figure 5.29. *Sample SB-7-1 with FRP removed.*

All three samples failed at relatively similar P_{ult}, with an average load at failure of 21.92 kN (Table 5.11). However, the standard deviation is not quite as low as in the previous tests. The third sample failed at a load lower than the other two, thus causing the lower average P_{ult}. Further testing should be completed regarding bond length (7 cm, etc.) to achieve a higher level of accuracy.

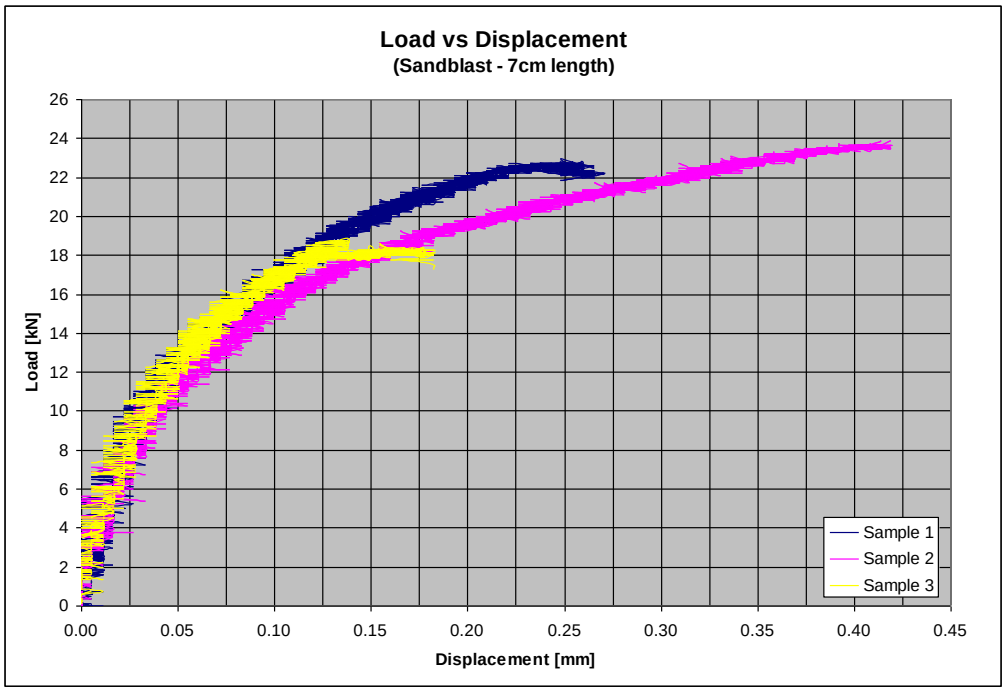

Figure 5.30. *Sandblasted – 7 cm: load vs. displacement.*

Table 5.11. *Ultimate load values (sandblast – 7 cm length)*

	P_{ult} [kN]
Sample 1	22.94
Sample 2	23.92
Sample 3	18.89
Average	21.92
Std. Dev.	2.67

5.1.2.12 Sandblast – 12 cm length

Three samples were made by setting the varying bond length to 12 cm. Two of the three samples failed via the debonding of the 12 cm side (see Figure 5.31), whereas the final sample failed via the debonding of the 13 cm side. As a result, it can be concluded that at the 12 cm length the two lengths are too similar, and thus the bond length does not have a significant effect on the method of failure. As illustrated in Figure 5.32 the load versus displacement curves for all three samples are almost identical.

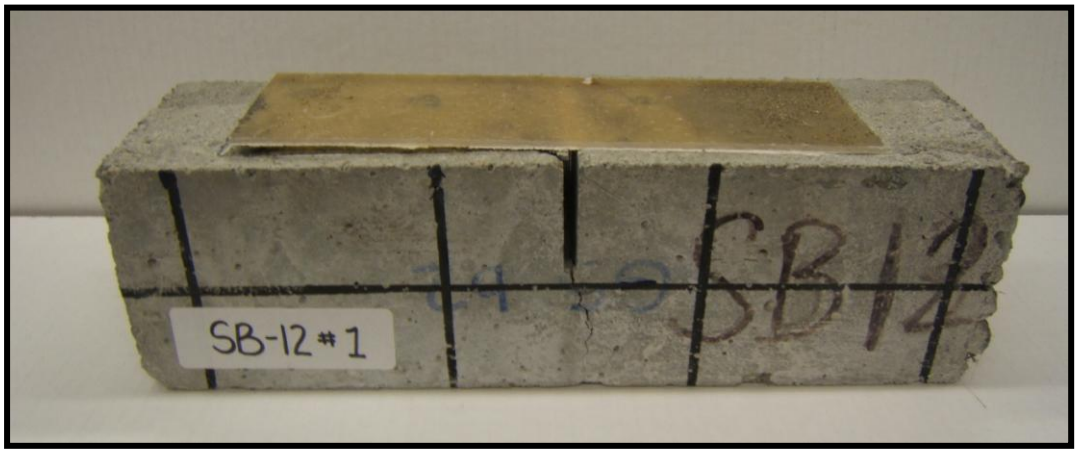

Figure 5.31. *Sample SB-12-1 after failure.*

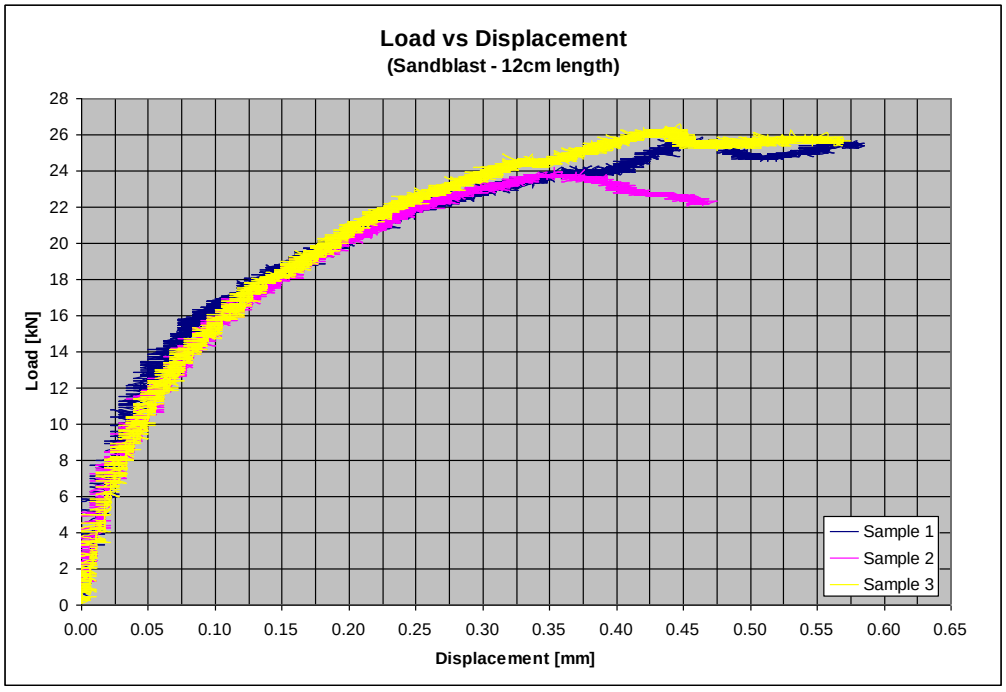

Figure 5.32. *Sandblasted – 12 cm: load vs. displacement.*

Fortunately, all three samples failed at a relatively consistent P_{ult}, at an average load of 25.56 kN. The small standard deviation relative to the P_{ult} further ensures the accuracy of the results. The load at failure for each sample can be found in Table 5.12.

Table 5.12. *Ultimate load values (sandblast – 12 cm length)*

	P_{ult} [kN]
Sample 1	25.89
Sample 2	24.17
Sample 3	26.62
Average	**25.56**
Std. Dev.	1.26

5.1.3 Surface treatment versus ultimate strength

To study the effects of surface treatment on ultimate strength, the resin type and bond length were held constant while the surface treatments were varied. For all cases, the effective bond length was set at 10 cm and the resin type used was spray-on FRP, Resin 1. The following surface treatments were applied to the samples: none, water jet, sandblast, and jackhammer. Again, three tests were done for each configuration. The average strength results are shown in the Figure 5.33.

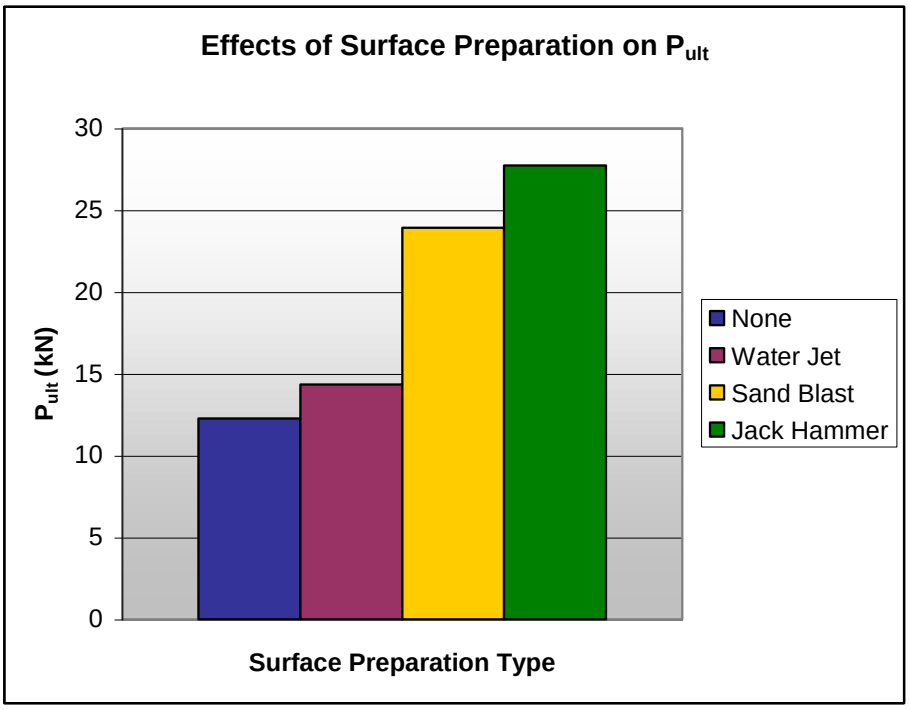

Figure 5.33. *Surface preparation comparison.*

The samples that received the water jet (power washing) surface treatment showed a minimal increase in strength over the samples with no surface treatment whatsoever. This is not surprising, as the water jet did little more than remove loose particles from the surface of the sample. Hence, the sample surface remained relatively smooth even after the surface treatment.

With the sandblasting surface treatment, the bond strength and the resultant ultimate strength were significantly increased. In fact, the strength exhibited by these specimens exceeded that of the unnotched control samples. Because the sandblasting caused the bonding surface to become quite rough, the FRP was able to bond more effectively with the concrete.

As illustrated in Figure 5.33, the highest ultimate strength was achieved by treating the concrete bonding surface with a jackhammer. Of all the treatments studied, jackhammering produced the roughest bonding surface. As such, the surface area (area where a bond could occur) between the FRP and concrete was maximized.

5.1.4 Fiber type versus ultimate strength

To study the effects of fibre type on the ultimate strength, the surface treatments and effective bond lengths were held constant. For the following samples, the concrete surface was sandblasted and the effective bond length was set at 10 cm. In all, three different fibre types were studied: glass fibre reinforced polymer (GFRP) using Resin 1, carbon fibre reinforced polymer (CFRP), and an FRP wrap. Note that the Resin 1 data that appears in Figure 5.34 is the same data (sandblasted, Resin 1) presented in Figure 5.33.

As shown in Figure 5.34, the FRP wrap samples exhibited a significantly higher ultimate strength than the CFRP and Resin 1 GFRP samples. In fact, the strength of the bond for the wrap FRP was such that the failure occurred in the concrete and not in the bond or the wrap (fibre breakage). As such, no data regarding the ultimate bond strength were collected. However, as none of the six FRP wrap (including the jackhammered

samples) bonds failed before the concrete failed, it can be concluded that the ultimate load of debonding is greater than 30 kN.

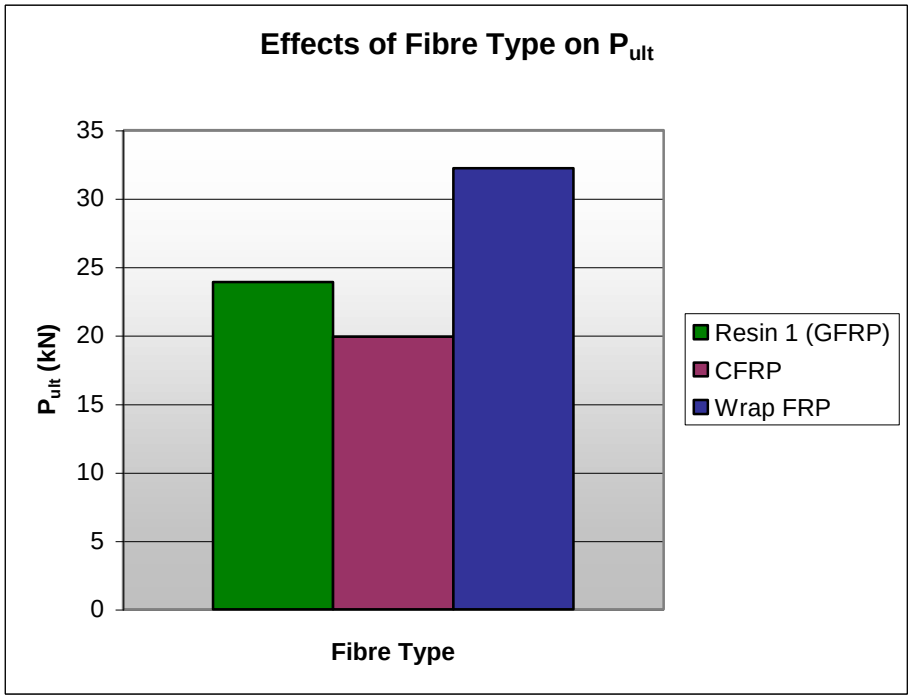

Figure 5.34. *Fibre type comparison.*

Of the three fibre types studied, the CFRP exhibited the lowest ultimate strength. However, this was due to the failure of the fibres and not debonding. In fact, two of the three samples failed in fibre breakage close to the notch and not in debonding. This is illustrated in Figure 5.35. As the carbon fibre has a higher ultimate tensile capacity compared with glass fibre, further research is to be done to assess the performance of carbon fibres in the FRP composite using different bonding agents.

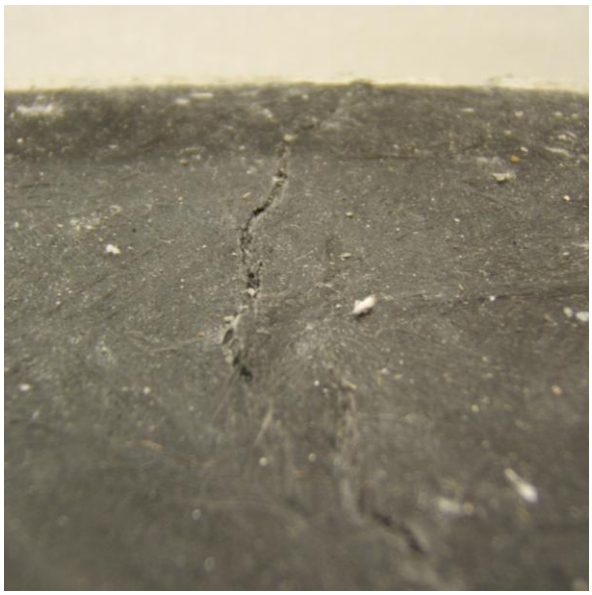

Figure 5.35. *CFRP failure mode through the fibres.*

However, even though the failure mechanisms were different, the load at which failure occurred was quite consistent. Since two different failure mechanisms were observed for these samples, it can be concluded that the CFRP bond strength is at least close to the measured ultimate load. Several changes were made in the next series of tests to help ensure that fibre breakage is not a failure mechanism for future tests.

5.1.5 Varying effective bond length

The final variant of this research was to investigate the effects of effective bond length on the strength of the FRP–concrete bond. For this study, the resin type and the surface treatment were held constant, using Resin 1 on a sandblasted surface. Three sets of samples were tested, corresponding to effective bond lengths of 7, 10, and 12 cm. The results are summarized in Figure 5.36 and Table 5.13.

As illustrated in Figure 5.36, the ultimate strength seems to increase as the effective bond length increases. However, as shown in Table 5.13, the location of failure does not always occur on the shorter side of the bond. This can be seen as counter-intuitive, since expectations were for the shorter side to always fail. Yet the trend shows

that as the difference in bond length reduces, the majority of the failures do in fact occur on the shorter side.

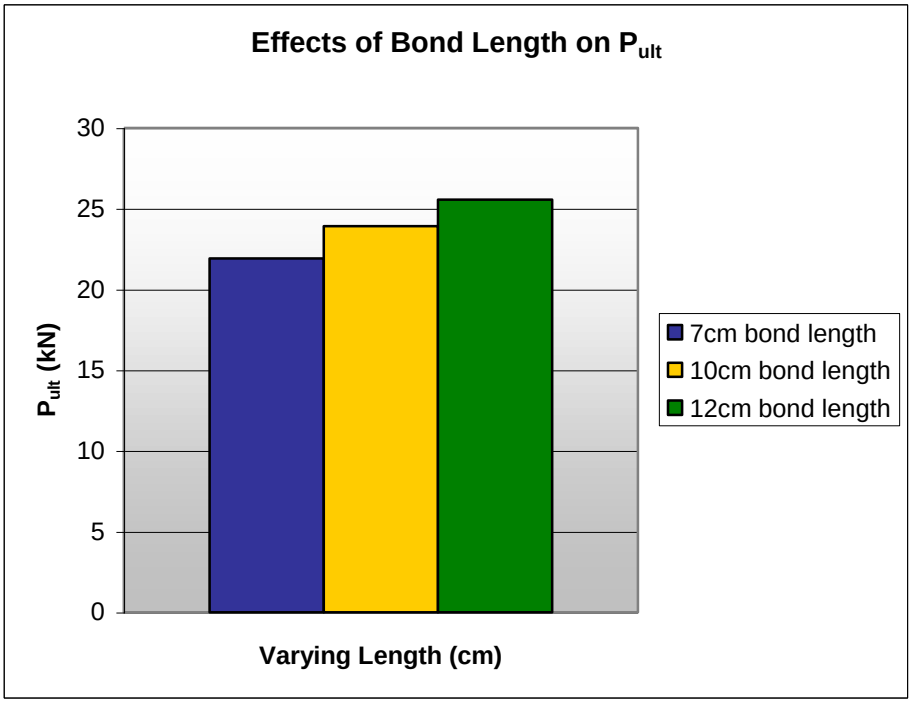

Figure 5.36. *Effective bond length comparison.*

Table 5.13. *Bond failure location*

		Sample number		
		1	2	3
Sample	**Effective bond length**	**Side failure occurred**		
SB-7	7 cm	7	7	7
SB-10	10 cm	13	10	10
SB-12	12 cm	12	13	12

The fact that the ultimate load increases as the bonded length increases is an indication of insufficient bond length developed. This was one of the other reasons that it was decided to increase the size of the specimen in this research.

5.1.6 Effect of loading rate

A separate set of specimens (12 beams) was made to study the influence of the loading rate. The specimens were notched and treated with water jetting. Sprayed FRP with ATPRIME® bonding agent (Resin 1) was used. Table 5.14 shows the results of quasi-static loading on samples without FRP and with FRP at different loading rates. As can be seen from this table, the maximum load significantly increased for samples with FRP relative to those without FRP. The average maximum load increased from approximately 8 kN for samples without FRP to 20 kN for samples with FRP, which is approximately 150%.

Table 5.14. *Results of quasi-static loading on samples without FRP and samples with FRP at different loading rates*

Type of load	FRP re-inforced	Specimen	Loading rate (mm/min)	Maximum load (kN)	Load at failure (kN)	Max. Displace-ment (mm)
Quasi-static	No	B1S1	0.010	11.900	8.530	3.500
Quasi-static	No	B1S6	0.010	7.300	4.200	3.500
Quasi-static	No	B4S12	0.010	5.800	2.500	3.500
Average				8.333	5.077	3.500
Quasi-static	Yes	B2S11	0.005	23.300	23.300	0.660
Quasi-static	Yes	B4S10	0.005	18.400	18.400	0.440
Quasi-static	Yes	B5S7	0.005	17.600	17.600	0.830
Average				19.767	19.767	0.643
Quasi-static	Yes	B2S5	0.050	23.200	23.200	0.650
Quasi-static	Yes	B4S9	0.050	15.700	15.700	0.260
Quasi-static	Yes	B5S12	0.050	19.400	19.400	0.530
Average				19.433	19.433	0.480
Quasi-static	Yes	B2S2	0.500	27.500	27.500	0.780
Quasi-static	Yes	B4S2	0.500	20.100	20.100	0.297
Quasi-static	Yes	B5S3	0.500	21.700	21.700	0.440
Average				23.100	23.100	0.506

The maximum loads for samples with and without FRP occur at nearly the same amount of displacement; hence, more energy is absorbed by the samples with FRP than by the untreated samples. Figure 5.37 illustrates the typical load–displacement

relationship for both the FRP reinforced sample and the untreated sample. It may not be evident from this figure that the FRP treated sample absorbs more energy, because data was not recorded after the bond between concrete and FRP fails. We can see clearly that if the load was maintained on the sample at the same rate, the area under the graph, which represents the absorbed energy, would be larger in the FRP reinforced sample.

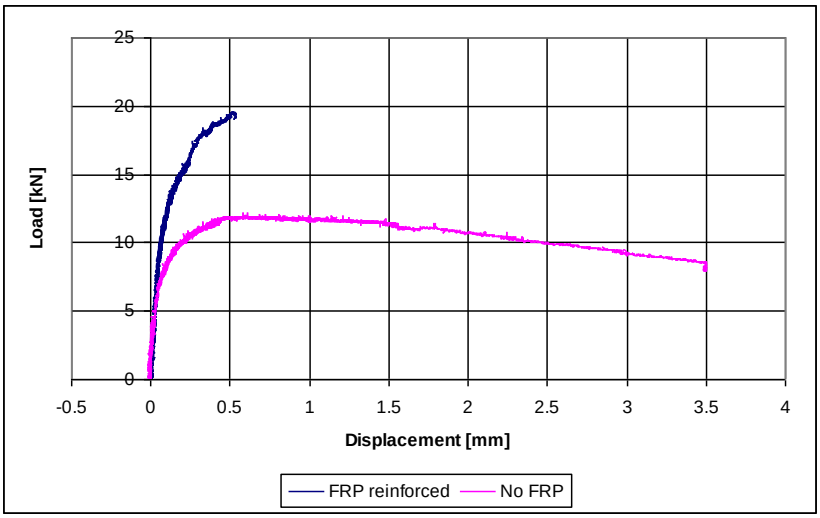

Figure 5.37. *Comparison between FRP reinforced concrete and untreated sample under 0.05 mm/min loading rate.*

Comparison of the samples with FRP at different loading rates with the samples loaded at 0.5 mm/min shows that the highest average maximum load is 23.1 kN, whereas the average maximum load of the samples at 0.05 and 0.005 mm/min loading rates are 19.4 and 19.8 kN, respectively. It is expected that the higher the loading rate, the higher the strength of a specimen. This assumption is based on the tests done on other materials, such as untreated concrete or wood samples, which show a higher strength at higher loading rates. Achieving the highest strength at the maximum loading rate in this experiment validates this assumption; however, the results of the 0.05 and 0.005 mm/min loading rates do not. Therefore, there is some uncertainty in our assumption and more tests must be performed before any convincing conclusions can be made.

Load vs. displacement graphs for the three samples tested under the three rates of loading considered are shown in Figures 5.38 to 5.40. These figures illustrate the variability of the results of each loading rate.

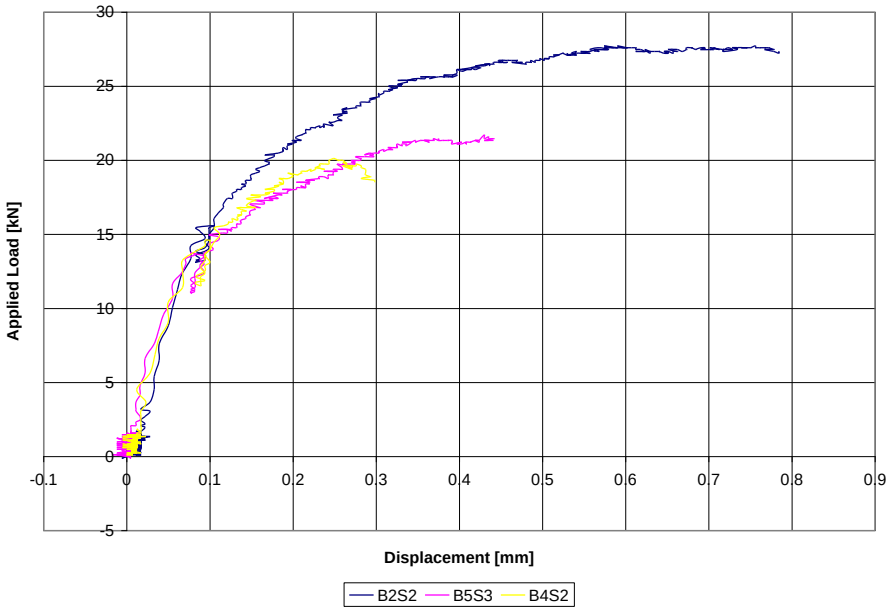

Figure 5.38. *Load vs. displacement for 0.5 mm/min loading rate.*

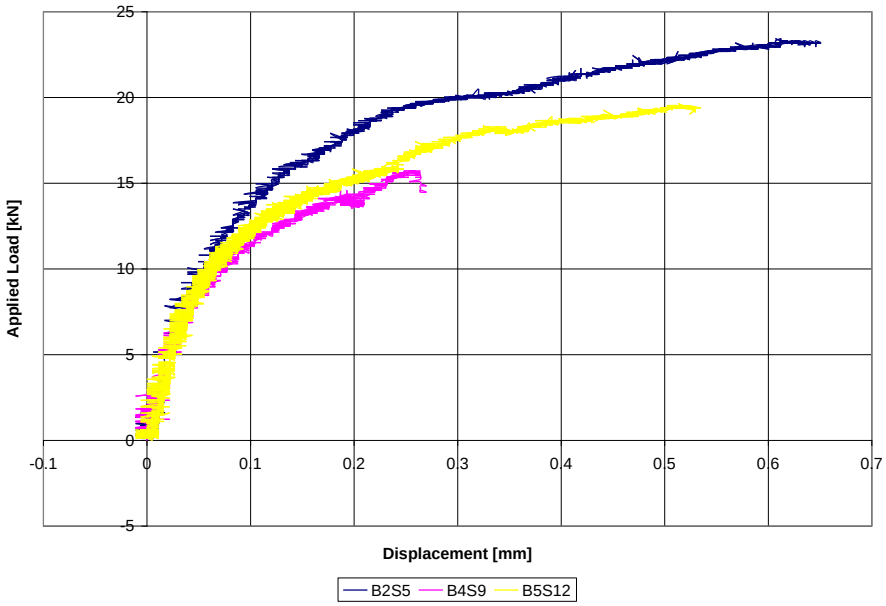

Figure 5.39. *Load vs. displacement for 0.05 mm/min loading rate.*

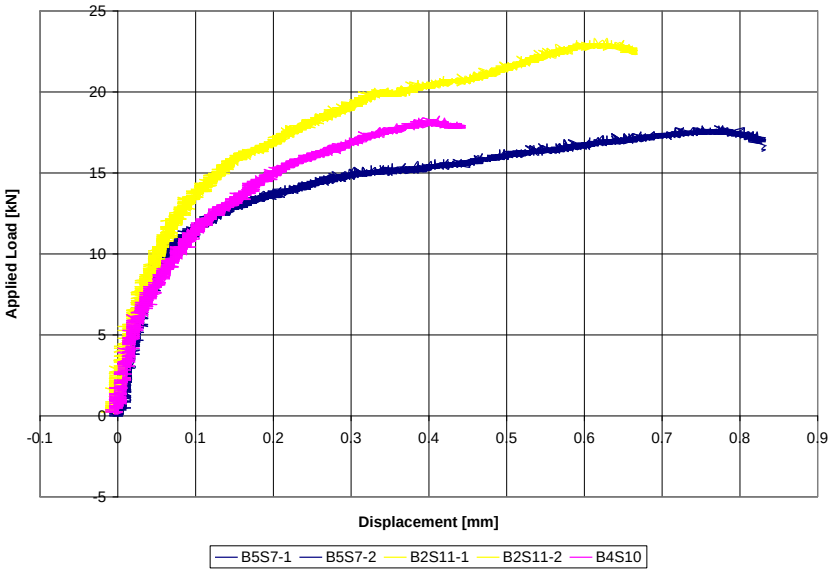

Figure 5.40. *Load vs. displacement for 0.005 mm/min loading rate.*

Figure 5.41 shows three specimens tested using different loading rates.

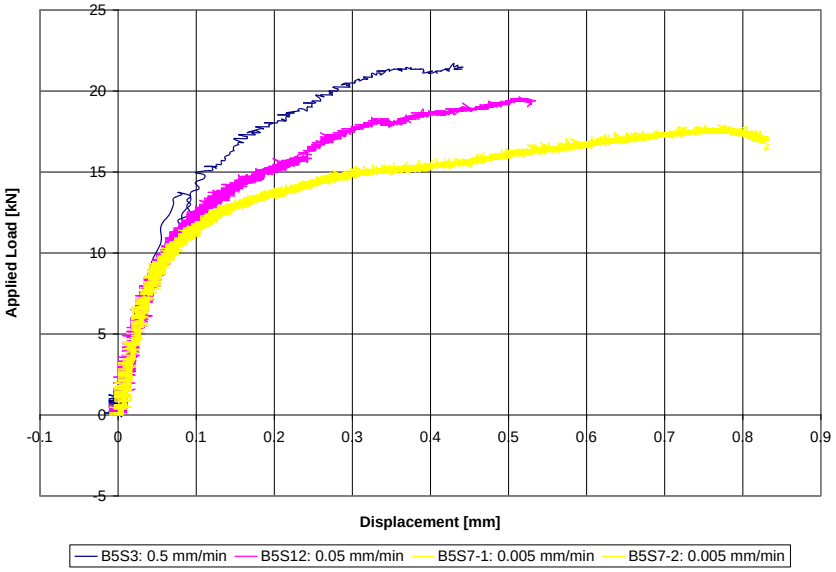

Figure 5.41. *Load vs. displacement for 0.5, 0.05, and 0.005 mm/min loading rates.*

The average ultimate loads show that the FRP–concrete bond strength is a function of strain rate. The maximum displacement decreased from an average of 0.643 mm to an average of 0.506 mm and the average failure load increased from 19.77

to 23.1 kN as a result of a loading rate increase from 0.005 to 0.5 mm/min. This parameter will be examined again as a part of this research under quasi-static and dynamic loading.

5.1.7 Modifications

Once the specimen is loaded, the shear stress builds up in the bond layer. The debonding zone moves away from the edge of the crack as the FRP is debonded resulting in higher displacements without significant load increase. The phenomena is called unzipping.

Studying the load vs. displacement curves shows the following:

1. The load vs. displacement curves do not show the full unzipping phenomenon. This indicates that the full debonding profile is not developed and the bonded length is insufficient.
2. The specimens with longer FRP showed higher ultimate load values, which is another indication of insufficient bonded length.

5.1.7.1 Modifications to materials

Because the objective was to test how loading influences the bond strength between FRP and concrete, it was important to ensure that failure would occur as a result of a debonding mechanism, not in the concrete or FRP itself. Samples were initially notched to encourage failure in a consistent location. The strength of the concrete was not intended to be a factor, but as observed during testing, this was not always the case. Samples with applied FRP wrap and CFRP displayed failures that did not occur in the bond, but rather in the CFRP material or concrete.

Failure in the wrap FRP for both types of surface preparation occurred as a result of critical diagonal cracking or shear in the concrete. As a result the ultimate bond strength was not found, since bond failure was not experienced. Assuming that the method of application of the wrap FRP was correct indicates that future testing should be performed using concrete with a higher strength resistance to shear failure. Steel

fibres used in the concrete mix allow for load sharing between the fibres and the concrete. By increasing the anchorage or density of the fibres used, the shear strength of the concrete could be improved, allowing the FRP to absorb the load to achieve debonding as desired. Reduction of the effective length of FRP would also support debonding using the mix design from this experiment, but results would not be comparable to conclusions found here. Also, to lessen the influence of concrete in the results, it was decided to increase the notch depth. As illustrated in Figure 5.42 the thicker the concrete, the larger the effect of compressive stress in concrete in the total moment bearing capacity.

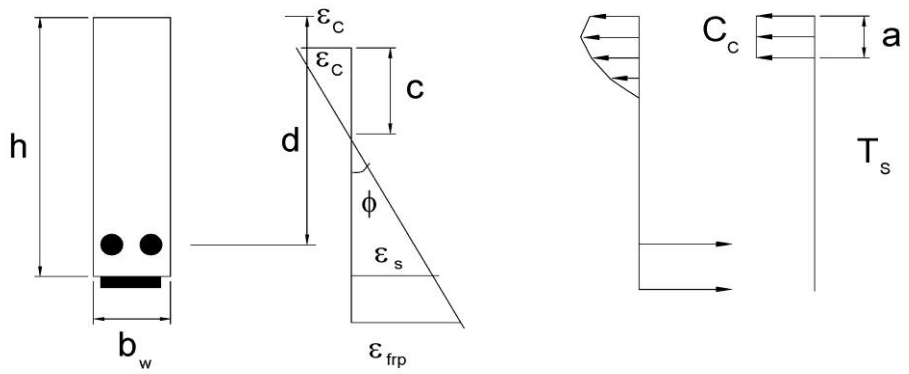

Figure 5.42. *Stress profile in a section of a typical strengthened beam.*

5.1.7.2 Modifications to sample sizes

The load vs. displacement curves do not show the full unzipping phenomenon. This indicates that the full debonding profile is not developed and the bonded length is insufficient. It was decided that specimen sizes be increased to allow an increased bond length.

5.1.8 Summary of the results for these series

The bond was most affected by the jackhammering preparation. The average ultimate load of the jackhammered samples with sprayed FRP using Resin 1 was found to be 27.73 kN. When samples were tested with wrapped FRP the average ultimate load

was 36.68 kN. Using the FRP wrap increased the ultimate load by 32.3%. The mode of failure was concrete strength, not debonding. Crack propagation occurred instantaneously at 30° below horizontal, progressing inward from the outside edges of the FRP wrap.

The second most effective surface preparation for increasing the bond strength was sandblasting. When samples were first sandblasted and then sprayed or wrapped with FRP the average ultimate loads were large but much less than those of the jackhammered samples. The average ultimate loads were 23.92, 25.15, and 32.22 kN for sprayed Resin 1 FRP, sprayed Resin 2 FRP, and wrapped FRP, respectively. Once again, the wrapped FRP achieved the largest ultimate loading.

The weakest bond strength (after the untreated control beams) was seen with samples that were water jet surface prepared. The average ultimate load for sprayed FRP Resin 1 was 14.35 kN. To see how water jetting samples affects the bond strength, samples were tested with Resin 1 under no surface preparation. The average ultimate load for the sample with no surface preparation was found to be 12.27 kN. Therefore, water jetting samples will increase the averaged ultimate load strength by roughly 2 kN.

In summary, the jackhammering surface preparation was found to produce the highest overall bonding strength of the three surface preparations. However, given the effort required to use the jackhammer and the increased possibilities for surface damage, it is likely more beneficial to use the sandblasting technique.

As expected, when comparing the effective bond length of the spray-on FRP samples, the longer bond (12 cm) performed better than the shorter lengths (7 and 10 cm). A few samples did, however, fail on the longer side of the notch, which is counterintuitive; further testing is recommended.

Lastly, a CFRP spray was used on three samples as an alternative reinforcing fibre. The average ultimate load upon failure was 19.91 kN, which was recorded as the

smallest ultimate load for all sandblasted samples. The mode of failure was at the concrete bond for one sample and through the carbon fibres for the remaining two samples.

5.2 Test series II: modified 350 mm × 100 mm × 100 mm specimens

When a FRP reinforced specimen undergoes quasi-static loading, the sharp right crack edge that was generated by notch generation induces some frictional resistance against the surface of fibreglass and creates some inconsistencies in the resulting data. This phenomena is called “bulging effect”. To avoid further complications, it was determined that this edge must be eliminated. Also, attempts were made to eliminate the concrete effect using a notch.

5.2.1 Sample preparation

To eliminate the bulging effect, two methods of edge grinding and notching were used.

1. As mentioned before, the top surface when cast is not used for FRP application. A notch was formed in the side of the mould to create a notch on the base of the sample (as tested). The side of the specimen against the mould is usually smoother. This method, used only on the 350 mm × 100 mm × 100 mm beams, accurately made samples geometrically alike and standardized the experiment. However, it required longer demoulding time and was not compatible with larger beams (used in Section 5.3). Thus, it was not very cost efficient.
2. The edges of the notch were ground with a portable hand grinder (Figure 5.43). This method, like the notch placement method, also had both advantages and disadvantages. This method can be applied to beams of variable sizes and is very time efficient, but it does not provide a very accurate geometric consistency.

Figure 5.43. *The portable grinder used to smooth the crack edges.*

5.2.2 Variables

The following variables were studied in this series of tests:

1. Bond surface area: The area is defined by the width and length of the FRP sprayed area and here is represented by the ratio of this length to the actual length of the concrete sample in percentage. For example; if the width of the sample block is 10 cm and the width of FRP sprayed area is 5 cm. This means that the bond width is 50%.
2. FRP resin: The resin was altered by the FRP shop.
3. Notch depth: The notch depth is the depth that the sample is cut prior to any surface preparation. This length is also presented in percentage relative to block depth.\
4. Surface preparation: This allows comparison of the effects of sandblasting on bond strength. The sandblasting process was categorized as
   a) No sandblasting, water pressure washing only.
   b) Mild sandblasting (A sample is mildly sandblasted when only one cycle of sandblasting is done.)
   c) Heavy sandblasting (A sample is heavily sandblasted when the sample has undergone three or more cycles of sandblasting)

d) Jackhammering: A “Chicago Pneumatic” jackhammer with rating of 90 PSIG/6.2 bar at maximum was used to roughen the concrete surface and provide maximum bonding.

5.2.3 Notch modification

Specimens with a modified notch are divided into three types: notched, ground, and hinged. At the beginning of this phase of study, it was hoped that by devising a method to create a smooth crack edge we would gain more efficiency. Therefore, 14 triangular-like aluminum notches with curved sides (Figure 5.44) were designed in a way that they could be easily placed on the inner side of the mould prior to casting, hence giving the samples the desired geometry. Samples made using these notches are called “samples with a cast notch” (Figure 5.45). It should be noted that these specimens were also saw cut to the desired notch depth after de-moulding and curing.

Figure 5.44. *Left: Small notched sample pre-casting setup. Right: An aluminum notch.*

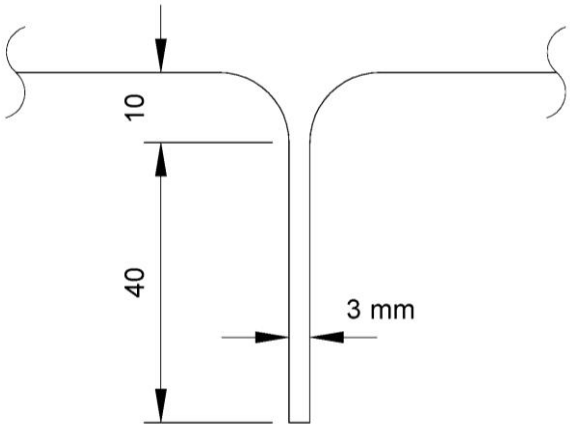

Figure 5.45. *Diagram of specimen with a cast notch.*

However, building these notches through the machine shop required some time. Thus, in order to maintain a steady testing pace and also to be able to compare the notched samples with the ones that simply had their crack edges smoothed by the grinder, a number of sample were prepared using the portable hand grinder. These samples are called "ground samples" in this chapter. It was attempted to make the grinding shape and dimensions similar to those created by the aluminum cast notch.

Hinged samples are somewhat different than the other two types, and their purpose was to give an accurate result for the FRP–concrete strength without load carrying involvement of the concrete. Hinged samples are two half samples connected at the top by a steel hinge. Testing was carried out on both notched hinged samples and ground/hinged samples.

5.2.4 Results

Figures 5.46 to 5.58 show the load vs. displacement behavior for different specimen characteristics.

5.2.4.1 Notched samples

1) Cast notched samples with a 40% notch depth, surface area length of 77% and width of 50%. Surface preparation: heavy sandblasting. Samples: B2S1, B2S2, B2S3.

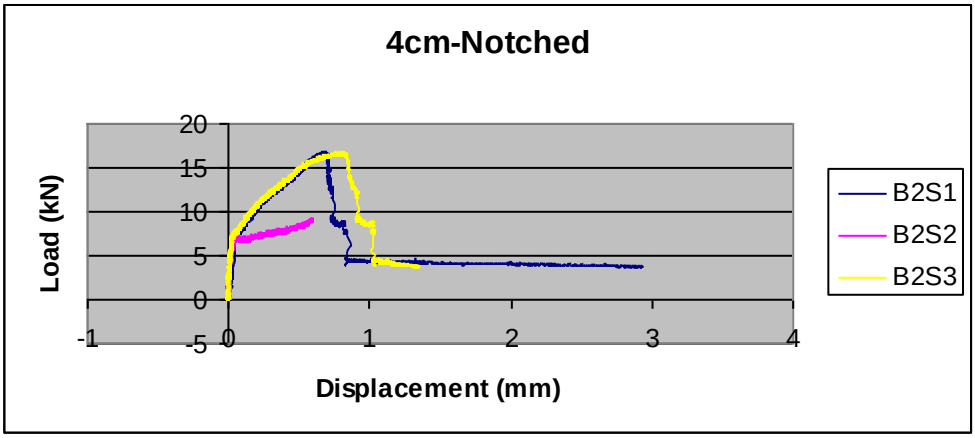

Figure 5.46. *Notched samples with a 40% notch depth.*

Cast notched samples with a 60% notch depth, surface area length of 77% and width of 50%. Surface preparation: heavy sandblasting. Samples: B2S4, B2S5, B2S6.

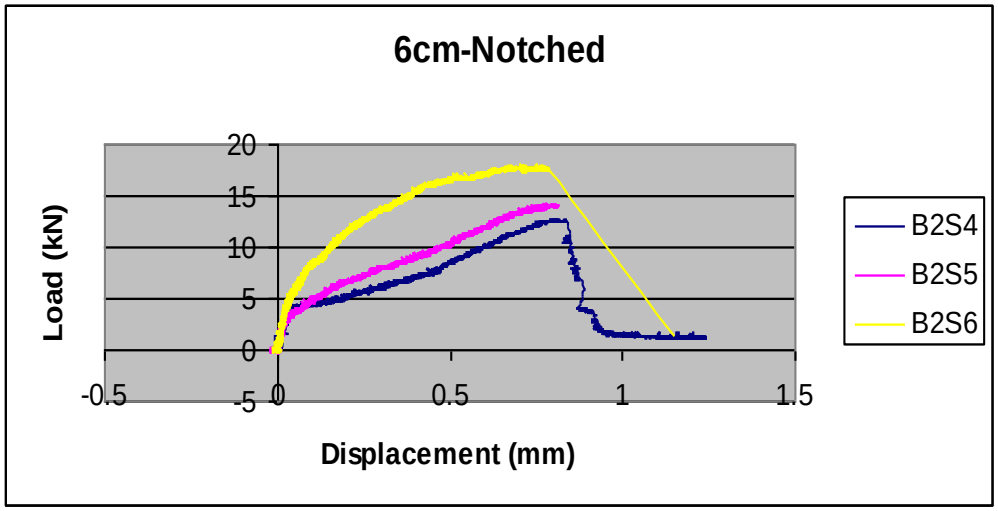

Figure 5.47. *Notched samples with a 60% notch depth.*

2) Cast notched samples with an 80% notch depth, surface area length of 77% and width of 50%. Surface preparation: heavy sandblasting. Samples: B2S7, B2S8, B2S9.

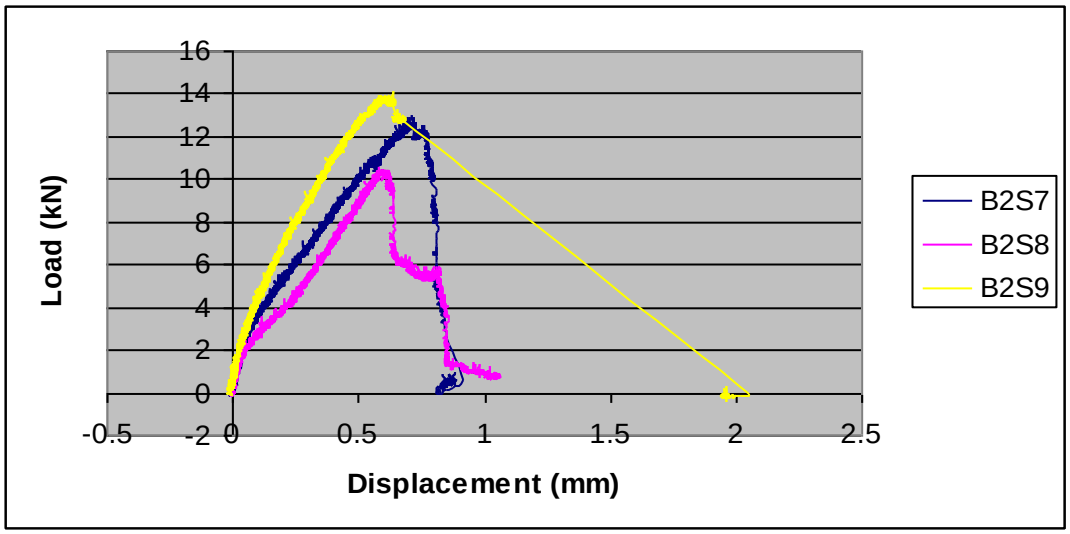

Figure 5.48. *Notched samples with an 80% notch depth.*

5.2.4.2 Ground sample

1) Ground samples with a 50% notch depth, surface area length of 77%, and width of 50%. Surface preparation: heavy sandblasting. Samples: B1S1, B1S2, B1S3 (Note: The data for B1S2 was accidentally lost.)

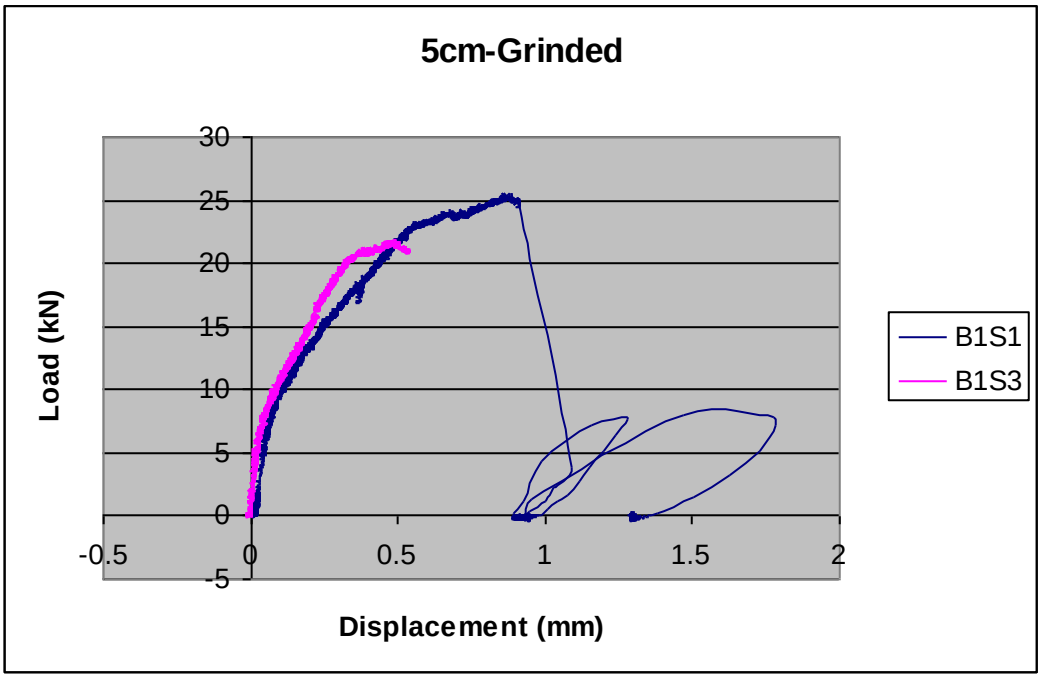

Figure 5.49. *Ground samples with a 50% notch depth.*

2) Ground samples with an 80% notch depth, surface area length of 77% and width of 50%. Surface preparation: heavy sandblasting. Samples: B1S7, B1S8.

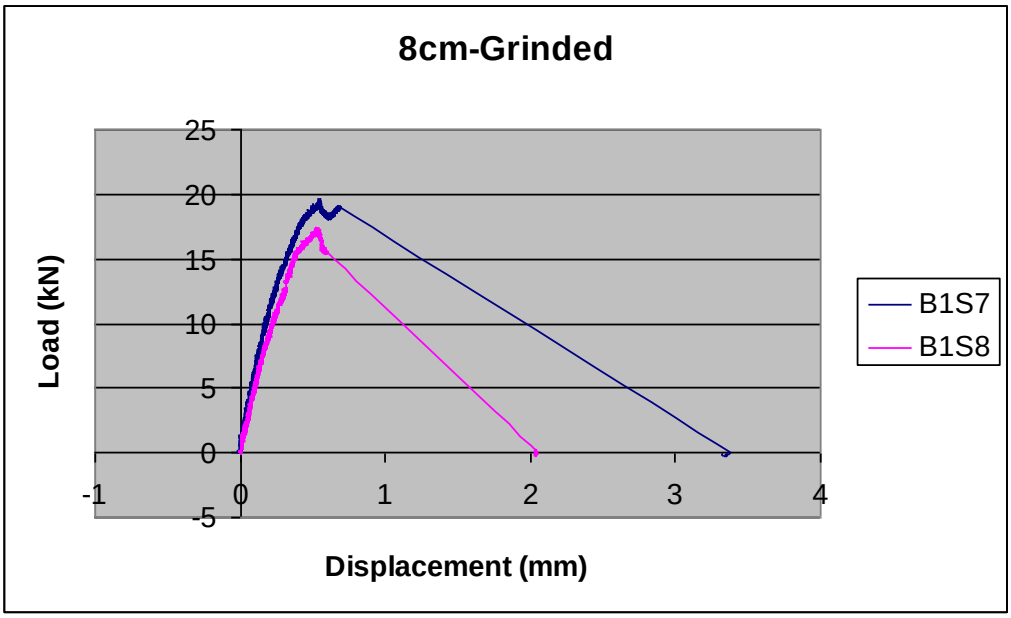

Figure 5.50. *Ground samples with an 80% notch depth.*

5.2.4.3 Hinged samples

1) Ground hinged samples with surface area length of 77% and width of 50%. Surface preparation: heavy sandblasting. Samples: B1S4, B1S5, B1S6.

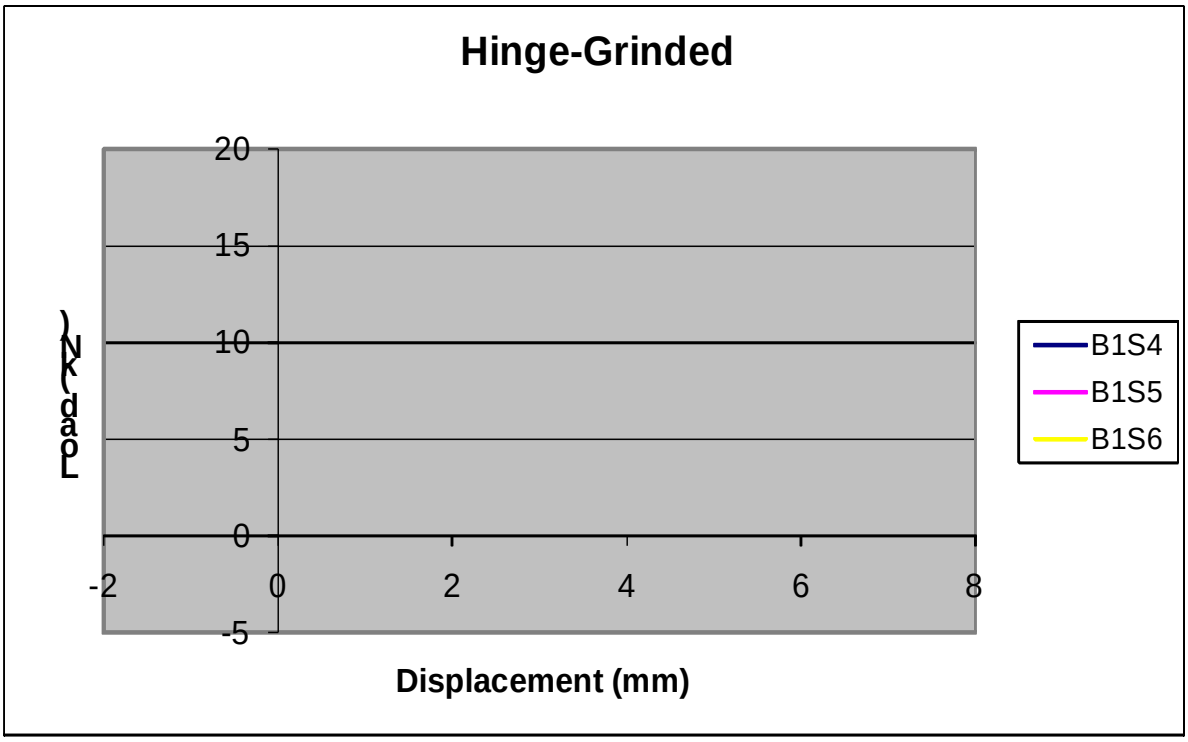

Figure 5.51. *Ground hinged samples with a 50% notch depth.*

2) Notched hinged samples with surface area length of 77% and width of 50%. Surface preparation: heavy sandblasting. Samples: B2S10, B2S11, B2S12.

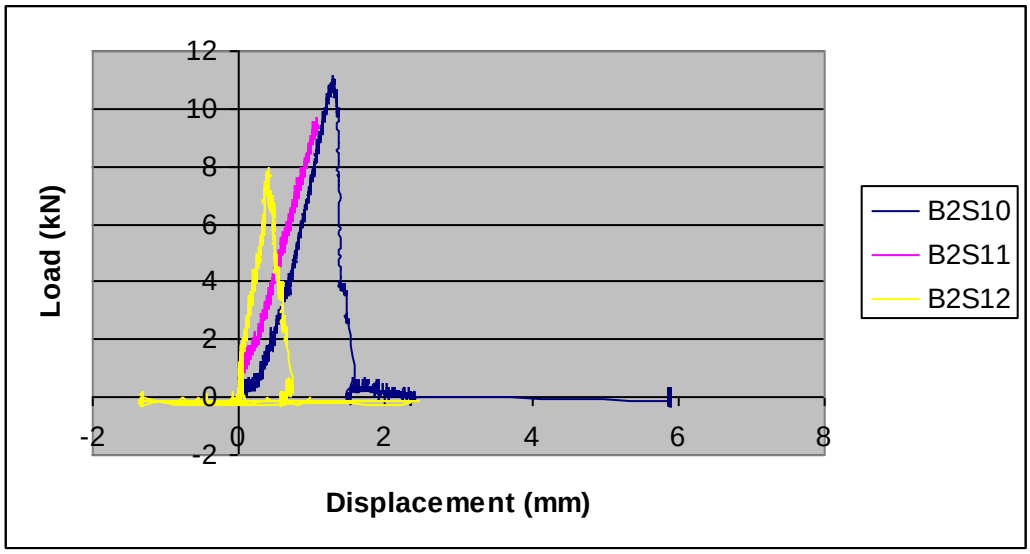

Figure 5.52. *Notched hinged samples with a 50% notch depth.*

5.2.5 Observations and modifications

As mentioned before, the load–displacement curve is not developed entirely because the bond length is insufficient. However, rounding the edges by grinding seems to eliminate the bulging effect. The hinged specimens showed a very catastrophic failure. The next series of the samples were 550 mm × 150 mm × 150 mm. These were the largest specimens that could fit the Instron machine. The hinge idea was not completely ruled out and was tried out with the larger specimens.

5.3 Test series III: large samples (150 mm × 150 mm × 550 mm)

Large samples are divided into two types: regular and hinged. Regular samples were prepared in the same manner as the small ground samples. However, the hinged samples were prepared by installing a custom-made steel hinge on the beam (Figure 5.53).

Figure 5.53. *Left: Steel hinge on a large sample. Right: Steel hinge on a small sample.*

It is worth mentioning that because of the costly process of customizing the hinge, only one hinge was made by the machine shop; hence the testing procedure was very slow. Even though the 350 mm × 100 mm × 100 mm hinged specimens did not produce the desirable load–displacement response (with fully developed unzipping profile), they were tried again with these series to see if the specimen geometry would make a difference in the hinge performance.

5.3.1 Regular samples

1) Reference samples with no FRP reinforcement and 80% crack depth. Samples: ref1, ref2, ref3.

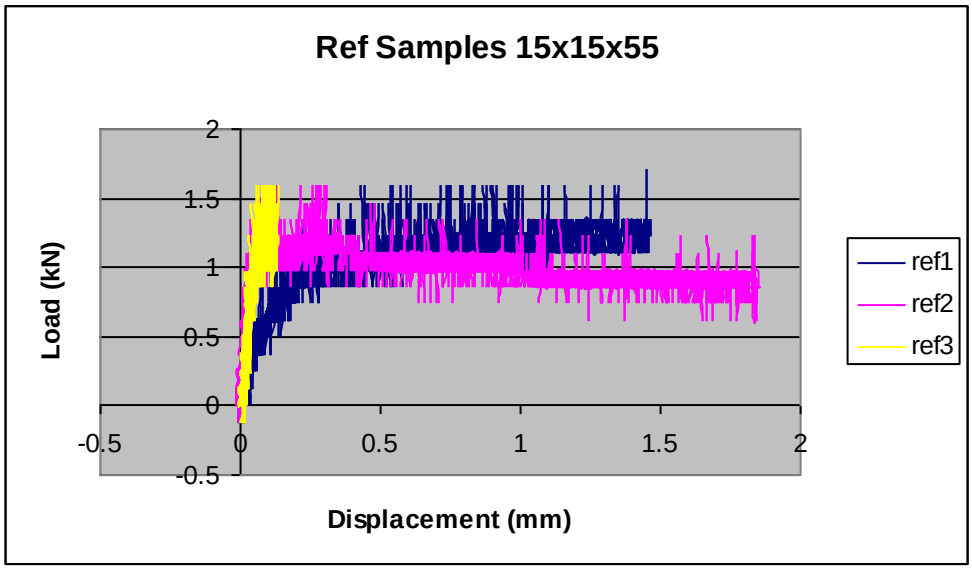

Figure 5.54. *Large reference samples with no FRP reinforcement and 80% crack depth.*

2) Samples with bond surface of 80% length and 50% width and 80% notch depth. Surface preparation: water jetting. Samples: B4S1, B4S2, B4S3.

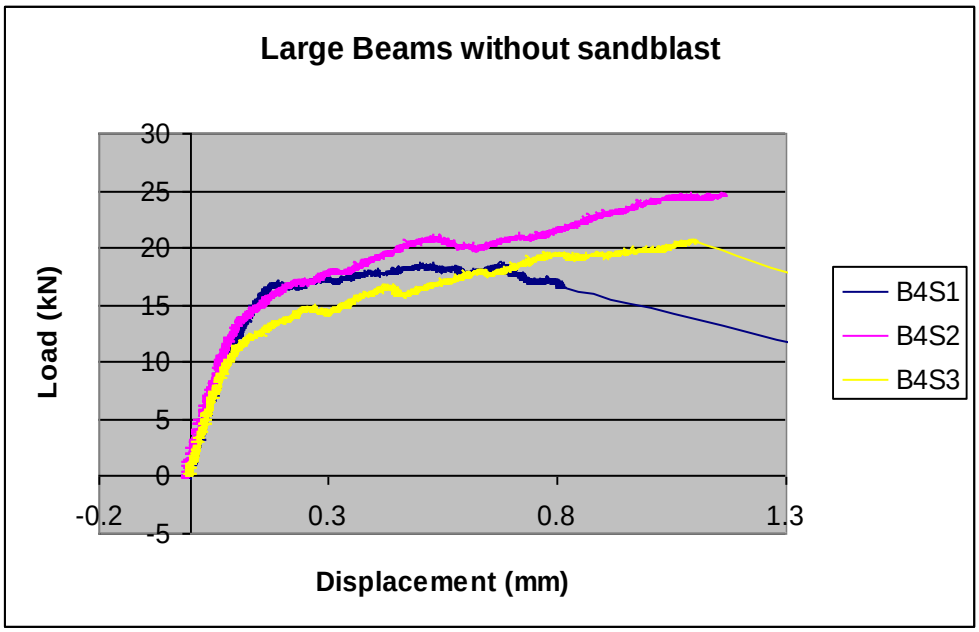

Figure 5.55. *Large samples with bond surface of 80% length and 50% width and 80% notch depth. Surface preparation: water jetting only. .*

3) Samples with bond surface of 80% length and 50% width; 50% notch depth. Surface preparation: mild sandblasting. Samples: B5S4, B5S5.

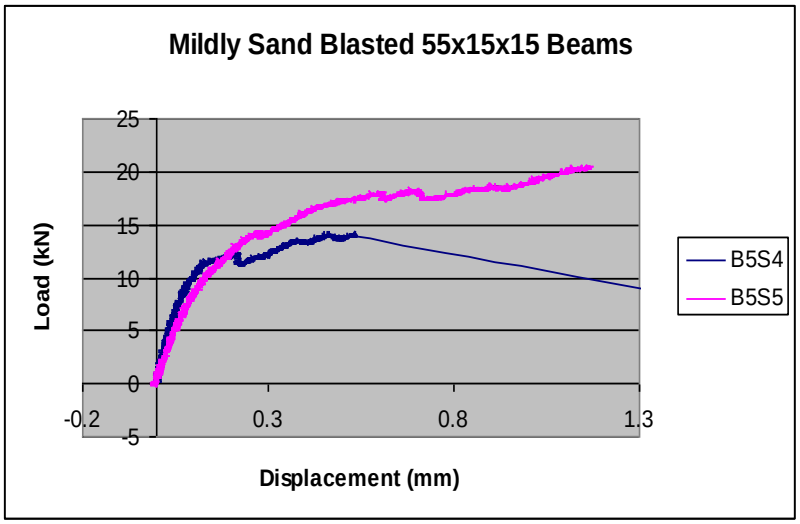

Figure 5.56. *Large samples with bond surface of 80% length and 50% width and 80% notch depth. Surface preparation: mild sandblasting.*

4) Samples with bond surface of 80% length and 50% width and 80% notch depth. Surface preparation: heavy sandblasting). Samples: B5S1, B5S2, B5S3.

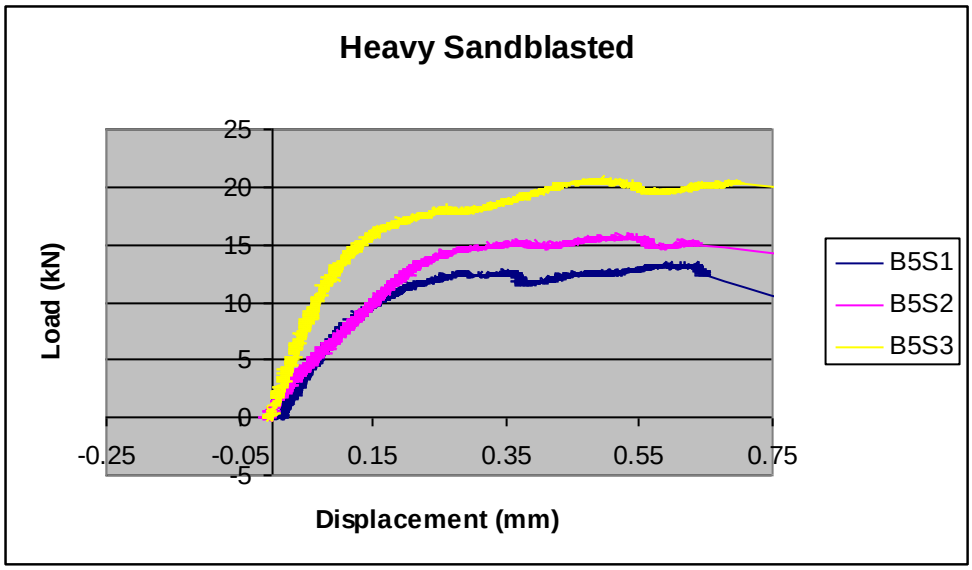

Figure 5.57. *Large samples with bond surface of 80% length and 50% width and 80% notch depth., Surface preparation: heavy sandblasting.*

5.3.2 Hinged samples

Hinged samples have a bond surface of 80% length and 50% width. The surfaces of these samples were not sandblasted. Hinged samples showed a very catastrophic failure. The unzipping curve was not observed in the test results. No more hinged samples were tested to avoid damaging the LVDTs and cables.

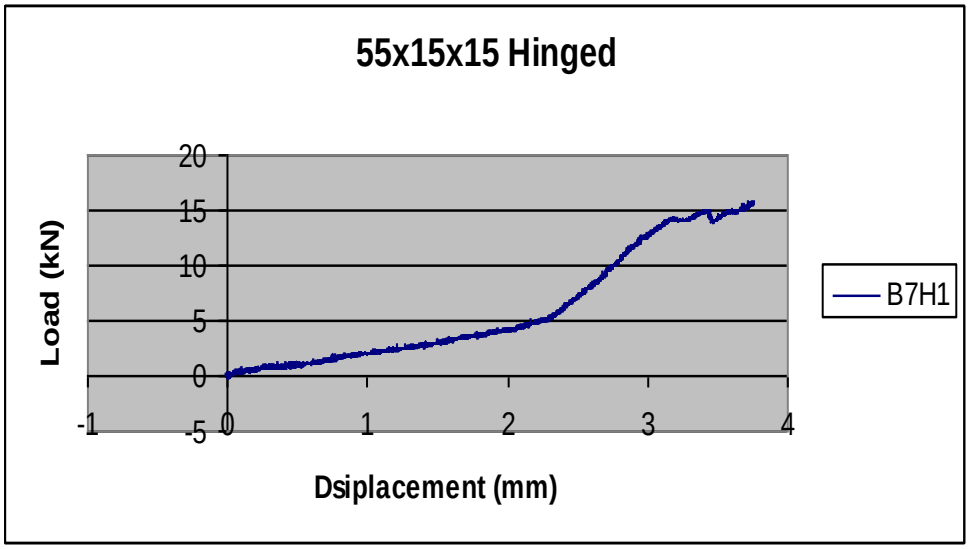

Figure 5.58. *Large hinged samples with bond surface of 80% length and 50% width and 80% notch depth, Surface preparation: no sandblasting.*

5.3.3 Summary

The hinged samples were ruled out because of damaging and catastrophic failure. Specimens with 40% and 60% notch depth seemed to show two types of load deflection pattern (one pattern with strain hardening). Table 5.15 shows a summary of results for different series discussed in this section. The 150 mm × 150 mm × 550 mm samples with bond surface of 80% length and 50% width and 80% notch depth showed consistency in the load-deflection pattern, and unzipping phenomena were observed. Therefore, this type of specimen was chosen to carry out further testing.

Table 5.15. *Summary of results for different specimen geometry*

Specimen size (mm)	Notch depth (mm)	Notch type	Hinge used	Surface preparation	Average ultimate load (kN)	Standard deviation
350×100×100	40	Cast	No	Heavy sandblasting	13.7	4.0
350×100×100	60	Cast	No	Heavy sandblasting	14.8	2.4
350×100×100	80	Cast	No	Heavy sandblasting	12.5	1.5
350×100×100	50	Ground	No	Heavy sandblasting	23.0	2.8
350×100×100	80	Ground	No	Heavy sandblasting	18.7	1.8
350×100×100	50	Ground	Yes	Heavy sandblasting	14.7	1.3
350×100×100	50	Cast	Yes	Heavy sandblasting	9.4	1.6
550×150×150	120	Ground	No	Water jetting	21.0	3.6
550×150×150	120	Ground	No	Mild sandblasting	17.5	4
550×150×150	120	Ground	No	Heavy sandblasting	16.8	3.3

CHAPTER 6
QUASI-STATIC TESTING

6.1 Introduction

Once the specimen geometry was decided on, the next step was to study the debonding phenomenon. This was done using several strain gauges applied on the FRP surface and studying strain profile, stress profile, and load displacement response. Several steps were necessary to prepare samples for strain gauge application. The following section outlines the processes by which all of the samples were prepared. All the specimens discussed in this and the next chapters will have the geometry decided on in the previous chapter, 550 mm × 150 mm × 150 mm with a notch of 120 mm and ground notch edges. The influence of surface preparation is studied in this chapter under quasi-static loading. The influence of impact loading and strain rate will be studied in Chapters 7 to 9.

6.2 FRP preparation

The FRP surface was initially untreated. In an effort to ensure that accurate results were obtained from the strain gauges, the surface of the FRP underwent a vigorous preparation process.

6.2.1 FRP measurement

All 12 samples were intended to have similar FRP dimensions so as to provide consistent data. However, there was some inherent variation in FRP size. In order to account for any differences and plan the optimal strain gauge layout, the FRP dimensions were first recorded for each sample. Measurements were taken of length and width at both ends. Using these measurements, an optimal strain gauge layout that would cover the FRP evenly was developed. The strain gauge layout will be explained in more depth in Section 6.3.1.

6.2.2 FRP surface preparation

After the spray FRP had been applied, the surface of the FRP was very rough and irregular. The strain gauges used are accurate to within micrometres; this accuracy is desired to produce complete results. To ensure that the strain gauges could measure strain as accurately as possible, it was very important that we applied them to a smooth, clean surface. More time spent carefully preparing the surface of the FRP yields less chance of gauge failure and loss of data. To level the FRP surface and remove the bumps, a belt sander with 80 grit paper was used. In an effort to minimize the health hazard associated with dust from sanding the FRP, proper dust masks were used. The belt sanding was a meticulous process because taking too much material could result in an uneven surface and skew test results. The belt sander used can be seen in Figure 6.1.

Figure 6.1. *Belt sander used in FRP surface preparation.*

After the FRP on each sample was levelled with the belt sander, it was necessary to use sandpaper by hand to smooth the surface down to its final state. The hand sanding was done with 80 grit sandpaper, 120 grit sandpaper, and 600 grit sandpaper. The 600 grit sandpaper was necessary to make the surface smooth enough for the strain gauges to bond without failure.

6.3 Strain gauge preparation

The strain gauges used in this experiment are accurate instruments of measurement, and the layouts were carefully chosen to optimize data collection. Uni-directional strain gauges 10 mm long were used.

6.3.1 Strain gauge layout

After the the FRP surface was prepared, the strain gauge layout was measured and drawn onto the sample. To ensure consistent results on every sample, a uniform layout method was used on all FRP surfaces. First, the centre line was found by bisecting each end of the FRP. A line was then drawn between these two centres to make the centre line. Perpendicular to this, a halfway line was drawn by tracing a line over the centre of the notch cut in the concrete. Finally, lines were drawn intersecting the centre line orthogonally at various distances to denote the final locations of the strain gauges. Two strain gauge layouts were used in this experiment; schematics with the associated dimensions are featured in Figures 6.2 and 6.3.

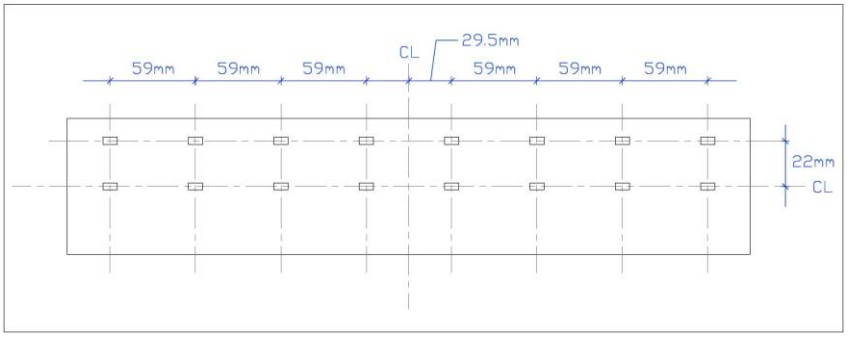

Figure 6.2. *Strain gauge layout 1.*

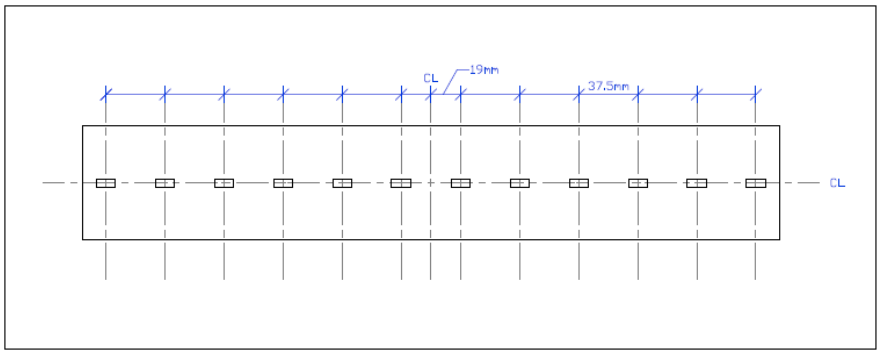

Figure 6.3. *Strain gauge layout 2.*

The layout in Figure 6.2 was developed with each gauge having a redundant gauge placed directly beside it. This was done to provide backup if the original gauge failed. This redundancy was eventually found to be unnecessary, as gauge failures were uncommon. The gauge layout in Figure 6.3 was adopted part way through the testing, which also included a closer spacing of gauges in order to obtain more strain information. The increased number of gauges along the central axis of the sample allows for a more accurate representation of the strain within the FRP. The process of transferring the strain gauge layout onto the FRP surface can be seen in Figure 6.4.

Figure 6.4. *Strain gauge layout application.*

6.3.2 Strain gauge application

The strain gauge layout was drawn on the surface, which was then cleaned with isopropyl alcohol. The alcohol removed any dust or oil that may have been on the surface and consequently also removed some ink from the layout lines. The strain gauges were aligned using the ink layout; removing too much ink would have resulted in inaccurately placed strain gauges.

The first step in applying the strain gauges was to temporarily secure the gauge to the FRP. This was done using Scotch tape because it is transparent, allowing the gauge to be properly aligned with the inked lines on the surface of the FRP. Figure 6.5 displays the temporary taping procedure. The tape and gauge were then peeled back to the wire leads in preparation for being permanently bonded in place.

Figure 6.5. *Strain gauge placement.*

The glue used to bond the gauges to the FRP is M-BOND 600. It is a two-part epoxy adhesive consisting of a resin and a catalyst. The catalyst improves the resin's initial setting time to about 30 s. Latex gloves were used during the gluing process to avoid bonding digits to one another or to the sample. A generous coat of catalyst was

applied to the entire bottom side of the strain gauge. The catalyst took 15–20 s to dry. A small drop of resin was placed at the base of the peeled-back strain gauge. Creating the correct drop size was important because a proper bond was crucial to the success of the strain gauges. After the drop of glue was applied the gauge was glued in place, and pressure was applied until the initial set was complete. The gluing process is featured in Figure 6.6. After all the gauges were glued, rubber strips were placed over the gauges and a weight was placed on top until the glue was fully set, which was approximately 24 h. To protect the strain gauges, epoxy was applied to the lead wires of each strain gauge. The epoxy prevented wires from being pulled accidentally, damaging or destroying the strain gauges.

Figure 6.6. *Gluing process.*

6.4 Testing procedure

The concrete samples were tested in a four-point bending machine to simulate straight tension on the FRP–concrete bond. The machine was configured to apply load at a constant rate of strain. The strain rate used for the testing was 0.05 mm/min. A schematic of the test apparatus can be seen in Figure 6.7. As discussed before, the beam dimensions are 550 mm × 150 mm × 150 mm. The beam is simply supported on the bottom with supports 500 mm apart (25 mm from the edges).

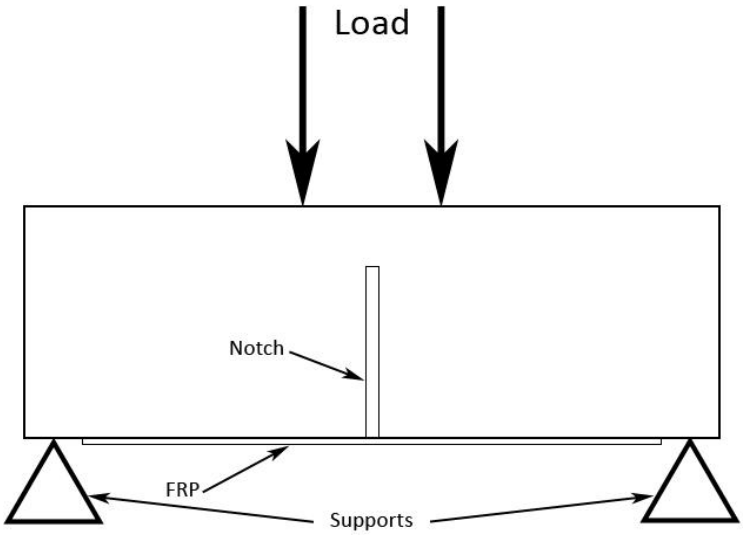

Figure 6.7. *Test apparatus schematic.*

6.4.1 Electrical connection

The electrical signals produced by the strain gauges were transmitted through wires to the data acquisition module. Each strain gauge has two wires that need to be connected to specific ports on the data acquisition module. For ease of connection, four quick-connecting strips were used, eliminating the need to reconnect the module end of the wires after every test. An example of the above-mentioned connection strips can be seen in Figure 6.8.

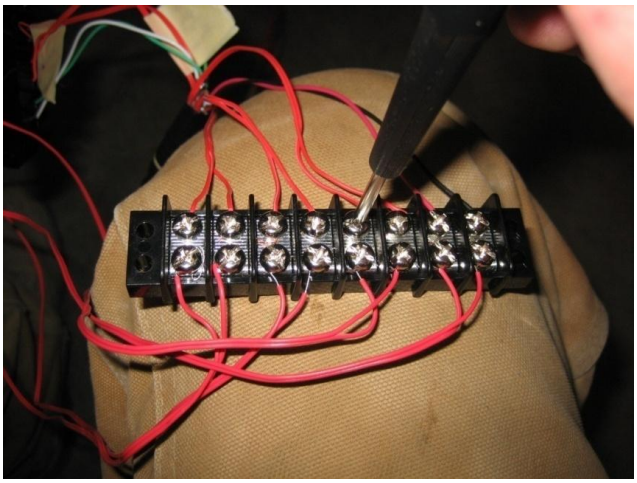

Figure 6.8. *Quick-connects*

Each strain gauge was numbered using a permanent marker on the surface of the concrete to keep the connections organized. The corresponding ports on the quick-connect bars were labelled on the back of the units.

6.4.2 Strain gauge calibration

During routine gluing and handling, each strain gauge was subjected to strains that can alter their calibration slightly. In order to record strain as accurately as possible, each strain gauge was calibrated individually. Calibration was performed using a shunt of predetermined resistance. The leads on the shunt were connected across the circuit of the strain gauge. The connection simulated a known strain, which was used to calibrate the software of the data acquisition module. Figure 6.9 shows the calibration screen of the data acquisition module.

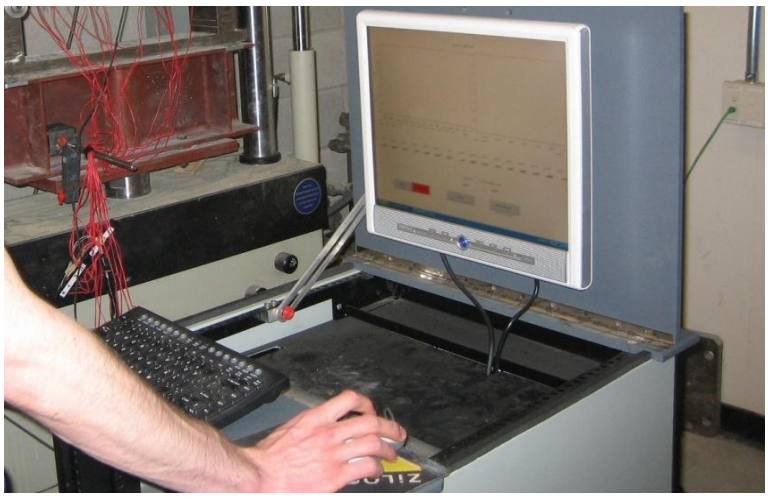

Figure 6.9. *Data acquisition*

6.4.3 Starting the test

The testing machine was set to “immediate strain” mode, and the desired strain rate was entered. The strain readings on the data acquisition module were zeroed, and recording of the data to an appropriately named data file started before the test began. The machine was started, and it began loading the sample at the predetermined strain rate entered previously. The data acquisition module provided real-time feedback of the

strains experienced by each gauge. If the strains were not being recorded properly, the test was stopped and all connections rechecked.

6.4.4 Mechanics of the test and analysis

6.4.4.1. Data analysis

After each test was completed, the data acquisition machine created a set of two data files containing the test results. In an effort to record as much data as possible, sample behavior was recorded every 0.05 s (20 Hz). This resulted in as many as 60,000 data points for some tests. Because these data files were much too large to evaluate in Microsoft® Excel, a data reduction program was created using MatLab. This program imported the original data files, deleted nine out of every ten data points, then wrote the condensed data to a new file. This resulted in data points taken every 0.5 s instead of every 0.05 s, which was much easier to analyze using Excel.

The condensed data sets were then imported into Excel and analyzed. Here the steps for a typical specimen (B9S7) is explained. Figure 6.10 shows a schematic of how the strain gauges are numbered:

Figure 6.10. *Strain gauge numbering.*

Strain vs. location profiles are presented in Figure 6.11, and Figure 6.12 shows the load displacement curve.

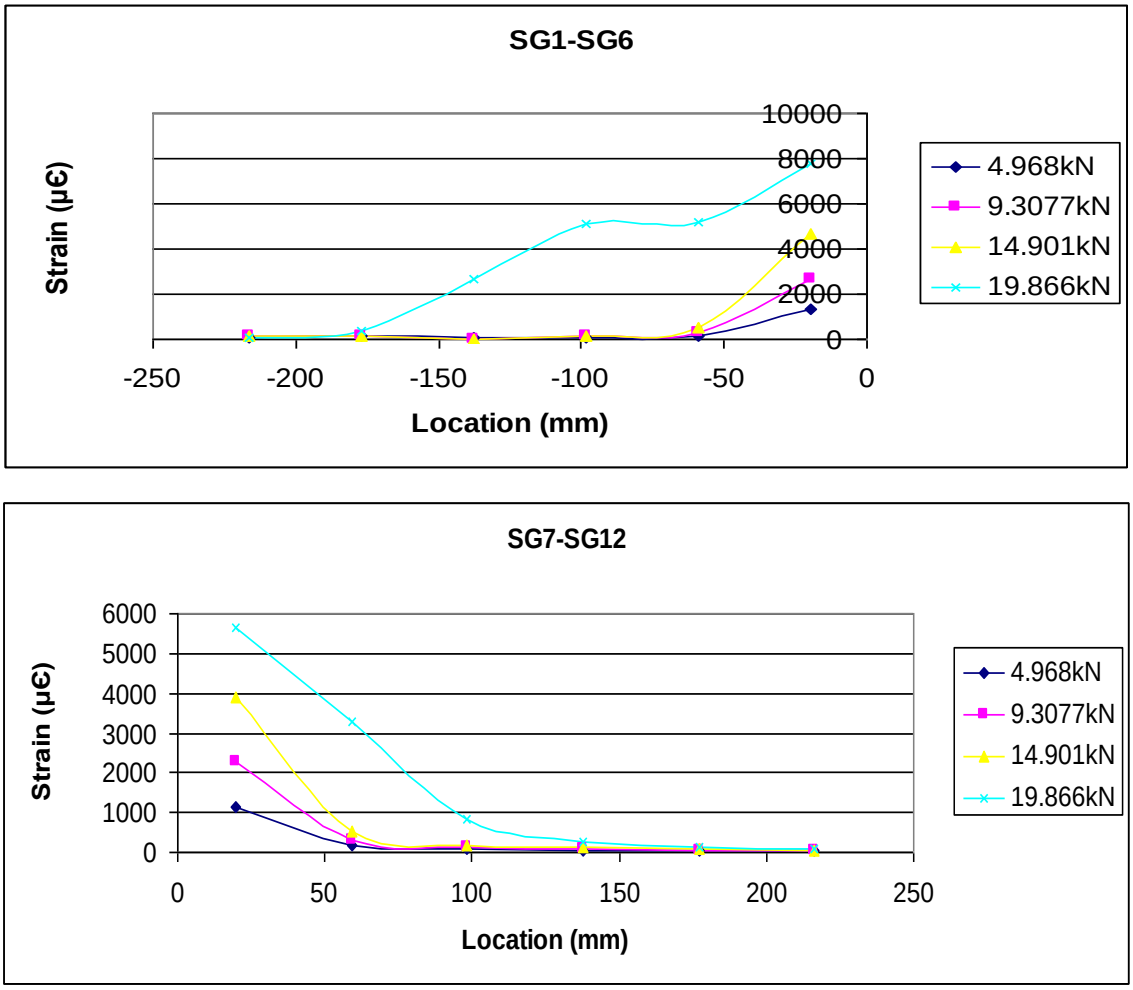

Figure 6.11. *Strain in the FRP vs. the distance along the FRP.*

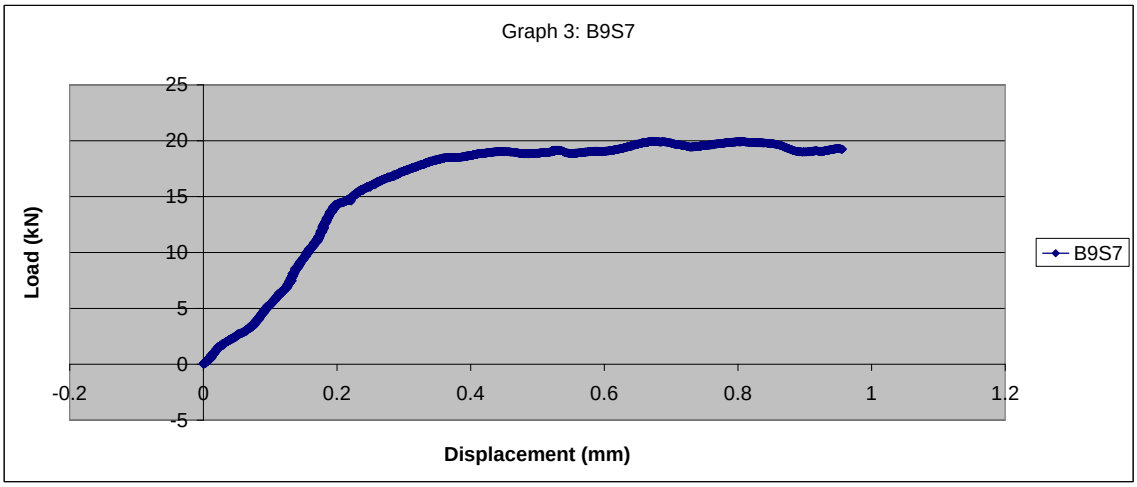

Figure 6.12. *Load displacement curve.*

Figure 6.13. *Schematic FRP block used to explain the bond stress calculation.*

The data acquisition system recorded the strain of the FRP at each time. The modulus of elasticity for FRP was separately obtained using a tensile test on a coupon of sprayed FRP. If the FRP strain and therefore stress are known at each point, the bond stress can be calculated as follows (see also Figure 6.13):

$$\tau_{\text{bond}} b dx + \sigma_{\text{FRP}} b t_{\text{FRP}} = (\sigma_{\text{FRP}} + d\sigma_{\text{FRP}}) b t_{\text{FRP}}$$

$$\tau_{\text{bond}} = \frac{t_{\text{FRP}} d\sigma_{\text{FRP}}}{dx}$$

where τ_{bond} is the bond stress of the dx element, t_{FRP} is the thickness of the sprayed FRP, and E_{FRP} is the modulus of elasticity of FRP.

$$\tau_{\text{bond}} = \frac{t_{\text{FRP}} E_{\text{FRP}} d\varepsilon_{\text{FRP}}}{dx}$$

Figures 6.14 and 6.15 represent shear stress vs. distance for strain gauges SG1-SG6 and SG7-SG12, respectively, for four loading values.

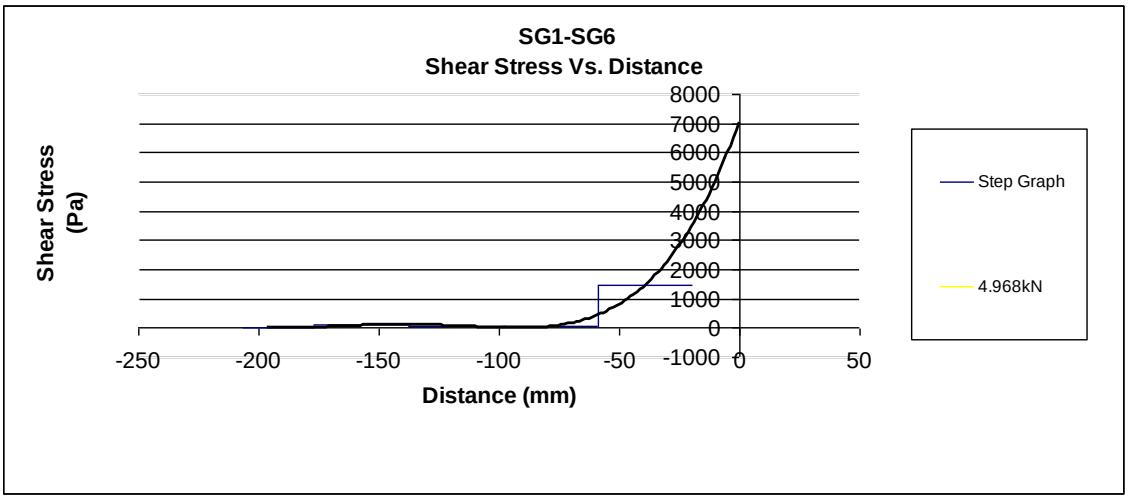
SG1-SG6
Shear Stress Vs. Distance
Shear Stress (Pa)
8000
7000
6000
5000
4000
3000
2000
1000
0
-1000
-250
-200
-150
-100
-50
0
50
Distance (mm)
Step Graph
4.968kN

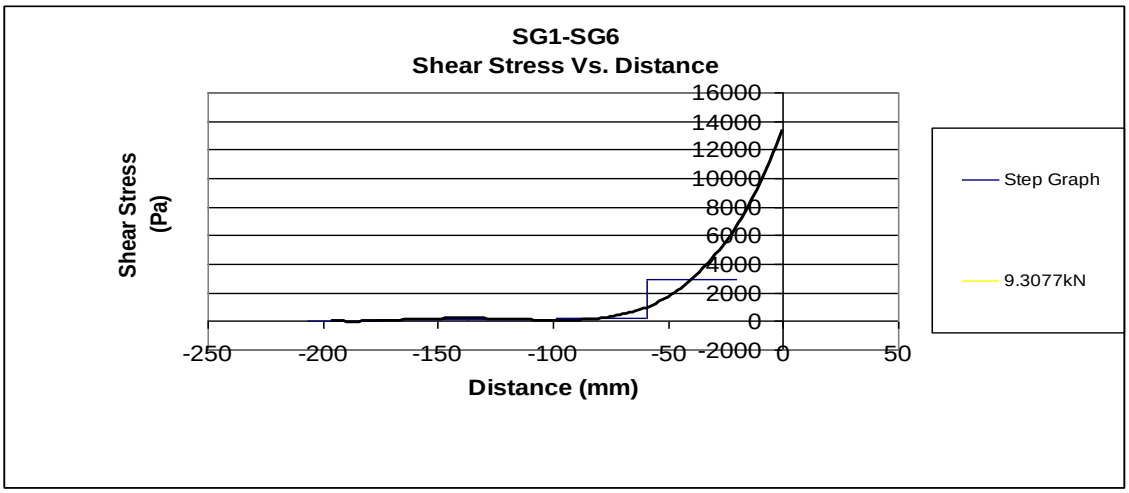
SG1-SG6
Shear Stress Vs. Distance
Shear Stress (Pa)
16000
14000
12000
10000
8000
6000
4000
2000
0
-2000
-250
-200
-150
-100
-50
0
50
Distance (mm)
Step Graph
9.3077kN

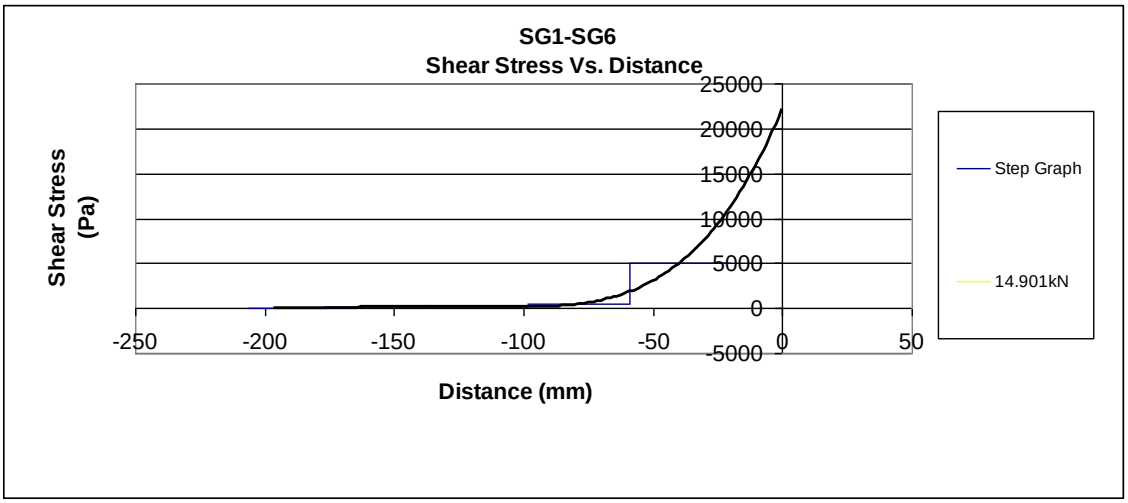
SG1-SG6
Shear Stress Vs. Distance
Shear Stress (Pa)
25000
20000
15000
10000
5000
0
-5000
-250
-200
-150
-100
-50
0
50
Distance (mm)
Step Graph
14.901kN

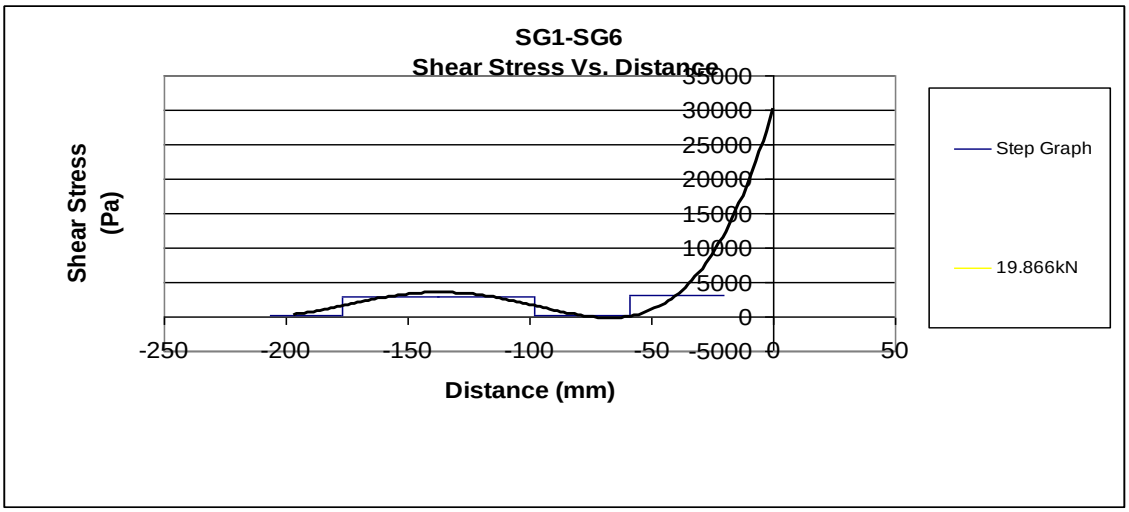

Figure 6.14. *Shear stress vs. distance for strain gauges SG1-SG6 for four loading values.*

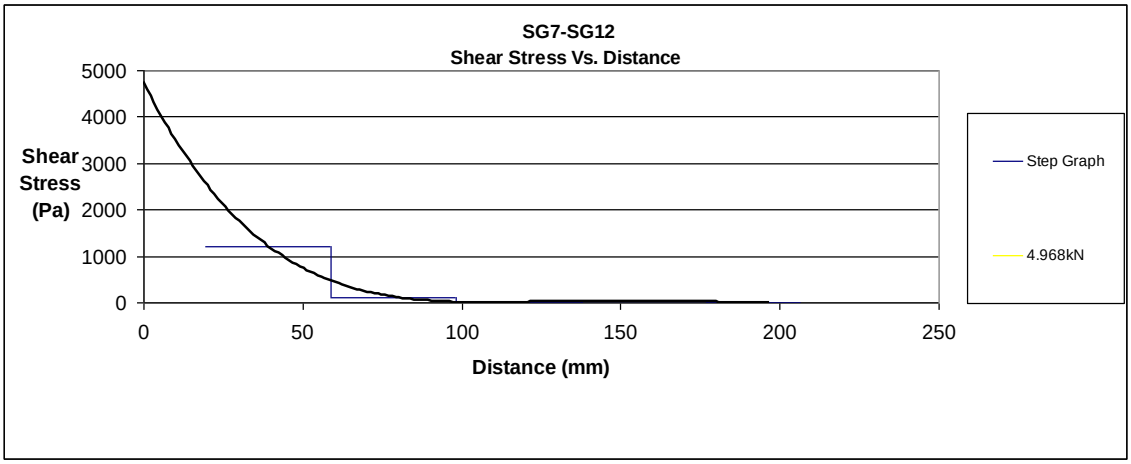

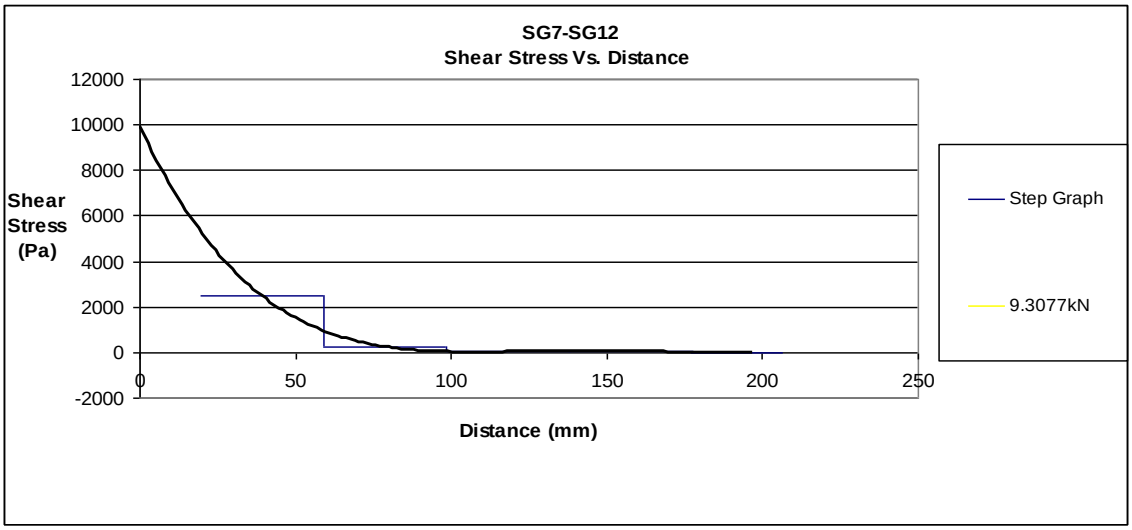

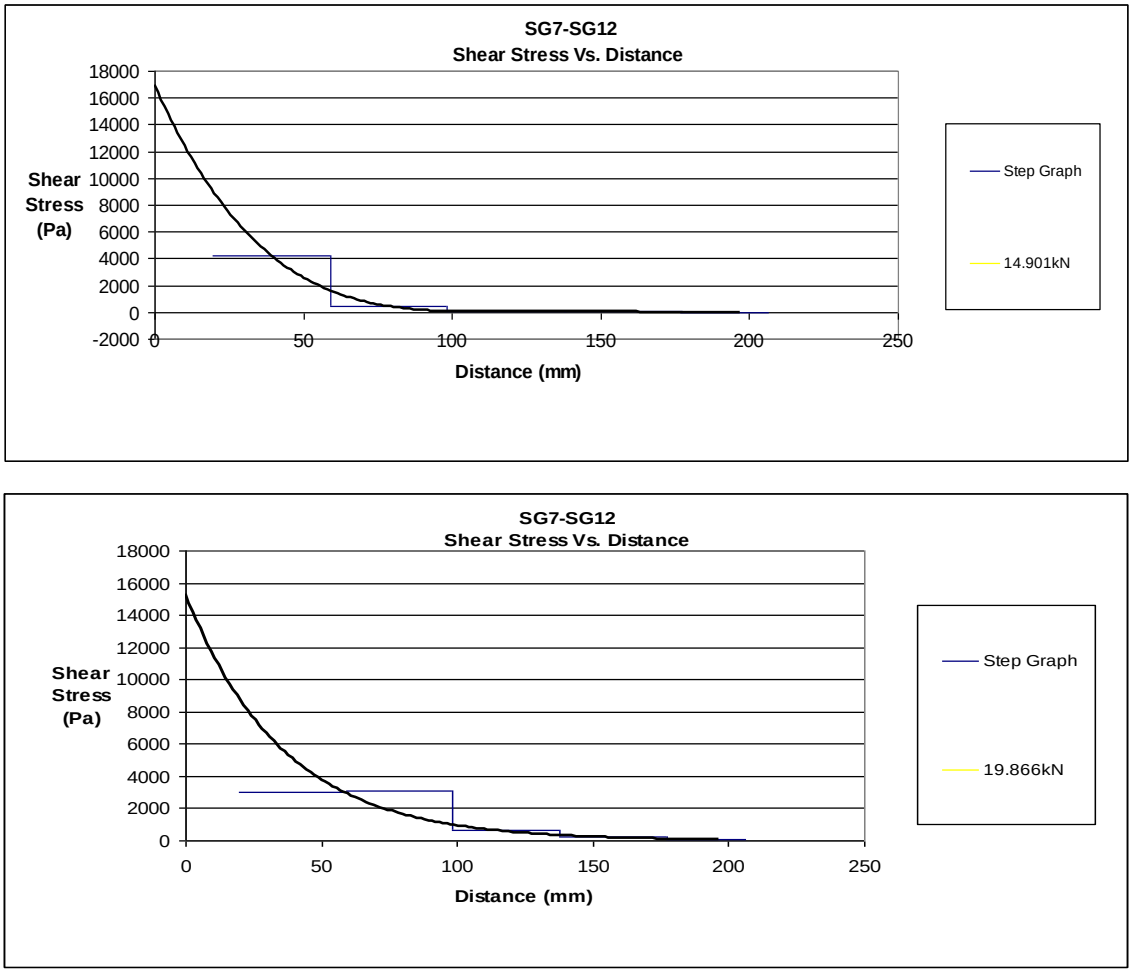

Figure 6.15. *Shear stress vs. distance for strain gauges SG7-SG12 for four loading values.*

Figure 6.16 shows the strain vs. load value for SG1-6 and SG7-12. Ultimate load bearing capacities and maximum shear stress are compared for specimens treated with different surface preparation methods in Sections 6.5 and 6.6

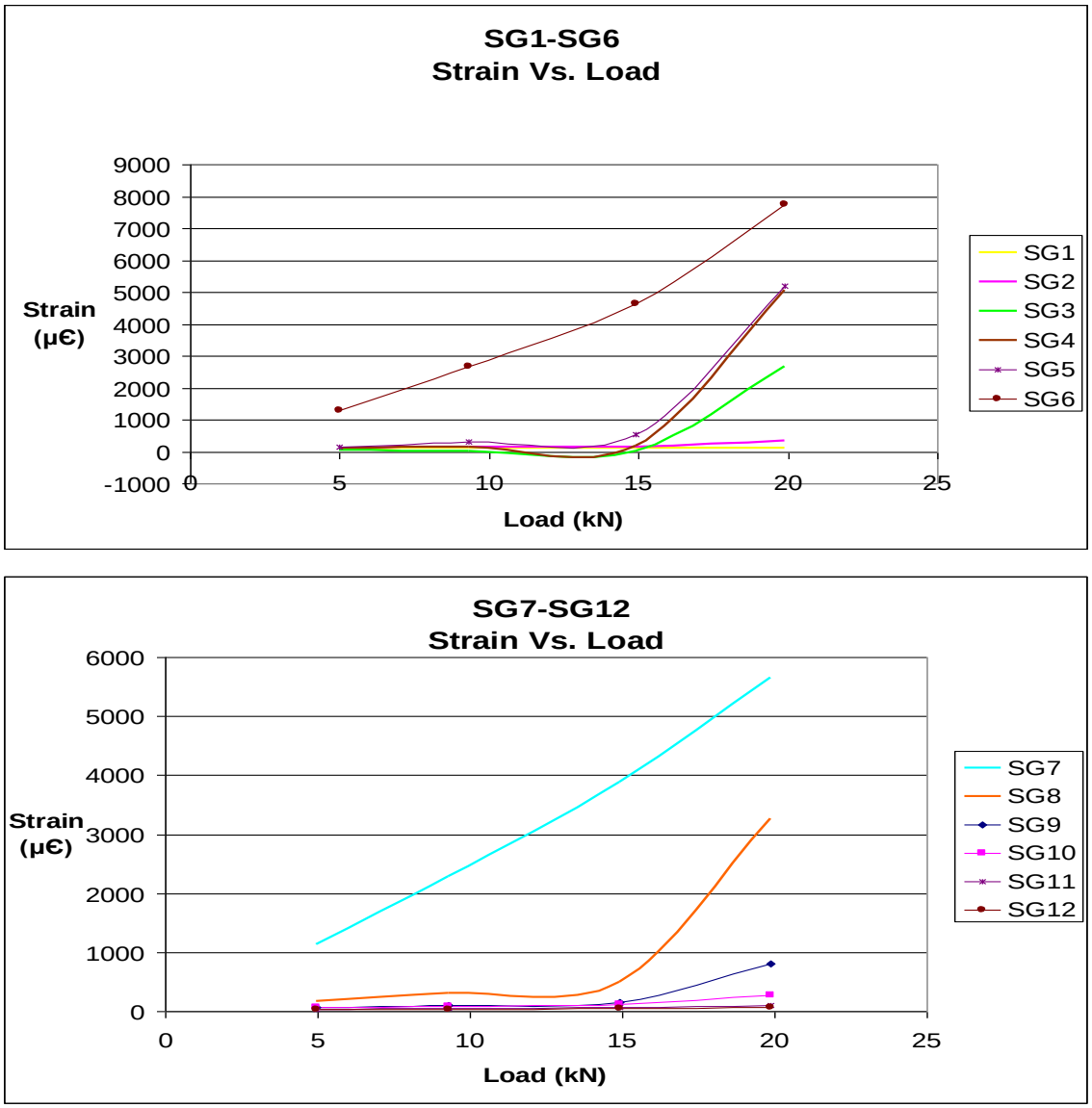

Figure 6.16. *Strain vs. load; each line represents an individual strain gauge over the loading cycle.*

6.4.4.2 Mechanics of the test

Figure 6.17 shows the shear diagram and bending moment diagram of the beam. There is a constant moment zone between the top supports. There is no shear for this zone. Figure 6.18 shows a free body diagram of a section of the beam adjacent to the notch. Because of the normal stress unbalance in the concrete and the elastic modulus incompatibility between FRP and concrete, shear stress is caused in the interface. This shear stress increases as the displacement increases. Figure 6.19 shows typical stress

profiles in a FRP strengthened beam as the test progresses. Once the shear stress next to the FRP at the notch reaches the maximum shear stress capacity of the interface, the interface begins to degrade, resulting in lower and lower stress until the stress reaches zero (complete debonding in the element). As this point, maximum shear stress is further down and the debonding has progressed.

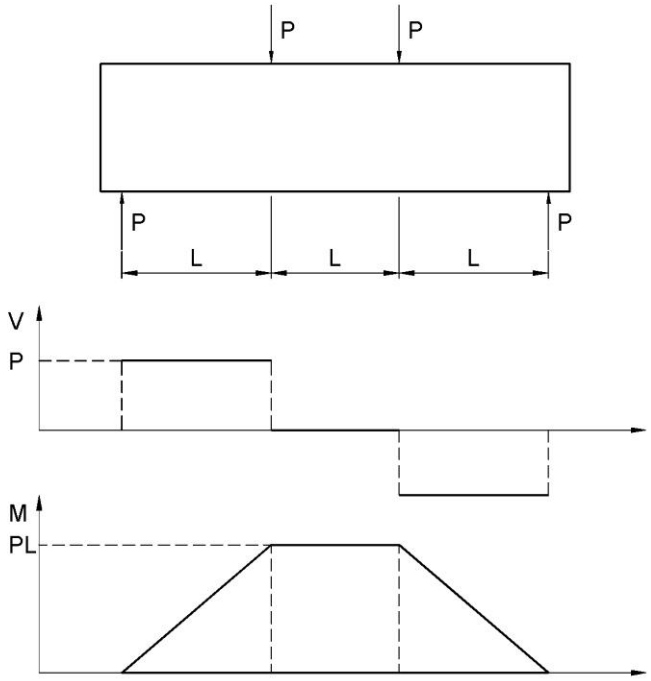

Figure 6.17. *Shear and moment body diagram of the test.*

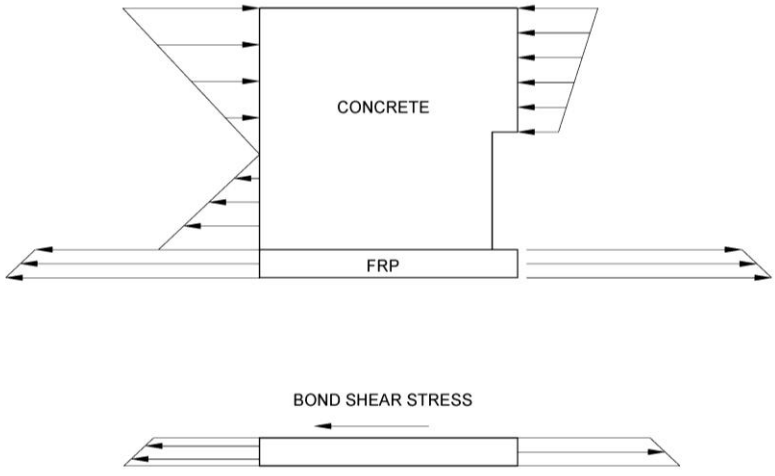

Figure 6.18. *Free body diagram of a strengthened beam section adjacent to the notch.*

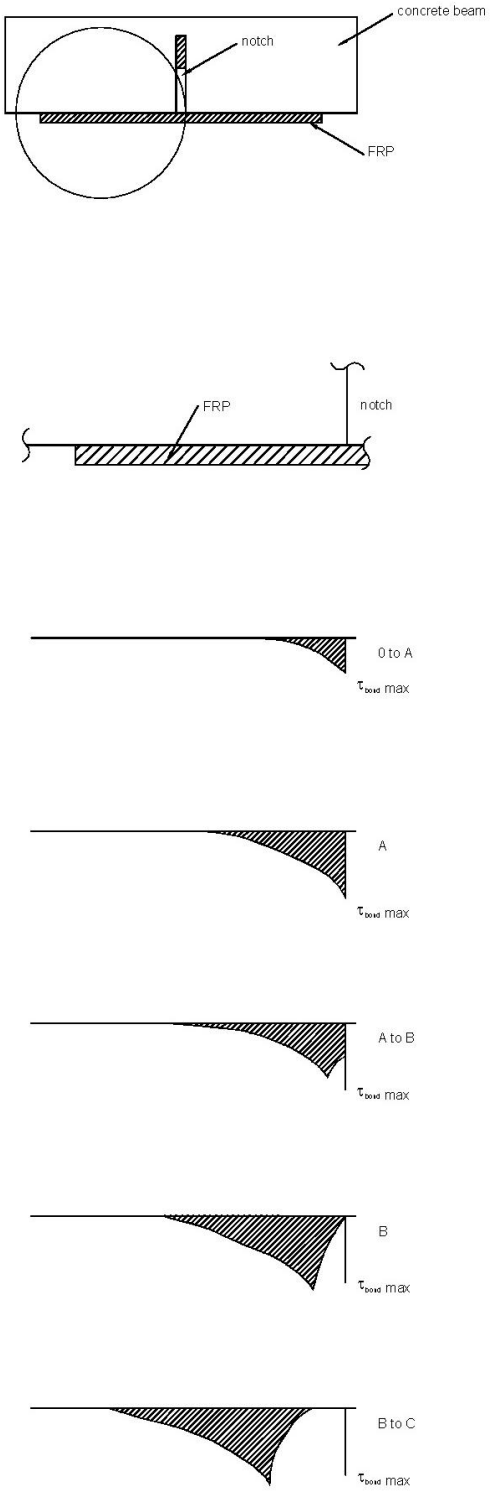

Figure 6.19. *Interfacial shear stress as the debonding progresses.*

6.4.4.3. Load displacement curve analysis

In Figure 6.20, the three different load vs. displacement behaviors have been separated; these represent linear, creation of the cohesive zone, and unzipping. Table 6.1 compares the load vs. displacement curve values for different specimens:

Table 6.1. *Initial slope in the load–displacement curves*

Specimen	Surface treatment	Ultimate failure load (kN)	Initial slope (kN/mm)
B9S1	Water jetting	3.77	72.5
B9S2	Water jetting	9.53	75.3
B9S3	Water jetting	5.55	71.5
B9S7	Sandblasting	5.12	71.4
B9S8	Sandblasting	4.62	69.5
B9S9	Sandblasting	8.31	73.2
B9S10	Jackhammering	5.39	60.1
B9S11	Jackhammering	6.06	72.5
B9S12	Jackhammering	6.70	70.8

It shows that, generally, specimens with higher bond values (due to different surface preparation) showed higher debonding load and ultimate load. The initial linear part remains unaffected by different surface preparations, proving that the debonding had not taken place in the linear part. Figures 6.19 and 6.20 compare the different phases of debonding with the load displacement curve. The load vs. displacement slope changes when the debonding starts. When the debonding zone is created, the debonding progresses; hence, higher displacement is noticed without increase in the load until the complete debonding occurs (point C).

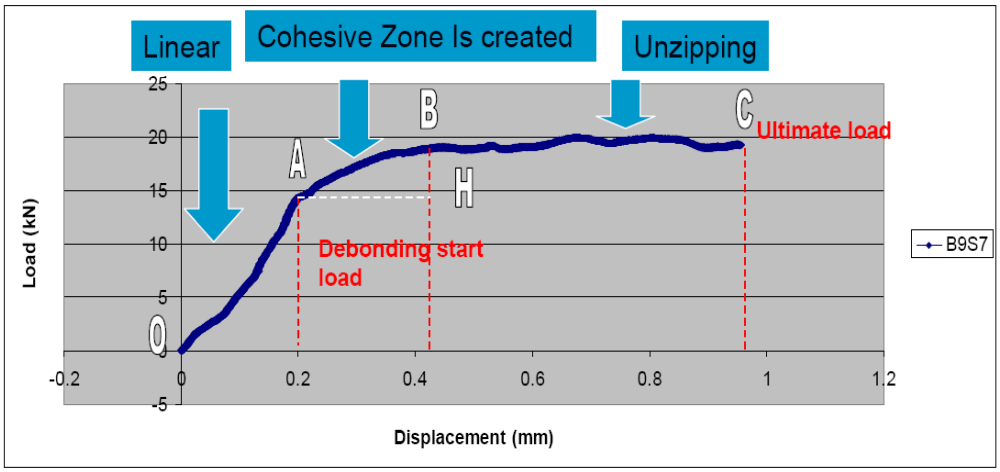

Figure 6.20. *Load vs. displacement curve analysis.*

6.5 Results

The results of the 12 tests conducted were predominantly as expected with a couple of exceptions. The samples were stressed until catastrophic failure occurred as the FRP debonded from the concrete, as seen in Figure 6.21.

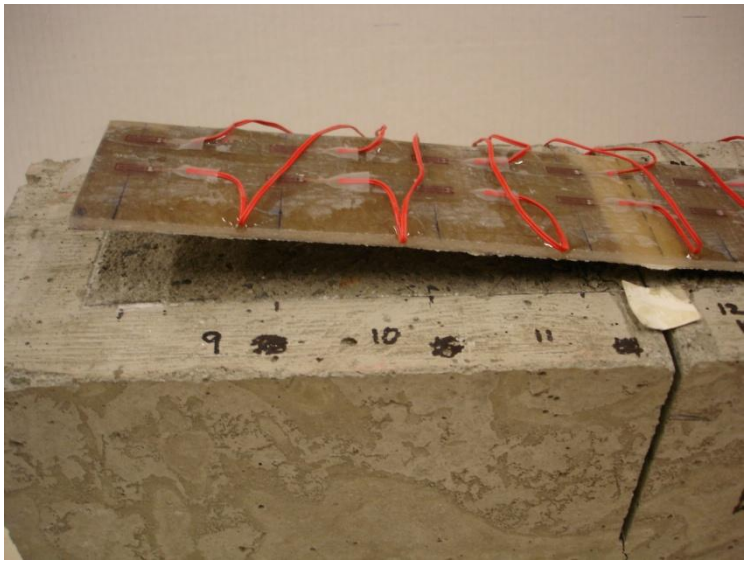

Figure 6.21. *Debonded sample.*

6.5.1 General findings

The 12 samples contained three different surface preparation types: water jetted, sandblasted, and jackhammered. Different relationships between results, such as gauge strain, location, shear stress, applied load, and beam centre deflection, were compared and analyzed. The comparisons of the relationships are discussed in detail in this section and the graphical representation of these analyses were plotted.

Sections 6.5.2 to 6.5.4 discuss the results of the samples as compared in various ways. Tables 6.2, to 6.5 give results of the shear stress analysis, as follows. First, the maximum shear stress at half of the maximum applied load was calculated. This is the maximum bond stress observed at any point in the specimen when the applied load is half of the ultimate load for that particular sample. The purpose of this analysis is to discover if a stress value exists that may be used to predict the load of failure. Second, the maximum shear stress before debonding is calculated. Once debonding is first observed in the strain gauge readings (typically near the centre of the sample), the shear stress at the adjacent strain gauge is calculated. This assumes that the area under this gauge will be next to fail; thus, the strain is near a peak.

The tabulated results for each of the surface preparation types are discussed in Sections 6.5.2 to 6.5.4 and compared in Section 6.6.

6.5.2 Water-washed samples

Six of the 12 samples tested were water-washed samples (B9S1 through B9S6). The maximum stresses were evaluated as seen in Table 6.2.

Table 6.2. *Shear stress analysis for water-washed samples*

Shear Stress Analysis				
Sample	**Surface Prep. (W, S, J)**	**Max. Stress at 1/2 Max. Load (MPa)**	**Max. Shear Stress Before Debonding (MPa)**	**Max. Load (kN)**
B9S1	W	1.957	3.771	20.430
B9S2	W	2.524	9.527	24.250
B9S3	W	1.437	5.552	22.230
B9S4	W	2.290	5.223	23.450
B9S5	W	0.184	N/A[1]	10.630
B9S6	W	0.376	5.425	21.160
Average		**1.461**	**5.899**	**20.358**
1 ~ Due to the premature failure of sample B9S5, there was no observed maximum shear stress before debonding				

Of the tabulated values, the maximum load appears to be the most consistent throughout the tests (with the exception of sample B9S5). The maximum stress at ½ maximum load does not appear to show any trend within these six samples. However, the average value of 5.889 MPa for the maximum shear stress before debonding appears to be consistent with a trend and would require further testing to reach a decisive conclusion regarding the expected value.

6.5.3 Sandblasted samples

Three of the 12 samples tested were sandblasted before applying the FRP. The results for these three samples were predominantly as expected and are tabulated in Table 6.3.

Table 6.3. *Shear stress analysis for sandblasted samples*

Shear Stress Analysis				
Sample	**Surface Prep. (W, S, J)**	**Max. Stress at 1/2 Max. Load (MPa)**	**Max. Shear Stress Before Debonding (MPa)**	**Max. Load (kN)**
B9S7	S	2.946	5.120	19.866
B9S8	S	2.300	4.623	23.419
B9S9	S	4.532	8.314	20.634
Average		**3.259**	**6.019**	**21.306**

The maximum load for these samples was the most consistent resulting value, while the maximum stress at ½ maximum load and the maximum shear stress before debonding were not very consistent and yielded inconclusive results.

6.5.4 Jackhammered samples

The surfaces of three samples were jackhammered prior to FRP application in an effort to improve bond quality. All three of the samples appear to have failed as expected, as shown in Table 6.4.

Table 6.4. *Shear stress analysis for jackhammered samples*

Shear Stress Analysis				
Sample	**Surface Prep. (W, S, J)**	**Max. Stress at 1/2 Max. Load (MPa)**	**Max. Shear Stress Before Debonding (MPa)**	**Max. Load (kN)**
B9S10	J	3.139	5.395	23.380
B9S11	J	3.489	4.298	20.446
B9S12	J	3.631	6.705	25.085
Average		**3.420**	**5.466**	**22.970**

However, these results are inconclusive because of the limited number of failed specimens. While sample B9S12 appears to have yielded at an appropriate maximum load, the FRP did not completely detach from the concrete, as seen in Figure 6.22.

Figure 6.22. *Sample B9S12.*

The FRP appears to have debonded on the middle two-thirds of the sample, while the ends remain attached. While the sample did not experience visible catastrophic failure, it did attain a maximum load and experience significant failure in the bond as seen in Figure 6.23.

Figure 6.23. *Sample B9S12 failure.*

6.6 Testing comparisons

After each surface preparation group was analyzed separately, as discussed in Section 6.5, the results of the three different surface preparations were compared. These comparisons were performed in hopes of observing trends in the behavior of different surface preparation methods. The comparisons include the shear stress analyses discussed in Section 6.5 and a debonding factor (as defind below). These factors were created in an effort to summarize the testing results into numerical values that would hopefully correspond to the bond behavior.

6.6.1 Shear stress analyses

The shear stress analyses of each surface preparation method discussed in Sections 6.5.2 to 6.5.4 were compared in an effort to observe a significant difference

among values for the three surface preparation methods. The results of this comparison are tabulated in Table 6.5.

Table 6.5. *Shear stress analysis*

Sample	Surface treatment	Maximum stress at ½ max. load (MPa)	Maximum shear stress before debonding (MPa	Maximum load (kN)
B9S1	Water jetting	1.957	3.771	20.430
B9S2	Water jetting	2.524	9.527	24.250
B9S3	Water jetting	1.437	5.552	22.230
B9S4	Water jetting	2.290	5.223	23.450
B9S5	Water jetting	0.184	N/A*	10.630
B9S6	Water jetting	0.376	5.425	21.160
Average		1.461	5.899	22.304
B9S7	Sandblasting	2.946	5.120	19.866
B9S8	Sandblasting	2.300	4.623	23.419
B9S9	Sandblasting	4.532	8.314	20.634
Average		3.259	6.019	21.306
B9S10	Jackhammering	3.139	5.395	23.380
B9S11	Jackhammering	3.489	6.065	24.320
B9S12	Jackhammering	3.631	6.705	25.085
Average		3.420	6.055	24.262

*Due to the premature failure of sample B985, there was no observed maximum shear stress before debonding,

As seen in Table 6.5, the average maximum loads for the three different surface preparations appear to be very similar. For this specific set of data, this suggests that the surface preparation method has minimal effect on the maximum load sustained by the sample. Also, the averages of the maximum shear stress before debonding appear to be fairly similar. One could conclude that load bearing capacity in the 550 mm specimens, owing to the larger size, is less sensitive to the bond properties compared with 350 mm specimens. However, the 550 mm specimens provide full unzipping in the load–displacement response.

While the majority of the shear stress analyses results appear similar, the maximum shear stress at ½ maximum load results show significantly lower values for water-washed samples. Not only is the average value significantly lower, but the maximum value for any one of the water-washed samples is significantly lower than the averages of the jackhammered and sandblasted samples. This may suggest a more uniform bond in the water-washed samples, resulting in a more even distribution of strain. However, further testing is necessary to formulate any conclusions regarding this advantage of water-washed preparation.

6.6.2 Debonding factor

The debonding factor was created in an effort to relate the asymmetry of strain distribution to the failure point at that particular location in the sample. This factor was created in hopes of finding a correlation between the calculated factor and the propagation of failure within the sample.

6.6.2.1 Definition

The debonding factor is calculated as

$$\text{Debonding\_Factor} = \frac{\left|SG_{1+z} - SG_{12-z}\right|}{\Delta L}, \qquad (z = 0 \text{ to } 5)$$

where SG_1 is the strain reading in strain gauge 1 and ΔL is the distance between strain gauge 1 and strain gauge 12. The bond is said to have failed if the debonding factor is greater than one. Gauge numbers are identified in Figure 6.11.

6.6.2.2 Application of the debonding factor

The debonding factor is calculated for each strain gauge pair at each ¼ maximum ½ maximum, ¾ maximum, and maximum load for the particular sample, as seen in Table 6.6. Table 6.6 numerically displays the propagation of the failure as the applied load increases. The application of the debonding factor is explained in detail for sample B9S11 as follows.

Table 6.6. *Debonding factors for sample B9S11 ($\mu\varepsilon/mm$)*

		SG1-SG12 ΔL	SG2-SG11 ΔL	SG3-SG10 ΔL	SG4-SG9 ΔL	SG5-SG8 ΔL	SG6-SG7 ΔL
	5.29kN	0.0254238	0.0169492	0.02179179	0.0101695	0.0338983	0.432207
	10.58kN	0.0416025	0.0169492	0.00363197	0.0305086	0.4152542	25.32225
	15.87kN	0.064715	0.7627119	5.7639295	24.823813	40.211864	59.87339
	21.16kN	0.7696468	8.5960452	22.3656445	26.156021	10.627119	79.06847
	ΔL (mm)	433	354	275	197	118	39.3
Condition of Section	5.29kN	bond	bond	bond	bond	bond	bond
	10.58kN	bond	bond	bond	bond	bond	FAIL
	15.87kN	bond	bond	FAIL	FAIL	FAIL	FAIL
	21.16kN	bond	FAIL	FAIL	FAIL	FAIL	FAIL

6.6.2.2.1 At ¼ maximum load (5.29 kN)

The strain distribution at ¼ maximum load is shown in Figure 6.24.

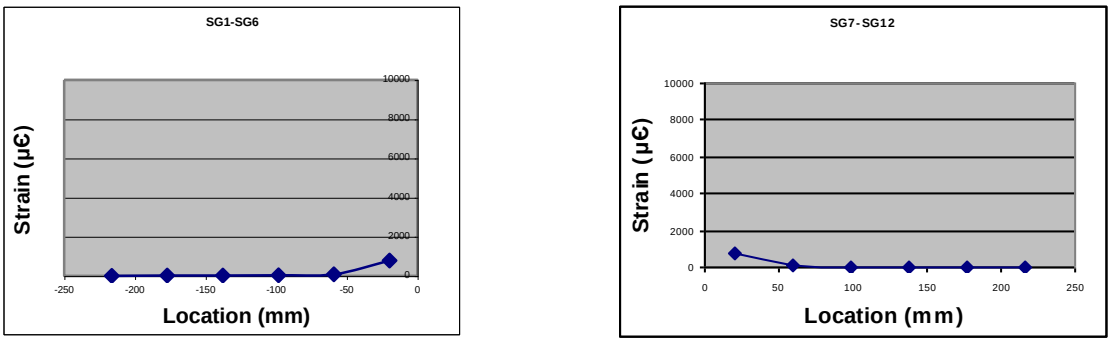

Figure 6.24. *Strain distribution at ¼ maximum load.*

At this early stage in loading, the strain appears to be relatively symmetric, which can be proven numerically by the debonding factor.

Table 6.7. *Debonding factor at ¼ maximum load ($\mu\varepsilon/mm$)*

		SG1-SG12	SG2-SG11	SG3-SG10	SG4-SG9	SG5-SG8	SG6-SG7
	5.29kN	0.0254238	0.0169492	0.02179179	0.0101695	0.0338983	0.432207
	10.58kN	0.0416025	0.0169492	0.00363197	0.0305086	0.4152542	25.32225
	15.87kN	0.064715	0.7627119	5.7639295	24.823813	40.211864	59.87339
	21.16kN	0.7696468	8.5960452	22.3656445	26.156021	10.627119	79.06847

There are no debonding factors greater than 1 at this applied load, which suggests a completely bonded sample as seen in Figure 6.25. (black bar indicates bonding)

Figure 6.25. *Debonded region at ¼ maximum load.*

While there may be some bond failure at the centre of the sample between strain gauges 6 and 7, the failure has not yet propagated to either of these two gauges. Thus, the sample is still fully capable of supporting a load.

6.6.2.2.2 At ½ maximum load (10.58 kN)

Strain distribution is shown in Figure 6.26.

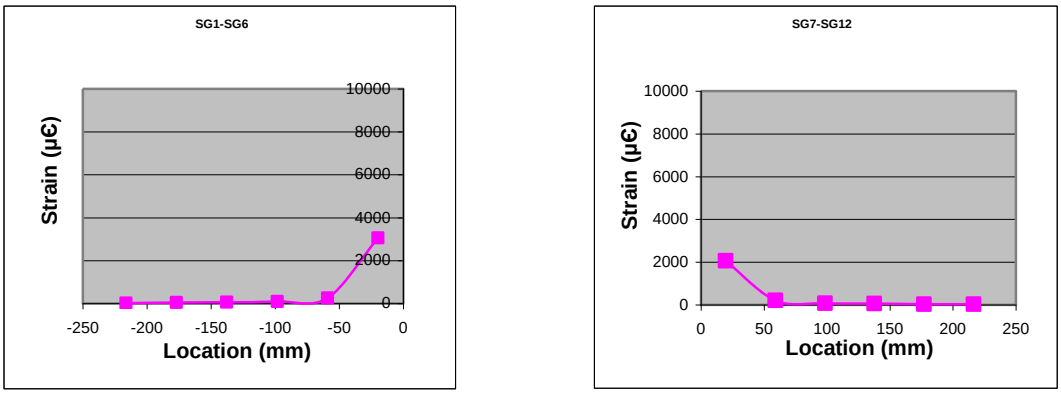

Figure 6.26. *Strain distribution at ½ maximum load.*

At this stage in loading, the strain appears to be slightly greater on one side of the sample, resulting in the debonding factors seen in Table 6.8.

Table 6.8. *Debonding factor at ½ maximum load ($\mu\varepsilon/mm$)*

	SG1-SG12	SG2-SG11	SG3-SG10	SG4-SG9	SG5-SG8	SG6-SG7
5.29kN	0.0254238	0.0169492	0.02179179	0.0101695	0.0338983	0.432207
10.58kN	0.0416025	0.0169492	0.00363197	0.0305086	0.4152542	25.32225
15.87kN	0.064715	0.7627119	5.7639295	24.823813	40.211864	59.87339
21.16kN	0.7696468	8.5960452	22.3656445	26.156021	10.627119	79.06847

The debonding factor in the middle of the sample is much greater than 1, suggesting a bond failure at this point as demonstrated graphically in Figure 6.27.

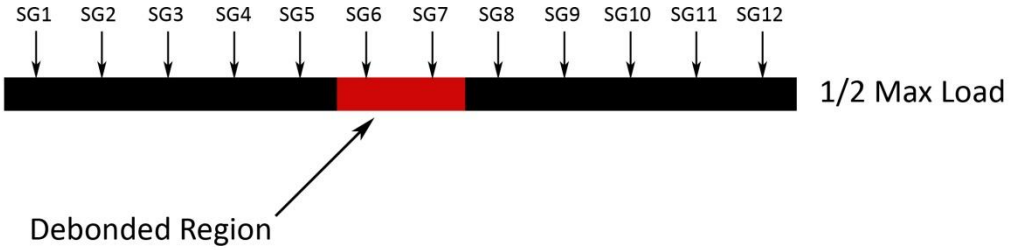

Figure 6.27. *Debonded region at ½ maximum load.*

These results suggest that failure has propagated past at least one of strain gauges 6 or 7 and will likely continue to fail as loading increases. In Figure 6.27, the red bar shows the probable debonded region.

6.6.2.2.3 At ¾ maximum load (15.87 kN)

Strain distribution is shown in Figure 6.28.

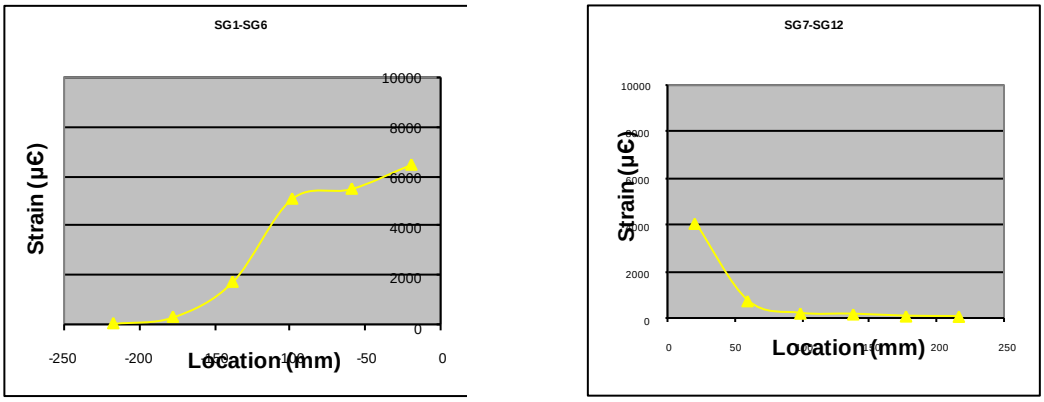

Figure 6.28. *Strain distribution at ¾ maximum load*

At this stage in loading, the sample is clearly undergoing a very asymmetric strain distribution as displayed by the debonding factors shown in Table 6.9.

Table 6.9. *Debonding factor at ¾ maximum load ($\mu\varepsilon/mm$)*

	SG1-SG12	SG2-SG11	SG3-SG10	SG4-SG9	SG5-SG8	SG6-SG7
5.29kN	0.0254238	0.0169492	0.02179179	0.0101695	0.0338983	0.432207
10.58kN	0.0416025	0.0169492	0.00363197	0.0305086	0.4152542	25.32225
15.87kN	0.064715	0.7627119	5.7639295	24.823813	40.211864	59.87339
21.16kN	0.7696468	8.5960452	22.3656445	26.156021	10.627119	79.06847

The debonding factors are now beginning to show significant failure propagation in the sample.

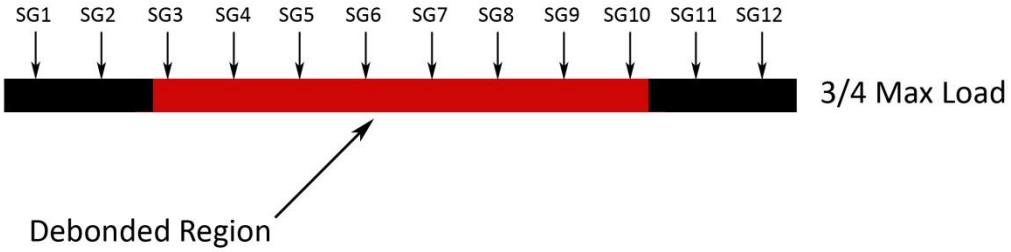

Figure 6.29. *Debonded region at ¾ maximum load.*

These results suggest that a majority of the bond has failed and that the sample will not be able to support much additional loading before catastrophic failure occurs. Please note that the red bar shows the probable debonded region.

6.6.2.2.4 At maximum load (21.16 kN)

Strain distribution is shown in Figure 6.30.

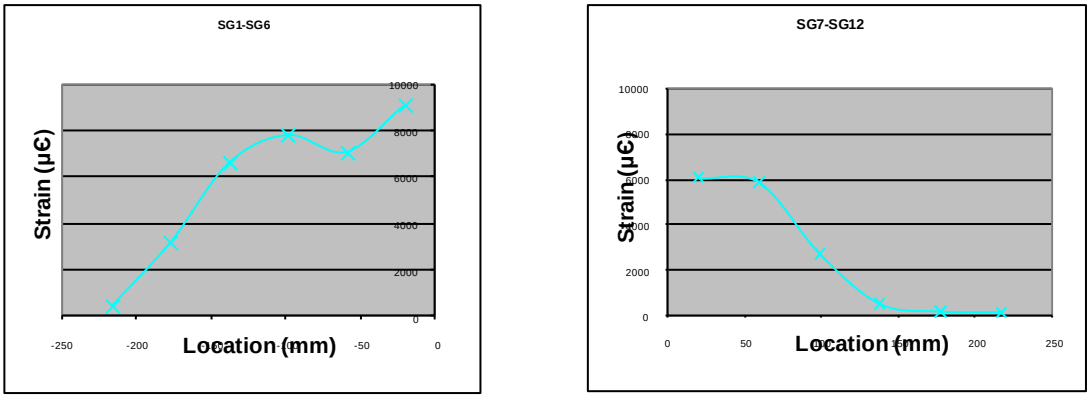

Figure 6.30. *Strain distribution at maximum load.*

At the maximum load supported before catastrophic failure, the strain appears to be significantly greater on one side of the sample.

Table 6.10. *Debonding factor at maximum load ($\mu\varepsilon/mm$)*

	SG1-SG12	SG2-SG11	SG3-SG10	SG4-SG9	SG5-SG8	SG6-SG7
5.29kN	0.0254238	0.0169492	0.02179179	0.0101695	0.0338983	0.432207
10.58kN	0.0416025	0.0169492	0.00363197	0.0305086	0.4152542	25.32225
15.87kN	0.064715	0.7627119	5.7639295	24.823813	40.211864	59.87339
21.16kN	0.7696468	8.5960452	22.3656445	26.156021	10.627119	79.06847

The debonding factors now suggest that all but the outer edges of the sample have failed, which explains the catastrophic failure that would take place momentarily as shown in Figure 6.31.

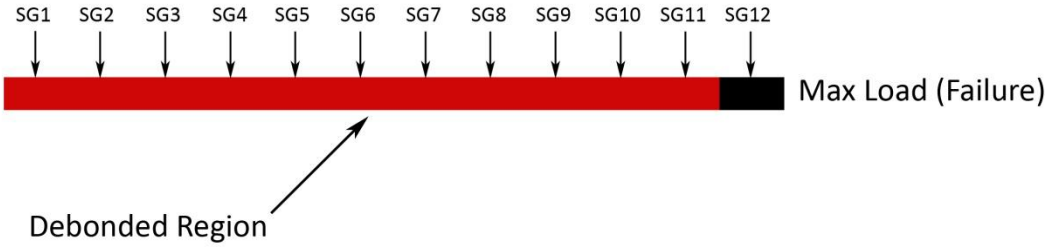

Figure 6.31. *Debonded region at maximum load.*

The bond has now failed completely on one side of the specimen as suggested numerically by the debonding factor. Throughout this example, the debonding factor has allowed us to numerically monitor the propagation of bond failure as the applied load was increased. The example showed that bond failure progresses on one side if asymmetric. It should be noted that if the bond failure was purely symmetrical, no prediction could have been made.

6.6.2.3 Summary

The results for the debonding factor show that there is a distinct relationship between the asymmetry of the strain distribution and failure propagation. This factor tends to increase significantly as failure starts to occur. This conclusion leads to the idea that strain gauges could be applied to an FRP reinforcement in the field and monitored. If the debonding factor rises above a critical value, a value of 1 was chosen in this case, then the proper authorities would be notified. The value of 1 was arbitrarily chosen for these tests, but further testing would be required to obtain a more appropriate value. The monitoring of the debonding factor in the field may be a good way to accurately gauge the current bond condition in the specimen. However, further testing would be required to investigate this possibility further. It should also be noted that another parameter that could warn us of potential debonding is unusually high strain values on the FRP. Further research is needed to set criteria for strain values for this application.

6.7 Conclusion

The debonding factor was developed to read the asymmetry of the strain distribution during loading, which would ultimately lead to the ability to accurately map the progression of the debonding between FRP and concrete. It yielded very conclusive results regarding the correlation between bond failure and a debonding factor greater than 1. The value of 1 was arbitrarily chosen, and further testing would be required to obtain a more appropriate number. The failure location (FL) factor was developed in an effort to predict the side of ultimate failure of the FRP–concrete bond. The FL factor

yielded inconclusive results, and more testing would be required to determine the validity of the factor.

The debonding factor developed in this experiment has a promising application, and more testing should be done to determine its accuracy. Provided the factor is correct, it could be applied to structure maintenance monitoring. An aging concrete structure that is reinforced with FRP could have strain gauges placed on the surface of the FRP, which constantly monitor the bond between the FRP and concrete. If the bond begins to fail, the debonding factor would allow a computer to detect the propagation of the debonded region and notify the appropriate authorities before catastrophic failure of the structure takes place. This application of the factor could one day lead to improved structural monitoring and higher levels of safety.

CHAPTER 7
DEVELOPMENT OF IMPACT TEST SETUP

7.1 Introduction

The behavior of concrete and steel reinforced concrete and FRP strengthened beams under impact loading has been investigated by several researchers. However, the FRP–concrete bond properties under impact had never been looked at. One of the main objectives of this research was to design and build a specimen and impact testing setup to answer some of the questions on how FRP to concrete bond behaves under impact. In many research studies, the total load as recorded by the instrumented tup (impact loading hammer) was one of the main measurements carried out. The bending load applied on the beams was then calculated by subtracting the inertia load (i.e., the load required to accelerate the specimen) from the recorded tup load. It was noted that for brittle materials like concrete, the values of the inertia load could be much larger than the load consumed in stressing the beam.

In a previous study by Soleimani [3.2], to overcome the problem associated with the inertia effects, instrumented support anvils as well as an instrumented tup were used. This system was modified in association with the newly developed specimen as described in Chapters 5 and 6 to study the bond between FRP and concrete. A health monitoring system using strain gauges was developed to measure the FRP strain under impact.

7.2 Drop weight impact machine

A drop weight impact machine with a capacity of 14.5 kJ was used in this research study. A mass of 591 kg (including the striking tup) can be dropped from as high as 2.5 m (2.5 m × 591 kg × 9.81 m/s^2 ÷ 1000 = 14.5 kJ). During a test, the hammer is raised to a sepcific height above the specimen using a hoist and chain system. At this position, air brakes are applied on the steel guide rails to release the chain from the hammer. When the brakes are released, the hammer falls and strikes the specimen. Figure 7.1 shows the impact machine.

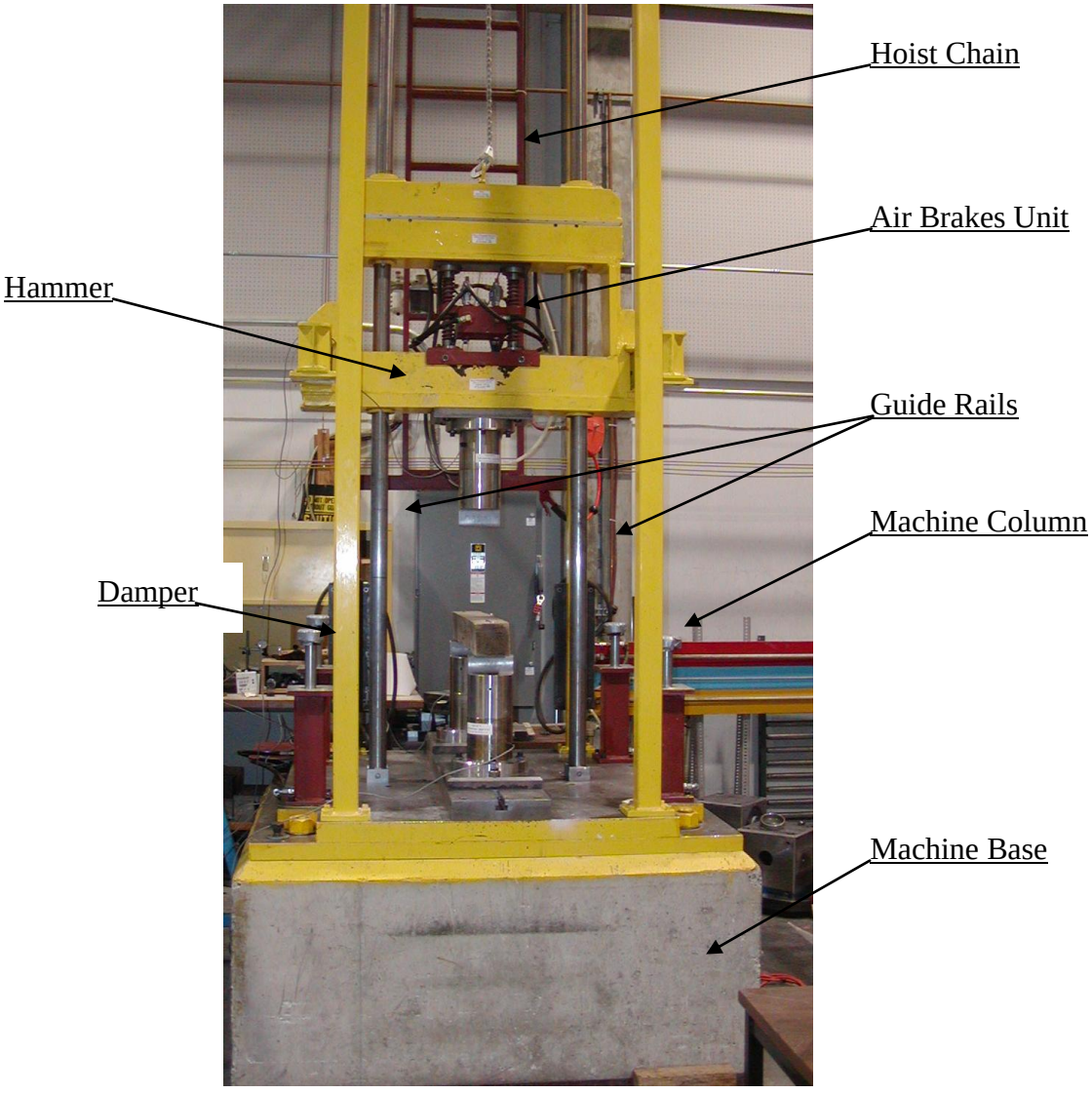

Figure 7.1. *The 14.5 kJ drop weight impact machine [3.2].*

7.3 Test setup

This setup was made using accurate load cells which were designed, built, and calibrated at the University of British Columbia.

7.3.1 Load cells

Three load cells were designed and built at the University of British Columbia for previous research by Soleimani [3.2]. Load cell assemblies and their details are shown in Figures 7.2 to 7.4. Two load cells sitting on a 1.524 m steel anvil (rail) will be referred to as load cells A and C, while the third one, which is bolted to the impact machine's hammer (striking tup), will be referred as load cell B. Beam span can be adjusted by moving the two support load cells and is in the range of 370 to 1150 mm for this setup.

7.3.2 Steel yoke at the supports

In this research study simply supported FRC beams were tested under quasi-static and impact loading conditions. In previous research study at UBC, it was discovered that if the specimen was not prevented from vertical movement at the supports, within a very short period of first contact of the hammer with the specimen, contact with the support was lost, and as a result loads read by the support load cells were not correct. This phenomenon was further verified by using a high-speed camera (1700 frames per second). As a result loads recorded by the support load cells for two identical tests were totally different [3.2].

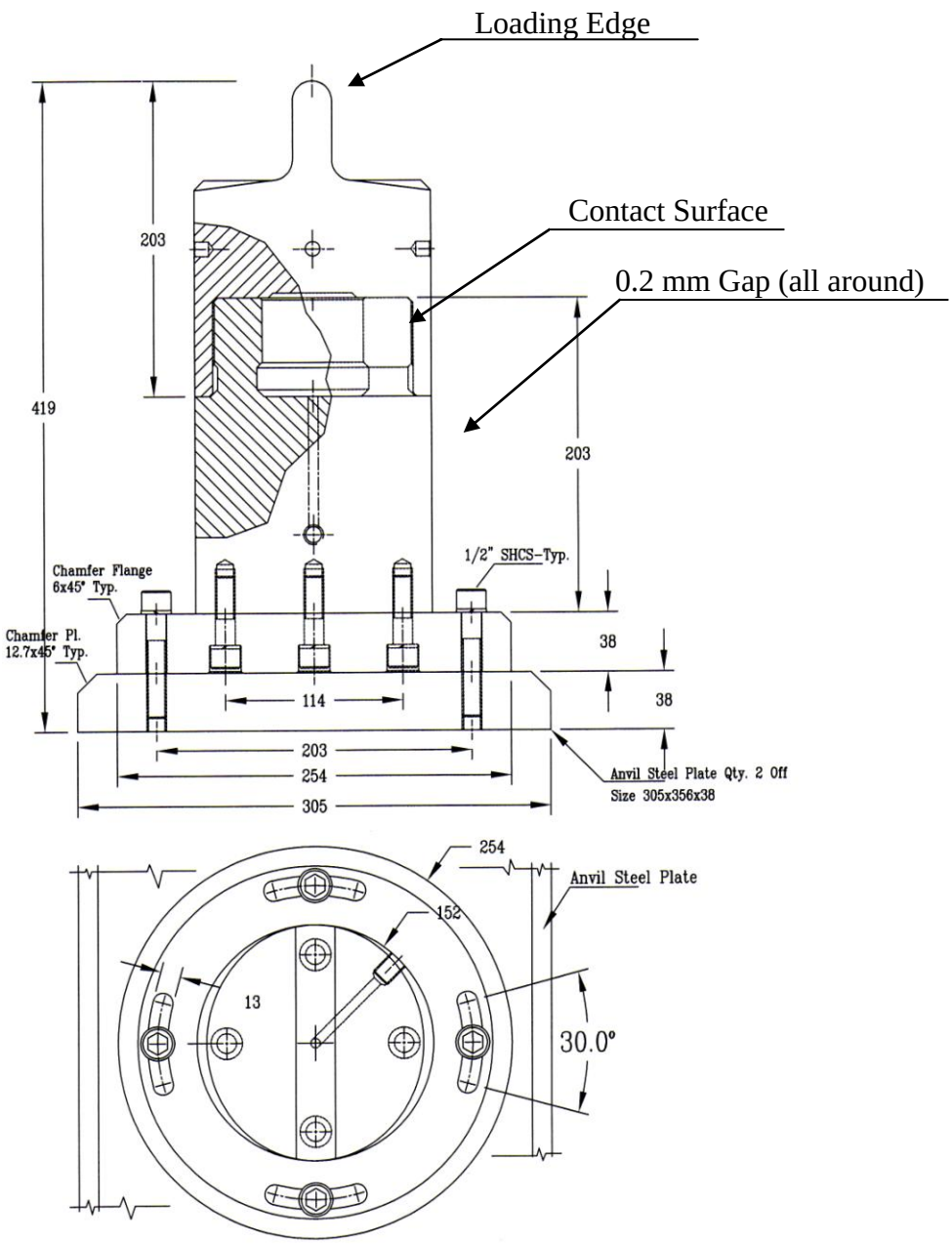

Figure 7.2. *Anvil support load cell assembly – plan and elevation view[3.2].*

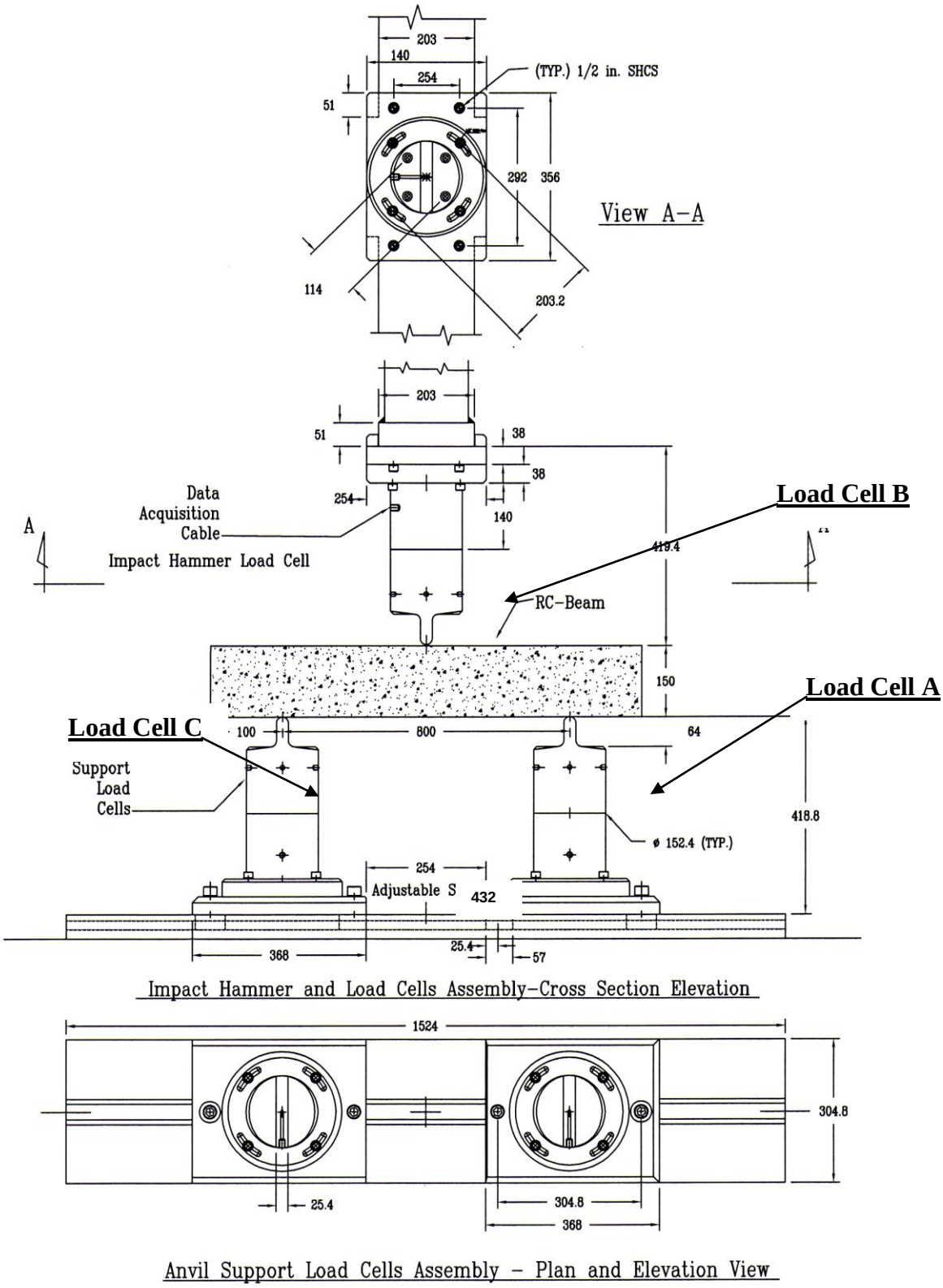

Figure 7.3. *Load cell assembly (before improvements). Figure 7.13 shows the setup after improvements [3.2].*

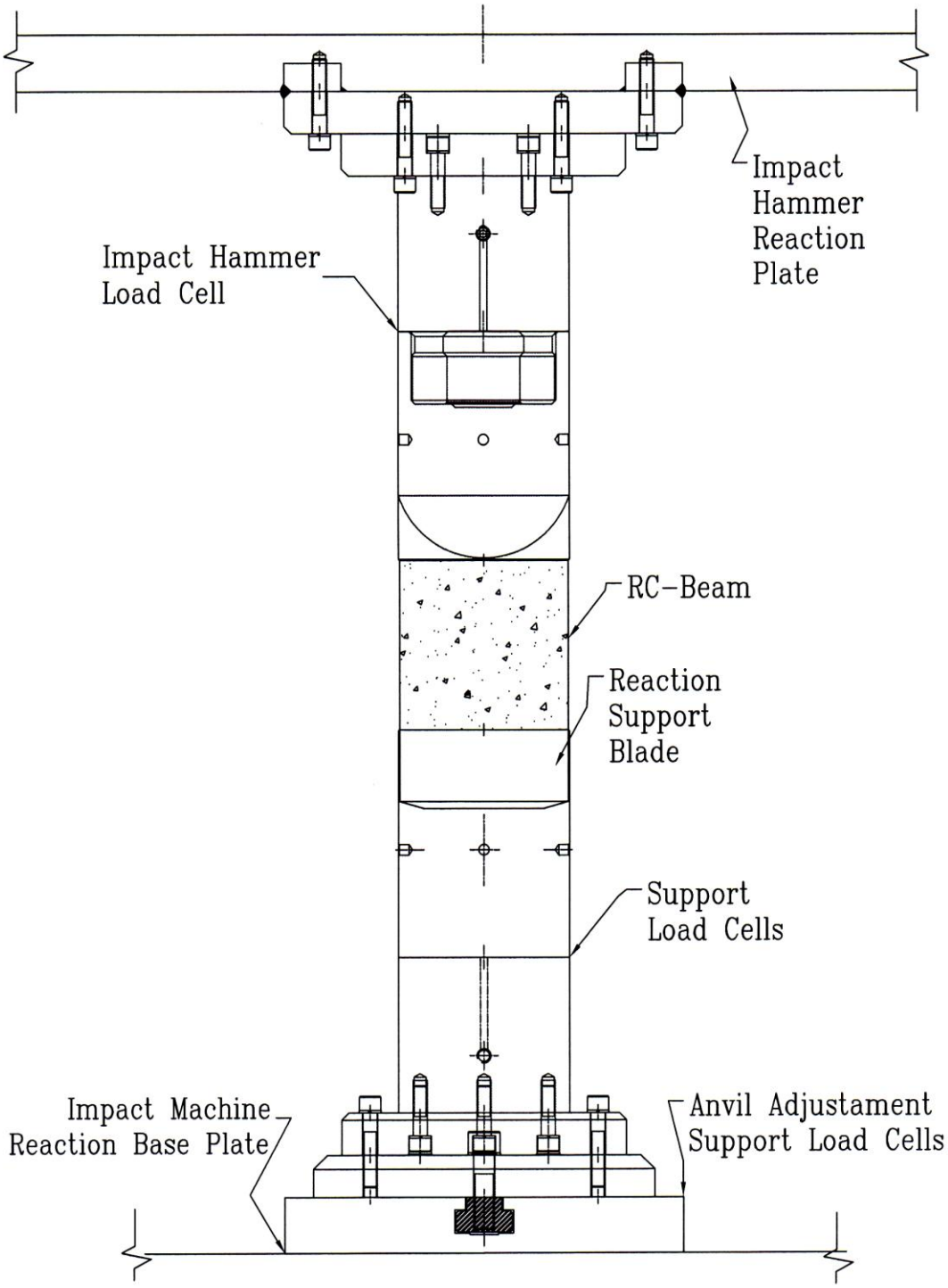

Figure 7.4. *Impact hammer and load cells – side elevation [3.2].*

To overcome this problem, the vertical movement of FRP Strengthened beams at the supports was restrained using two steel yokes. The addition of a strap ensured that the hold-downs worked as expected instead of being thrown in the wrong direction (Figure 7.5). In order to assure that the beams are still simply supported, these yokes are pinned at the bottom, to allow rotation during beam loading (Figure 7.6). To allow an easier rotation, a round steel bar was welded underneath the top steel plate where the yoke touched the beam (Figure 7.7).

Figure 7.5. *Impact test setup with steel yokes.*

Figure 7.6. *Steel yokes are pinned at the bottom end (i.e., rotation is free).*

Figure 7.7. *Beam placed in impact machine with FRP facing down0*

7.4 Impact testing

7.4.1. Testing procedure

When the impact machine hits the beam it applies a single point load at the mid-span of the beam, subjecting it to bending. This results in tension on the bottom face of the beam and compression on the top. Because the objective was to test the strength and ductility (defined as the area under the load vs. displacement curve) of the FRP–concrete bond, the beams were tested with the FRP on the lower beam face to induce shear stresses as a result of tension due to bending, as shown in Figure 7.7. Additionally, the notch in the beam prevented the concrete from adding to the tensile resistance of the beam, ensuring that only the tensile capacity of the beam was provided by the FRP strip. It should be noted that there will still be compression stress in the concrete above the notch. Figure 6.18 shows a free body diagram of a section of the beam.

The expected failure modes for the impact test are failure of the FRP–concrete bond or rupture of the FRP strip. As mentioned before, while failure of the concrete in shear is possible, the risk of shear failure was minimized by the addition of steel fibres to the concrete.

Because there have been no previous investigations into the impact response of FRP–concrete bond, one of the goals for this research was to develop a testing procedure that could be use to reliably and efficiently test the beams and obtain the desired data. As a result, the method used to test the beams was modified and improved as the work progressed.

The beams tested were all fully prepared, i.e., they all had notches, prepared surfaces, FRP strips, and strain gauges on the beams to collect strain data. The first step in the process used to prepare the beams for testing was to attach the accelerometers to the beam. The method used in early tests was to use fast drying epoxy glue to glue U-shaped wooden blocks to both sides of the beams. The blocks had nuts glued into the bottom of the U that allowed the accelerometers to be attached to the block. Figure 7.8 illustrates how the blocks were attached. The blocks were used to provide a place close to the centre of the beam to attach the accelerometers and to protect the accelerometers during the impact.

Figure 7.8. *Wooden blocks used to attach accelerometers.*

However, after the first four tests it was decided that the data obtained from the accelerometer were not reliable. Figure 7.9 shows the acceleration data obtained from

one sample. As can be observed, no acceleration was captured that is in the magnitude of impact accelerations; what is measured was suspected to be only noise. It was assumed that this is due too many different materials interacting between the accelerometers and the concrete beam.

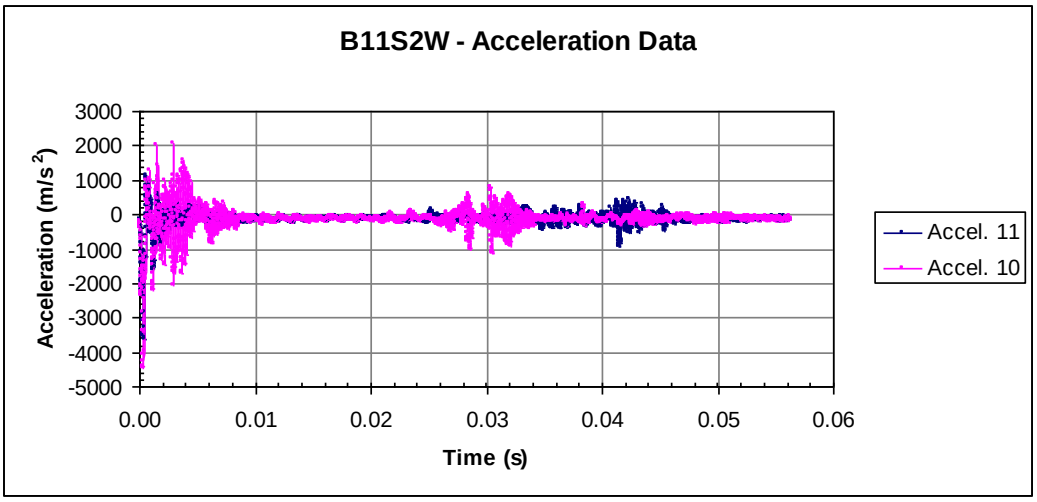

Figure 7.9. *Acceleration data with the accelerometer attached to the side with a wooden block.*

The accelerations would have to travel through two layers of glue and one wooden block before they could be measured. The solution was to glue two nuts to the top of the beam, 13 cm from the ends, and attach the accelerometers directly, as can be seen in Figure 7.10. This reduced the number of materials between the beam and the accelerometers to only one. The nuts were placed in such a way as to limit the conflict between the dropping hammer and restraints. As verified by Banthia [7.1], since the top of the beam deflects in a linear manner, the accelerations measured could be scaled up to give the correct values for the centre of the beam.

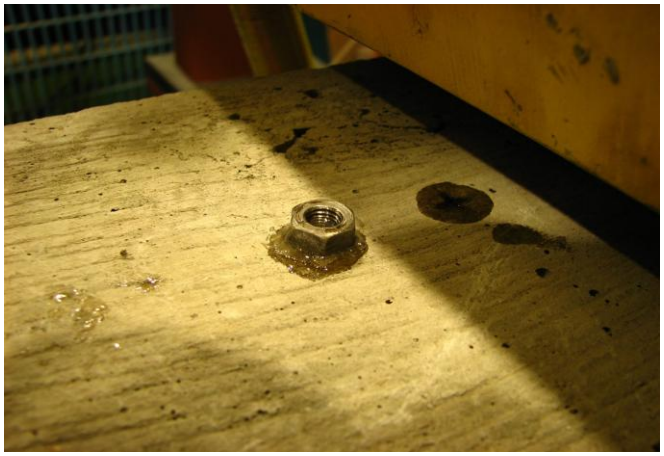

Figure 7.10. *Nut glued to top of beam ready to have accelerometer attached.*

Once the glue used for the accelerometer attachment had dried, the beam was placed into the impact machine. It was centred on the supports and the accelerometers were screwed into the nuts. The hold-downs were also placed over the ends of the beams at this time and secured with the strap. Once secured, the accelerometers, and strain gauges if applicable, were connected to the data acquisition computer. Later in the tests, the metal nuts were changed to plastic nuts, as some cases of failure in the bond between the metal nut and epoxy were observed. This was eliminated when the plastic nuts were used.

Next, the drop hammer was lifted off the safety pins, allowing them to be removed. The dropping hammer was then lowered or raised as appropriate to the desired height and locked in place with the air brakes. Once it was ensured that all personnel were safely clear of the impact machine, the test was ready to be run.

The first step in running the actual impact test was to start the data capturing software. Once the software was started and capturing data, the signal was given to release the air brakes on the dropping hammer. The dropping hammer would then fall freely until it hit the beam below, causing the beam to break and fall off the supports. After the impact was completed, the data capture was stopped, completing the test.

Because the impact happened over a few tenths of a second, the data capturing software, which is produced by National Instrument, recorded data at a rate of 100 kHz. This high rate of data acquisition was used to ensure that the point of first contact was not missed.

7.4.2 Improvements to test setup

As testing progressed, deficiencies in the testing procedure were identified and the procedure was modified accordingly.

Initially the accelerometers were attached to the concrete specimens on either side of the beams at mid-span. Wooden blocks were epoxied directly to the concrete, acting as a protective housing for the accelerometers. A failure to account for the effects of changes in wave speed through the varying media will have had an adverse affect on the early test specimens. In later tests the accelerometers were relocated to 13 cm from the ends of the beam and directly adhered to the top surface using epoxy to eliminate the wooden block. As verified by Banthia [7.1], beam deflections are small enough to linearly translate these deformations to maximum deflections at mid-span.

The initial test had no control mechanism to minimize the destructiveness at failure. This caused damage to the accelerometer in one of the preliminary tests, which resulted in the loss of accelerometer data. These issues were rectified with the use of padding and vertical tie-downs to help maintain control of the test specimen at failure.

As the number of test runs increased, it became apparent that the beams would have to be prevented from crashing off the supports when hit by the dropping hammer. The solution was to use dense foam to build up a platform under the beam. The platform stopped approximately 20 cm below the beam, which allowed the impact machine to rest on its supports after the test without being in contact with the beam, as shown in Figure 7.11. Another solution could be to use a smaller hammer; this was not possible because of limitations of the laboratory facilities.

Figure 7.11. *A broken beam being supported by the foam platform.*

This system was used for the last two tests performed in this trial stage and it worked very well. The decision was made to use this method for all subsequent investigations into the FRP–concrete bond under impact loading. A diagram of the final testing setup is shown in Figure 7.12.

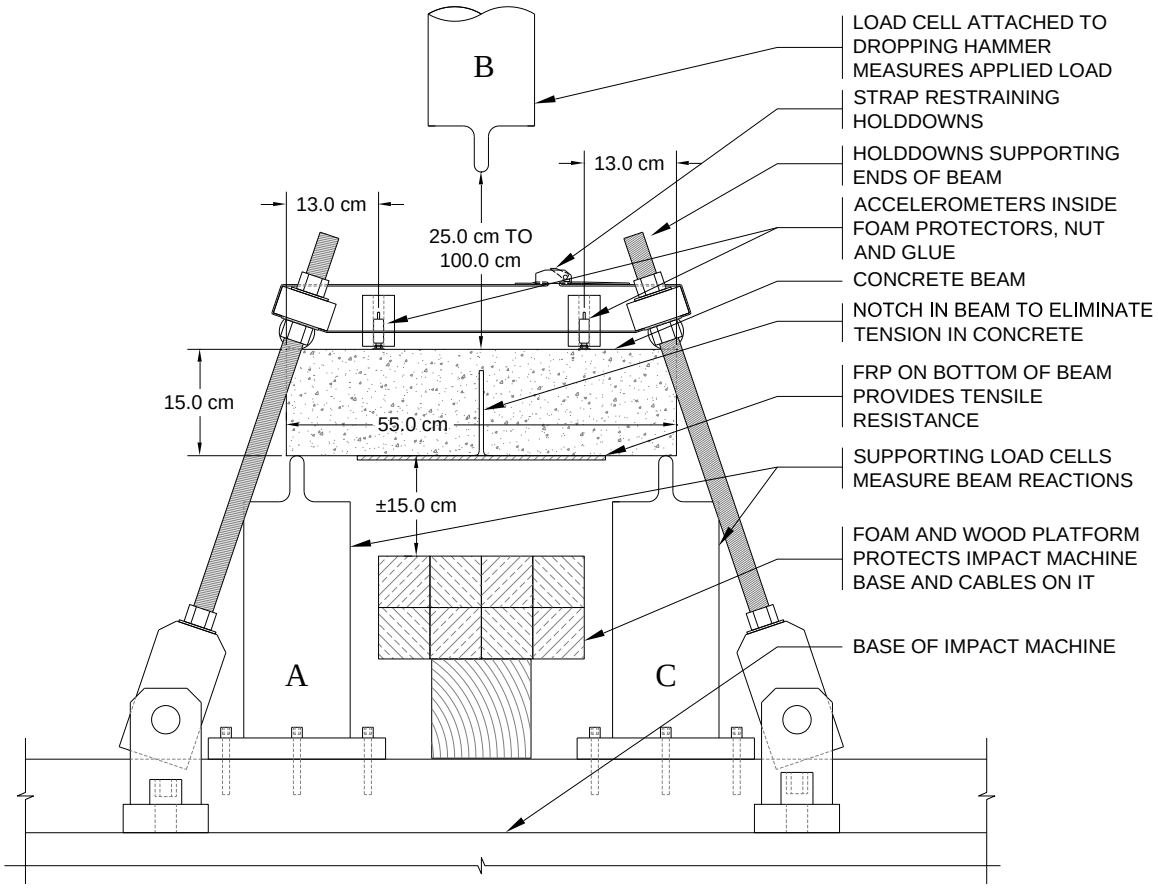

Figure 7.12. *Final testing setup (cables not shown for clarity).*

7.4.3 Data acquisition system

A National Instruments VI Logger, a flexible tool specifically designed for data logging applications, was used in this research (Figure 7.13). VI Logger is a stand-alone, configuration-based data logging software. Using this software, data from up to eight channels were recorded with a frequency of 100 kHz (i.e., up to 800,000 data points per second). A sample of this software user interface is shown in Figure 7.14.

Figure 7.13. *Data acquisition system.*

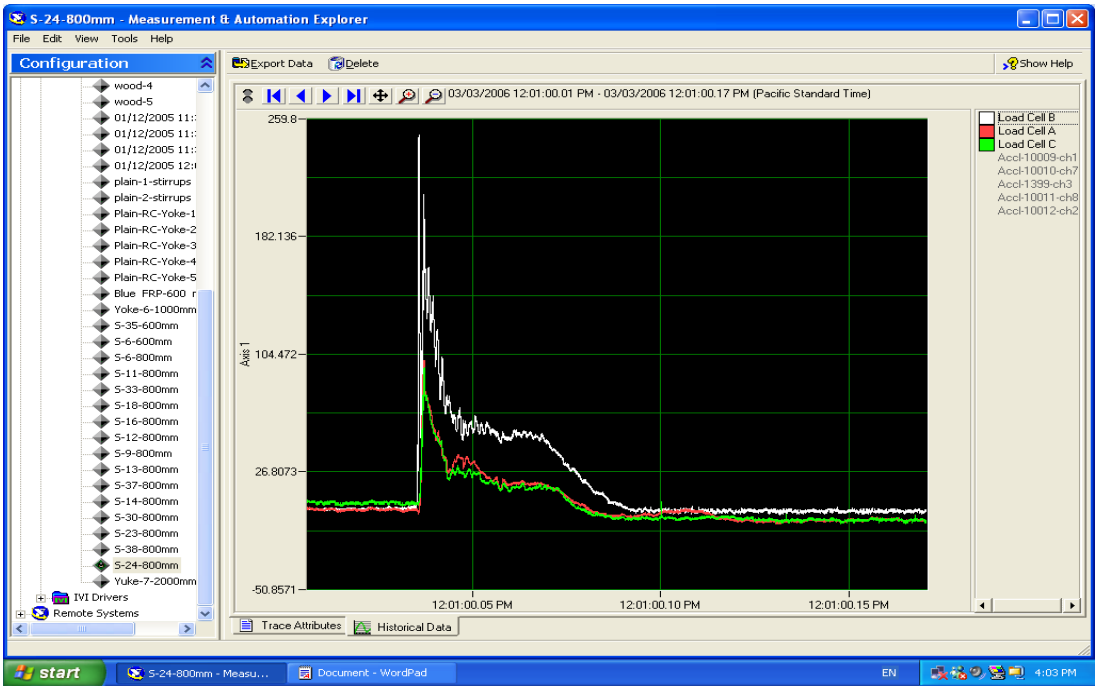

Figure 7.14. *User interface of VI Logger software.*

7.5. Preliminary tests

Once the test setup was finalized (as in Figure 7.12), a handful of preliminary tests were conducted on specimens having a pressure washed surface preparation. These initial tests were performed to allow the deficiencies in the testing procedure to be identified and were imperative for the development of a more consistent testing procedure. Data from impact tests conducted on these first few specimens was captured from load cells at the beam supports and accelerometers near mid-span of the beams, as well as strain gauges on the final test specimen. Using the measured accelerations, displacements of the beam at mid-span can be calculated (as explained in chapter 8).

7.5.1 Results for preliminary specimens

Maximum loads and shearing stresses in the bond have been computed, force displacement curves have been developed, and an attempt has been made to find some measure of consistency in the testing results in the preliminary tests. The results are summarized in Table 7.1. It should again be noted that in these tests, the test setup as in Figure 7.12 was already developed. Accelerometers at the mid-span were added to the setup for displacement measurement.

Table 7.1. *Summary of results for preliminary tests*

Specimen	Failure mode	Drop height (m)	Strain gauges used?	Comments
B15S3W	Debonding	0.25	No	
B21S3W	Rupture*	0.25	No	Load cell cable cut due to accidental impact of the half-beam
B11S2W	Debonding	0.25	No	No data from laser gauge
B14S2W	Debonding	1.00	No	
B20S4W	Debonding	1.00	No	No data from laser gauge
B10S2W	Debonding	0.25	Yes	

*In the failure mode, the FRP reaches its ultimate tensile capacity before it is debonded from concrete.

In all of the data collected there was a time lag between the initial readings registered from the accelerometers and the first readings registered from the load cells.

This time lag is presumably due to the wave speed or transfer rate of the load through the materials to the supports. The lag time ranged from 0.001 to 0.002 s. This lag time was accounted for in developing the force displacement curves for each group of data by matching the start point of load vs. time response with displacement vs. time response. Figure 7.15 shows the load data, which was collected from impact testing conducted on specimen B14S2W (This graph is directly from the data acquisition machine.) It should be noted that the initial impact is responsible for debonding of FRP from concrete (small peaks at the beginning of load vs. time spectrum). The second peak is due to post-impact phenomena, from the second impact of the hammer on to the broken specimen that is restrained by the lower protection platform.

Using the relationship between acceleration and displacement, beam section deflections can be calculated using the integration method as will be explained in Sections 8.4 and 8.5. The calculated deflections can then be plotted against the loads determined from the load cell readings.

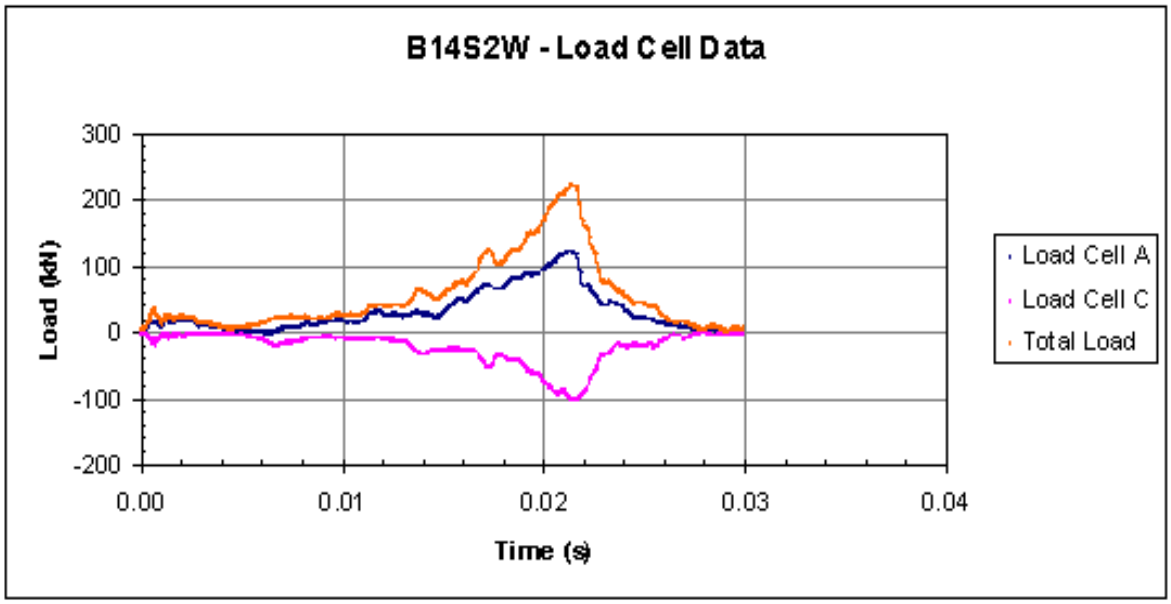

Figure 7.15. *B14S2W – Load cell data directly from DaisyLab software. The curves show total load, load cell A, and load cell C, respectively, from top to bottom.*

7.5.2. Methods of measuring displacement

As an alternative to the accelerometer, using a laser gauge to measure displacement was considered. Figures 7.16 and 7.17 show the readings from an accelerometer and laser gauge used for the same test. The challenge with use of the laser gauge was the high rate of failure, as the laser gauge failed to report any data in three tests of the six preliminary tests. Therefore, the accelerometer and integration method was chosen as the method to calculate displacements. The analysis is discussed in detail in Chapter 8.

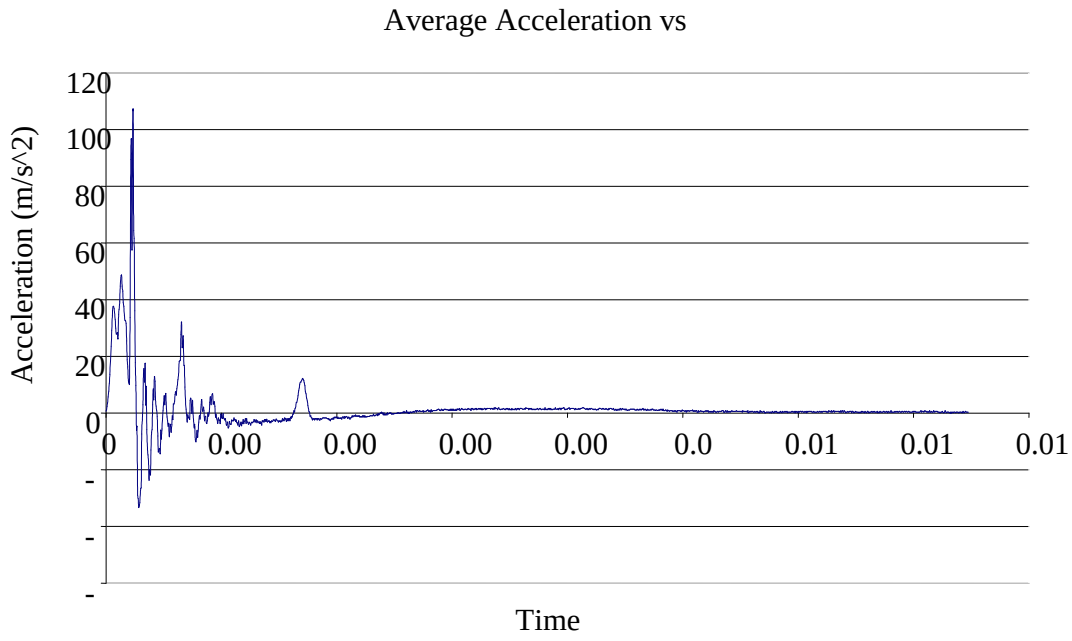

***Figure 7.16**. Average acceleration vs. time for specimen B14S2W.*

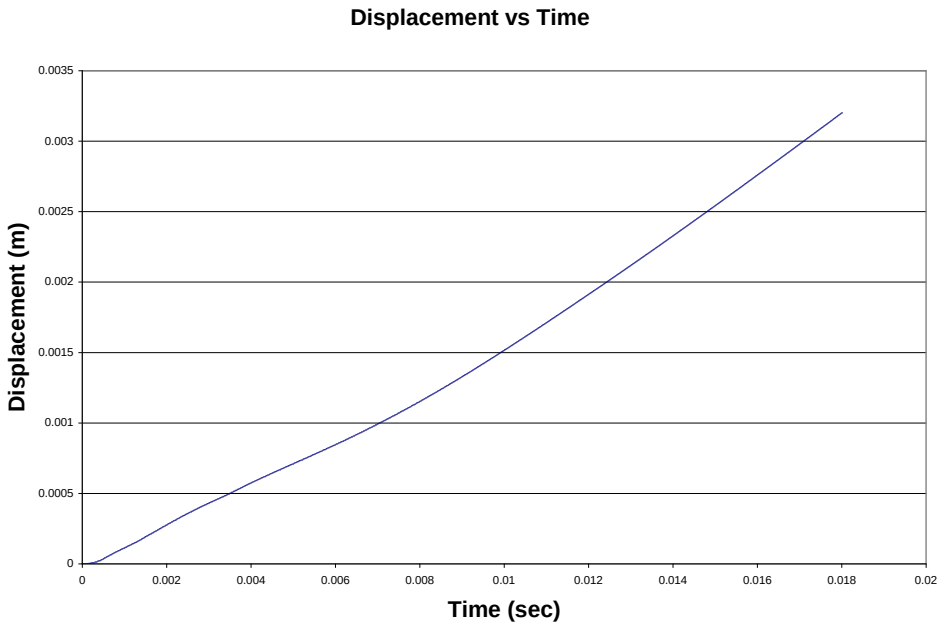

Figure 7.17. *Displacement of the beam centre vs. time as measured by a laser gauge.*

7.5.3. Lessons learned from preliminary tests

1. The initial peak load is responsible for the debonding of FRP–concrete. The second higher peak is due to post impact phenomena.
2. The thickness of FRP applied was changed from 2 to 4 mm to ensure that the beams fail under debonding mode.
3. Accelerometers are more reliable than a laser gauge to measure the displacement under impact.
4. All the load-cell and accelerometer cables should be protected using foam blocks to prevent cable cuts and loss of load and/or acceleration data.

CHAPTER 8
DYNAMIC TESTING

8.1 Chapter objectives

The goal of this chapter was to investigate the performance of the bond between spray-on fibre reinforced polymer (FRP) and concrete under impact loading. FRP is generally used in the re-strengthening, retrofitting, and repairing of damaged concrete structures. It is known that FRP can increase the ductility, strength, and stiffness of concrete structures when they are subjected to impact loads, but the current understanding of the bond behavior under these loading conditions is limited.

Through the use of structural health monitoring (monitoring the structure using gauges) combined with destructive tests, insight will be gained into the bond between the concrete and the spray-on FRP.

8.2 Testing program, variables studied

8.2.1 Mechanical fasteners

In addition to three methods of surface preparation and different types of FRP, use of mechanical fasteners to enhance the bond was studied. After the FRP strips had been applied, mechanical fasteners were used to further attach them to the concrete. A Hilti gun was used to shoot 1-inch nails (the mechanical fasteners used here) into the concrete through the bonded FRP in the pattern shown in Figure 8.1. A powder actuated

fastening tool was used to shoot stainless steel Hilti nails on to the sides of the reinforced concrete beam. There were eight Hilti X-AL-H 32P8 nails with a diameter of 4.5 mm and a length of 32 mm on each side of the FRP strip, spaced approximately 50 mm apart..

As the nails were discharged they acted in an unpredictable manner; some would be shot right through the FRP and others would break the FRP–beam bond. These samples were discarded.

Figure 8.1. *Mechanical fasteners.*

8.2.2 Testing program

Table 8.1 shows the number and characteristics of the specimens used in these series of tests to look at the response of the bond under impact loading. A new method of strengthening, using mechanical fasteners, was also studied.

Table 8.1. *Testing program*

Test set	Number of beams	Primary goal	Parameters studied
Preliminary tests	6 (1 with strain gauge)	Setup and data check	N/A
Specimens without strain gauges	27	Influence of surface preparation, mechanical fastener and type of materials on the strength and ductility of FRP–concrete bond	Type of FRP surface preparation; use of mechanical fasteners
Specimens monitored with strain gauges	30	Strain rate sensitivity of FRP–concrete bond strength	Loading rate; drop height; strain rate

8.3. Impact loading

An instrumented drop-weight impact machine, as explained in Section 7.2, was used in the course of this research program. Potential energy stored in the hammer at height h is transferred to the reinforced concrete beam by dropping it freely. The guide rails (shown in Figure 6.2) were cleaned to make sure that the hammer would drop freely. Assuming negligible friction, at the instant of impact the hammer develops a velocity V_h.

$$V_h = \sqrt{2gh} \tag{8.1}$$

where

V_h = velocity of the falling hammer at the instance of impact (m/s)

g = acceleration due to gravity (m/s^2) = 9.81 m/s^2

h = drop height (m)

Equation 8.1 can be rewritten as:

$$V_h = 4.43\sqrt{h} \tag{8.2}$$

For all impact tests using the drop-weight machine, PCB Piezotronics™ accelerometers were employed (see Figure 8.2). These accelerometers were screwed into mounts which were glued to the specimens prior to testing. Piezoelectric accelerometers rely on the piezoelectric effect of quartz or ceramic crystals to generate an electrical signal that is proportional to applied acceleration. The piezoelectric effect produces an accumulation of charged particles on the crystal. This charge is proportional to the applied force or stress. In an accelerometer the stress on the crystals occurs as a result of the seismic mass (shown as (m) in Figure 8.3) imposing a force on the crystal. The structure shown in Figure 8.3 obeys Newton's second law of motion:

$$F = ma \tag{8.3}$$

where

F = applied force (N)

m = mass (kg)

a = acceleration (m/s^2)

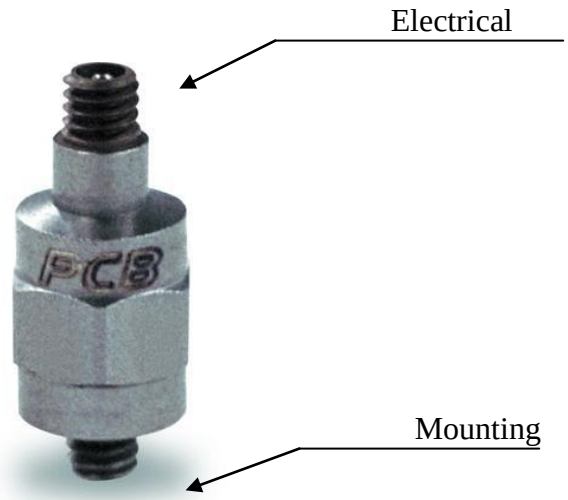

Figure 8.2. *PCB Piezotronics™ accelerometer.*

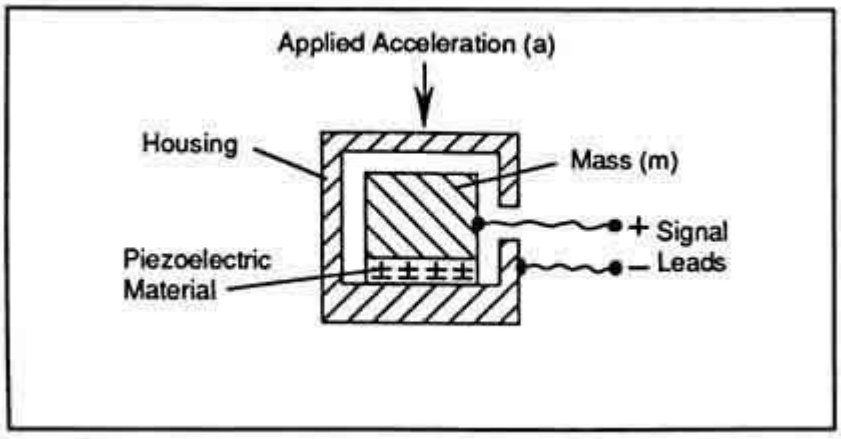

Figure 8.3. *Structure of a piezoelectric accelerometer.*

Therefore, the total amount of accumulated charge is proportional to the applied force, and the applied force is proportional to acceleration. Electrodes collect and wires transmit the charge to a signal conditioner that may be remote or built into the accelerometer. Once the charge is conditioned by signal conditioning electronics, the signal is available for display, recording, analysis, or control. Properties of the accelerometer used in this research project are tabulated in Table 8.2.

Table 8.2. *Properties of PCB Piezotronics™ accelerometer*

Property	Value	Unit
Measurement range	±4900	m/s^2
Sensitivity (±10%)	1.02	$mV/(m/s^2)$
Frequency range (±5%)	2.0 to 10 000	Hz
Resonant frequency	≥60	kHz
Non-linearity	≤1	%
Overload limit	±98 100	m/s^2
Sensing element	Quartz	—
Housing material	Titanium	—
Weight	1.7	Gr
Electrical connector	5-44 Coaxial	—
Mounting thread	5-40 Male	—
Mounting torque	90 to 135	N·cm

The velocity and displacement histories at the location of accelerometers were obtained by using the following equations to integrate the acceleration history with respect to time:

$$\dot{u}_0(t) = \int \ddot{u}_0(t)\,dt \tag{8.4}$$

$$u_0(t) = \int \dot{u}_0(t)\,dt \tag{8.5}$$

where

$\ddot{u}_0(t)$ = acceleration at the location of the accelerometer

$\dot{u}_0(t)$ = velocity at the location of the accelerometer

$u_0(t)$ = displacement at the location of the accelerometer

Accelerations at different locations along the beam were recorded with a frequency of 100 kHz using National Instruments™ VI Logger software. Locations of the accelerometers are shown in Figure 8.4.

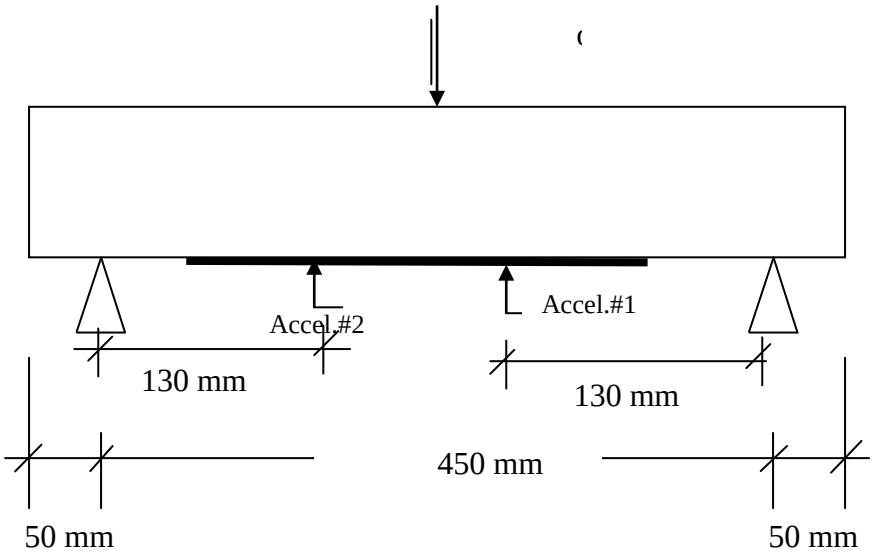

Figure 8.4. *Location of the accelerometers in impact loading.*

During the impact, National Instruments™ VI Logger software was used to record striking load at the tup load cell as well as reaction forces at the support load cells with the same frequency of 100 kHz.

The contact load between the specimen and the hammer is not the true bending load on the beam because of the inertia reaction of the beam. A part of the tup load is used to accelerate the beam from its rest position. Since structural engineers have been trained to think in terms of equilibrium of forces, they use D'Alembert's principle of dynamic equilibrium to write equilibrium equations in dynamic load conditions. This principle is based on the notion of a fictitious inertia force. This force is equal to the product of mass times its acceleration and acts in a direction opposite to the acceleration. D'Alembert's principle of dynamic equilibrium states that, with inertia forces included, a system is in equilibrium at each time instant. As a result, a free-body diagram of a moving mass can be drawn, and principles of statics can be used to develop the equation of motion. Thus, one can conclude that in order to obtain the actual bending load on the specimen the inertia load must be subtracted from the observed tup load. It is also important to note that the tup load throughout this study was taken as a point load acting at the mid-span of the beam, whereas the inertia load of the beam is a body force

distributed throughout the body of the beam. This distributed body force can be replaced by an equivalent inertia load, $P_i(t)$, which can then be subtracted from the tup load, $P_t(t)$, to obtain a true bending load, $P_b(t)$, which acts at the mid-span. Therefore, at any time, *t*, the following equation can be used to obtain the true bending load that the beam is experiencing [3.3]:

$$P_b(t) = P_t(t) - P_i(t) \tag{8.6}$$

where

$P_b(t)$ = true bending load at the mid-span of the beam at time t

$P_t(t)$ = tup load at time t

$P_i(t)$ = a point load representing inertia load at the mid-span of the beam at time t equivalent to the distributed inertia load

According to Banthia [7.1], the inertia load (and as a result the true bending load) can be calculated using equations 8.7 and 8.8.

When the displacements between the supports are assumed to be linear

$$P_i(t) = \rho A \ddot{u}_0(t)\left[\frac{l}{3} + \frac{8l_{oh}^3}{3l^2}\right] \tag{8.7}$$

When the displacements between the supports are assumed to be sinusoidal while the displacements on the overhanging portion of the beam are assumed to be linear

$$P_i(t) = \rho A \ddot{u}_0(t)\left[\frac{l}{2} + \frac{2\pi^2 l_{oh}^3}{3l^2}\right] \tag{8.8}$$

In both equations 8.7. and 8.8

ρ = mass density of the beam material (kg/m^3)

A = cross-sectional area of the beam (m^2)

$\ddot{u}_0(t)$ = acceleration at the centre of the beam at time *t* (m/s^2)

l = span of the beam between two supports (m)

l_{oh} = length of the overhanging portion of the beam (m)

In this research program, support anvils in addition to the tup were instrumented in order to obtain the valid and true bending load directly from the experiment at any time *t*. Therefore, true bending load $P_b(t)$ at time *t*, which acts at the mid-span, can also be obtained by adding the reaction forces at the support anvils at time *t*:

$$P_b(t) = R_A(t) + R_C(t) \tag{8.9}$$

where

$P_b(t)$ = true bending load at the mid-span of the beam at time t

$R_A(t)$ = reaction load at support A at time t

$R_C(t)$ = reaction load at support C at time t

as shown in Figure 8.5.

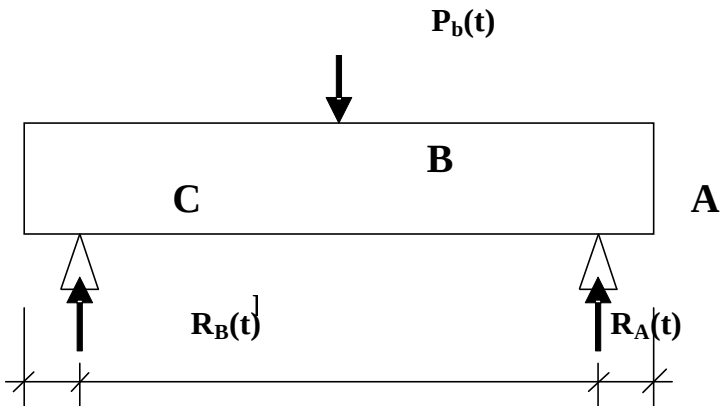

Figure 8.5. *True bending load and reaction forces at time t.*

8.4 Results

8.4.1 Understanding the load response

Figure 8.6 shows a typical load response for a water jetting treated specimen strengthened with sprayed FRP. The following should be noted.

1. The first peak for load cell B represents the first impact. This load is responsible for the debonding of the specimen. Some post-impact peak loads are observed for load B. The beam after debonding hits the base and the

hammer reaches the beam for the second time. These phenomena are responsible for the post-impact behavior.

2. Load cells A and C respond with a time lag. This is due to the impact wave travelling time through concrete. To calculate maximum A+C load (which is the true bending load), the start point of the load behaviors are matched. Load cells A and C response lags that of load cell B response due to the traveling time of the impact wave through concrete.

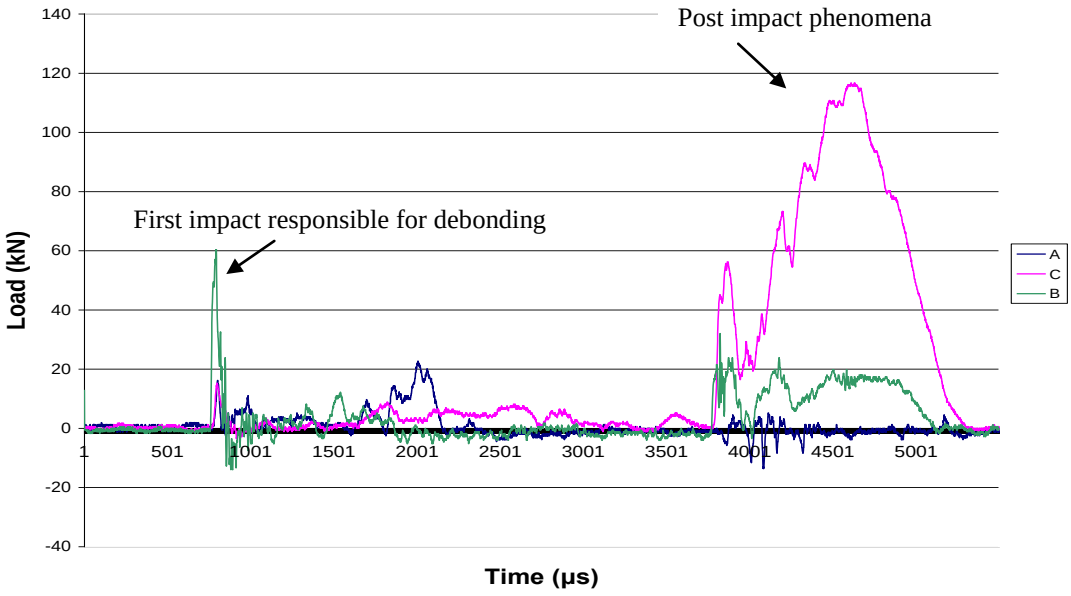

Figure 8.6. *Support loads vs. time for specimen B6S10W.*

8.4.2 Understanding the impact phenomena

As an example, the velocity vs. time calculated by equation 8.2 for beam B6S10W is shown in Figure 8.7. Interestingly, the velocity of the hammer at the instant of impact (3.13 m/s, from equation 8.2, for a drop height of 500 mm) and the maximum velocity of the beam (which occurred 0.001 s after the impact, as show in Figure 7.5) are very similar. This, at least to some extent, can explain why the tup load at the beginning of impact decreased almost to zero after a very rapid increase to a maximum value (see Figure 8.6). In other words, the beam was accelerated by the hammer and reached its maximum velocity while at the same time (i.e., t = 0.001 s) the tup load (load cell B) decreased to zero as the beam sped away from the hammer and lost contact. The

hammer was then back in contact with the beam (in the case of B6S10W, after about 0.0005 s) and the load rose again. Some time after impact the velocity of both hammer and beam decreased to zero.

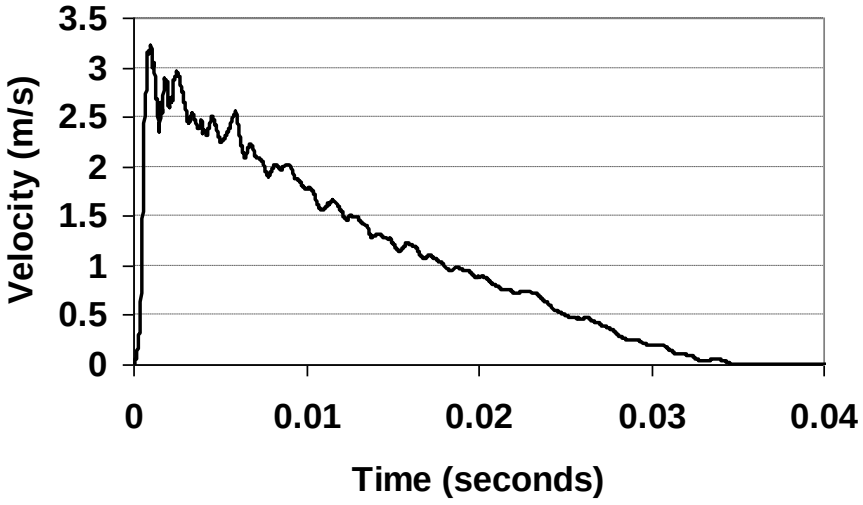

Figure 8.7. *Velocity vs. time at the mid-span.*

8.4.3 Specimens without strain gauges

Once the preliminary tests were studied, the testing setup was modified to address the issues discussed in the previous chapter. Samples without strain gauges were tested in the hopes of comparing the strength and toughness values of the bond between FRP and concrete under impact loading. The influences of surface treatment, mechanical fasteners, and FRP type (sprayed vs. wrap) were studied. Table 8.3 shows the test plan. Tables 8.4 and 8.5 show the maximum load and fracture energy for each specimen. The fracture energy values are calculated by measuring the area under the load displacement curve.

Table 8.3. Specimen chart for samples without strain gauges

Sample name	Surface preparation	Retrofit type	Mechanical fastener used	Drop height (mm)
B15S1N	None	Sprayed FRP	No	250
B15S2N	None	Sprayed FRP	No	250
B15S3N	None	Sprayed FRP	No	250
B12S1W	Water jetting	Sprayed FRP	No	250
B10S4W	Water jetting	Sprayed FRP	No	250
B17S2W	Water jetting	Sprayed FRP	No	250
B13S2S	Sandblasting	Sprayed FRP	No	250
B13S3S	Sandblasting	Sprayed FRP	No	250
B16S4S	Sandblasting	Sprayed FRP	No	250
B11S4J	Jackhammering	Sprayed FRP	No	250
B13S4J	Jackhammering	Sprayed FRP	No	250
B15S2J	Jackhammering	Sprayed FRP	No	250
B10S5M	Water jetting	Sprayed FRP	Yes	250
B10S6M	Water jetting	Sprayed FRP	Yes	250
B18S1M	Water jetting	Sprayed FRP	Yes	250
B31N2WR	None	FRP Wrap	No	250
B31N3WR	None	FRP Wrap	No	250
B31N4WR	None	FRP Wrap	No	250
B30W1WR	Water jetting	FRP Wrap	No	250
B30W2WR	Water jetting	FRP Wrap	No	250
B30W3WR	Water jetting	FRP Wrap	No	250
B30S2WRA	Sandblasting	FRP Wrap	No	250
B30S3WRA	Sandblasting	FRP Wrap	No	250
B30S4WRA	Sandblasting	FRP Wrap	No	250
B30J2WRA	Jackhammering	FRP Wrap	No	250
B30J3WRA	Jackhammering	FRP Wrap	No	250
B30S1M	Water jetting	FRP Wrap	Yes	250
B30S3M	Water jetting	FRP Wrap	Yes	250

Table 8.4. Summary of the test results on specimens retrofitted with sprayed FRP

Sample name	Surface preparation	Failure mode	Max. load (A+C) (kN)	Fracture energy (J)*
B15S1N	N	Debonding	35.3	1.589
B15S2N	N	Debonding	25.5	1.152
B15S3N	N	Debonding	32.8	1.476
Average			31.2	1.41
B12S1	WJ	Debonding	39.8	1.684
B10S4	WJ	Debonding	36.8	1.546
B17S2	WJ	Debonding	35.0	1.483
Average			47.6	1.57
B13S2S	SB	Debonding	35.2	1.408
B13S3S	SB	Rupture	68.4	2.736
B16S4S	SB	Debonding	51.2	2.048
Average			67.5	2.06
B11S4J	JH	Debonding	23.2	0.928
B13S4J	JH	Rupture	52.1	1.129
B15S2J	JH	Debonding	22.8	0.912
Average			26.9	0.99
B10S5	WJ(MF)	Rupture	16.2	0.648
B10S6	WJ(MF)	Rupture	30.6	0.865
B18S1	WJ(MF)	Rupture	17.0	0.680
Average			21.3	0.731

* Area under the load displacement curve

Sandblasting has resulted in the highest load bearing capacities in the beams among all types of surface preparations. Jackhammering has reduced the load bearing capacity. This can be due to the micro-cracks developed in the concrete during the jackhammering procedure. This was not seen in the specimens tested under quasi-static loading that were prepared with the same procedure. Sprayed FRP specimens showed a higher load-bearing capacity compared with FRP wrapped specimens. Figure 8.8 summarizes the average load bearing capacities of the specimens. It should be noted that the micro-cracks had a more severe negative influence in the specimens strengthened

using sprayed FRP compared with wrapped FRP. One could conclude that the bond in the wrapping system is less influenced by the surface micro-cracked, or the micro-cracks cannot join to form an interfacial crack as quickly in the wrapped system.

Table 8.5. *Summary of the test results on specimens retrofitted with FRP wrap*

Sample name	Surface preparation	Failure mode	Max. load (A+C) (kN)	Fracture energy (J)
B31N2WRAP	N	Debonding	29.5	1.35
B31N3WRAP	N	Debonding	31.2	1.162
B31N4WRAP	N	Debonding	24.9	0.982
Average			28.5	1.16
B30W1WRAP	WJ	Debonding	33.5	1.410
B30W2WRAP	WJ	Rupture (Partial debonding)	28.8	1.350
B30W3WRAP	WJ	Debonding	36.2	1.408
Average			32.8	1.39
B30S2WRAP	SB	Rupture	52.5	1.890
B30S3WRAP	SB	Debonding	49.8	2.09
B30S4WRAP	SB	Debonding	45.8	1.913
Average			19.4	1.96
B30J2WRAP	JH	Rupture	28.1	0.864
B30J3WRAP	JH	Rupture	53.8	0.925
Average			40.9	0.89
B30S1M	WJ(MF)	Rupture	37.8	1.198
B30S3M	WJ(MF)	Rupture	57.0	0.869
Average			47.4	1.03

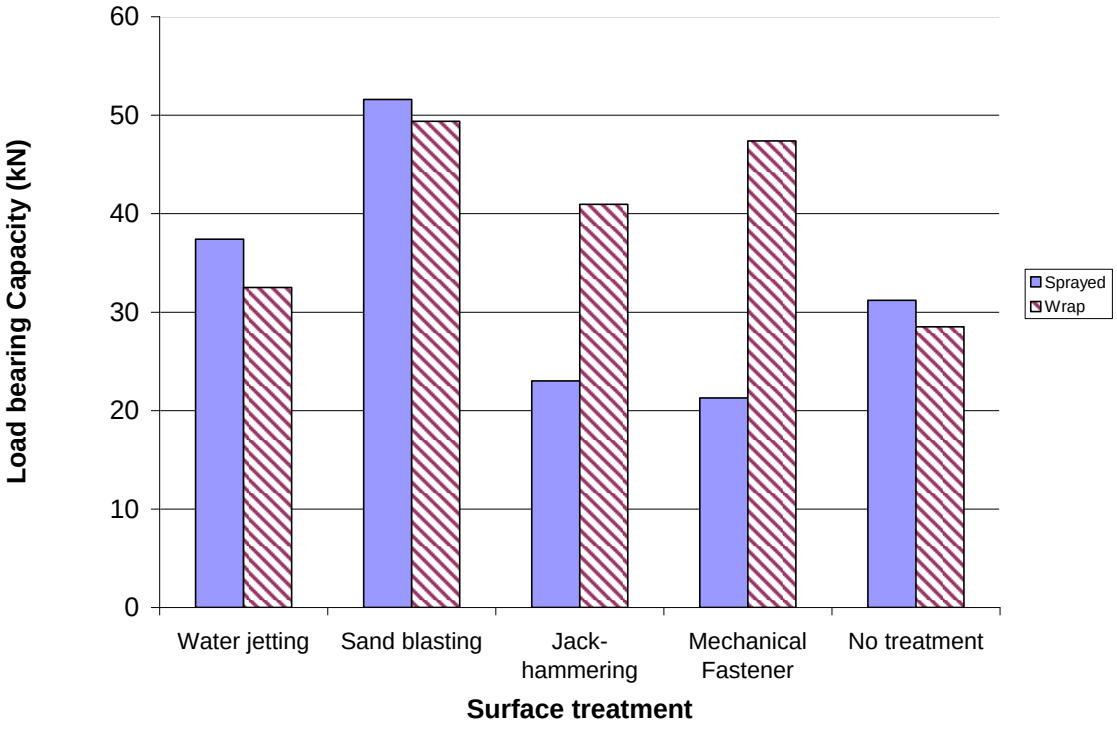

Figure 8.8. *Load bearing capacities of FRP strengthened specimens with different surface treatment and FRP used.*

Figure 8.9 compares the ductility of specimens strengthened with different FRP systems with concrete surfaces treated with water jetting, sandblasting, and jackhammering. All specimens with mechanical fasteners failed with FRP rupture; therefore, the area calculated under the curve was not an indication of bond energy.

Of all surface treatments, sandblasting has proved to have the highest enhancement effect on the ductility of the bond. Water jetting is the second best method. Mechanical fasteners reduced the load bearing capacity in sprayed beams; however, they helped to increase the load bearing capacity in wrapped specimens. This can be explained by the brittleness of sprayed FRP. It could also be observed that the Hilti nails had pre-fractured the sprayed FRP.

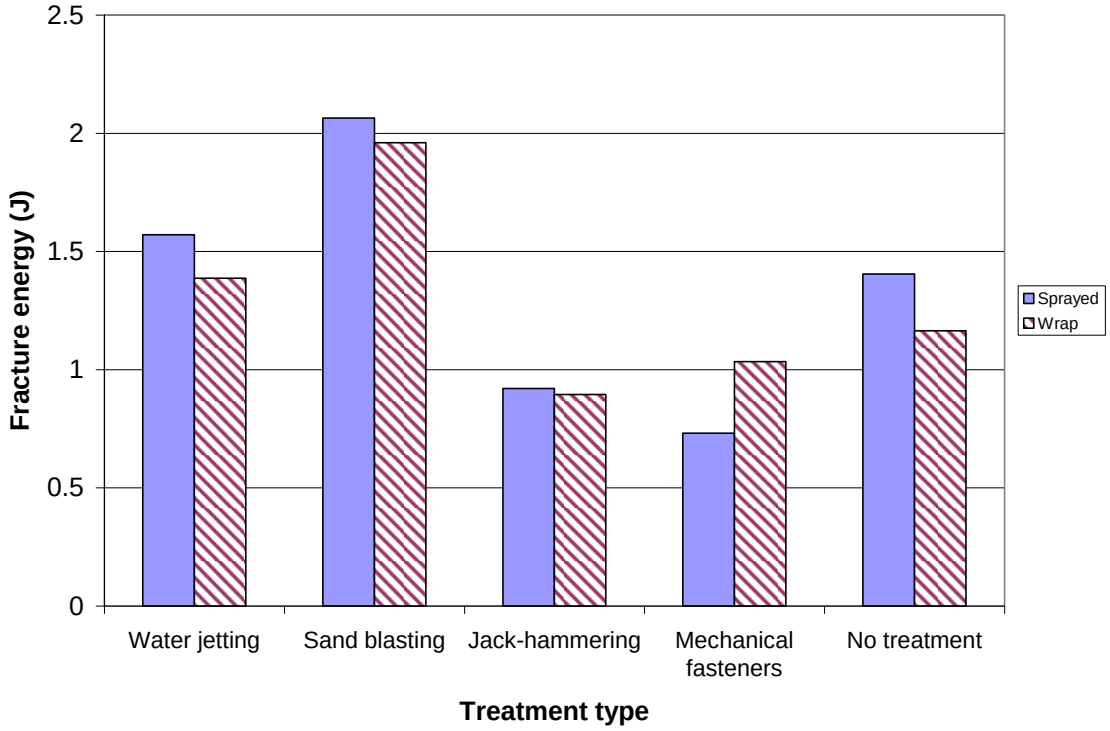

Figure 8.9. *Fracture energy of FRP strengthened specimens with different surface treatment and FRP used.*

Figures 8.10 and 8.11 show a visual comparison between the bond strength in two identical specimens with different surface preparations under impact loading. The water jet treatment leads into debonding of the FRP and concrete; however, the sandblasted surface increased the bond strength and led into the rupture of FRP. Figure 8.12 compares the load displacement behavior of a FRP strengthened specimen treated with the same surface preparation. It should be noted that higher strain rate has increased the maximum load bearing capacity and decreased the ultimate displacement. One could also conclude that due to higher shear stress, the bond length required to see complete unzipping under impact loading is higher than that of quasi-static loading.

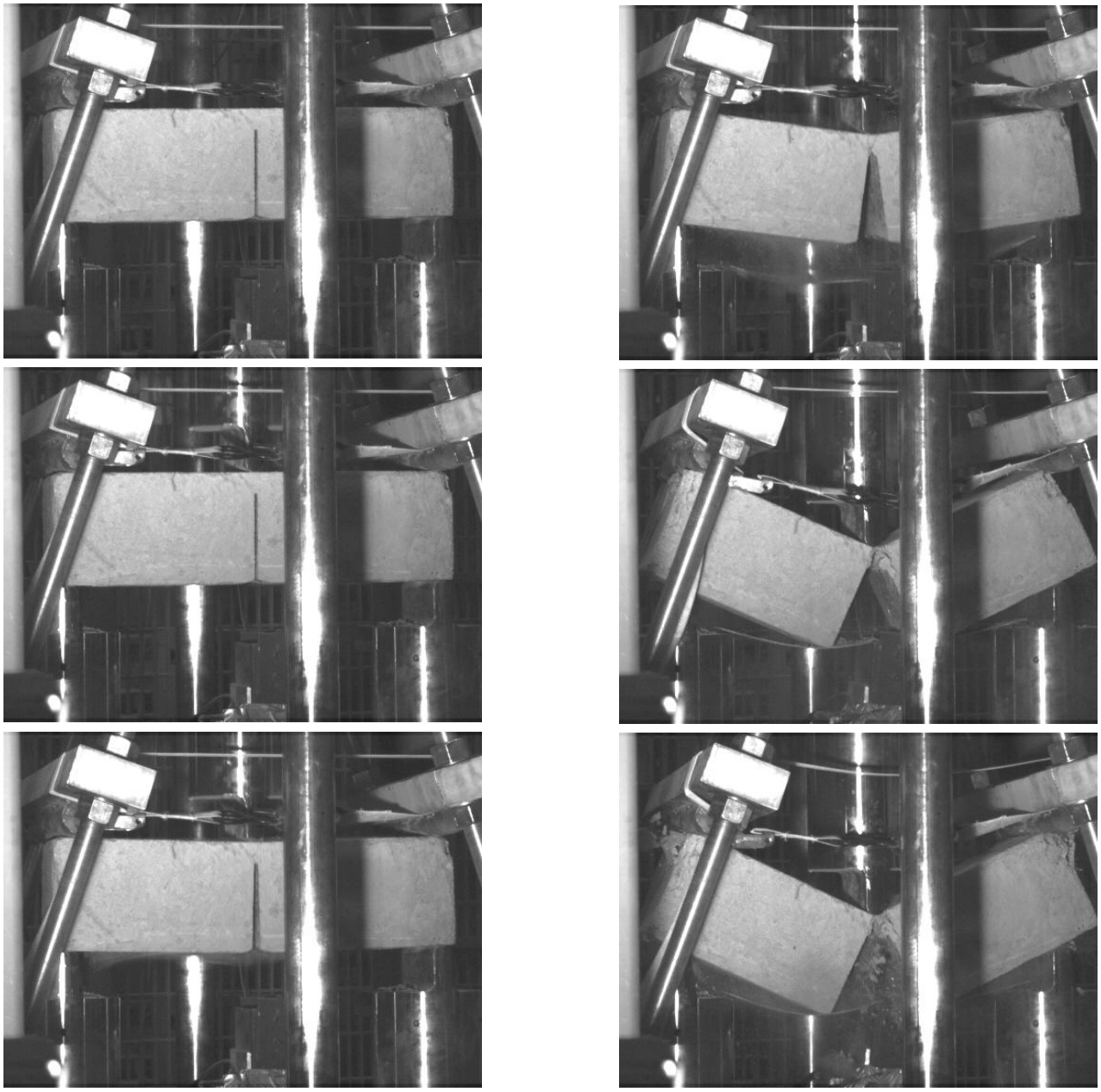

Figure 8.10. *Sample B10S4-W-250-D (water jet surface treatment).*

The FRP failed in all the specimens in which mechanical fasteners were used. The fracturing of the concrete surface and FRP using the powder actuated fastening tool, as observed during the nail shooting, can explain, at least to some extent, why this technique was not successful.

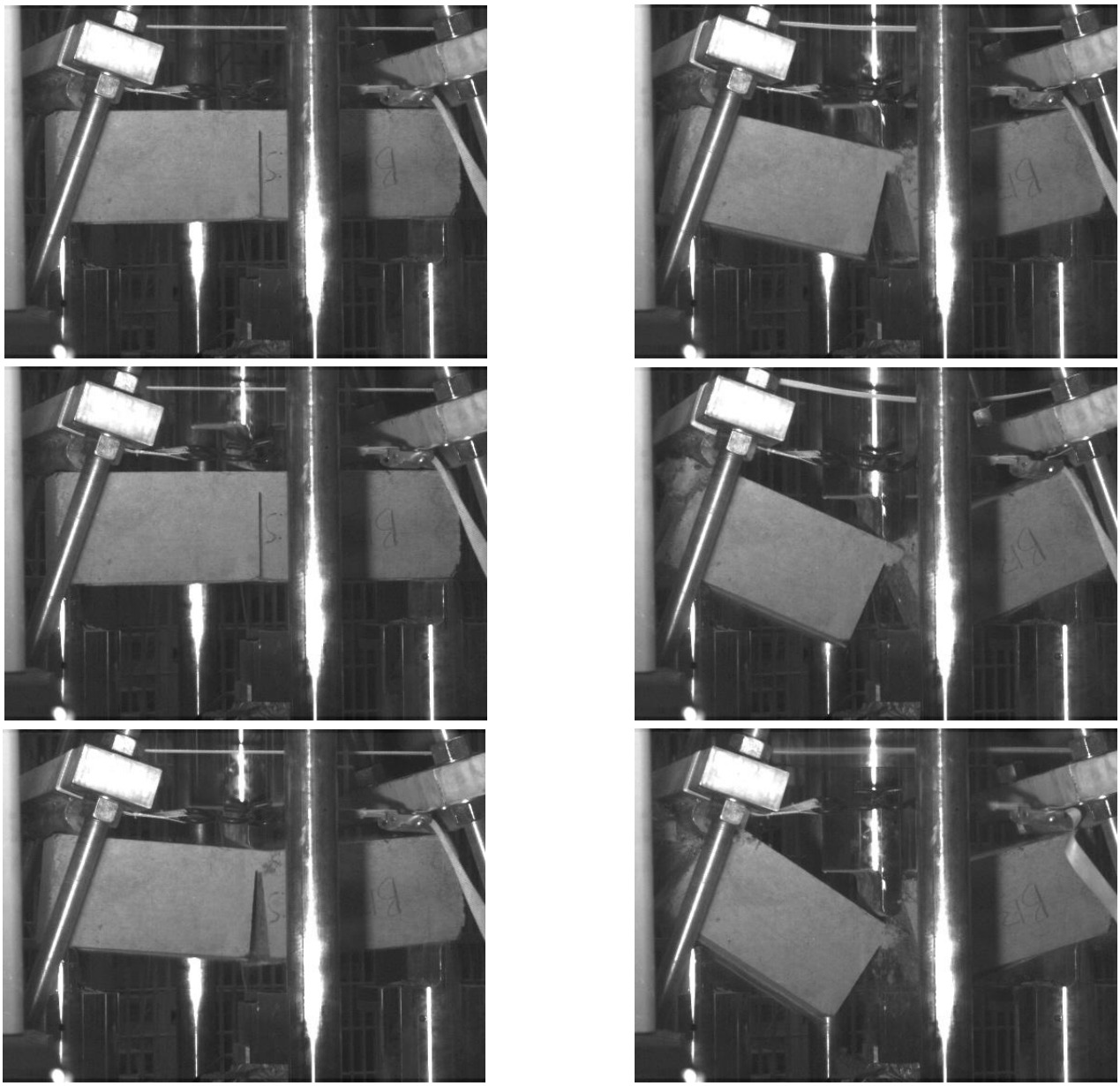

Figure 8.11. *Sample B13S4-S-250-F (sand-blasted).*

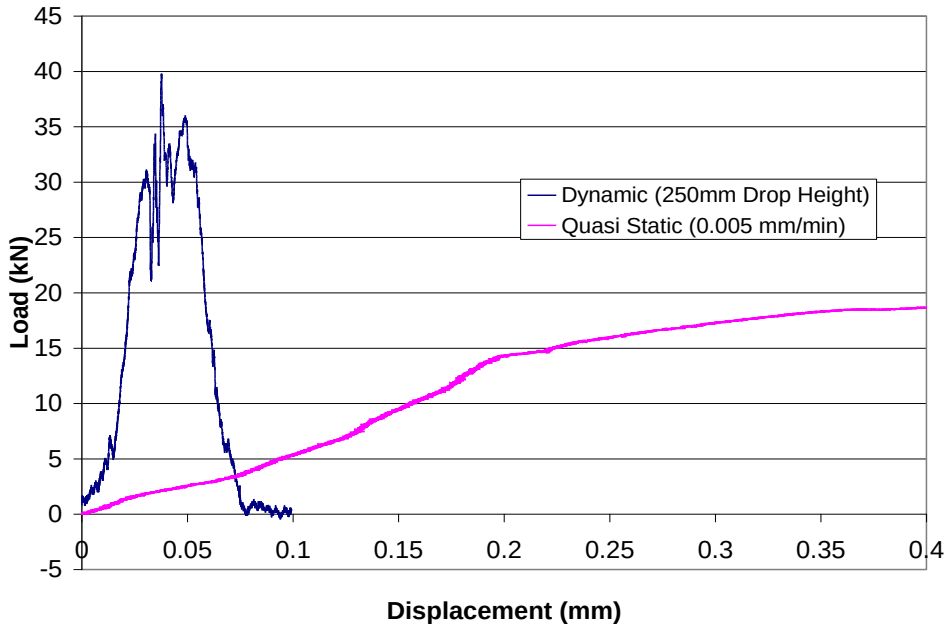

Figure 8.12. Load vs. displacement behavior under dynamic loading behavior vs. quasi-static behavior

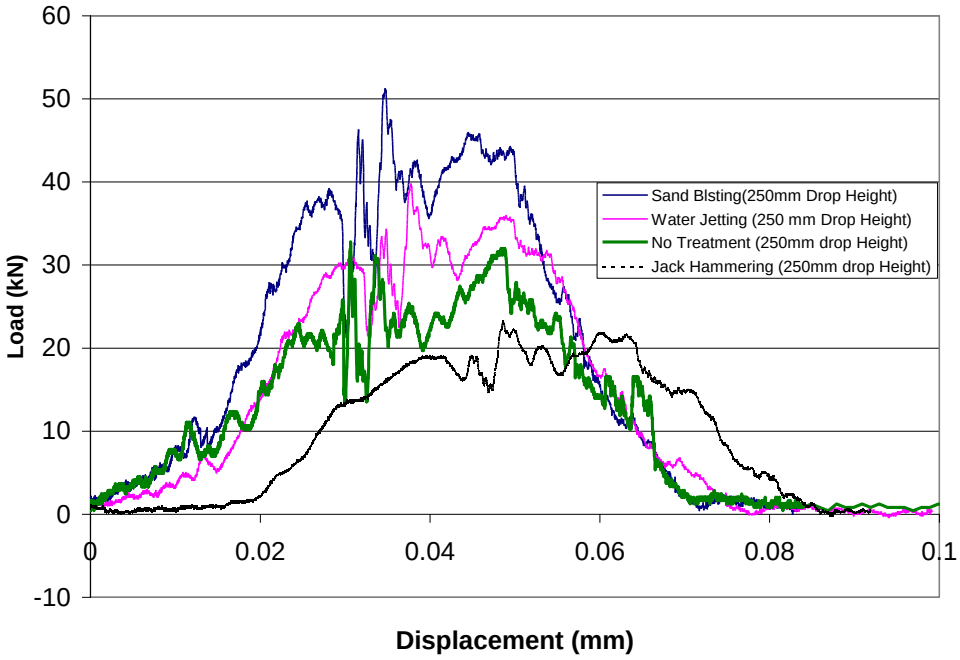

Figure 8.13. *Load vs. displacement for specimens with different surface treatments.*

It is worth noting that the specimens strengthened using FRP with higher drop height (higher strain rate) have higher impact failure load. The effect of strain rate will be discussed later in this chapter. Figure 8.13 compares the load displacement behavior for three specimens treated with jackhammering, water jetting, and sandblasting and a specimen with no treatment. It is observed that sandblasting and water jetting increase the load bearing capacity and decrease the maximum displacement; however, they increase the overall ductility. Jackhammering reduces the ductility of the specimen.

8.4.4 Specimens with strain gauges

Specimens were tested under the same testing conditions and were monitored using strain gauges to study the stress profile of the bond and debonding mechanism under impact loading. The same strain gauge plan as in quasi-static tests was used. The procedure is explained here for one sample (B6S10W), and final data for other samples is presented in the tables.

Figure 8.14 shows the load values as a function of time. Strain gauge readings throughout the test are shown in Figure 8.15. To better understand the strain gauge values, the readings just before and after debonding are magnified in Figure 8.16.

Table 8.6. *Specimen chart for samples with strain gauges*

Sample Name	Surface preparation	Retrofit type	Mechanical fastener used	Drop height (mm)
B30S1N	None	Sprayed FRP	No	250
B30S2N	None	Sprayed FRP	No	250
B30S3N	None	Sprayed FRP	No	250
B32S2N	None	Sprayed FRP	No	1000
B32S3N	None	Sprayed FRP	No	1000
B32S4N	None	Sprayed FRP	No	1000
B6S10W	Water jetting	Sprayed FRP	No	250
B10S2W	Water jetting	Sprayed FRP	No	250
B19S4W	Water jetting	Sprayed FRP	No	250
B10S1W	Water jetting	Sprayed FRP	No	500
B10S3W	Water jetting	Sprayed FRP	No	500
B11S2W	Water jetting	Sprayed FRP	No	500
B11S3W	Water jetting	Sprayed FRP	No	750
B15S3W	Water jetting	Sprayed FRP	No	750
B15S4W	Water jetting	Sprayed FRP	No	1000
B17S4W	Water jetting	Sprayed FRP	No	1000
B17S2W	Water jetting	Sprayed FRP	No	1000
B18S2S	Sandblasting	Sprayed FRP	No	250
B18S3S	Sandblasting	Sprayed FRP	No	250
B18S4S	Sandblasting	Sprayed FRP	No	250
B32S1S	Sandblasting	Sprayed FRP	No	1000
B32S2S	Sandblasting	Sprayed FRP	No	1000
B32S3S	Sandblasting	Sprayed FRP	No	1000
B11S1J	Jackhammering	Sprayed FRP	No	250
B21S5J	Jackhammering	Sprayed FRP	No	250
B13S5J	Jackhammering	Sprayed FRP	No	250
B31S1J	Jackhammering	Sprayed FRP	No	1000
B31S2J	Jackhammering	Sprayed FRP	No	1000
B31S3J	Jackhammering	Sprayed FRP	No	1000

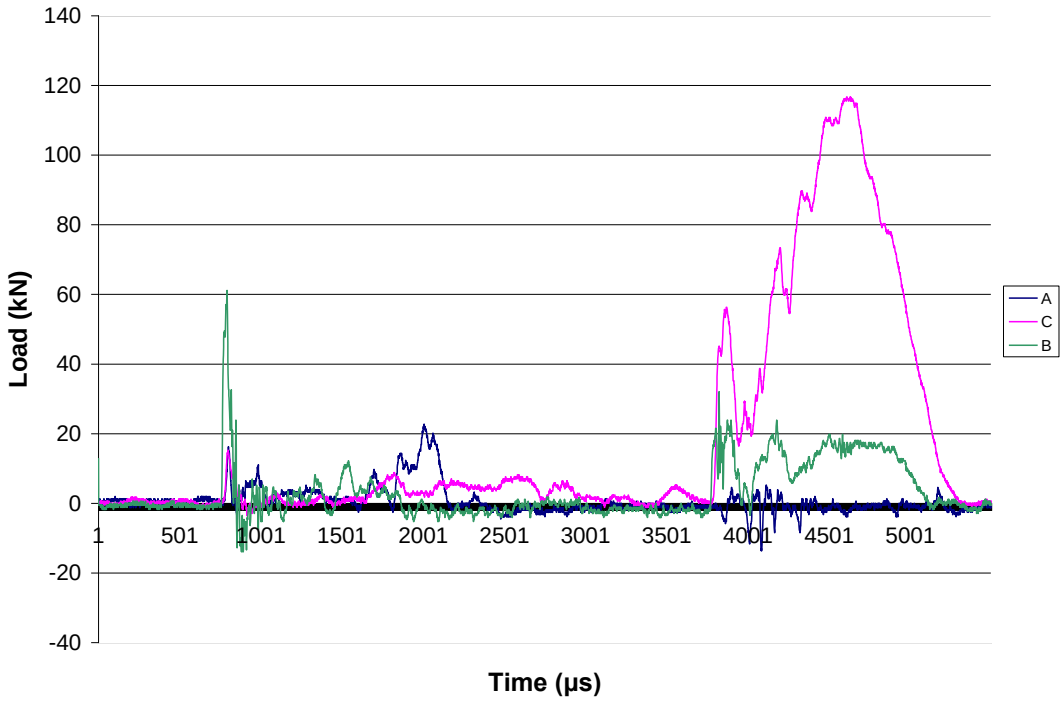

Figure 8.14. *Support loads vs. time for specimen B6S10W.*

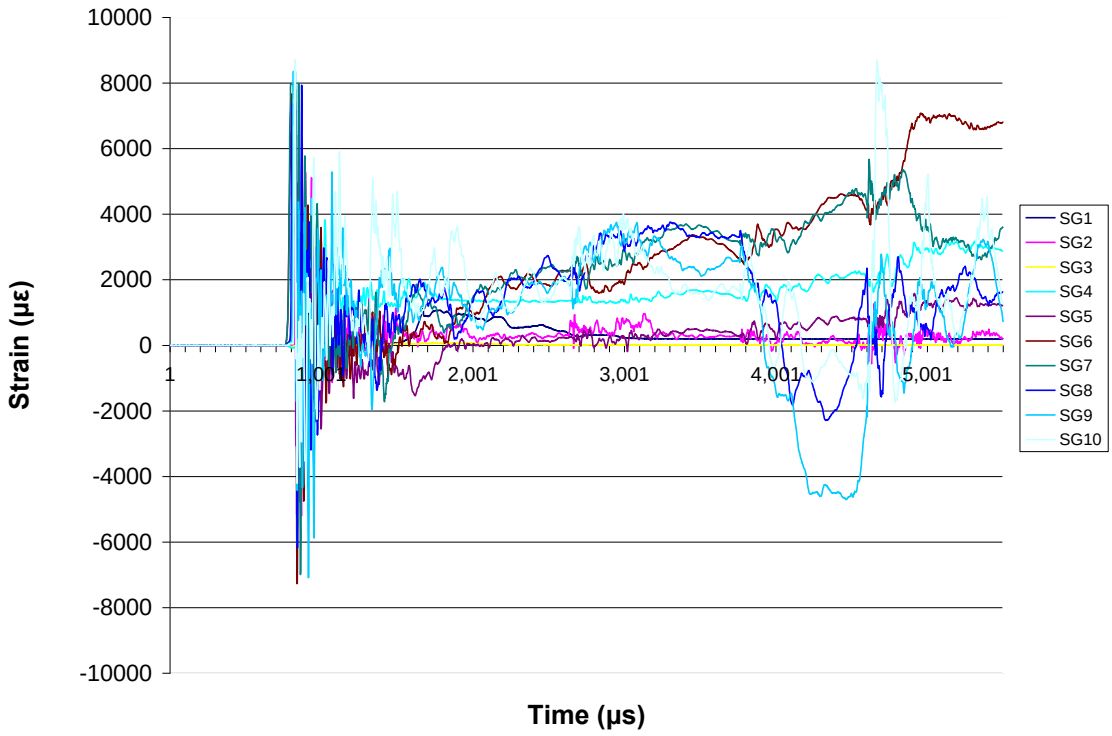

Figure 8.15. *Strain gauge reading vs. time for specimen B6S10W.*

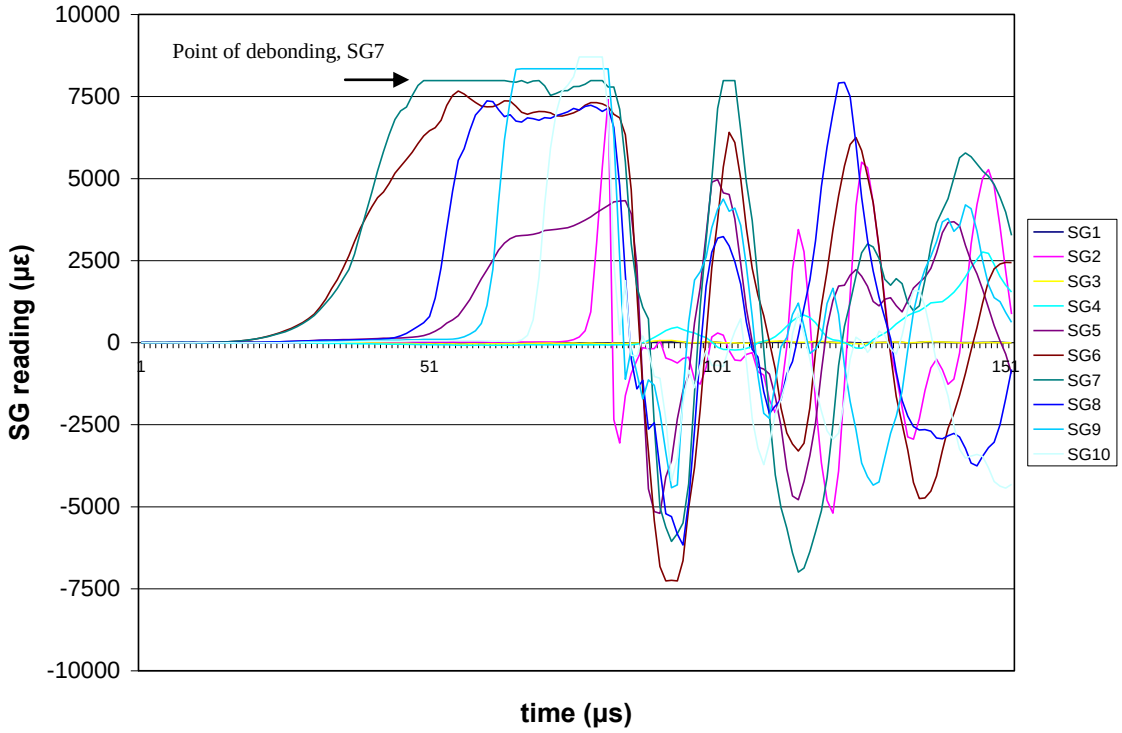

Figure 8.16. *Strain gauge reading vs. time for specimen B6S10W at the debonding time (magnified from the plot in Figure 8.15).*

The data acquisition system recorded the strain of the FRP at each time. As explained in Chapter 6, the bond stress can be calculated from the FRP strain gauge readings as follows:

$$\tau_{\text{bond}} = \frac{t_{\text{FRP}} E_{\text{FRP}} d\varepsilon_{\text{FRP}}}{dx} \tag{8.10}$$

where τ_{bond} is the bond stress of the dx element, t_{FRP} is the thickness of the sprayed FRP, and E_{FRP} is the modulus of elasticity of FRP.

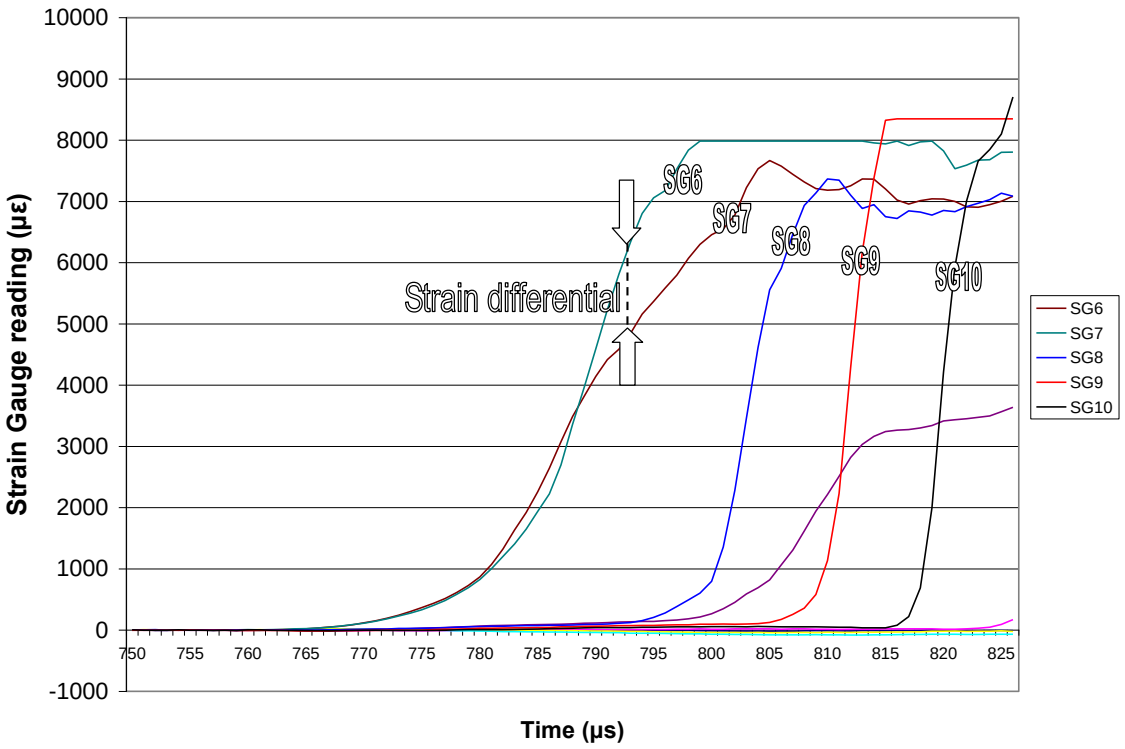

Figure 8.17. *Strain gauge readings on the debonded side (gauges 6 to 10).*

As in equation 8.10, the bond stress at each point is calculated from the strain differential of the FRP. The maximum bond stress at each point is when this differential strain is maximum, and as observed, the strain values after this point remain constant. Figure 8.18 represents the average values of maximum bond stress for different types of surface treatments with a drop height of 250 mm. Specimens treated with water jetting with higher drop height were tested to study the strain-rate sensitivity of the bond stress by using different drop heights. The higher drop height changed the failure mode to FRP rupture from debonding. It can be concluded that the higher strain rate increases the bond strength; however, numerical values for bond strength cannot be calculated owing to the fracture of FRP. The bond stress values and their sensitivity to strain rate are discussed in detail in the next chapter.

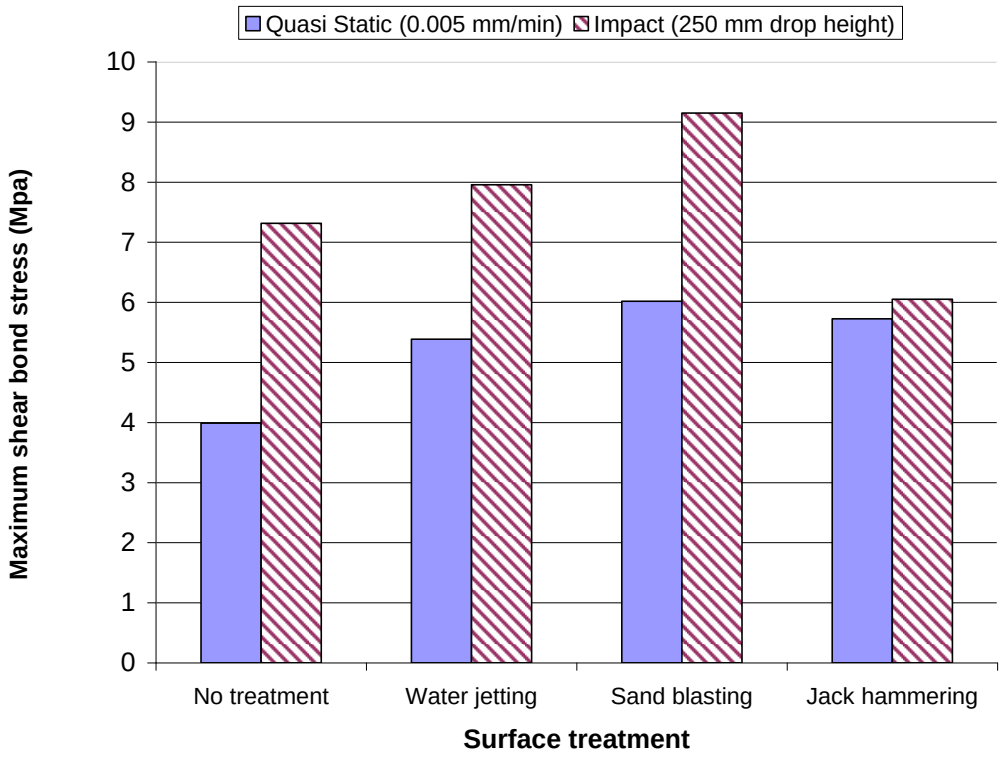

Figure 8.18. *Bond strength under impact and quasi-static loading for specimens with different surface treatments (quasi-static values are from Chapter 6).*

8.5 Conclusions

1. An impact setup was successfully developed to measure the bond stress and fracture energy of the FRP–concrete bond.
2. Of all surface treatments, sandblasting proved to provide the highest enhancement effect on the ductility of the bond. Water jetting is the second best method.
3. Beams sprayed with FRP showed slightly better bond strength and ductility under impact loading when water-jetting and sandblasting treatment methods were used. On the other hand, beams wrapped with FRP showed significantly better results when jack-hammering and mechanical fasteners were used. This showed that the wrapping method is less sensitive to the micro-cracks created on the concrete surface due to surface preparation.

4. Jackhammering decreases the ductility and strength of the sprayed FRP bond to concrete because of micro cracks it creates on the surface of the concrete. It is not generally recommended as a method of surface treatment.
5. Mechanical fasteners reduced the ductility and strength of the bond between sprayed FRP and concrete; however, they improved the same parameters in wrapped FRP.

CHAPTER 9
STRAIN RATE SENSITIVITY ANALYSIS

9.1 Introduction

The strength and the ultimate strain of many materials such as concrete, fibre reinforced concrete (FRC), and FRP have been found to increase under higher strain rate values. For plain concrete under quasi-static loading, cracks originate from defects or weak points, including the interface between the aggregate and the cement matrix and voids with the cement matrix, and then propagate to form micro-cracks. Under impact loading, however, the cracks tend to go through the stronger components of concrete as well, including coarse aggregate and cement paste. As strain sensitivity in concrete is due to the composite nature of concrete, one could expect that the strength and ductility of other composite systems that have a weak bond could be strain sensitive. The FRP strengthened concrete system was shown to be strain sensitive during the first sets of tests using 350 mm × 100 mm × 100 mm beams under different quasi-static strain rates. The present chapter discusses the strain rate behavior of FRC ranging from quasi-static loading, to high strain loading, and then to impact loading. The strain rate sensitivity of the FRP–concrete bond has not been investigated before.

9.2 Strain rate behavior

The strain rate behavior of both concrete and FRC are often represented as shown in Figure 9.1. The dynamic improvement factor (DIF) is the strength increase that

accompanies increasing strain rate. CEB [9.1] uses a bi-linear model to describe the strain rate behavior of concrete in compression and tension. The strain rate behavior is characterized by the fact that DIF (strength) increases slowly as strain rate increases from quasi-static loads to high strain rate loads and then increases much more rapidly as the strain rate reaches the range of impact loads [9.2].

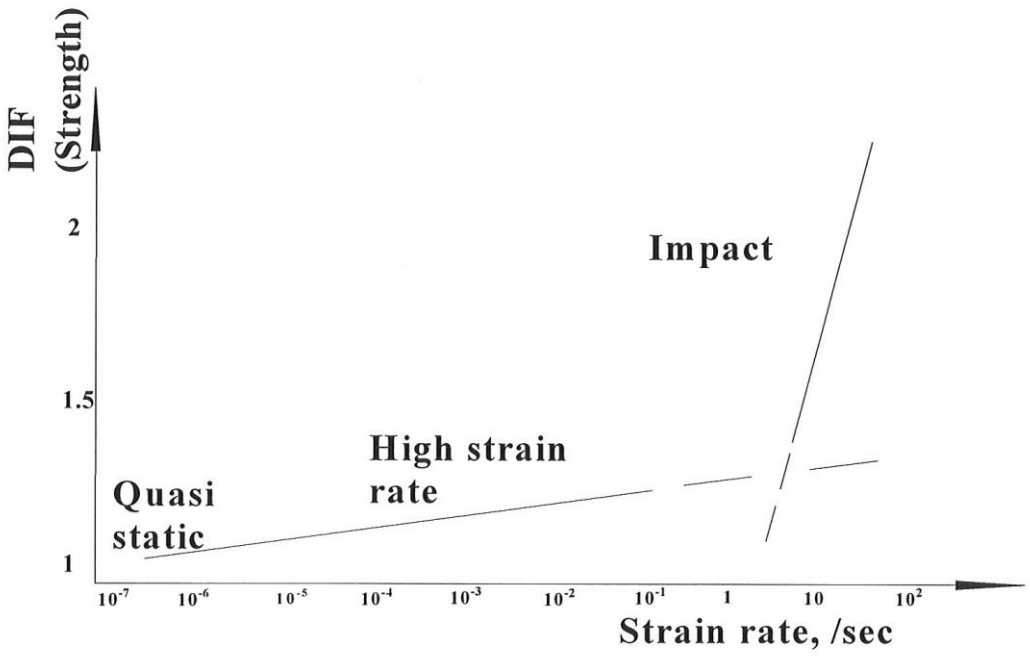

Figure 9.1. *Strain rate behavior of both concrete and FRC [9.2].*

In the present research, the strain rate was increased from about 10^{-7} to about 10^{1} as the load rate was increased from quasi-static (i.e., by about 8 orders of magnitude) as shown in Table 9.1. The FRP–concrete bond response varied considerably with increasing strain rate. The impact velocities at the instant of impact for a hammer with a mass of 591 kg for different drop heights are calculated as described previously and given in Table 9.2.

Table 9.1. *Strain rates for different tests*

Test	**Quasi-static**	**High strain rate**	**Impact**
Strain Rate (1/s)	10^{-7}–-10^{-6}	10^{-3}–10^{-2}	1–10
Test method	Instron machine	Instron machine	Drop weight impact

Table 9.2. *Impact velocity for different drop heights*

Drop height (mm)	Velocity (m/s)
250	2.22
500	3.13
750	3.84
1000	4.43

9.3 Strain sensitivity of the FRP–concrete bond as a function of loading rate

Table 9.3 presents the strength values of shear bond vs. loading rate. For quasi-static tests, which were done under strain control, the rate of strain applied is used. For impact tests, the velocity of the hammer at the point of impact is used. It should be noted that in addition to surface preparation and strain rate, the system also influences the shear bond strength values, as the testing equipment is changed from quasi-static tests to impact tests. Therefore, the results reflect not only the strain sensitivity of the bond but also the system toughness.

Table 9.3. *Strength of bond vs. loading rate*

Test	Sample name	Loading rate (mm/min)	Loading rate (m/s)	Surface preparation	Shear strength of bond	Failure mode
Quasi-static	B7S1	0.005	8×10^{-8}	None	3.77	Debonding
	B7S2	0.005	8×10^{-8}	None	4.21	Debonding
	B9S3W	0.005	8×10^{-8}	Water jetting	5.55	Debonding
	B9S4W	0.005	8×10^{-8}	Water jetting	5.22	Debonding
	B9S2W	0.005	8×10^{-8}	Water jetting	9.53	Debonding
	B8S1W	0.05	8×10^{-7}	Water jetting	4.70	Debonding
	B8S2W	0.05	8×10^{-7}	Water jetting	5.69	Debonding
	B8S3W	0.05	8×10^{-7}	Water jetting	5.23	Debonding
	B8S4W	0.5	8×10^{-6}	Water jetting	4.79	Debonding
	B8S5W	0.5	8×10^{-6}	Water jetting	6.05	Debonding
	B8S6W	0.5	8×10^{-6}	Water jetting	5.81	Debonding
	B9S7S	0.005	8×10^{-8}	Sandblasting	5.12	Debonding
	B9S8S	0.005	8×10^{-8}	Sandblasting	4.62	Debonding
	B9S9S	0.005	8×10^{-8}	Sandblasting	8.31	Debonding
	B9S10J	0.005	8×10^{-8}	Jackhammering	5.39	Debonding

Test	Sample name	Loading rate (mm/min)	Loading rate (m/s)	Surface preparation	Shear strength of bond	Failure mode
	B9S11J	0.005	8×10^{-8}	Jackhammering	6.06	Debonding
	B9S12J	0.05	8×10^{-7}	Jackhammering	6.70	Debonding
		Drop height (mm)				Debonding
High strain rate and impact	B30N1	250	2.215	None	8.10	Debonding
	B30N2	250	2.215	None	7.08	Debonding
	B30N3	250	2.215	None	6.76	Debonding
	B10S1W	250	2.215	Water jetting	8.34	Debonding
	B10S2W	250	2.215	Water jetting	7.24	Debonding
	B11S2W	250	2.215	Water jetting	8.29	Debonding
	B13S2S	250	2.215	Sandblasting	10.02	Debonding
	B13S3S	250	2.215	Sandblasting	8.07	Debonding
	B13S4S	250	2.215	Sandblasting	9.36	Debonding
	B11S4J	250	2.215	Jackhammering	5.39	Debonding
	B13S4J	250	2.215	Jackhammering	6.06	Debonding
	B13S5J	250	2.215	Jackhammering	6.70	Debonding
	B11S3W	500	3.13	Water jetting	9.67	Debonding
	B12S1W	500	3.13	Water jetting	9.43	Debonding
	B15S1W	500	3.13	Water jetting	8.14	Debonding
	B15S2W	750	3.84	Water jetting	9.54	Debonding
	B15S3W	750	3.84	Water jetting	10.39	Debonding
	B31N2	1000	4.43	None	8.74	Debonding
	B31N3	1000	4.43	None	10.38	Debonding
	B31N4	1000	4.43	None	11.10	Debonding
	B15S4W	1000	4.43	Water jetting	11.07	Debonding
	B17S4W	1000	4.43	Water jetting	10.77	Debonding
	B17S2W	1000	4.43	Water jetting	10.78	Debonding
	B32S1S	1000	4.43	Sandblasting	10.57	Debonding
	B32S2S	1000	4.43	Sandblasting	11.62	Rupture
	B32S3S	1000	4.43	Sandblasting	11.29	Rupture
	B31S1J	1000	4.43	Jackhammering	9.82	Debonding
	B31S2J	1000	4.43	Jackhammering	10.49	Debonding
	B31S3J	1000	4.43	Jackhammering	5.56	Debonding

Figures 9.2 to 9.6 present the shear strength values vs. loading rate for different surface preparations used. Shear strength values up to 11.62 MPa are calculated. Sandblasting showed the highest improvement in shear strength of bond. It should be noted that in two of the specimens prepared with sandblasting and tested under the

impact of a drop hammer elevated to 1000 mm, FRP ruptured before the debonding happened, so the values indicate the minimum values of shear bond strength. Shear bond values increase as the loading rate increases. Specimens with lower initial quasi-static strength show higher improvement (higher DIFs) compared with the specimens with higher initial quasi-static strength (better surface preparation). This suggests that under quasi-static loading the initial defect (crack) propagates through the interface between the FRP and the concrete. Under impact loading, however, the crack tends to go through the stronger components of the system as well, including the cement paste.

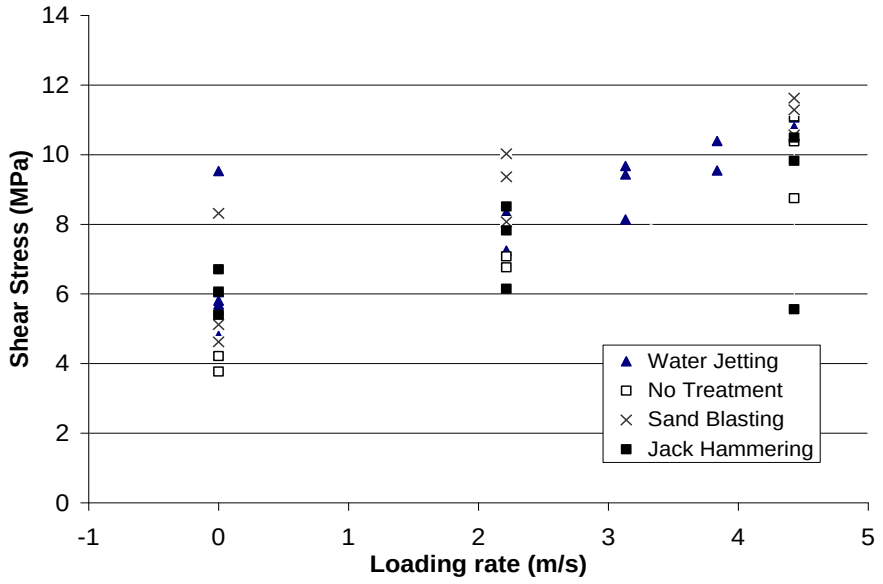

Figure 9.2. *Maximum shear stress vs. loading rate for different samples treated with four different surface preparations.*

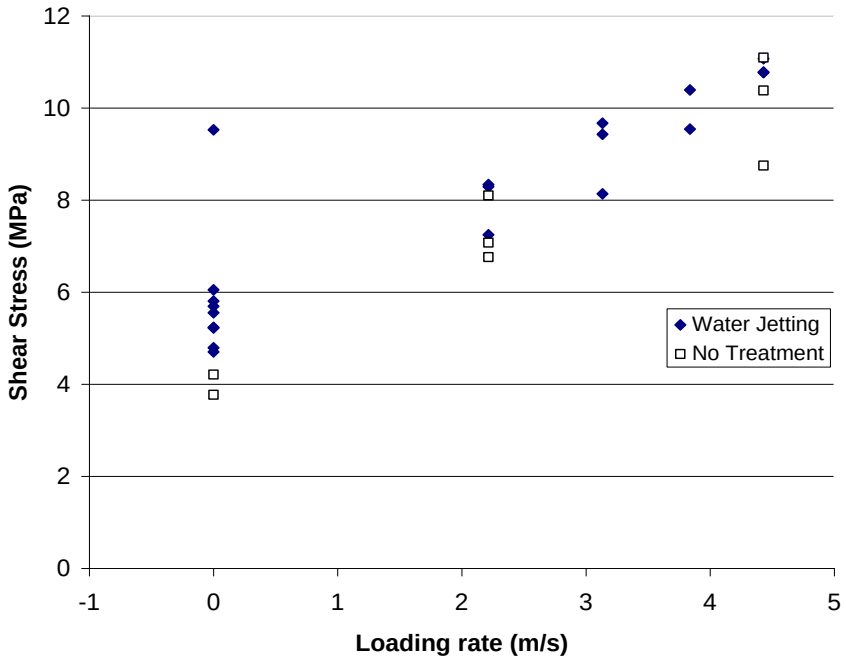

Figure 9.3. *Maximum shear stress vs. loading rate for different samples treated with water jetting compared with samples with no treatment.*

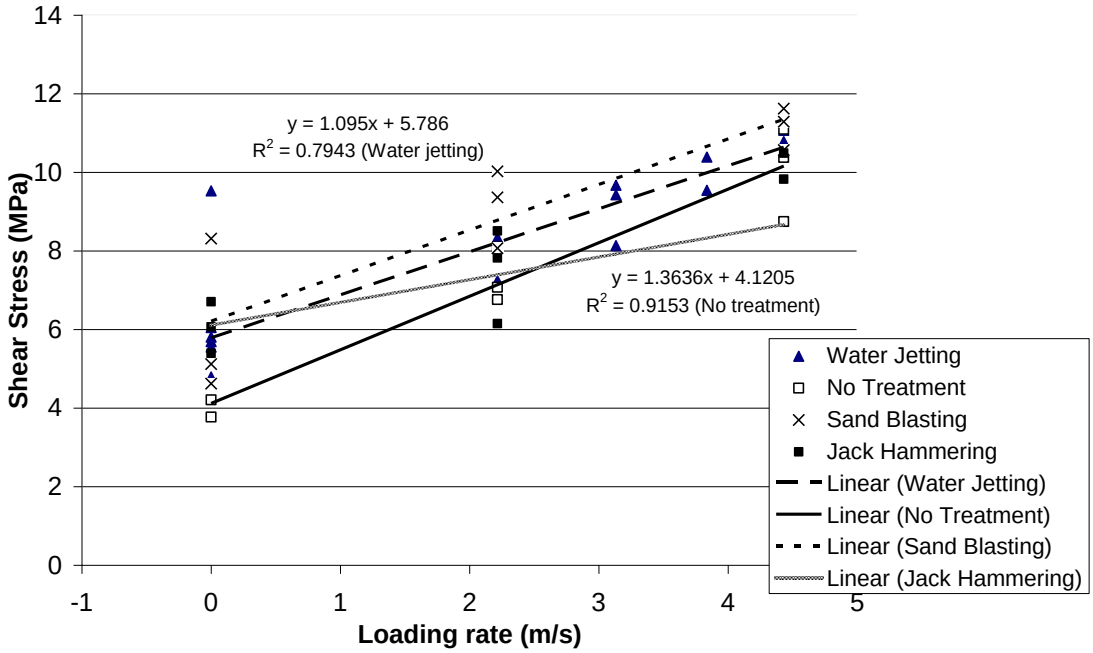

Figure 9.4. *Correlation between maximum shear stress and loading rate.*

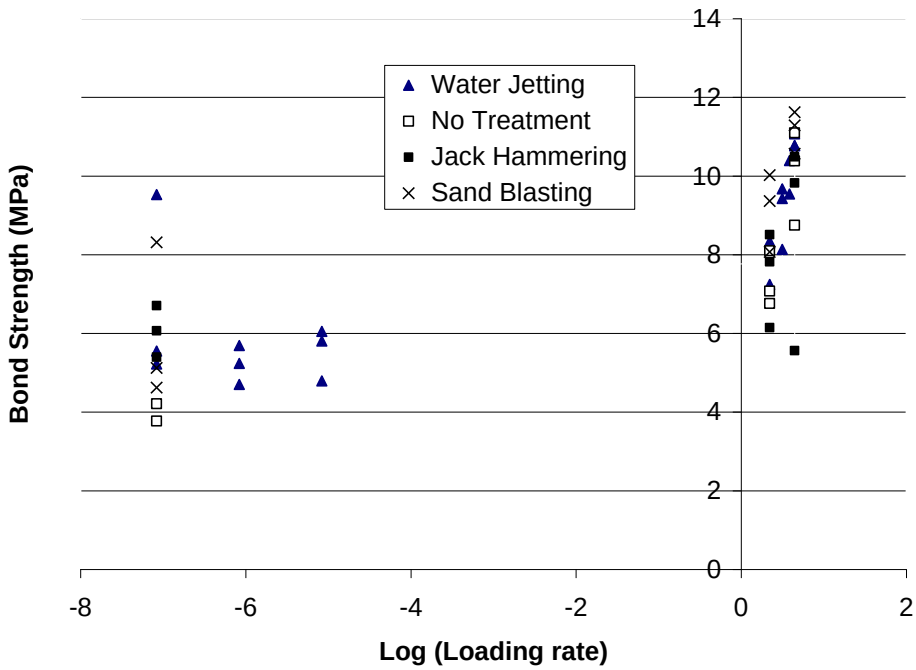

Figure 9.5. *Maximum bond stress vs. loading rate for different samples treated with four different surface preparations.*

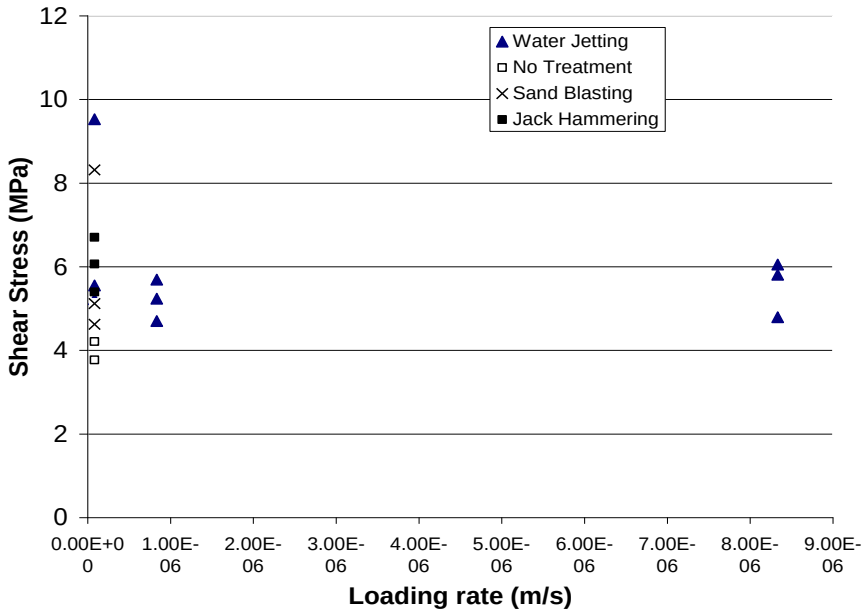

Figure 9.6. *Maximum shear stress vs. quasi-static loading rate for different samples treated with four different surface preparations.*

As described in Chapter 6, the bond values are calculated using the following relationship:

$$\tau_{\text{bond}} = \frac{t_{\text{FRP}} E_{\text{FRP}} d\varepsilon_{\text{FRP}}}{dx}$$

It should be noted that the elastic modulus is also a strain sensitive material property. The shear stress values are therefore corrected and presented in Figure 9.7 using the following relationship [9.1]:

$$\frac{E_d}{E_s} = \left(\frac{\dot{\varepsilon}_d}{\dot{\varepsilon}_s} \right)^{0.026}$$

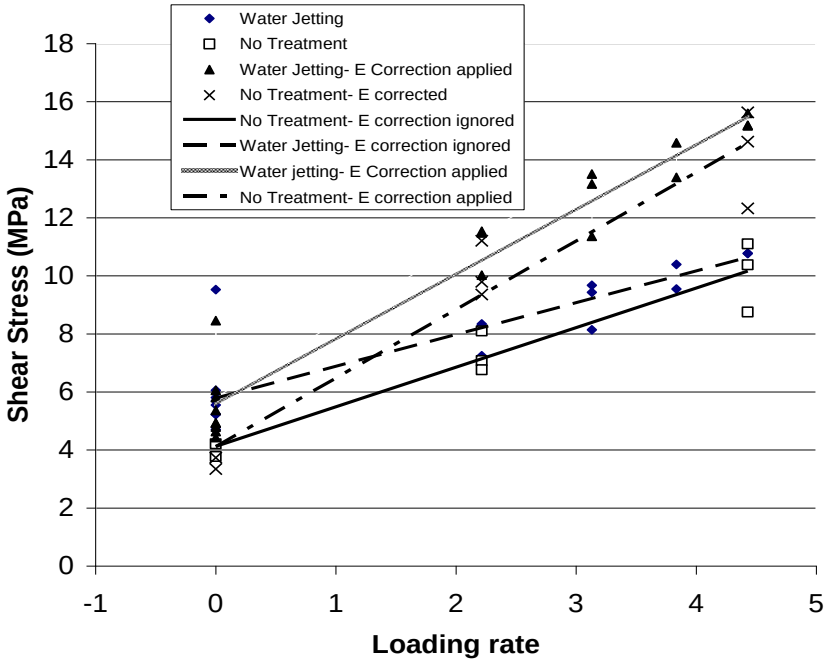

Figure 9.7. *Maximum shear stress vs. loading rate for different samples treated with two different surface preparations (elastic modulus is corrected under impact).*

9.4 Strain sensitivity of FRP–concrete bond as a function of strain rate

To fully evaluate the strain sensitivity of the FRP–concrete bond as a material property, the values and relationships should be calculated as a function of the direct

strain rate. Figure 9.8 represents the geometry of the specimen before and after impact schematically.

$$\frac{x+t}{y}=\frac{y}{l}$$

$\varepsilon=\frac{x}{x+t}$, ε is strain of FRP

$$\frac{d\varepsilon}{dx}=\frac{x+t-x}{(x+t)^2}=\frac{t}{(x+t)^2} \tag{9.2}$$

$$x=\frac{y^2}{L}-t$$

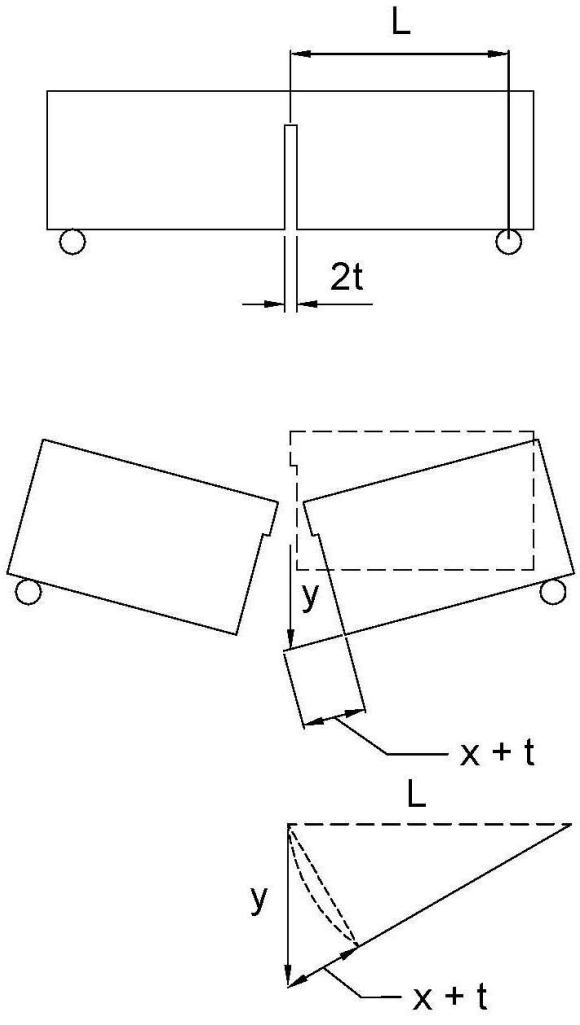

Figure 9.8. *Schematic view of the specimen before and after impact.*

$$\frac{dx}{dt} = \frac{2y}{L}\frac{dy}{dt} \tag{9.3}$$

$$\frac{d\varepsilon}{dt} = \frac{d\varepsilon}{dx}\frac{dx}{dt} \tag{9.4}$$

Substituting 9.2 and 9.3 into 9.4 gives

$$\frac{d\varepsilon}{dt} = \frac{t}{(x+t)^2}\frac{2y}{L}\frac{dy}{dt}$$

$$\frac{t}{x+t} \cong 1$$

$$\frac{d\varepsilon}{dt} = \frac{2y}{Lt}\frac{dy}{dt}$$

$$\frac{d\varepsilon}{dt}_{\text{Max}} = \frac{2\delta_{\max}}{Lt}\frac{dy}{dt} \tag{9.5}$$

Figures 9.9 and 9.10 present the maximum shear bond values as a function of strain rate using equation 9.4 to convert the loading rate to strain rate. It is worth noting that there is very little correlation among specimens treated with jackhammering. This could be due to micro-cracks and damage that jackhammering could create on the concrete surface. Also the uneven surface after jackhammering adds to the variability of the surface, which can influence the bond. Figure 9.11 shows the shear strength of concrete after the modulus of elasticity correction is applied. It should be noted that the corrected values show better correlation with E corrected for strain rate applied.

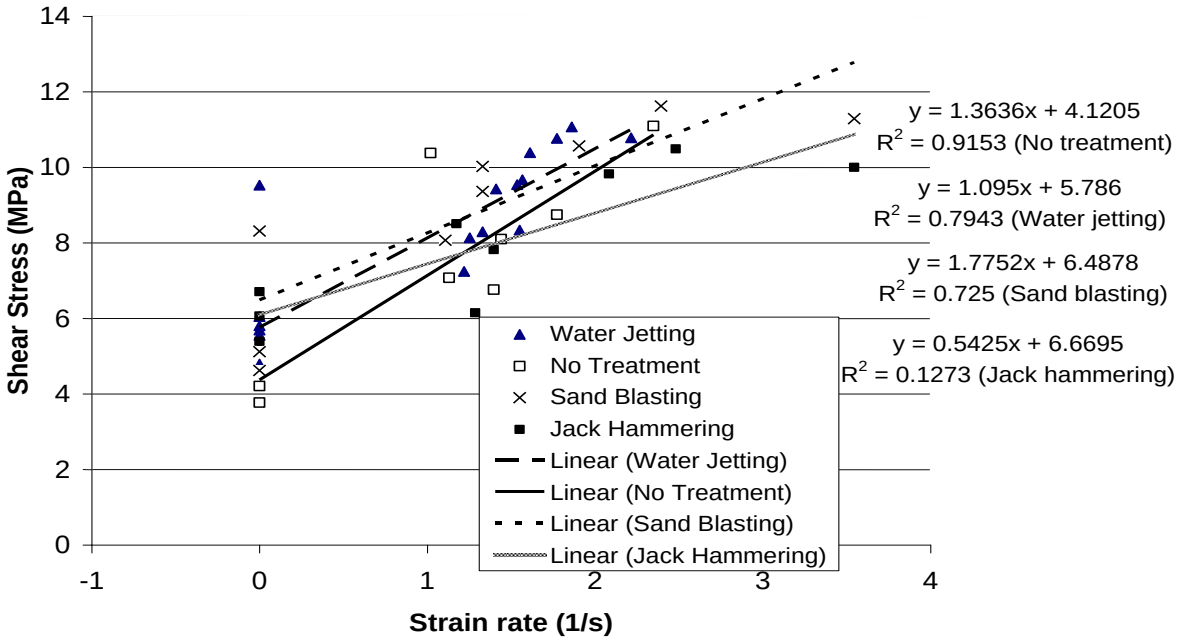

Figure 9.9. *Correlation between maximum shear stress and. strain rate.*

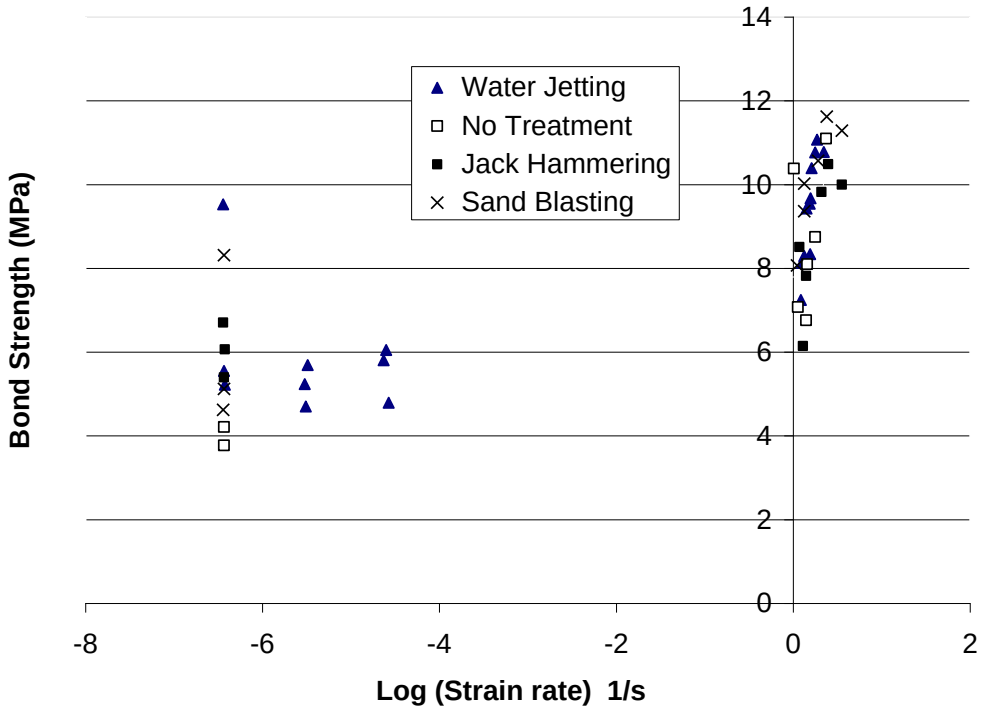

Figure 9.10. *Maximum shear stress vs. strain rate for different samples treated with four different surface preparations.*

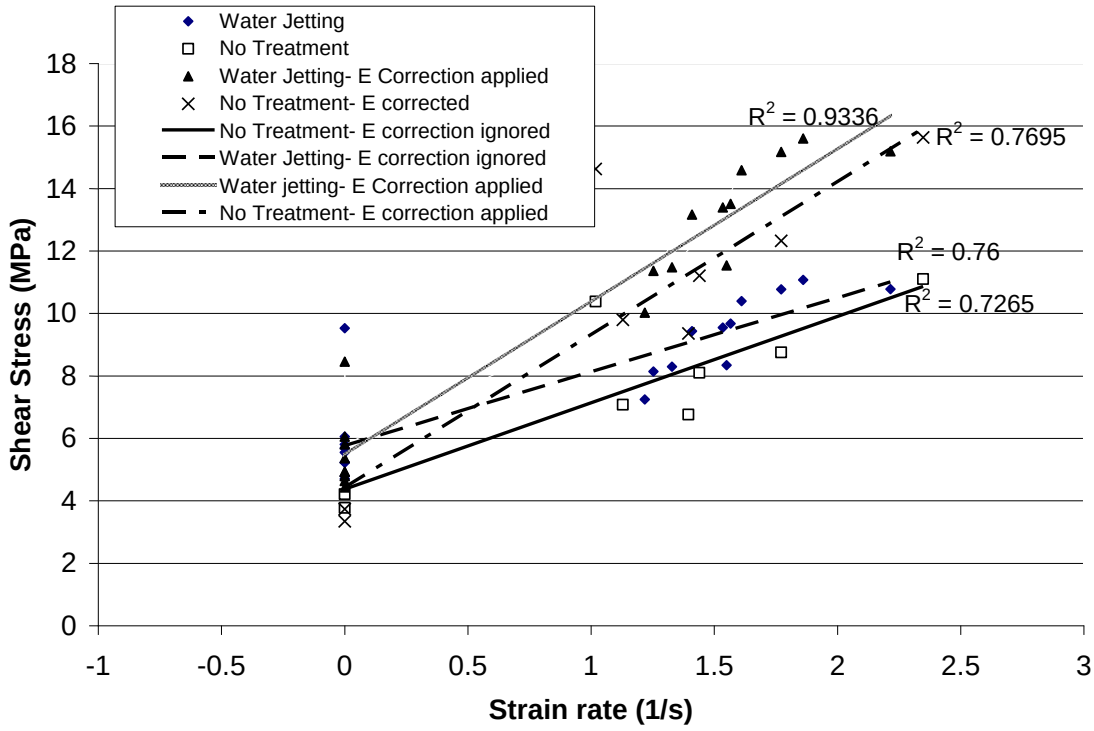

Figure 9.11. *Maximum shear stress vs. strain rate for different samples treated with two different surface preparations (elastic modulus is corrected under impact).*

9.5 Dynamic improvement factor of the FRP–concrete bond as a function of strain rate

The dynamic improvement factor (DIF) is defined as follows:

$$\text{DIF} = \frac{\text{Dynamic strength}}{\text{Quasi-static strength}}$$

Figure 9.12 represents the dynamic improvement factor of the FRP–concrete bond as a function of strain rate for different surface preparations. Figure 9.13 compares the correlation between uncorrected DIF and corrected DIF values as a function of strain rate sensitivity. Corrected values show a slightly better correlation. Figure 9.14 compares three different correlation types: linear, logarithmic, and exponential for water jetted specimens. The exponential relationship is chosen here. Other researchers have also used power-type correlations [9.1].

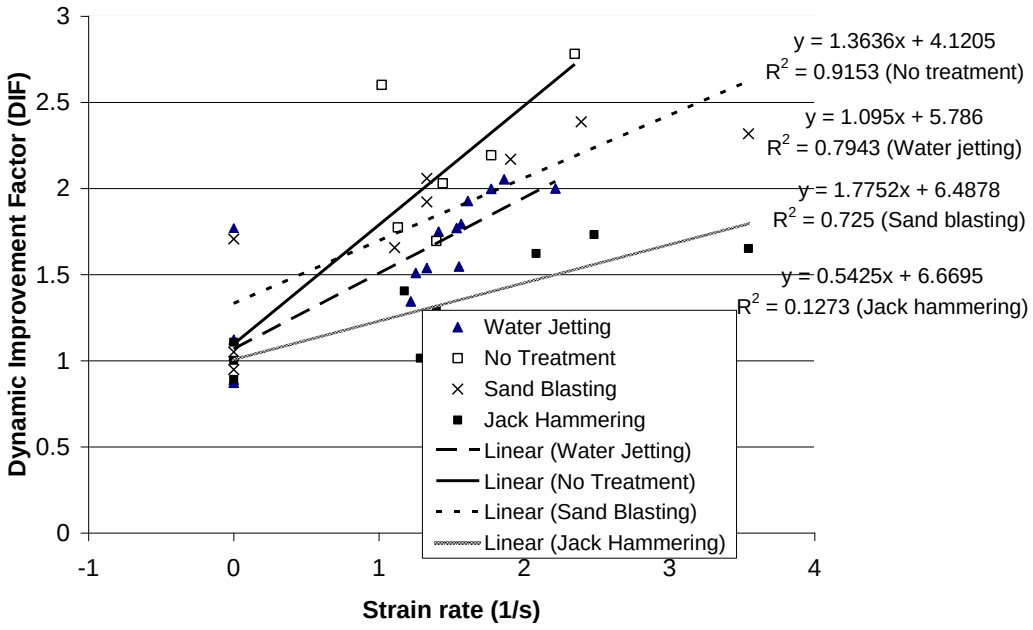

Figure 9.12. *DIF vs. strain rate for different samples treated with different surface preparation methods.*

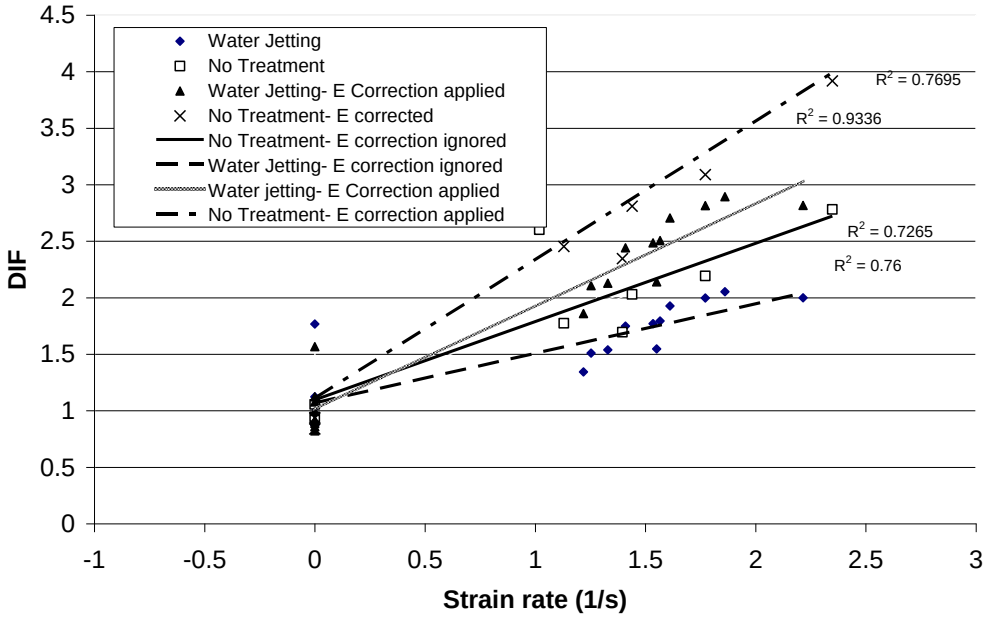

Figure 9.13. *DIF vs. strain rate for different samples treated with two different surface preparations (elastic modulus is corrected under impact).*

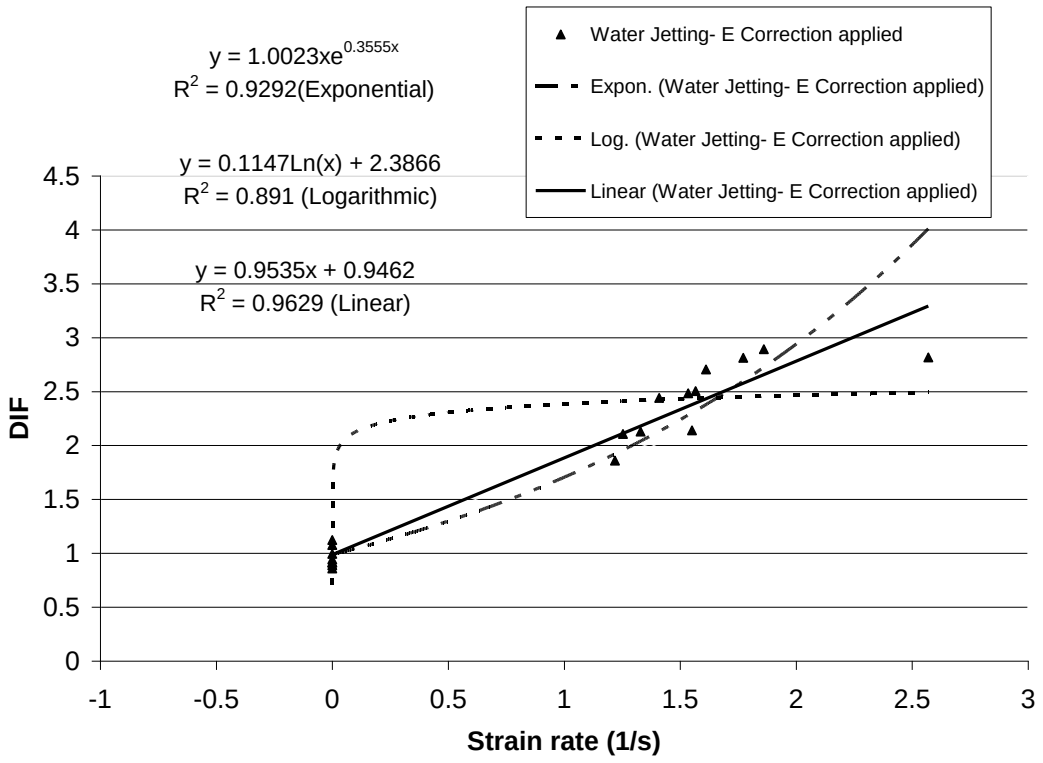

Figure 9.14. *DIF vs. strain rate for different samples treated with water jetting (elastic modulus is corrected under impact). Different correlation types are compared.*

For this test, one could assume that the following relationship governs the correlation between DIF and strain rate, where strain rate is in seconds^{-1}.

$$\mathrm{DIF} = ae^{b\dot{\varepsilon}} \tag{9.6}$$

$\dot{\varepsilon}_s$ is the static strain rate that is used in the quasi-static test:

$\dot{\varepsilon}_s = 3.67 \times 10^{-7}$

Values are offered in Table 9.4. It should be noted that more testing needs to be done to create enough data points for a higher correlation.

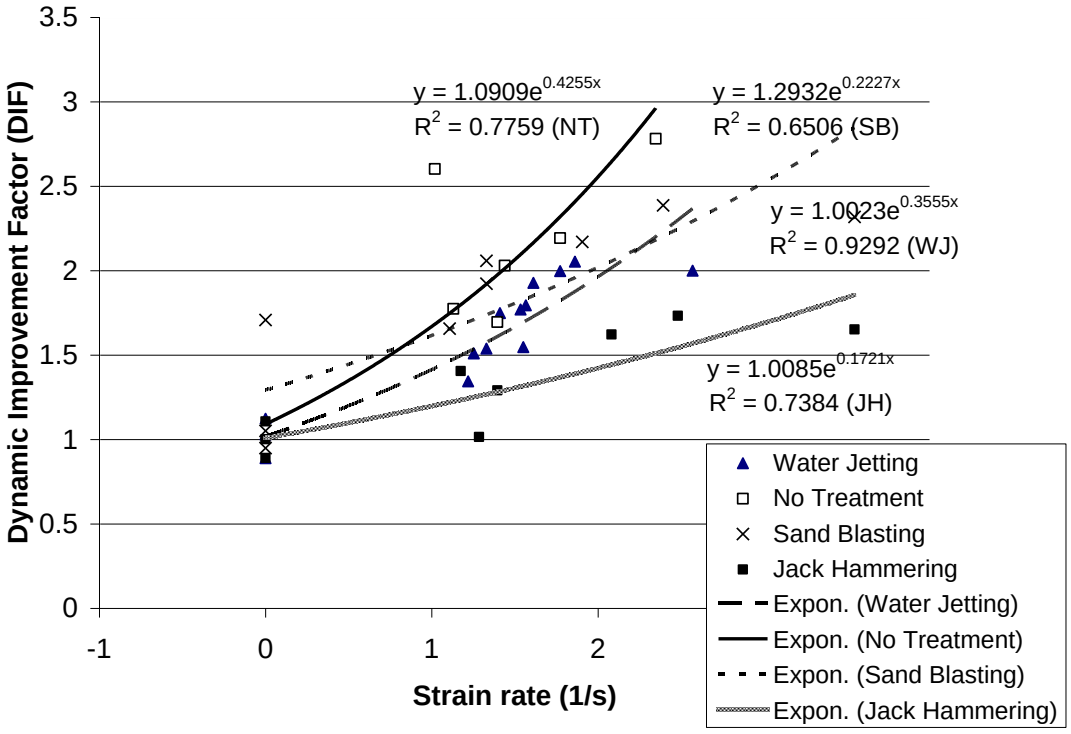

Figure 9.15. *DIF vs. strain rate for samples treated with different surface preparation methods (elastic modulus is corrected under impact). Different correlation types are compared.*

Table 9.4. *Factors a and b for strain rate sensitivity of the FRP–concrete bond used in equation 9.6*

Type of surface preparation	Factor a	Factor b	Correlation factor (R^2)
No treatment	1.09	0.43	0.77
Water jetting	1.00	0.36	0.93
Sandblasting	1.29	0.22	0.65
Jackhammering	1.01	0.17	0.74

9.6 Dynamic improvement factor of the FRP–concrete bond as a function of strain rate to static strain rate

In the hopes of finding a dimensionless relationship, values of DIF are plotted as a function of $\dot{\varepsilon}/\dot{\varepsilon}_s$ in Figure 9.16.

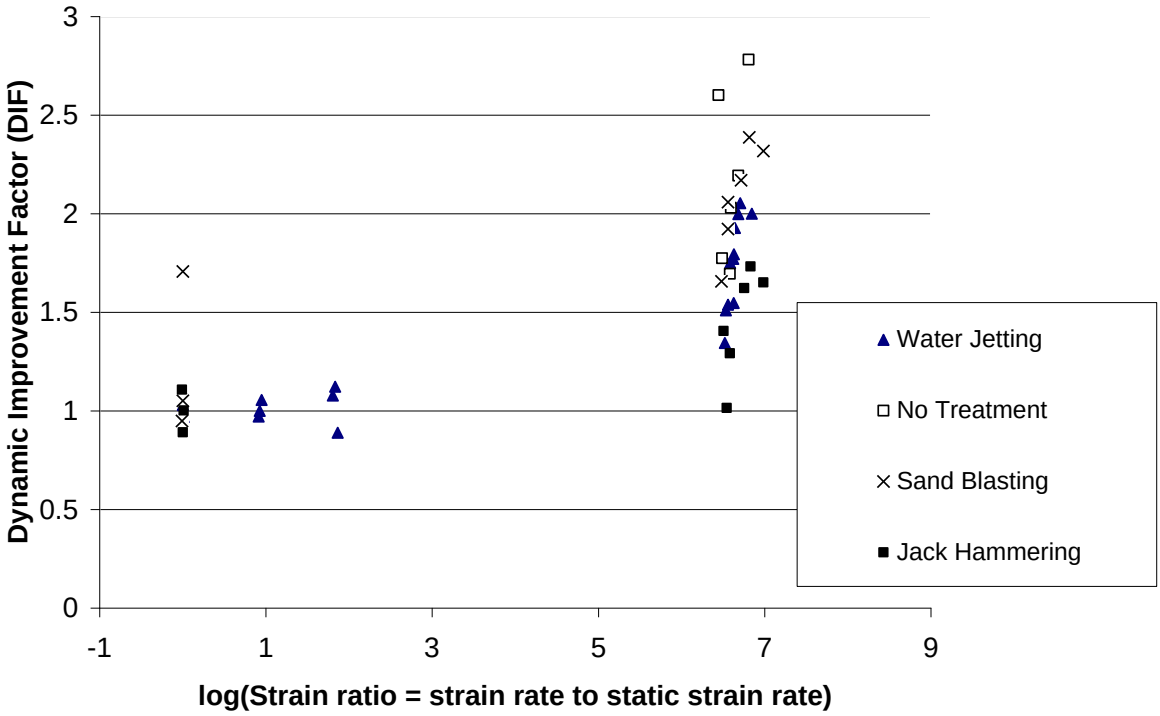

Figure 9.16. *DIF vs.* $\dot{\varepsilon}/\dot{\varepsilon}_s$ *for samples treated with different surface preparation methods (elastic modulus is corrected under impact).*

It is observed that the DIF values for dynamic testing do not correlate with the quasi-static values; therefore, they are studied in the absence of static values. The results are shown in Figure 9.16.

9.7 Conclusions

1. The FRP–concrete bond strength is a strain sensitive parameter and increases as the strain rate increases.
2. A correlation can be found to relate the dynamic improvement factor (DIF) to strain rate for different surface preparation types.
3. Specimens with lower initial quasi-static strength show higher improvement (higher DIFs) compared with the specimens with higher initial quasi-static strength (better surface preparation). This suggests that under impact loading a crack also tends to go through the stronger components of the system including the cement paste.

CHAPTER 10
FINITE ELEMENT MODELING

10.1 Introduction

Modeling packages are commonly used by engineers and researchers to model the performance of structures under load combinations. In order to correctly model the structures strengthened with FRP, the bond properties between FRP and concrete should be represented and modelled appropriately. In this chapter, an attempt is made to calibrate the energy and traction parameters of the cohesive element in ABAQUS to reproduce the same load displacement behavior as observed in the test from a modeled beam.

10.2 Modeling

The full three-dimensional model consists of three parts as shown in Figure 10.1:

1. Concrete: 550 mm × 150 mm × 150 mm with a hole 2 mm × 150 mm × 120 mm
2. Cohesive: two parts of 219 mm × 75 mm × 0.01 mm to model adhesives between concrete and FRP
3. FRP: 440 mm × 75 mm × 4 mm

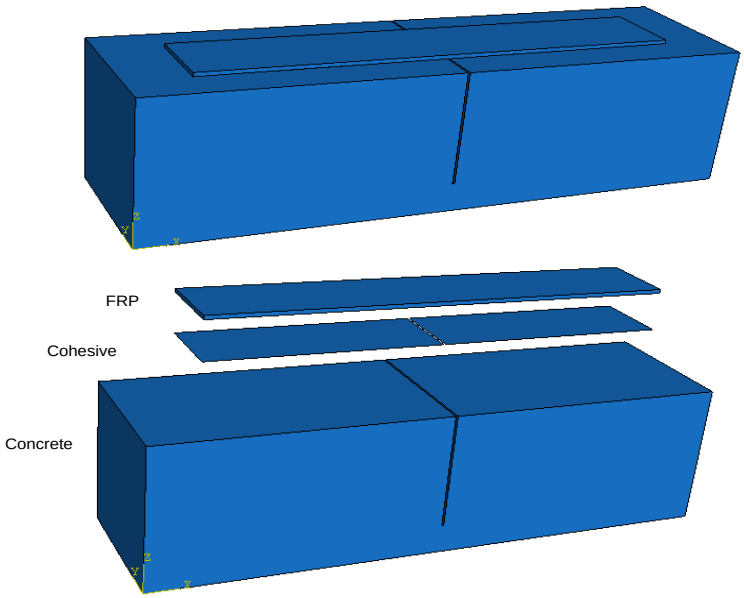

Figure 10.1. *3D model consisting of concrete, cohesive, and FRP.*

10.2 Material property

10.2.1 Concrete

Concrete is modeled as an isotropic linear elastic with E = 30 (GPa) and v = 0.20.

10.2.2 FRP

Fibre reinforced polymer (FRP) is modeled as an isotropic linear elastic with E = 14 (GPa) and v = 0.25.

10.2.3 Cohesive

The features described in this section are primarily intended for bonded interfaces where the interface thickness is negligibly small, which can be used for modeling the adhesive between concrete and FRP. In such cases it may be straightforward to define the constitutive response of the cohesive layer directly in terms of traction versus separation. Therefore, cohesive behavior defined directly in terms of a traction–separation

1. can be used to model the separation of concrete and FRP
2. assumes a linear elastic traction–separation law prior to damage (separation)

3. assumes that failure of the elements is characterized by progressive degradation of the material stiffness, which is driven by a damage process

10.2.3.1 Linear elastic traction–separation behavior

The available traction–separation model in ABAQUS assumes initially linear elastic behavior. For cohesive elements used to model bonded interface between concrete and FRP, ABAQUS offers an elasticity definition that can be written directly in terms of the nominal tractions and the nominal strains. Both uncoupled and coupled behaviors are supported. For uncoupled behavior each traction component depends on only its conjugate nominal strain (equation10.1), while for coupled behavior the response is more general (equation 10.2). In the local element directions the stress–strain relations for uncoupled behavior are as follows:

$$\begin{Bmatrix} t_n \\ t_s \\ t_t \end{Bmatrix} = \begin{bmatrix} K_{nn} & & \\ & K_{ss} & \\ & & K_{tt} \end{bmatrix} \begin{Bmatrix} \varepsilon_n \\ \varepsilon_s \\ \varepsilon_t \end{Bmatrix} \tag{10.1}$$

The quantities t_n, t_s, and t_t represent the nominal tractions in the normal and the two local shear directions, respectively, while the quantities ε_n, ε_s, and ε_t represent the corresponding nominal strains. For coupled traction separation behavior the stress–strain relations are as follows:

$$\begin{Bmatrix} t_n \\ t_s \\ t_t \end{Bmatrix} = \begin{bmatrix} K_{nn} & K_{ns} & K_{nt} \\ K_{ns} & K_{ss} & K_{st} \\ K_{nt} & K_{st} & K_{tt} \end{bmatrix} \begin{Bmatrix} \varepsilon_n \\ \varepsilon_s \\ \varepsilon_t \end{Bmatrix} \tag{10.2}$$

In this problem for simplicity the uncoupled behavior is selected.

10.2.3.2 Damage modeling

The initial response of the cohesive element is assumed to be linear as discussed above. However, once a damage initiation criterion is met, material damage can occur according to a user-defined damage evolution law. Figure 10.2 shows a typical traction–separation response with a failure mechanism. If the damage initiation criterion is

specified without a corresponding damage evolution model, ABAQUS will evaluate the damage initiation criterion for output purposes only; there is no effect on the response of the cohesive element (i.e., no damage will occur). The cohesive layer does not undergo damage under pure compression

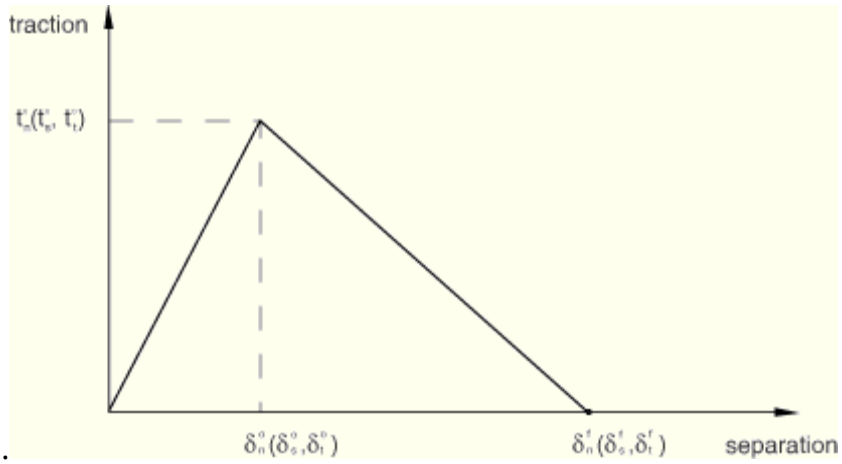

Figure 10.2. *Typical traction–separation response.*

10.2.3.3 Damage initiation

As the name implies, damage initiation refers to the beginning of degradation of the response of a material point. The process of degradation begins when the stresses and/or strains satisfy certain damage initiation criteria that you specify. Several damage initiation criteria are available and are discussed below. In the discussion below, t_{n}^{0}, t_{s}^{0}, and t_{t}^{0} represent the peak values of the nominal stress (traction) when the deformation is either purely normal to the interface or purely in the first or the second shear direction, respectively. Likewise, $\varepsilon_{\mathrm{n}}^{0}$, $\varepsilon_{\mathrm{s}}^{0}$, and $\varepsilon_{\mathrm{t}}^{0}$ represent the peak values of the nominal strain when the deformation is either purely normal to the interface or purely in the first or the second shear direction, respectively. With the initial constitutive thickness $T_0 = 1$, the nominal strain components are equal to the respective components of the relative displacement, δ_{n}, δ_{s}, and δ_{t}, between the top and bottom of the cohesive layer. The symbol $\langle\ \rangle$ used in the discussion below represents the Macaulay bracket with the usual interpretation. The Macaulay brackets are used to signify that a pure compressive deformation or stress state does not initiate damage.

10.2.3.3.1 Maximum nominal stress criterion (which is used in this problem)

Damage is assumed to initiate when the maximum nominal stress ratio (as defined in the expression below) reaches a value of one. This criterion can be represented as

$$\max\left\{\frac{\langle t_{\mathrm{n}}\rangle}{t_{\mathrm{n}}^{0}}, \frac{t_{\mathrm{s}}}{t_{\mathrm{s}}^{0}}, \frac{t_{\mathrm{t}}}{t_{\mathrm{t}}^{0}}\right\} = 1 \tag{10.3}$$

10.2.3.3.2 Maximum nominal strain criterion

Damage is assumed to initiate when the maximum nominal strain ratio (as defined in the expression below) reaches a value of one. This criterion can be represented as

$$\max\left\{\frac{\langle \varepsilon_{\mathrm{n}}\rangle}{\varepsilon_{\mathrm{n}}^{0}}, \frac{\varepsilon_{\mathrm{s}}}{\varepsilon_{\mathrm{s}}^{0}}, \frac{\varepsilon_{\mathrm{t}}}{\varepsilon_{\mathrm{t}}^{0}}\right\} = 1 \tag{10.4}$$

10.2.3.3.3 Quadratic nominal stress criterion

Damage is assumed to initiate when a quadratic interaction function involving the nominal stress ratios (as defined in the expression below) reaches a value of one. This criterion can be represented as

$$\left\{\frac{\langle t_{\mathrm{n}}\rangle}{t_{\mathrm{n}}^{0}}\right\}^{2} + \left\{\frac{t_{\mathrm{s}}}{t_{\mathrm{s}}^{0}}\right\}^{2} + \left\{\frac{t_{\mathrm{t}}}{t_{\mathrm{t}}^{0}}\right\}^{2} = 1 \tag{10.5}$$

10.2.3.3.4 Quadratic nominal strain criterion

Damage is assumed to initiate when a quadratic interaction function involving the nominal strain ratios (as defined in the expression below) reaches a value of one. This criterion can be represented as

$$\left\{\frac{\langle \varepsilon_{\mathrm{n}}\rangle}{\varepsilon_{\mathrm{n}}^{0}}\right\}^{2} + \left\{\frac{\varepsilon_{\mathrm{s}}}{\varepsilon_{\mathrm{s}}^{0}}\right\}^{2} + \left\{\frac{\varepsilon_{\mathrm{t}}}{\varepsilon_{\mathrm{t}}^{0}}\right\}^{2} = 1 \tag{10.6}$$

10.2.3.4 Damage evolution

The damage evolution law describes the rate at which the material stiffness is degraded once the corresponding initiation criterion is reached. Different models are available in ABAQUS, such as

1- Evolution based on effective displacement

2- Evolution based on energy

Herein we describe the evaluation based on energy, which is used in this problem.

10.2.3.4.1 Evolution based on energy

Damage evolution can be defined based on the energy that is dissipated as a result of the damage process, also called the fracture energy. The fracture energy is equal to the area under the traction–separation curve (see Figure 10.3). The fracture energy is specified as a material property, and either a linear or an exponential softening behavior is chosen. ABAQUS ensures that the area under the linear or the exponential damaged response is equal to the fracture energy (exponentially damage evolution is used in this problem).

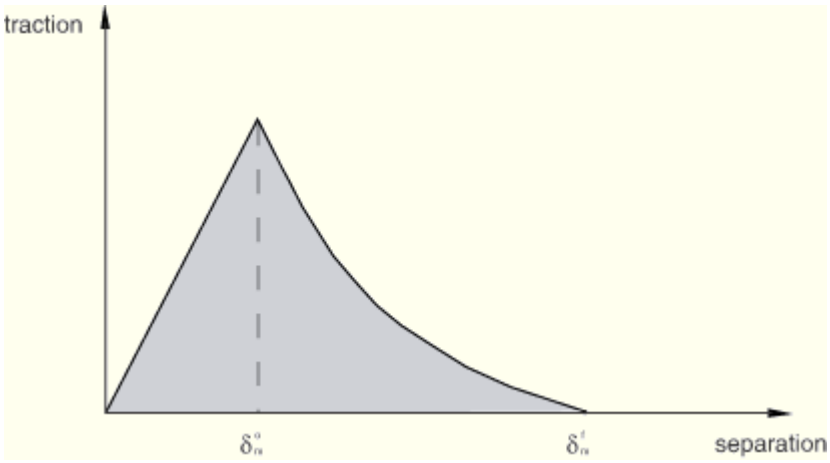

Figure 10.3. *Exponential damage evolution.*

10.3 Interaction

10.3.1 Concrete–cohesive and FRP–cohesive interaction

If the two neighboring parts do not have matched meshes, such as when the discretization level in the cohesive layer differs (typically finer) from the discretization level in the surrounding structures, the top and/or bottom surfaces of the cohesive layer can be tied to the surrounding structures using a tie constraint. Figure 10.4 shows an example in which a finer discretization is used for the cohesive layer than for the neighboring parts.

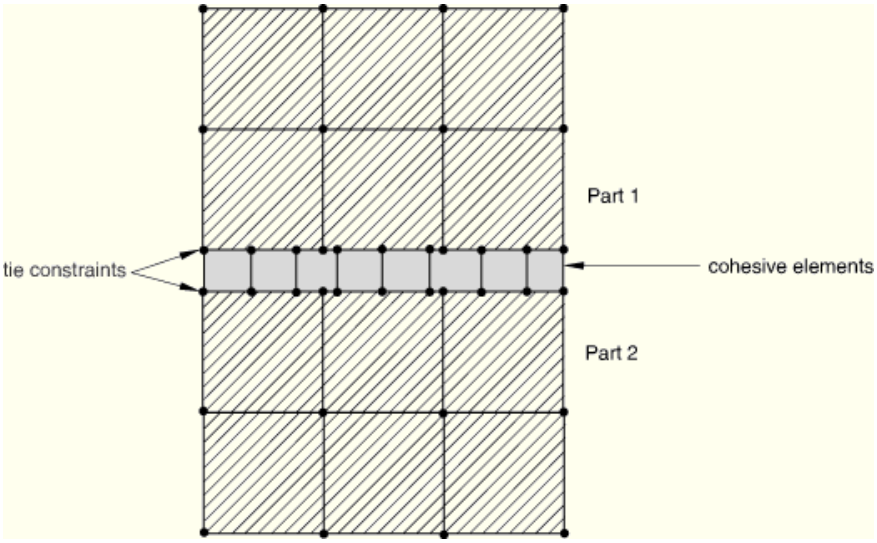

Figure 10.4. *Independent meshes with tie constraints.*

10.3.2 Concrete–FRP interaction

Cohesive elements are used to bond two different components. Often the cohesive elements completely degrade in tension and/or shear as a result of the deformation. Subsequently, the components that are initially bonded together by cohesive elements may come into contact with each other. The approach used herein is to define contact between the surfaces of the concrete and FRP that could potentially come into contact and to delete the cohesive elements once they are completely damaged. For this purpose the simple tangential and normal contact behaviors are selected. It is assumed that the normal behavior is hard contact and tangential behavior is with friction coefficient 0.2 (do not have significant effect).

10.4 Loading

As shown in Figure 10.5 the concrete part is constrained at a distance of 10 mm from FRP on both sides on the top surface (*x*, *y*, and *z* directions on left side and *z* direction on right side). The uniform displacements are applied to the bottom surface of the concrete at the distance of 75 mm from centre on both sides.

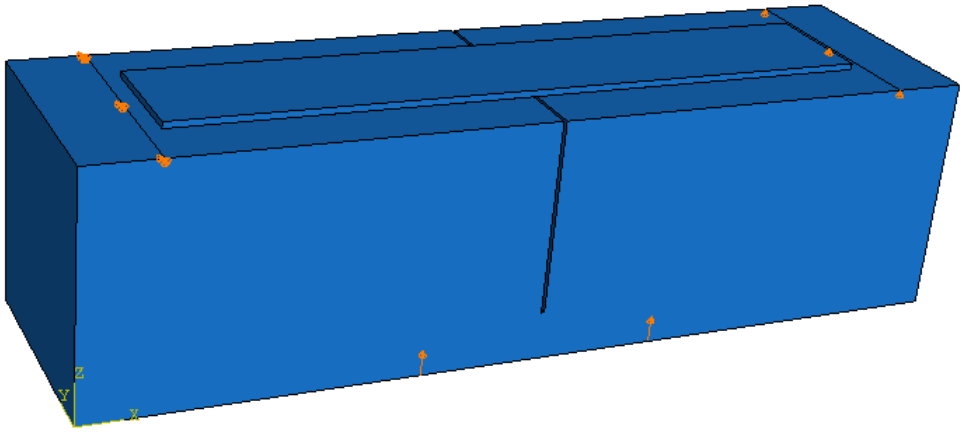

Figure 10.5. *Applied loads and constraints.*

10.5 Meshing

For both FRP and concrete parts a 20-node quadratic brick element (Figure 8.6) is selected.

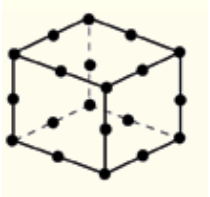

Figure 10.6. Quadratic element (20-node brick, C3D20).

However, for the cohesive part the only option is an 8-node linear cohesive element, as shown in Figure 10.7.

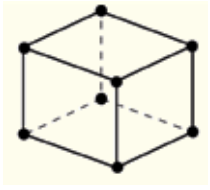

Figure 10.7. *8-node three-dimensional cohesive element (COH3D8).*

Figure 10.8 shows the meshed model. During the analysis finer meshes are used for convergence purposes.

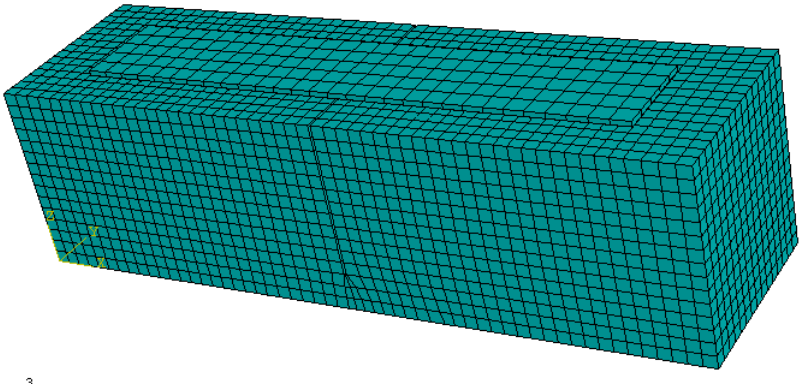

Figure 10.8. *Meshed model.*

10.6 Analysis

Nonlinear static analysis using a Newton–Rophson scheme is selected for this problem. Also, the nonlinear effects of large displacements are included in the analysis.

10.7 Results

Table 10.1 shows the different *K* factor used for different runs of test (for each case). Figure 10.9 shows the predicted load vs. displacement curves with different cohesive element parameters used. Figure 10.10 shows the exaggerated model of specimen before complete failure.

Table 10.1. *Cohesive zone parameters used in the model*

Case	K_{nn}	K_{ss}	K_{tt}	Nominal stress			Fracture energy
				Normal-only mode	First direction	Second direction	
1	2.00E+06	2.00E+06	2.00E+06	0.05	0.05	0.05	1.00E-05
2	1000	1000	1000	7	7	7	0.04
3	10000	10000	10000	1	1	1	0.001
4	10000	10000	10000	0.1	0.1	0.1	0.0001
5	10000	10000	10000	7	7	7	0.001
6	10000	10000	10000	7	7	7	0.005
7	10000	10000	10000	5	5	5	0.002
8	1000	1000	1000	7	7	7	0.025
9	1000	1000	1000	1	1	1	0.002
10	1000	1000	1000	3	3	3	0.006
11	1000	1000	1000	1	1	1	0.003
12	1000	1000	1000	0.1	0.1	0.1	0.003
13	1000	1000	1000	0.01	0.01	0.01	0.003
14	1000	1000	1000	0.001	0.001	0.001	0.003
15	1000	1000	1000	0.0001	0.0001	0.0001	0.003
16	1000	1000	1000	0.00001	0.00001	0.00001	0.003

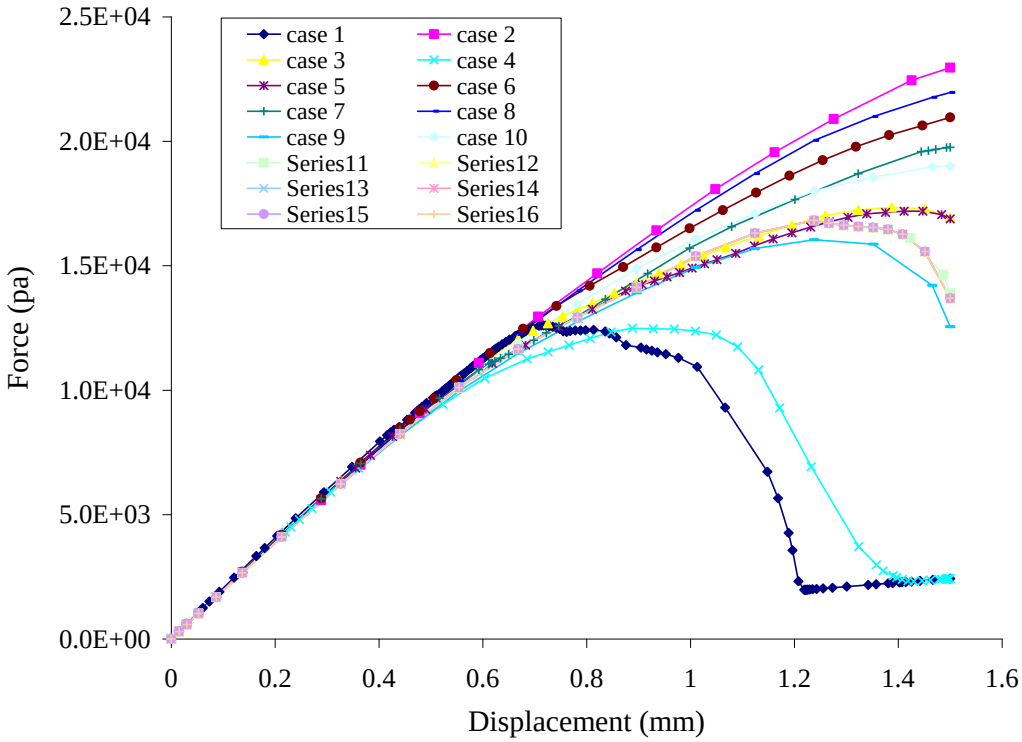

Figure 10.9. *Predicted load vs. displacement curves with different cohesive element parameters used.*

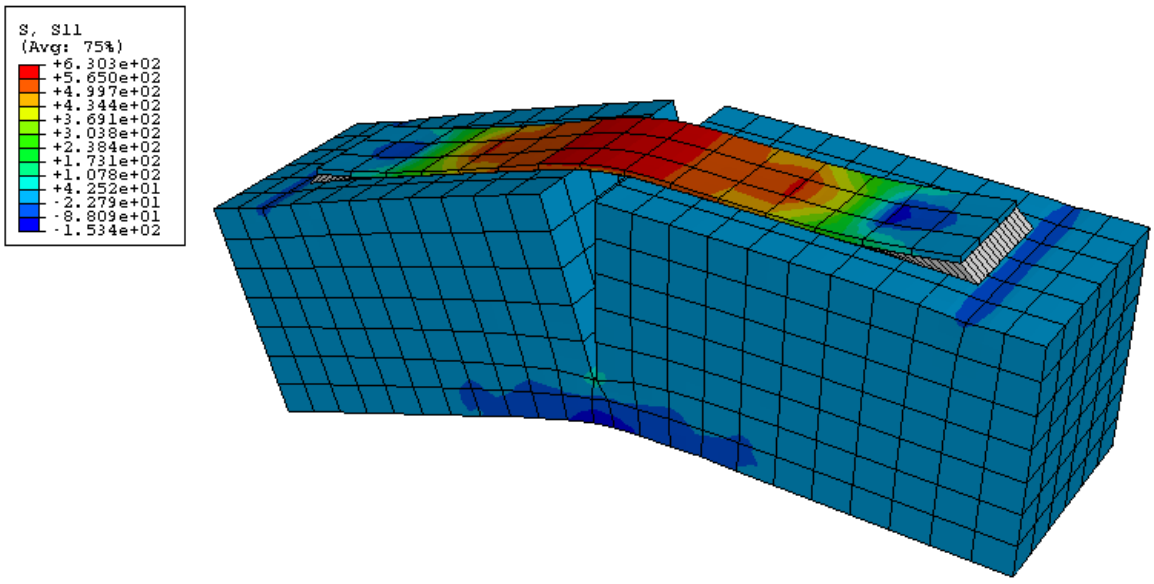

Figure 10.10. *Exaggerated model of specimen before complete failure.*

Displacement 0.03 mm

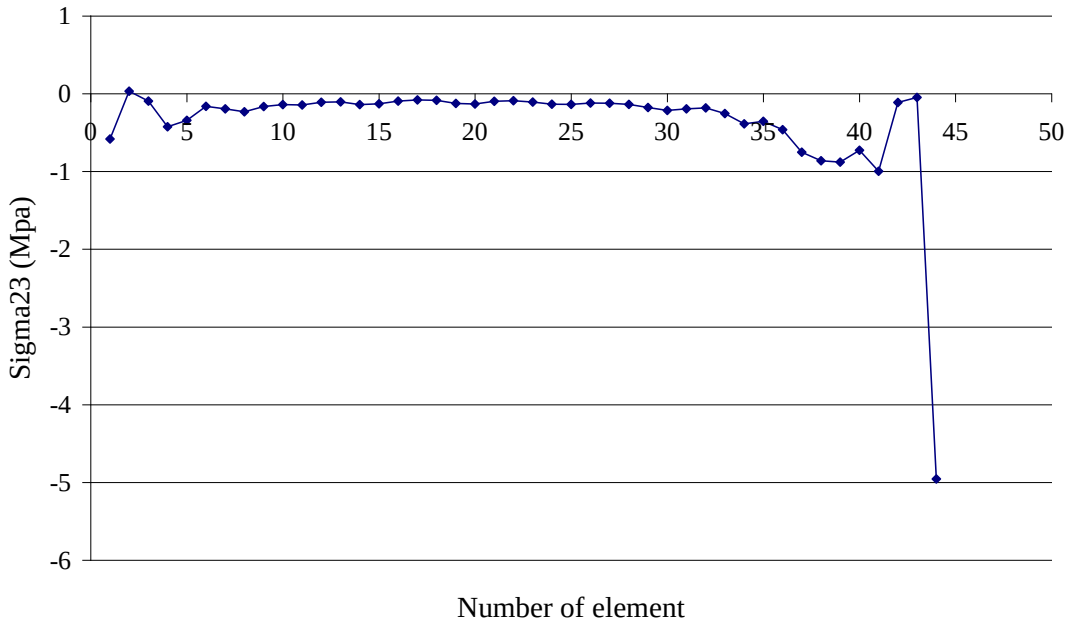

Displacment 0.33 mm

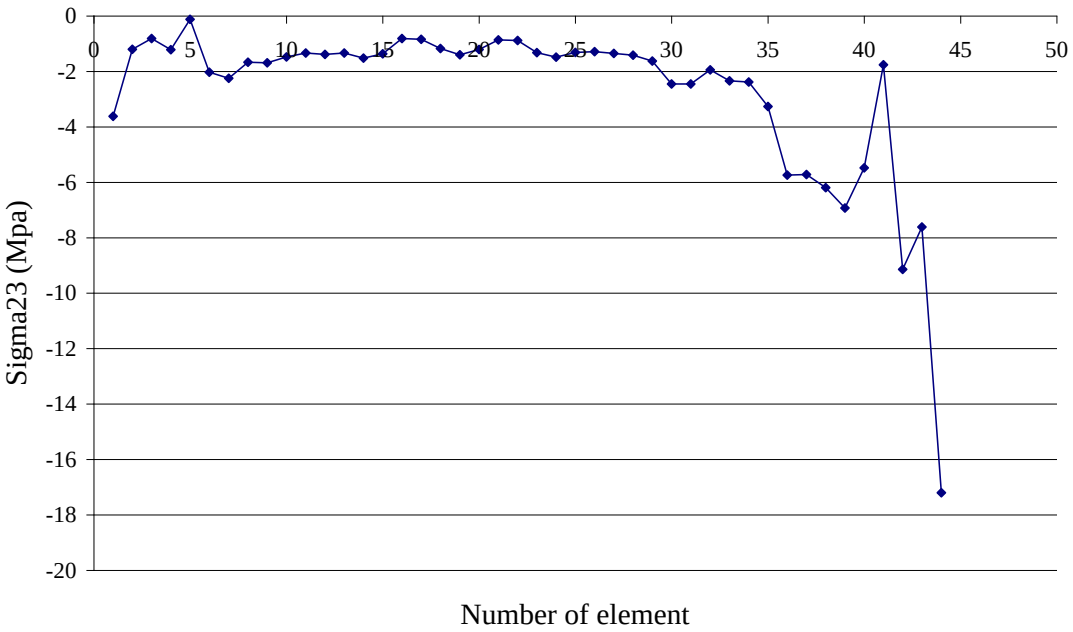

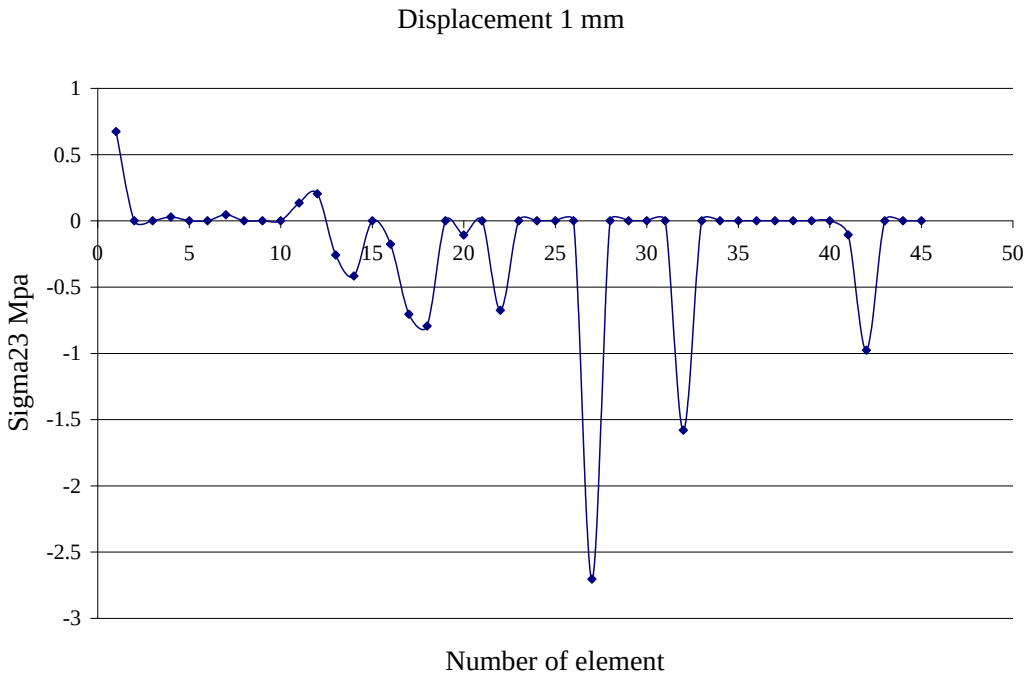

Figure 10.11. *Bond stress profile at two displacements of 0.03 and 0.33 mm.*

Figure 10.10 shows the load displacement response of the modelled beam. After several attempts, the researcher was not able to reproduce the same unzipping in the load displacement curves seen in the test. However, case 5 was found to be the closest response of all in terms of the load deflection behavior. Case 5 parameters predicted a maximum deflection of 1.45 mm and a maximum failure load of 17.1 kN. As a comparison with specimens treated with water jetting with an average ultimate tested value of 20.3 kN, the predicted ultimate load is 18.7% lower. The predicted ultimate load is shown in Figure 10.11, which presents the bond stress profiles at two displacements of 0.03 and 0.33 mm.

10.8 Conclusion

An attempt was made to calibrate the energy and traction parameters of the cohesive element in ABAQUS to re-produce the same load displacement behavior as observed in the test from a modeled beam. Even though the same unzipping phenomenon was not produced, a reasonable close load vs. displacement behavior was achieved. Future research is necessary to develop a practical bond finite element.

CHAPTER 11
CONCLUSIONS AND FUTURE RESEARCH

11.1 Specimen development

An experimental program was carried to develop an appropriate specimen that accurately evaluates the bond between FRP and concrete. The following criteria were followed:

1. Load to be transferred indirectly to the bond between FRP and concrete as in real life situation.
2. Specimens to be easy to fabricate and the test to be performed using regular instruments.
3. Bond length to be adequate to create a complete unzipping load–displacement behavior.

First, 350 mm × 100 mm × 100 mm beam specimens were evaluated. However, in order to obtain the complete unzipping profile, the specimen size was increased to 550 mm × 150 mm × 150 mm. Different notch depths and shapes as well as hinges were used. The final specimen that produced satisfactory results was 550 mm × 150 mm × 150 mm with a 120 mm notch over which the FRP was applied. Four-point bending tests were performed.

11.2 Quasi-static behavior of the FRP–concrete bond

Behavior of the interface bond between FRP and concrete was investigated using the novel specimen developed. Three surface treatment methods, water jetting, sandblasting, and jackhammering, were used. The beams were then retrofitted using the sprayed FRP method. The FRP strip was 440 mm by 75 mm with a thickness of 4 mm. The strain on the FRP was monitored using 12 strain gauges symmetrically placed on the FRP surface, and the bond stress was derived based on the differential FRP stress.

A typical load–displacement curve was developed using the test procedure. The curves were analyzed and the key points on the curves discussed. Results demonstrated that water jetting improved the bond only minimally. Sandblasting, on the other hand, significantly increased the bond strength, but the highest bond strength was achieved by jackhammering. The debonding factor was developed to read the asymmetry of the strain distribution during loading, which would ultimately lead to the ability to accurately map the progression of the debonding between FRP and concrete. The debonding factor developed in this experiment showed a promising results, and more testing should be done to determine its accuracy. The debonding factor would allow a computer to detect the propagation of the debonded region and notify the appropriate authorities before catastrophic failure of the structure took place.

11.3 Dynamic behavior of the FRP–concrete bond

The specimen developed was used to understand the debonding mechanism under impact loading. An impact setup was successfully developed to measure the bond stress and fracture energy of the FRP–concrete bond. It was discovered that if the specimen was not prevented from vertical movements at the supports, within a very short period of first contact of hammer with the specimen, contact with the support was lost and as a result, loads read by the support load cells were not correct. This phenomenon was further verified by using a high-speed camera. To overcome this problem, the vertical movement of FRP strengthened beams at the supports was restrained using two steel yokes. In order to assure that the beams are still simply

supported, these yokes are pinned at the bottom. Support anvils in addition to the tup were instrumented in order to obtain the valid and true bending load directly from the experiment at any time.

Strain gauges were used to monitor the strain of FRP during the test. The strain differential of FRP was used to calculate the FRP-Concrete bond shear stress. A National Instruments VI Logger, a flexible tool specifically designed for data logging applications, was used and data from up to 16 channels were recorded with a frequency of 100 kHz.

The bond behavior under impact loading was successfully evaluated and compared. Of all surface treatments, sandblasting proved to most enhance the effect on the ductility of bond under dynamic loading. Water jetting is the second best method. Jackhammering decreases the ductility and strength of the sprayed FRP bond to concrete owing to micro-cracks it creates on the surface of the concrete, and it is not generally recommended as a method of surface treatment. Mechanical fasteners reduced the ductility and strength of the bond between sprayed FRP and concrete; however, they improved the same parameters in wrapped FRP.

Beams sprayed with FRP showed slightly better shear strength and ductility under impact loading when water-jetting and sandblasting treatment methods were used. On the other hand, beams wrapped with FRP showed significantly better results when jack-hammering and mechanical fasteners were used. This showed that the wrapping method is less sensitive to the micro-cracks created on the concrete surface by surface preparation.

11.4 Strain rate sensitivity of the FRP–concrete bond

Using the impact setup and variable drop heights, the strain sensitivity of FRP was studied. FRP–concrete bond strength was found to be a strain sensitive parameter

that increases as the strain rate increases. A correlation was found to relate the dynamic improvement factor (DIF) to strain rate for different surface preparation types.

The following relationship was developed to govern the correlation between DIF and strain rate, where strain rate is in seconds^{-1} in which the factors *a* and *b* are given in Table 9.4.

$$\text{DIF} = ae^{b\dot{\varepsilon}}$$

Specimens with lower initial quasi static strength showed higher improvement (higher DIFs) compared with the specimens with higher initial quasi-static strength (more effective surface preparation). This suggested that under impact loading the crack tends to go through the stronger components of system as well, including the cement paste.

11.5 Finite element modeling of FRP–concrete bond behavior

An attempt was made to calibrate the energy and traction parameters of the cohesive element in ABAQUS to reproduce the same load displacement behavior as observed in the test from a modeled beam. Even though the same unzipping phenomenon was not produced, however, a reasonably close load vs. displacement behavior was achieved. Future research is necessary to develop a practical bond finite element. With proper fracture criteria, the model predicted very similar displacement and ultimate load values.

11.6 Future research

The following areas of future research are recommended:

1. Higher bond strength values under impact compared with quasi-static bond values mean that longer bond length is required to observe the full un-zipping

phenomena. It is recommended that larger beams be used in future research on the bond between FRP and concrete.

2. The impact study described here was limited to the evaluation of the dynamic response of the bond between sprayed FRP and concrete. This limitation was due to unsuccessful measurement methods for wrapped FRP strain using strain gauges. Future research is encouraged to either eliminate the need to use strain gauges in evaluating the dynamic behavior of the bond or to develop an accurate method of incrementing wrapped FRP. \

3. Future research is also recommended to develop a practical finite element that accurately models the FRP–concrete bond. This will enable the designers to predict the response of more complex structures designed or strengthened with FRP under different loading scenarios.

BIBLIOGRAPHY

1.1 ASCE Report on New Jersey Bridges, 2006: http://sections.asce.org/newjersey/bridges.html.

2.1. Meier, U. (1995), "Strengthening of structures using carbon fibre/epoxy composites". *Construction and Building Materials*, 9(6): 341–351.

2.2. Austin, S.A. and Robins, P.J. (1993), "Development of patch test to study behavior of shallow concrete patch repairs." *Magazine of Concrete Research,* 45(164): 221–229.

2.3. Austin, S.A. and Robins, P.J. (1995), "A unified failure envelope from the evaluation of concrete repair bond tests." *Magazine of Concrete Research,* 47(170): 57–68.

2.4. Weimer, C. and Haupert, F. (2000), "Influence of aggregate structure on mode-III interfacial fracture between concrete and CFRP." *Applied Composite Materials,* Kluwer Academic Publishers, Netherlands, 7: 183–193.

2.5. Etman, E.E. and Beeby, A.W. (2000), "Experimental programme and analytical study of bond stress distributions on a composite plate bonded to a reinforced concrete beam." *Cement & Concrete Composites*, 22: 281–291

2.6. Lim, Y.K. and Li, V.C. (1997), "Durable repair of aged infrastructure using trapping mechanism of engineered cementitious composites." *Cement & Concrete Composites*, 19: 373–385.

2.7. Kuneida M., Kurihara, K., Uchida Y., and Pokugo, K. (2000), "Application of tension softening diagrams to evaluation of bond properties at concrete interfaces." *Engineering Fracture Mechanics,* 65: 299–315.

2.8. Sun, R., SuanSuwan, N., Kilpatrick, N., and Swain, M. (2000), "Characterization of tribochemically assisted bonding of composite resin to porcelain and metal." *Journal of Dentistry,* 28: 441–445.

2.9. Ali, M., Kurihara, S., and Matsui, S. (1998), "Bonding shear strength at the interface between old and new concrete." *Technology Reports of Osaka University,* 48(2327): 237–246.

2.10. Ming, J., and Sansalone, M. (1996), "Impact-echo studies of interfacial bond quality in concrete: Part I – Effects of unbonded fraction of area." *ACI Materials Journal,* 93(3): 223–232.

2.11. Ming, J., Sansalone, M., and Poston, R. (1996), "Impact-echo studies of interfacial bond quality in concrete: Part II – Effects of bond tensile strength of area." *ACI Materials Journal,* 93(3): 223–232.

2.12. Wilson, A., Sbiaa, Z., Hopcroft, M., and Laskowski, B.C. (2001), "MEMS adhesive bond degradation sensor." *Proceedings of SPIE,* 4236, 252–259.

2.13. Saiidi, M., Vrontinos, S., and Douglas, B. (1990), "Model for the response of concrete beams strengthened by concrete overlays." *ACI Structural Journal,* 87(6): 687–695.

2.14. Granju, J.L. (2001), "Debonding of thin cement based overlays," *Journal of Materials in Civil Engineering,* 13(2): 114–120.

2.15. Rahman, M.K., Baluch, M.H., and Al-Gadhiv, A.H. (2000), "Simulation of shrinkage distress and creep relief in concrete repair." *Composites,* 31: 541–553.

2.16. Warner, J., Bhuyan, W., Smoak, G., Hindo, K.R., and Sprinkel, M.M. (1998), "Surface preparation of overlays." *Concrete International,* May: 43–46.

2.17. Kasselouri, V., Koulombi, N., and Thompoulos, Th. (2001), "Performance of silica fume–calcium hydroxide mixture as a repair material." *Cement & Concrete Composites,* 23: 103–110.

2.18. Banthia, N. ,Benmokrane, B. and Karbhari, V. (2006), *Durability of Fiber Reinforced Polymers in Civil Infrastructure*, ISIS Canada.

2.19. Xiao, J., Li, J. and Zha, Q. (2004), "Experimental study on bond behavior between FRP and concrete", *Construction and Building Materials*, 18(10): 745–752.

2.20. Woods, J. (2003), Accelerated Testing for Bond Reliability of Fiber-Reinforced-Polymers (FRP) to Concrete and Steel in Aggressive Environments, Ph.D. Thesis, The University of Arizona.

2.21. Karbhari, V.M., Engineer, M., and Eckel, D.A. (1997), "On the durability of composite rehabilitation schemes for concrete: use of a peel test." *Journal of Materials Science*, 32(1): 147–156.

2.22. Au, C. and Büyüköztürk, O. (2006), "Peel and shear fracture characterization of debonding in FRP plated concrete affected by moisture." *ASCE Journal of Composites for Construction,* 10(1): 35–47.

2.23. Soutis, C., Duan, D-M., and Goutas, P. (1999), "Compressive behavior of CFRP laminates repaired with adhesively bonded external patches." *Composite Structures,* 45: 289–301.

2.24. Abrams, D.A. (1917), "The effect of rate of application of load on the compressive strength of concrete". *Proceedings ASTM*, 17: 364–365.

2.25. Atchley, B.L. and Furr, H.L. (1967), "Strength and energy absorption capabilities of plain concrete under dynamic and static loadings." *ACI Journal*, 64: 745–756.

2.26. Scott, B.D., Park, R., and Priestley, M.J.N. (1982), "Stress strain behaviour of concrete confined by overlapping hoops at low and high strain rates." *ACI Journal*, 79(1): 13–27.

2.27. Dilger, W., Koch, R., and Kowalczyk, R. (1984), "Ductility of plain and confined concrete under different strain rates." *ACI Journal*, 81: 73–81.

2.28. Malkar, P.F. Vitaya-Udom, K.P., and Cole, R.A. (1985), "Dynamic tensile-compressive behaviour of concrete." *ACI Journal*, 82(4): pp 484–491.

2.29. Soroushian, P., Choi, K-B., and Alhamad, A. (1986), "Dynamic constitutive behaviour of concrete." *ACI Journal*, 83: 251–259.

2.30. Watstein, D. (1953), "Effect of straining rate on the compressive strength and elastic properties of concrete." *ACI Journal*, 49(8): 729–744.

2.31. Malvar, L.J. and Ross, C.A. (1998), "Review of strain rate effects for concrete in tension." *ACI Material Journal*, 95(6): 735–739.

2.32. Sparks, P.R., and Menzies, J.B. *(*1973), "The effect of rate of loading upon the static and fatigue strengths of plain concrete in compression." *Magazine of Concrete Research*, 25(83): 73–80.

2.33. Spooner, D.C. (1971), "Stress-strain-time relationships for concrete." *Magazine of Concrete Research*, 23(75/76): 127–131.

2.34. US Department of the Army Technical Manual (1990), *Design of Structures to Resist the Effects of Accidental Explosions*. TM 5-1300.

2.35. Norris, G.H., Hansen, R.J., Holly, M.J., Biggs, J.M., Namyet, S., and Minami, J.K. (1959), *Structural Design for Dynamic Loads*. McGraw-Hill Book Company Inc., New York, USA,

2.36. Wakabayashi, M., Nakamura, T., Yoshida, N., Iwai, S., and Watanabe, Y. (1980), "Dynamic loading effects on the structural performance of concrete and steel materials and beams." *Proceedings of the 7th World Conference on Earthquake Engineering*, Istanbul, Turkey, Vol. 6, pp. 271–278.

2.37. Fu, H.C., Erik, M.A., and Seckin, M. (1991), "Review of effects of loading rate on reinforced concrete." *Journal of Structural Engineering*, 117(12): 3660–3679.

2.38. Malvar, L.J. (1998), Review of static and dynamic properties of steel reinforcing bars. *ACI Material Journal*, 95(5): 609–616.

2.39. Bertero, V.V., Rea, D., Mahin, S., and Atalay, M.B. (1973), "Rate of loading effects on uncracked and repaired reinforced concrete members." *Proceedings of 5th World Conference on Earthquake Engineering*, Rome, Vol. 1, pp. 1461–1470.

2.40. Takeda, J. and Tachikawa, H. (1971), Deformation and fracture of concrete subjected to dynamic load. *Proceedings of the International Conference on Mechanical Behaviour of Materials*, Kyoto, Japan, pp. 267–277.

2.41. Banthia, N.P. (1987), *Impact Resistance of Concrete*. PhD Thesis, The University of British Columbia, Vancouver, BC.

2.42. Bentur, A., Mindess, S. and Banthia, N. (1986), "The behaviour of concrete under impact loading: experimental procedures and method of analysis." *Materials and Structures*, 19(5): 371–378.

2.43. Kishi, N., Nakano, O., Matsuoka, K.G., and Ando, T. (2001), "Experimental study on ultimate strength of flexural-failure-type RC beams under impact loading." *Proceedings of the International Conference on Structural Mechanics in Reactor Technology*, Washington, DC, Paper # 1525, 7 pages.

2.44. Ando, T., Kishi, N., Mikami, H., and Matsuoka, K.G. (2000), "Weight falling impact tests on shear-failure type RC beams without stirrups." *6th International Conference on Structures under Shock and Impact.* Editors: N. Jones and C.A. Brebbia. Cambridge, England, UK, pp. 579–587.

2.45. Kishi, N., Mikami, H., and Ando, T. (2002), "Impact-resistance behavior of shear-failure-type RC beams under falling-weight impact loading." *7th International Conference on Structures under Shock and Impact*, Editors: A.M. Rajendran, N. Jones, and C.A. Brebbia. Montreal, Quebec, Canada, pp. 499–508.

2.46. Kishi, N., Mikami, H., Matsuoka, K.G., and Ando, T. (2002) "Impact behavior of shear-failure-type RC beams without shear rebar." *International Journal of Impact Engineering*, 27: 955–968.

2.47. Abbas, H., Gupta, N.K., and Alam, M. (2004), "Nonlinear response of concrete beams and plates under impact loading." *International Journal of Impact Engineering*, 30: 1039–1053.

3.1. Young, J.F., Mindess, S., Gray, R.J. and Bentur, A. (1997), *The Science and Technology of Civil Engineering Materials*, Prentice Hall. pp 192–193.

3.2. Soleimani Ziabari, S.M. (2007), Sprayed Glass Fiber Reinforced Polymers in Shear Strengthening and Enhancement of Impact Resistance of Reinforced Concrete Beams. Ph.D. Thesis, The University of British Columbia, Vancouver, BC.

3.3. Boyd, A.J. (2000), *Rehabilitation of Reinforced Concrete Beams with Sprayed Glass Fiber Reinforced Polymers*. Ph.D. Thesis, The University of British Columbia, Vancouver, BC.

3.4. ASTM International (1985), Standard Test Method for Ignition Loss of Cured Reinforced Resins. ASTM D 2584-68, 2 pages.

3.5. http://wbaweb.buffnet.net/main_pages/mbrace_eg900.htm

3.6. ASTM International (2000). Standard Test Method for Tensile Properties of Polymer Matrix Composite Materials. ASTM D 3039, 13 pages.

7.1. Banthia, N. (1987), *Impact Resistance of Concrete*, Ph.D. Thesis, The University of British Columbia, Vancouver, BC.

9.1. Comite Euro-International du Beton (CEB) (1988), *Concrete Structures under Impact and Impulsive Loading*, Bulletin No. 187.

9.2. Ross, C.A. (1997), "Review of strain rate effects in materials, structures under extreme loading conditions," *ASME Pressure Vessels and Piping Conference*, July 27–33, pp. 257–262.

9.2. Zhang, L. (2008), *Impact Resistance of High Strength Fibre Reinforced Concrete,* . Ph.D. Thesis, The University of British Columbia, Vancouver, BC,